

Interfacial Behaviour and Foaming Potential of Polymer-coated Nanoparticles

Kai Yu

Submitted in accordance with the requirements for the degree of

Doctor of Philosophy

The University of Leeds

School of Chemical and Process Engineering

December, 2017

The candidate confirms that the work submitted is his own, except where work which has formed part of jointly-authored publications has been included. The contribution of the candidate and the other authors to this work has been explicitly indicated below. The candidate confirms that appropriate credit has been given within the thesis where reference has been made to the work of others.

The research relating to the adsorption of PVP on silica (Paper 1) is presented in Chapter 3. The foaming studies investigating foamability and stability (Paper 2) are presented Chapter 4. The interfacial rheology study of composite particle-laden air-water interfaces (Paper 3) is reported in Chapter 5.

Published papers or manuscripts in review:

1. Yu, K.; Hodges, C.; Biggs, S.; Cayre, O. J.; Harbottle, D. Polymer molecular weight dependence on lubricating particle-particle interactions. *Submitted to Industrial & Engineering Chemistry Research*, DOI: 10.1021/acs.iecr.7b04609.

2. Yu, K.; Zhang, H.; Hodges, C.; Biggs, S.; Xu, Z.; Cayre, O. J.; Harbottle, D. Foaming Behavior of Polymer-Coated Colloids: The Need for Thick Liquid Films. *Langmuir* 2017, 33 (26), 6528-6539.

3. Yu, K.; Zhang, H.; Biggs, S.; Xu, Z.; Cayre, O. J.; Harbottle, D. Interfacial rheology of composite particle-laden interfaces. *Submitted to Langmuir, reviewed – corrections to be submitted in 2018.*

4. Zhang, H.; Yu, K.; Cayre, O. J.; Harbottle, D. Interfacial Particle Dynamics: One and Two Step Yielding in Colloidal Glass. *Langmuir* 2016, 32 (50), 13472-13481.

The PhD candidate (Kai Yu) performed all experimental work and prepared the first draft for Papers 1, 2 and 3. Experimental guidance was initially provided by Dr. Zhang and Dr. Hodges for the DWR interfacial rheology and AFM measurements, respectively – Paper 2. The co-authors, Dr. Huagui Zhang, Dr. Chris Hodges, Prof. Simon Biggs, Prof. Zhenghe Xu, Prof. Olivier Cayre, and Prof. David Harbottle supervised the research and provided guidance to improve the quality of the submitted manuscripts.

This copy has been supplied on the understanding that it is copyright material and that no quotation from the thesis may be published without proper acknowledgement.

The right of Kai Yu to be identified as Author of this work has been asserted by her accordance with the Copyright, Designs and Patents Act 1988.

Acknowledgements

It was 31st August 2014 that I arrived in Leeds and started my PhD. It was from that day that I was introduced into a brand new world, a world that built on nanoscale. Driven by curiosity, each day became so important and every little effort was put together to make the whole story better. Three years go pass very quickly, and at the end of my PhD, I would like to show my gratitude to everybody who had ever given me a hand.

I truthfully appreciate the help from Associate Profs. David Harbottle and Olivier Cayre who offered excellent ideas and supervisions. They are always ready to give constructive suggestions when the project is not proceeding well, whilst pointing out the problems to stop me going astray. To provide a better understanding of the mechanism of foam stability, David helped me with the application for the research mobility award. The award enabled me to do some research in University of Alberta (Canada) using a unique equipment – the Interfacial Shear Rheometer (ISR400), which is not available in Leeds. The visit also provided a great opportunity for me to develop my academic skills and network. Except from academic research, David and Olivier also provided strong supports to my personal life when misfortune happened. To me, David and Olivier are not only supervisors of my PhD but also real friends of mine.

Prof. Zhenghe Xu helped me a lot when I was in Canada. Although he is extremely busy, he kept finding out time to meet with me and provided helpful suggestions. I am particularly grateful to Prof. Simon Biggs who offered me the PhD offer in the first

place. He paid closely attention to my project and spent a lot of time on my first paper that being published in Langmuir.

I would like to thank Dr. Chris Hodges for his help with the AFM measurements, who also trained me how to use the QCM-D and OR. Dr. Huagui Zhang, and Dr. Yuanyuan Zhou gave me tremendous supports when I newly arrived, and we became very close friends in the coming days. Thanks to Dr Timothy Hunter's advices whenever I presented my data in the group meeting. Thanks to Dr Nicole Hondow's help in the cryo-SEM and cryo-TEM experiments. Thanks to everybody in our research group for their help and encouragement.

I sincerely thank for the funding from China Scholarship Council - University of Leeds Scholarship (CSC NO. 201406450027).

Finally, I want to show my deeply gratitude to my great parents, my close friends and family members. I could not make any achievements without their support.

Abstract

The current study examines the interfacial behaviour and foaming potential of poly(vinylpyrrolidone) (PVP, 40 kDa)-silica composite nanoparticles. Individually, the two components, PVP and hydrophilic silica nanoparticles, exhibit very little foaming potential. In contrast, combining the two components to form silica-PVP core-shell nanocomposites via polymer physisorption leads to good ‘foamability’ and long-term foam stability. Optical reflectivity (OR) measurements showed that the adsorption of PVP on silica can be regarded as irreversible with the saturated polymer surface excess around 1 mg/m^2 , in good agreement with the thermogravimetric analysis (TGA) data. The adsorbed 40 kDa PVP film is highly hydrated (contained water 40-55 wt%), behaving as a steric barrier, which helps to keep the particles apart.

Addition of an electrolyte (Na_2SO_4) was shown to have a marked effect on the foam stability. By varying Na_2SO_4 concentration between 0 and 0.55 M, three regions of foam stability were observed: rapid foam collapse ($\leq 0.01 \text{ M}$), delayed foam collapse at 0.1 M, and long-term stability (~ 10 days) at 0.55 M. The observed transitions in foam stability were better understood by studying the microstructure and rheological properties of the particle-laden interfaces using different techniques such as Langmuir trough, Interfacial Shear Rheometer (ISR400), Brewster angle microscopy (BAM) and cryo scanning electron microscope (cryo-SEM). Meanwhile, the 2D structure of particle-laden interfaces surrounding an air bubble and deposited at a planar interface were correlated using cryo-SEM and BAM images to elucidate the interfacial shear rheology of particle-stabilized bubbles and its relation to foam stability.

For rapidly collapsing foams, the interfaces were characterized as being “liquid-like”. By contrast, the enhanced foam stability at 0.1 M and 0.55 M Na₂SO₄ was attributed to the formation of solid-like (pseudo solid-like for the 0.1 M particle layer) interfacial particle layers surrounding bubbles, at a compression state in the region of the liquid to solid (L-S) phase transition. The increased interfacial rigidity was attributed to adhesion between interpenetrating polymer layers. For the most stable foam (prepared in 0.55 M Na₂SO₄), particles strongly aggregated at the interface into a connected particle network, forming a strongly elastic interfacial layer. Hence, bubble-bubble coalescence was found to be significantly retarded by the aggregation of nanocomposite particles at 0.55 M, with the long term destabilization resulting from bubble coarsening. For rapidly destabilizing foams, however, the contribution from bubble-bubble coalescence was shown to be more significant. Further investigations need to be carried out to prevent bubble coarsening.

Table of Contents

Acknowledgements	III
Abstract	V
Table of Contents	VII
List of Figures	XI
List of Tables	XXII
Abbreviations	XXIII
Chapter 1: Introduction	1
1.1 Aqueous Foams	1
1.2 Research Novelty and Opportunities	2
1.3 Research Aim and Objectives	4
1.4 Thesis Outline	5
Chapter 2: Theoretical Background and Literature Review	8
2.1 Polymers in Solution and Adsorption at the Solid-liquid Interface	8
2.1.1 Polymers in solution	9
2.1.2 Adsorption of polymers at a solid-liquid interface	10
2.2 Particles at Liquid Interfaces	12
2.2.1 Particle wettability and desorption energy	13
2.2.2 Microgel particles at liquid interfaces	15
2.2.3 Pseudo-microgel particles at liquid interfaces	18
2.2.4 Interfacial aggregation of particles	19

2.3 Aqueous Foams, Foamability and Foam Stability	20
2.3.1 Foam destabilization	20
2.3.2 Aqueous foams stabilized by particles	24
2.3.3 Long lived foams and foam based light-weight materials	29
Chapter 3: PVP Adsorption on Silica Surface and Lubricating Properties of the Adsorbed PVP Films.....	33
3.1 Synopsis	33
3.2 Literature Review.....	34
3.2.1 Poly(vinylpyrrolidone) (PVP).....	34
3.2.2 Lubricating properties of polymer films	36
3.3 Materials and Experimental Methods	39
3.3.1 Materials.....	39
3.3.2 Experimental methods.....	39
3.4 Results and Discussion.....	46
3.4.1 PVP adsorption measured by OR.....	46
3.4.2 PVP film hydration	50
3.4.3 PVP Sauerbrey film thickness and conformation	54
3.4.4 Lubrication effects	59
3.5 Conclusion	64
Chapter 4: Foaming Behaviour of PVP-coated Silica Particles.....	65
4.1 Synopsis	65
4.2 Literature Review.....	66

4.2.1 Foaming potential of surfactant-particle composites and interfacial rheology	68
4.2.2 Foaming potential of polymers and polymer-surfactant mixtures	70
4.2.3 Foaming potential of microgel particles and pseudo-microgel particles	71
4.3 Materials and Experimental Methods	72
4.3.1 Materials.....	72
4.3.2 Experimental methods.....	73
4.4 Results and Discussion.....	81
4.4.1 Characterization of composite particles	81
4.4.2 Foamability and foam stability	84
4.4.3 Compression, microstructure and relaxation of the particle-laden interfaces	90
4.4.4 Interfacial rheology of deposited particle layers.....	99
4.4.5 Interaction forces between PVP coated surfaces	102
4.4.6 Optical microscope observations	104
4.4.7 Discussion of foam destabilization mechanism	109
4.5 Conclusion	112
Chapter 5: Interfacial Rheology of Composite Particle-laden Planar and Curved Interfaces.....	114
5.1 Synopsis	114
5.2 Literature Review.....	115
5.3 Materials and Experimental Methods	120

5.3.1 Characterization of particle-laden interfaces	120
5.3.2 Cryo-SEM	127
5.4 Results and Discussion.....	128
5.4.1 <i>IT</i> -A isotherms and interfacial structure (BAM).....	128
5.4.2 Linear rheology	135
5.4.3 Nonlinear rheology	140
5.4.4 Rheology of particle-laden interfaces surrounding bubbles	143
5.5 Conclusion	147
Chapter 6: Conclusions and Future Work.....	149
6.1 Conclusions.....	149
6.1.1 PVP adsorption and lubricating properties of PVP films	149
6.1.2 Foaming behaviour of the composite particles	150
6.1.3 Interfacial rheology of composite particle-laden planar and curved interfaces	151
6.2 Initial Investigations and Future Work	152
6.2.1 Increase particle surface coverage and solidify particle-laden interface...	152
6.2.2 Seal the pores on the bubble surface and rigidify the particle-laden interface using beta-escin.....	154
6.2.3 Enhance particle affinity at the interface and increase the yield stress of the particle-laden interface.....	156
List of References	158

List of Figures

Figure 1.1 Commonly used foams in the natural world and as used in various products: (1) a freezing bubble, (2) detergency, (3) foams in beer, (4) foams in ice cream, (5) foams in fire extinguisher, (6) foams in makeup remover.	2
Figure 1.2 Flow diagram of the thesis outline.....	5
Figure 2.1 Schematic of polymer conformations in solution when $\alpha > 1$, $\alpha = 1$ (R_g), and $\alpha < 1$ respectively.....	9
Figure 2.2 Schematic of a simplified conformation of an adsorbed polymer chain on a solid surface. ³⁰	10
Figure 2.3 Possible conformations of adsorbed single polymer chain at a liquid-solid interface: ³¹ (a) adsorbing by single point; (b) adsorbing by loops; (c) adsorbing with flat conformation; (d) adsorbing by random coil; (e) adsorbing with non-uniform segment distribution; (f) multilayer adsorption.	11
Figure 2.4 Rearrangement of an adsorbed polymer chain on a solid surface. ³⁰	12
Figure 2.5 (a) Particle location at the oil-water interface depending on the particles contact angle; (b) Deformation of the particle-stabilized film as a consequence of the particles contact angle ⁴⁷	13
Figure 2.6 Relationship between particle desorption energy and particle radius at the air-water interface, assuming the particle contact angle is 90° . The dashed line shows the desorption energy for most surfactants.	15
Figure 2.7 Temperature and pH dependence of the mean hydrodynamic diameter of PNIPAM microgel particles in an aqueous dispersion. ⁵²	16
Figure 2.8 Schematic of deformed microgel particles at the oil-water interface. ¹⁸	16

Figure 2.9 Scheme illustrating the effect of cross-linker density on the microgel conformation at the interface. The higher cross-linked microgel particle is less deformable due the densely cross-linked core. ⁵⁶	17
Figure 2.10 Π -A isotherms of pMMA ₁₆ -b-pDMAEMA ₂₅₄ stabilized PS latexes particles as a function of the sub-phase pH at the air-liquid interface. ⁵⁸	18
Figure 2.11 Image of a draining foam: bubbles near the top of the foam are considered “dry” and polyhedral, while bubbles near the bottom of the foam are considered “wet” and spherical. ⁹	21
Figure 2.12 Schematic of foam demonstrating for the dependence on the liquid volume fraction. ⁷¹	22
Figure 2.13 Time sequence of a dry foam coarsening. ⁷⁰	22
Figure 2.14 Possible mechanisms for film rupture: (B–C) direct rupture, (B–M–C) via bilayer to monolayer transition and (B–V–C) via void formation. ⁷³	23
Figure 2.15 (a) Images of particle dispersions in water, particle stabilized wet foams and water-in-air powders. Particles become increasingly hydrophobic from left to right with increasing surface SiOR groups. ⁷ (b) Advancing contact angle, θ , of pure water droplets on flat surfaces formed from fumed silica particles of different percentages of surface SiOR groups (SiOR% = 100 - SiOH%). ⁹	25
Figure 2.16 Schematic of (a) air-in-water foams and (b) water-in-air powders; (c) Photo of water drops in air stabilized by particles. ⁷	26
Figure 2.17 Schematic of PDMA-PS particles as a pH- and temperature-responsive foam stabilizer. Images show aqueous solutions of the PDMA homo-polymer at different pH and temperature conditions. ⁷⁵	28
Figure 2.18 Schematic of PDEA-PS particles as a temperature-responsive foam stabilizer. ⁴⁹	29

Figure 2.19 Foamability and foam stability of foams that stabilized by amphiphiles-particle composites (C_a : concentration of n-amylamine, C_p : concentration of particles). ⁷⁶	30
Figure 2.20 (a) Image of foam based porous materials prepared using 15.7 wt% silica particles (d_{50} (agglomerate) $\sim 3.5 \mu\text{m}$, particle density: $\sim 2.1 \text{ g/cm}^3$) and 2.2 wt% tetradecyl trimethyl ammonium bromide (TTAB); (b) SEM image of the formed foam structure. ³⁷	31
Figure 2.21 Capillary foams prepared using polyvinyl chloride particles ($d_{50} = 14.8 \mu\text{m}$, particle density = 1.41 g/cm^3 , particle concentration $> 20 \text{ wt}\%$), bulk fluid (water based), and a secondary fluid which is Trimethylolpropane trimethacrylate (TMPTMA). ^{77, 78}	32
Figure 3.1 Structural formula of a PVP molecule.....	34
Figure 3.2 Interactions between silica and PVP through hydrogen bond. ⁸⁹	36
Figure 3.3 Correlation between lubrication and conformation of polymer brushes. ¹⁰⁴	38
Figure 3.4 Schematic of the OR working principle.	41
Figure 3.5 Images of the E4 QCM-D system (a), the flow channel (b), and the quartz crystal oscillator (c).....	42
Figure 3.6 Schematic of the lateral force measurement using colloid probe technique.	44
Figure 3.7 Surface excess isotherms for (a) 40 kDa PVP and (b) comparison of isotherms for 8 kDa, 40 kDa, 360 kDa and 1300 kDa PVP measured by OR at $25 \text{ }^\circ\text{C}$	46

Figure 3.8 Adsorption kinetics for 8 kDa PVP as a function of the PVP concentration measured by OR. Adsorption kinetics described by Eq. 3.3 are shown as solid lines. Arrows indicate the injection time of Milli-Q water (rinse-off).	47
Figure 3.9 Adsorption kinetics for 40, 360 and 1300 kDa PVP measured by OR at 1 ppm. Adsorption kinetics described by Eq. 3.3 are shown as solid lines. Arrows indicate the injection time of Milli-Q water (rinse-off).	49
Figure 3.10 Initial PVP adsorption rate dependence on the PVP concentration and molecular weight. Semi-log data shown inset.	50
Figure 3.11 Time dependent resonance frequency (black filled squares) and dissipation (red filled triangles) for 8 kDa, 40 kDa, 360 kDa, and 1300 kDa PVP at 1 ppm. Arrows indicate the injection time of Milli-Q water (rinse-off).	51
Figure 3.12 PVP molecular weight dependent equilibrium surface excess as determined by Sauerbrey and Voigt models, PVP concentration = 1 ppm.....	52
Figure 3.13 Adsorption kinetics for 1 ppm PVP of different molecular weights measured by both OR (black squares) and QCM-D (red circles). Arrows indicate the injection time of Milli-Q water (rinse-off).....	53
Figure 3.14 Equilibrium surface excess as a function of the PVP molecular weight measured by OR and QCM-D.....	54
Figure 3.15 Comparison of the PVP Sauerbrey film thickness and the QCM-D equilibrium dissipation as a function of the PVP molecular weight at 1 ppm.....	55
Figure 3.16 ΔD as a function of Δf for the 1300 kDa PVP at 1 ppm. All the $\Delta D/\Delta f$ values shown should be multiplied by a factor of 10^{-6} . Schematic to show the likely polymer orientation to reach the equilibrium state.	56
Figure 3.17 ΔD as a function of Δf for the 8 kDa 40 kDa and 360 kDa PVP at 1 ppm. All the $\Delta D/\Delta f$ values shown should be multiplied by a factor of 10^{-6}	59

Figure 3.18 Lateral forces measured between silica-silica, 8 kDa PVP-PVP, 40 kDa PVP-PVP, 360 kDa PVP-PVP, and 1300 kDa PVP-PVP surfaces by a colloid AFM probe.....	60
Figure 3.19 Suspension viscosity (closed symbols) and shear stress (open symbols) as a function of the applied shear rate for a 59 vol% uncoated silica suspension. Dashed line represents the Herschel-Bulkley model used to determine the suspension yield stress (τ), consistency index (k) and flow index (n), see Table 3.1.	62
Figure 3.20 Suspension yield stress as a function of the apparent particle volume fraction for uncoated silica particles (No PVP), 8 kDa and 40 kDa PVP coated silica particles in water.	63
Figure 4.1 Self-assembled PVP coated (a) Ag nano-cubes, (b) Ag octahedra, (c) Ag nanowires and (d) Au nanoprisms films at the air-water interface. ^{120, 121, 122}	67
Figure 4.2 Crumpled bubbles stabilized by surfactant-particle composites. ¹²⁶	69
Figure 4.3 Schematic of a thin liquid film stabilized by polymer–surfactant complexes, Δh indicates the distance between two neighbouring polymer branches. ¹⁷	71
Figure 4.4 Schematic of composite particle preparation.....	74
Figure 4.5 Schematic of the Langmuir-Blodgett deposition method.....	78
Figure 4.6 Image of a stress-controlled Discovery Hybrid Rheometer equipped with a double wall ring (DWR) geometry.	79
Figure 4.7 SEM image of the silica colloid mounted on a tipless silicon nitride AFM cantilever.....	80
Figure 4.8 (a) TGA data for silica nanoparticles, PVP, and composite particles; (b) TEM image of the formed composite particles.....	82

Figure 4.9 Measured hydrodynamic diameter of composite particles (symbol: circle), and particle electrophoretic mobility (symbol: square) as a function of the electrolyte concentration. Lines to guide the eye.....	84
Figure 4.10 Contact angle of a sessile drop at rest on PVP coated silicon wafer as a function of the electrolyte concentration.	85
Figure 4.11 Air-aqueous surface tension in the presence of 0.5 wt% PVP as a function of the electrolyte concentration.....	87
Figure 4.12 (a) Time-dependent stability of foams prepared using composite particles as a function of the electrolyte concentration (lines to guide the eye); (b) Images showing changes in foam height with aging time. The electrolyte concentrations are shown below each glass vial depicted at t = 1 min. Height of glass vial = 9 cm.....	88
Figure 4.13 Time-dependent liquid volume fractions for 0.1 M and 0.55 M Na ₂ SO ₄ foams. Data calculated from foam heights in Fig. 4.12b.	90
Figure 4.14 Π-A isotherms for silica and composite particles spread at the air-aqueous interface. The particle concentration and spreading volume were fixed at 0.5 wt% and 40 μL, respectively. The inflection points were identified by the changing of the isotherm slope.	92
Figure 4.15 Compressional elasticity of composite particle layers deposited on aqueous sub-phases of increasing electrolyte concentration 0.01 M, 0.1 M and 0.55 M Na ₂ SO ₄	93
Figure 4.16 SEM images showing the surface pressure dependent micron-scale structure of deposited composite particle layers transferred from the air-aqueous interface. Sub-phase electrolyte concentration equal to 0 M, 0.01 M, and 0.1 M, as labelled. Trough area and film surface pressure provided for each micrograph.....	95

Figure 4.17 SEM images showing the micron-scale structure of deposited silica particle layers transferred from the air-aqueous interface at minimum trough area. Sub-phase electrolyte concentrations as labelled.....	96
Figure 4.18 Relaxation/reorganization of particle layers compressed to a constant surface pressure of (a) 7 mN/m and (b) 3 mN/m.	97
Figure 4.19 First and second compression isotherms for a composite particle film deposited on 0.01 M Na ₂ SO ₄ . Inset: equivalent data for a composite particle film deposited on 0.55 M Na ₂ SO ₄	98
Figure 4.20 Strain dependent viscoelasticity of the composite particle layers spread at the air-aqueous interface. Sub-phase electrolyte concentration: 0.01 M, 0.1 M and 0.55 M Na ₂ SO ₄ ; particle spreading concentration = 0.5 wt%; spreading volume = 10 μL.	101
Figure 4.21 AFM force curves showing the influence of Na ₂ SO ₄ concentration on the interactions between two approaching PVP coated silica surfaces using the colloid probe method. (a) Approach force curves shown on a linear scale; inset shows the adhesion data obtained between PVP polymer coated silica surfaces. (b) Approach force curves shown on a semi-log scale including the AdG theory (solid line) with fitting parameters $s = 1.69$ nm and $L = 31$ nm; inset highlighting the likely interactions between the approaching polymer layers in a poor solvent. (i) out of contact, (ii) jump-in due to intersegment attraction, (iii) push-through associated with the fusion of polymer layers.....	103
Figure 4.22 Average bubble size (symbol: closed squares) and number of bubbles (symbol: closed triangles) as a function of the foam aging time. Open symbols (circle) correspond to the time-dependent growth of a typical bubble (electrolyte concentration	

= 0.1 M Na₂SO₄). The inset shows an optical microscope image of fresh foam bubbles prepared in 0.1 M Na₂SO₄..... 105

Figure 4.23 Image time sequence demonstrating an increase in bubble size and polydispersity in a foam prepared in 0.1 M Na₂SO₄ electrolyte solution. 106

Figure 4.24 Average bubble size (symbol: closed squares) and number of bubbles (symbol: closed triangles) as a function of foam aging time. Electrolyte concentration = 0.55 M Na₂SO₄. The inset shows an optical microscope image of fresh foam bubbles prepared in 0.55 M Na₂SO₄..... 107

Figure 4.25 Optical microscope images of an isolated bubble aging in 0.55 M electrolyte solution. 108

Figure 4.26 Time-dependent changes in the size of individual bubbles: (a) small bubbles, and (b) large bubbles. (c) Normalized bubble size (b_i/b_0) and coarsening time (t_i/t_∞) for nine selected bubbles. Empirical fitting is described by Eq. 4.5. Foams prepared by dispersing composite particles in 0.55 M Na₂SO₄. 109

Figure 5.1 Structure of silica particle monolayer at the octane-water interface, the particle contact angle in (a) and (b) is 65° and 152° respectively.¹⁵⁹ 116

Figure 5.2 Time-dependant aggregation of octyl-coated silica particles at the air–toluene interface (a) t = 4 min, (b) t = 90 min, (c) t = 270 min, and (d) t = 400 min.⁶⁷ 117

Figure 5.3 Schematic to represent the likely particle-laden structures formed via the (a) RLCA and (b) DLCA processes, the red lines denote the “bond” between particle clusters.⁴⁸ 117

Figure 5.4 Phase diagram illustrating two regimes of interfacial particle dynamics as a function of particle concentration and shear rate.¹⁶² 119

Figure 5.5 Summary of the interfacial particle forces: (1) force required to push particles into the bulk; (2) force required to displace particles laterally along the interface; (3) force due to gravity. ¹⁶³	119
Figure 5.6 Image of the Brewster angle microscope combined with Langmuir trough.	121
Figure 5.7 Working principle of the Brewster angle microscopy	122
Figure 5.8 Image of (a) the Interfacial Shear Rheometer (ISR400) with Langmuir trough and (b) schematic of the magnetic needle positioned in the glass channel at the air-water interface. ¹⁶⁶	124
Figure 5.9 Photos of (a) the cryo-SEM system, (b) the cryo transfer device with a universal specimen shuttle (AL200077B) and (c) the Quilo cryo preparation chamber with the twin fracturing manipulators.....	128
Figure 5.10 Π -A isotherms of composite particles deposited at the air-aqueous interface, with the particle concentration and spreading volume remained fixed at 0.5 wt% and 80 μ L, respectively. The surface pressure was measured continuously at a compression rate of 50 cm^2/min . All particle-laden interfaces exhibit gas (G), liquid (L), and solid (S) phase transitions, with collapse of the particle-laden interfaces measured at approximately $\sim 50 \text{ cm}^2$	130
Figure 5.11 BAM images of deposited composite particles at the air-water interface as a function of the sub-phase electrolyte concentration (0.01 M, 0.1 M, and 0.55 M as labelled) and surface pressures. Increasing electrolyte concentration increases voidage in the particle-laden films, which can be attributed to aggregation of the composite particles. Surface pressure driven densification of the particle-laden films is qualitatively verified by reduced voidage and increased brightness of the BAM images.	133

Figure 5.12 Apparent particle surface coverage (ϕ) of 0.1 M and 0.55 M Na₂SO₄ particle-laden interfaces. BAM images were processed using ImageJ, first correcting for varying illumination using a band pass filter and thresholded to differentiate between the sub-phase and particle layer..... 134

Figure 5.13 (a) Dynamic surface shear moduli (G' – closed symbols and G'' – open symbols) and (b) G'/G'' ratio of the particle-laden interfaces as a function of the sub-phase electrolyte concentration and surface pressure. The magnetic needle was oscillated at constant frequency ($\omega = 3.14$ rad/s) and amplitude in the linear viscoelastic region. The dynamic surface shear moduli were determined using Eq. 5.1. 136

Figure 5.14 Frequency dependent viscoelastic moduli (G' – closed symbols and G'' – open symbols) of the particle-laden interfaces as a function of the sub-phase electrolyte concentration and surface pressure. The power-law scaling confirms the transition from liquid-like at $\Pi = 0.5$ mN/m (all systems) to solid-like behaviour with increasing surface pressure and sub-phase electrolyte concentration..... 140

Figure 5.15 Dynamic strain sweep of an elastically dominant particle-laden interface (0.01 M Na₂SO₄). At small strains the dynamic shear moduli are independent of strain before the particle-laden interface yields ($G' = G''$) at higher strains, lines to guide the eye. 141

Figure 5.16 (a) Yield modulus ($G' = G''$) and (b) apparent yield strain and apparent yield stress (0.1 M Na₂SO₄) of particle-laden interfaces as a function of the surface pressure and the sub-phase electrolyte concentration. The apparent yield strain and apparent yield stress were determined based on the cross-over ($G' = G''$) condition as shown in Fig. 5.15..... 143

Figure 5.17 Schematics of a particle positioned at (a) a planar interface and (b) a curved interface. The particle centre is point B and the bubble centre is point F. Centre-to-contact line (BC), and edge-to-contact line (AD) are identified by the dashed lines.....	144
Figure 5.18 Particle-laden interfaces surrounding air bubbles: a) 0.1 M Na ₂ SO ₄ foam, and b) 0.55 M Na ₂ SO ₄ foam. The individual bubbles are shown in the inset of the higher magnification interfacial images.....	145
Figure 6.1 (a) Images of sample 1 and sample 2 when t = 150 min; (b) Measured foam height for sample 1 and sample 2 as a function of time.	153
Figure 6.2 Viscoelasticity of beta-escin films as a function of time and solution concentration, measured by PhD student Emily James in our group.....	155
Figure 6.3 (a) Time-dependent stability of foams prepared using 0.1 wt% beta-escin in water, 0.1 wt% beta-escin in 0.55 M Na ₂ SO ₄ , 0.1 wt% beta-escin + 1 wt% composite particles in 0.55 M Na ₂ SO ₄ , and 1 wt% composite particles in 0.55 M Na ₂ SO ₄ (lines to guide the eye); (b) Images showing changes in foam height with aging time. Sample 1: 0.1 wt% beta-escin in water; sample 2: 0.1 wt% beta-escin in 0.55 M Na ₂ SO ₄ ; sample 3: 0.1 wt% beta-escin + 1 wt% composite particles in 0.55 M Na ₂ SO ₄ . Height of glass vial = 9 cm.....	156

List of Tables

Table 1.1 Stabilization mechanisms for aqueous foams stabilized by different stabilizers.	3
Table 5.1 Strain sweep settings for the ISR measurements.	126
Table 5.2 Frequency sweep settings for the ISR measurements.	127
Table 5.3 Average compressibility of particle-laden interfaces in the L- and S-phase.	131

Abbreviations

PVP: poly(vinylpyrrolidone)

IPA: isopropanol alcohol

OR: optical reflectivity

QCM-D: quartz crystal microbalance with dissipation monitoring

TGA: thermogravimetric analysis

AFM: atomic force microscopy

SEM: scanning electron microscope

TEM: transmission electron microscopy

Cryo-SEM: cryo scanning electron microscope

LB: Langmuir-Blodgett deposition method

Π-A: surface pressure-area

BAM: Brewster angle microscope

ISR: Interfacial Shear Rheometer

DWR: double wall ring

Chapter 1: Introduction

This chapter provides a brief introduction to aqueous foams (the focus of this study) and the commonly used foaming agents, including surfactants, particles, and polymers. Subsequently, research novelty, research aims and objectives are highlighted. Finally, an outline of the topics to be discussed in each chapter of the thesis are given.

1.1 Aqueous Foams

Foams can be classified into two main groups: solid foams and wet foams (predominantly aqueous foams) according to the nature of the continuous phase. Solid foams fabricated with metals and polymers have been applied in catalysis, thermal and sound insulation, drug delivery, and tissue engineering, etc.¹ As shown in Fig. 1.1, aqueous foams are also commonly encountered and have wide applications in detergency (e.g. laundry detergent and dishwashing), food science (e.g. ice cream, coffee and beer), cosmetics and personal care products (e.g. makeup remover, shower gel, shampoo and toothpaste), foam extinguisher (to isolate O₂), enhanced oil recovery² (bubbles can deform when going through porous medium and exert pressure on the trapped oil), and mineral flotation (carriers for mineral particles).^{3, 4, 5, 6, 7, 8}



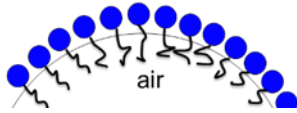
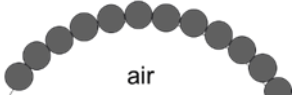
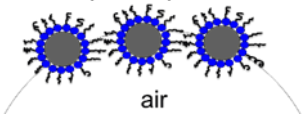

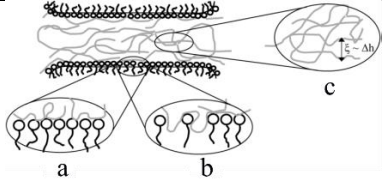
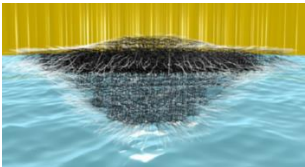
Figure 1.1 Commonly used foams in the natural world and as used in various products: (1) a freezing bubble, (2) detergency, (3) foams in beer, (4) foams in ice cream, (5) foams in fire extinguisher, (6) foams in makeup remover.

However, aqueous foams are thermodynamically unstable and destabilize very quickly through different de-foaming mechanisms such as evaporation, coarsening, liquid drainage and coalescence.⁹ Hence, making stable foams that can meet demands for different areas and applications is a challenging task, which has given rise to lots of research interests in the past decades.¹⁰

1.2 Research Novelty and Opportunities

So far, several agents have been shown to be effective foam stabilizers, for example surfactants, surfactant mixtures,⁹ surfactant-polymer mixtures,¹¹ solid colloidal particles,¹⁰ surfactant-particle mixtures,¹² microgel particles,¹³ and pseudo-microgel particles (formed by grafting polymers onto the surface of solid particles)¹⁴. Foaming potential of these foaming agents will be heavily influenced by their behaviours at the air-water interface, and the related mechanisms for foam stabilization are described in Table 1.1.

Table 1.1 Stabilization mechanisms for aqueous foams stabilized by different stabilizers.

Foam stabilizers	Schematics	Stabilization mechanism
Surfactants	<p style="text-align: center;">Aqueous phase</p>  <p style="text-align: center;">air</p>	<p>Disjoining pressure¹⁵</p> <p>Surface tension reduction¹⁰</p>
Solid particles	<p style="text-align: center;">Aqueous phase</p>  <p style="text-align: center;">air</p>	<p>Solid barrier formation surrounding bubbles¹⁰</p>
Surfactants + Particles	<p style="text-align: center;">Aqueous phase</p>  <p style="text-align: center;">air</p>	<p>Solid barrier formation and surface tension reduction¹⁰</p>
Polymers	<p style="text-align: center;">Aqueous phase</p>  <p style="text-align: center;">air</p>	<p>Poor foam stability due to weak adsorption of polymers at the gas-liquid interface¹⁶</p>
Surfactants + Polymers		<p>Increase the surface viscosity; steric repulsion between two approaching fluid interfaces¹⁷</p>
Microgel particles		<p>Deform at the interface to increase their desorption energy; response to environmental stimulus¹⁸</p>

To the best of our knowledge, the interfacial behaviour and foaming behavior of polymer-particle composites formed via polymer physisorption has not been considered in detail, despite the fact that polymers such as poly(vinylpyrrolidone) (PVP) are commonly used as co-stabilizers in many food, pharmaceutical, cosmetic and detergent formulations.¹⁶ PVP is widely used in formulating products because of its good solubility in water and organic solvents, as well as its ability to strongly adhere on different materials.^{11, 19, 20} The simpler physisorption than chemical grafting of polymer on nanoparticles is advantageous, especially when mass manufacturing is required for desired day-to-day applications. Polymers such as PVP adsorb at many sites per nanoparticle, and therefore are not likely to desorb once attached to the nanoparticle surface, which is also an important factor when removing excess surface active species prior to the needed formulation.²¹

The physical presence of such polymers can drastically modify the particle affinity at the interface, whilst controlling particle–particle interaction to adjust the structure and mechanical strength of interfacial layers, which will in turn influence the foamability and foam stability of the polymer-particle composite system.

1.3 Research Aim and Objectives

Aim: Investigate the governing mechanisms of foam stabilization using PVP-coated silica nanoparticles (composite particles).

Objectives:

(1) Understand the adsorption behaviour of PVP on silica surface and the lubricating properties of the adsorbed PVP films.

(2) Prepare PVP coated silica composite particles (composite particles); understand the interfacial behaviour of the composite particles and their overall foaming behaviour.

(3) Understand the interfacial rheology of composite particle-laden planar interfaces and rheology surrounding bubbles.

1.4 Thesis Outline

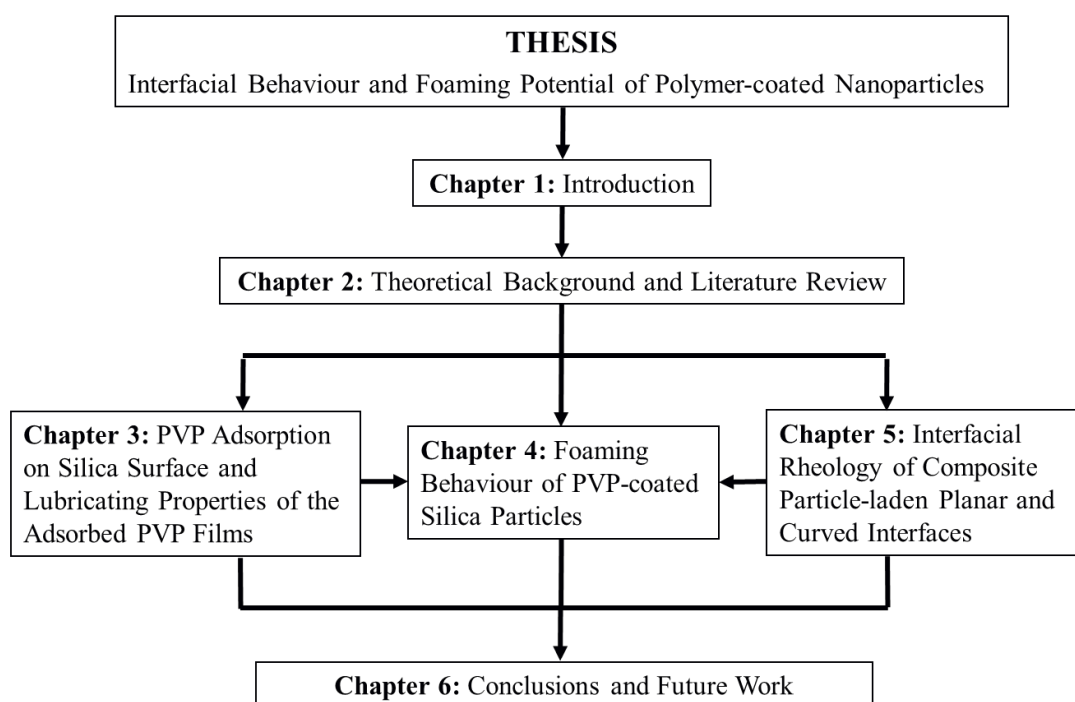


Figure 1.2 Flow diagram of the thesis outline.

A flow diagram highlighting the main contributions of the thesis is shown in Fig. 1.2. The adsorption of PVP (8 kDa, 40 kDa, 360 kDa and 1300 kDa) on silica was studied in Chapter 3 using optical reflectometry (OR) and Quartz Crystal Microbalance with Dissipation monitoring (QCM-D). OR measurements showed that the adsorption of PVP on silica was irreversible, with the saturated surface excess around 1 mg/m^2 . QCM-D data suggested that the 8 kDa PVP films were less hydrated

(~ 10 wt% trapped water), forming flat conformation (predominantly train orientation) on silica surface; while the high molecular weight PVPs (40 kDa, 360 kDa and 1300 kDa) slowly reorganized into more lossy films (loops and tails), with more water being contained (40-55 wt%). The lubricating properties of the adsorbed PVP films at the silica-water interface were measured by an atomic force microscope (AFM). The resultant lubrication effect was then highlighted by measuring the suspension rheology of uncoated and PVP-coated silica particles. The studies presented in Chapter 3 provide the fundamental knowledge for the composite particle preparation via polymer adsorption.

In Chapter 4, PVP (40 kDa)-coated silica composite particles (composite particles) were prepared (via polymer physisorption). The adsorbed 40 kDa PVP films are highly hydrated, behaving as steric stabilizers to separate the particles. Foaming behaviour of the composite particles was examined, and addition of an electrolyte (Na_2SO_4) was shown to have a marked effect on the foam stability. By varying the concentration of electrolyte between 0 and 0.55 M, three regions of foam stability were observed: rapid foam collapse (≤ 0.01 M), delayed foam collapse at 0.1 M, and finally long-term stability (~ 10 days) at 0.55 M. The observed transitions in foam stability were better understood by studying the microstructure and physical and mechanical properties of the particle-laden interface.

Chapter 5 develops these initial observations to elucidate the structure-rheology relationship for the composite particle-laden interfaces surrounding bubbles, an important property to better understand the foaming behavior presented in Chapter 4. The interfacial shear rheology of the composite particle-laden planar interfaces was first measured as a function of both the sub-phase electrolyte concentration and surface pressure using an Interfacial Shear Rheometer (ISR400) with a Langmuir

trough. The surface pressure-dependent rheology was correlated to the micron-scale structure of the particle-laden interfaces imaged using Brewster angle microscopy (BAM). These structures were further studied using cryo-scanning electron microscope (cryo-SEM) of particle-stabilized bubbles in foams. Combining different techniques (ISR, BAM and cryo-SEM), we are able to elucidate the likely rheology for particle-laden interfaces surrounding bubbles.

Thesis conclusions are provided in Chapter 6. This research was aimed at understanding the interfacial behaviour and foaming potential of polymer-nanoparticle composites. PVP coated silica composite particles (composite particles) were prepared via polymer physisorption, and the composite particles were shown to be effective foaming agents. Foam lifetimes were shown to increase with increasing electrolyte concentration, and the enhanced foam stability (0.1 M and 0.55 M) was attributed to the formation of solid-like (elastic dominant) interfacial particle layers surrounding bubbles. The absence of bubble coalescence in foams prepared using 0.55 M Na_2SO_4 was linked to the formation of large particle aggregates, preventing the formation of thin liquid films (plateau borders) between neighbouring bubbles, and bubble coarsening was identified to be the dominant foam destabilization mechanism in this chase. Opportunity for future work is also summarized.

**It is important to note that the materials and methods discussion is provided in each results chapter rather than a combined chapter. Due to the numerous techniques used throughout the study it was thought to be the most appropriate way of presenting the information.

Chapter 2: Theoretical Background and Literature

Review

This chapter generally reviews the existing literature which sets the context for the results sections of this thesis. Section 2.1 considers polymers in solution and their ability to adsorb at solid-liquid interfaces. Particle behaviours at liquid interfaces is discussed in Section 2.2. Section 2.3 summarizes the mechanisms of foam destabilization and reviews the foaming behaviours of the foaming agents utilized in the current study, which is helpful to better understand the foamability and foam stability of our PVP-coated silica composite particles.

More critical literature reviews relating to the experimental activities of the thesis can be found in each results chapter (Chapters 3, 4 and 5).

2.1 Polymers in Solution and Adsorption at the Solid-liquid Interface

A polymer is a macromolecule composed of many monomer units, which is named a homo-polymer if all the repeating monomers are identical, and otherwise a co-polymer. Polymers are commonly used in formulated products, behaving as foaming agents, rheology modifiers and steric stabilisers, etc. These macromolecules are able to form complex structures at the solid-liquid interface through self-assembly, which is a potential candidate for fabricating novel materials.^{22, 23} Surface modifications using self-assembled polymer layers are time and cost saving, whilst providing a straightforward route to coat surfaces with complexed shapes.²⁴ All those above-mentioned applications involve polymers in a bulk liquid or at interfaces (solid-liquid, liquid-liquid, and gas-liquid).

2.1.1 Polymers in solution

An isolated polymer chain can embody a series of conformations in solution depending on the solution quality or the net interactions between segments. In an ideal solvent where the net polymer segment-segment interactions are zero, the polymer chain is left unperturbed with a conformation called a random coil. An important length scale for an unperturbed polymer coil is the radius of gyration, R_g :

$$R_g = \frac{l\sqrt{n}}{\sqrt{6}} \quad (2.1)$$

where l and n are the length and number of segments respectively. R_g is regarded as the effective coil size for polymer chains in solution.

In a real solvent however, the apparent size of polymer coil can be larger or smaller than R_g depending on the solvent quality, and it is sometimes called the Flory radius, R_F , where $R_F = \alpha R_g$ (α is the expansion factor). In a good solvent, for instance, the net segment-segment interactions are repulsive, resulting in an expanded polymer coil ($\alpha > 1$). By contrast, the segments attract each other and the coil shrinks in a poor solvent ($\alpha < 1$), see Fig. 2.1.

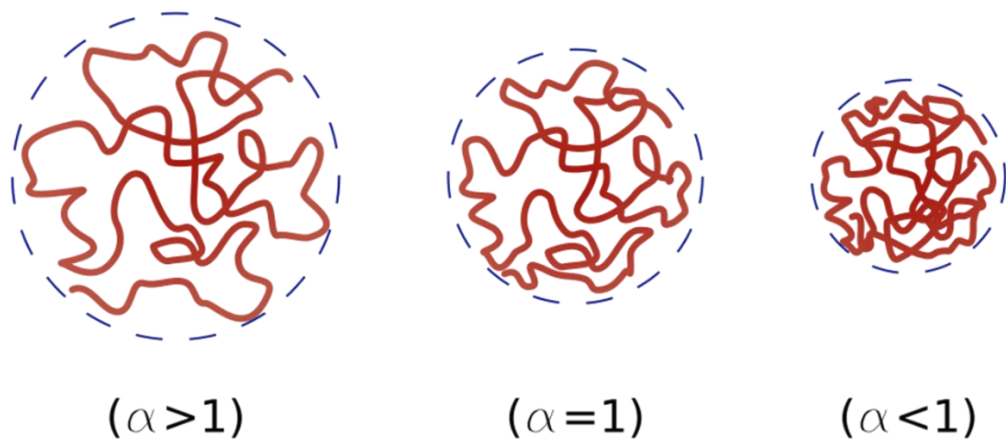


Figure 2.1 Schematic of polymer conformations in solution when $\alpha > 1$, $\alpha = 1$ (R_g), and $\alpha < 1$ respectively.

2.1.2 Adsorption of polymers at a solid-liquid interface

Polymers are able to self-assemble into nanoscale structure at the solid-liquid interface through physical absorption, which is found to be important for surface modifications, including: surface wettability, roughness, hardness, tribological properties, and surface-surface interactions.^{22, 25, 26, 27}

Adsorption normally leads to a conformational change of the polymer chain, from a random coil in the solution (see Fig. 2.1) to a more extended structure at the solid-liquid interface (see Fig. 2.2) with many attached segments to the surface.²⁸ Hence, the adsorption affinity per segment does not need to be high in order for the adsorption free energy of the whole polymer chain to compensate for the entropy loss upon adsorption.²⁹ The critical free energy needed for polymer adsorption was found to be $\sim 0.3 k_B T$ per segment (k_B is the Boltzmann constant, T is the thermodynamic temperature),³⁰ which can be easily satisfied by various interactions (between polymer molecules and solid surfaces), including electrostatic interactions, covalent interactions, hydrophobic forces and hydrogen bonding, etc.²¹ The adsorption of polymers on solids can be usually regarded as irreversible because of the small possibility that all the adsorbed train segments desorb from the surface simultaneously.²⁸

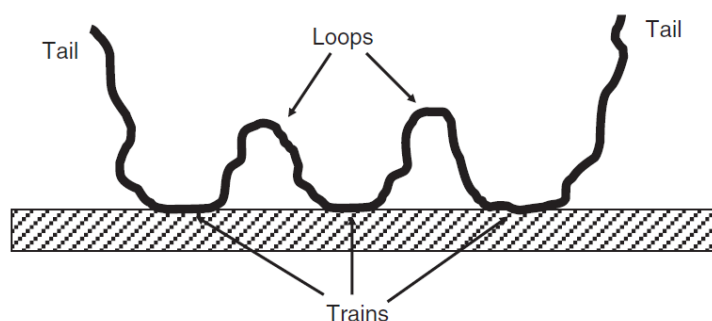


Figure 2.2 Schematic of a simplified conformation of an adsorbed polymer chain on a solid surface.³⁰

A simplified conformation of an adsorbed polymer chain on a solid surface is shown in Fig. 2.2, which shows segments attached to the surface in trains, separated by segments extending into the solution as loops and tails.³⁰ The fraction of train segments is an important parameter for describing the conformation of an adsorbed polymer layer, with this fraction having been reported to be 0.3 - 0.5 for uncharged polymers adsorbing on mineral surfaces.²⁸ In practice, polymer chains can form more complicated conformations on solid surfaces depending on the polymer molecular weight, polymer structure (e.g. homo-polymer or co-polymer, etc.), polymer concentration in the bulk solution, solvent quality (good solvent or bad solvent), available adsorption sites on the surface, and binding strength between polymer and surface (see Fig. 2.3).³¹

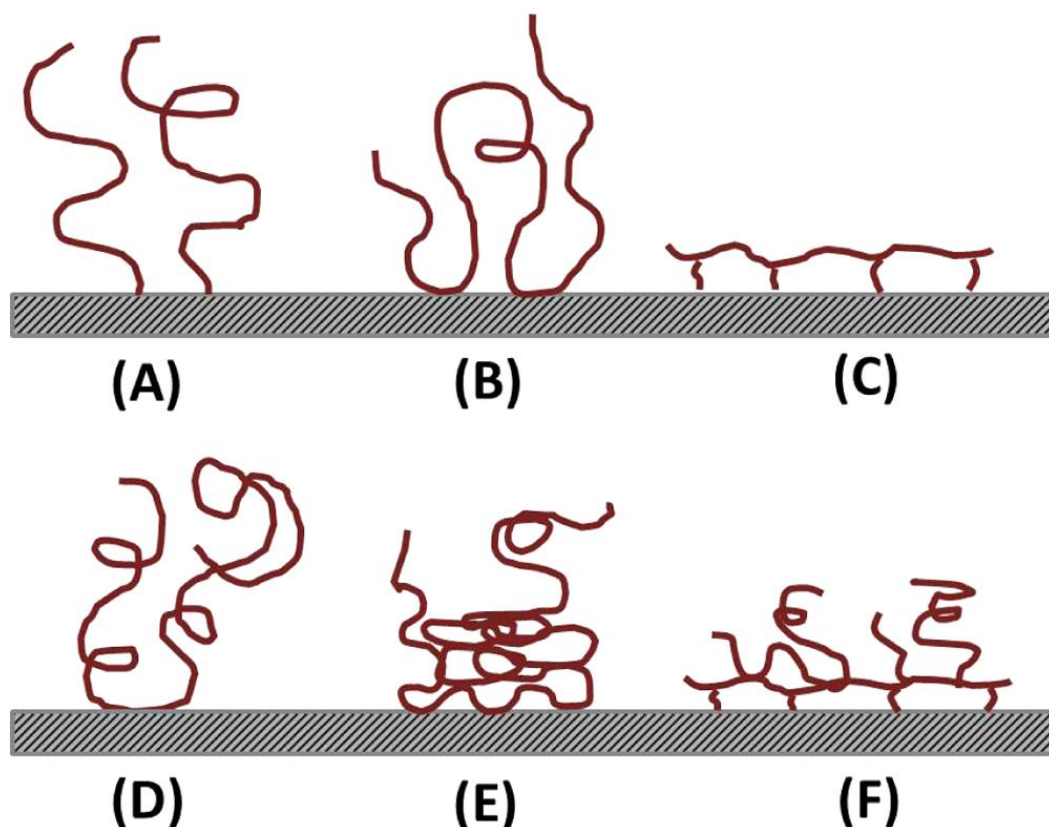


Figure 2.3 Possible conformations of adsorbed single polymer chain at a liquid-solid interface:³¹ (a) adsorbing by single point; (b) adsorbing by loops; (c) adsorbing with

flat conformation; (d) adsorbing by random coil; (e) adsorbing with non-uniform segment distribution; (f) multilayer adsorption.

The initial polymer adsorption on a solid surface is influenced by the polymer conformation in the bulk liquid, after which rearrangement of the adsorbed polymer chains may take place on the solid surface. An example is given in Fig. 2.4: after adsorption, the polymer chains collapse towards the surface to form a flatter conformation very quickly, within micro-seconds or seconds;³⁰ however, the final equilibrium state may take significantly longer time because of the slow rearrangement of the adsorbed polymer chains.

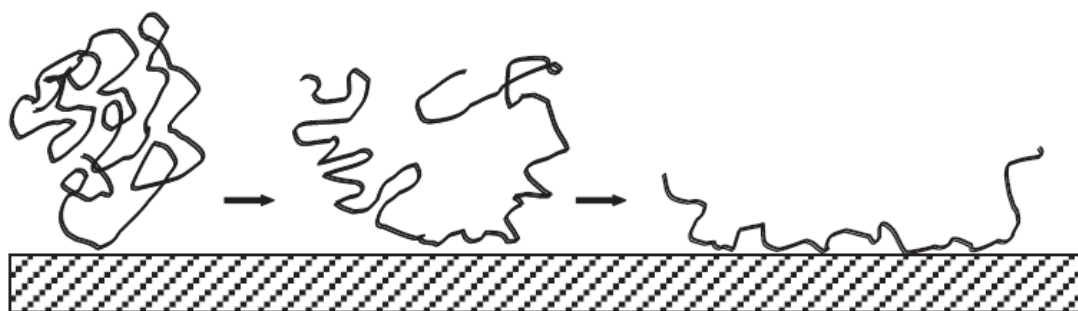


Figure 2.4 Rearrangement of an adsorbed polymer chain on a solid surface.³⁰

2.2 Particles at Liquid Interfaces

Colloidal particles at liquid interfaces (air–liquid or liquid–liquid) are of critical importance from both industrial and academic point of views due to their crucial role in stabilizing foams and emulsions and the related applications in cosmetics, food industries, pharmaceuticals, drug delivery, and oil recovery, etc.^{3, 4, 32, 33, 34, 35} These particle-laden films also provide routes for novel materials synthesis such as porous textures,³⁶ light-weight materials,³⁷ 2D arrays of nanocrystals,³⁸ microcapsules,³⁹ bijels,⁴⁰ membranes, photonic materials, and templates for nanowire arrays.^{41, 42}

2.2.1 Particle wettability and desorption energy

2.2.1.1 Wettability of particles. The potential for particles to reside at a liquid interface is determined by the particles wettability,⁴³ represented by the three phase contact angle (θ),¹⁰ which is measured in the aqueous phase. For example, for an oil-water interface the contact angle is given by:

$$\cos \theta = \frac{\gamma_{po} - \gamma_{pw}}{\gamma_{ow}} \quad (2.2)$$

where γ_{po} , γ_{pw} , γ_{ow} are the interfacial tensions of particle - oil, particle - water and oil - water interfaces respectively.¹⁰ Particles have equal preference to the water and oil phases when $\theta = 90^\circ$. Typically, hydrophilic particles are described as having a contact angle $\theta < 90^\circ$ ($\gamma_{po} > \gamma_{pw}$), whereas $\theta > 90^\circ$ ($\gamma_{po} < \gamma_{pw}$) indicates the particles are more hydrophobic (see Fig. 2.5a).^{10, 44, 45, 46} Hydrophilic particles normally stabilize oil-in-water (O/W) emulsions, while water-in-oil (W/O) emulsions can be stabilized using hydrophobic particles as the emulsifying agent (see Fig. 2.5b).^{10, 47}

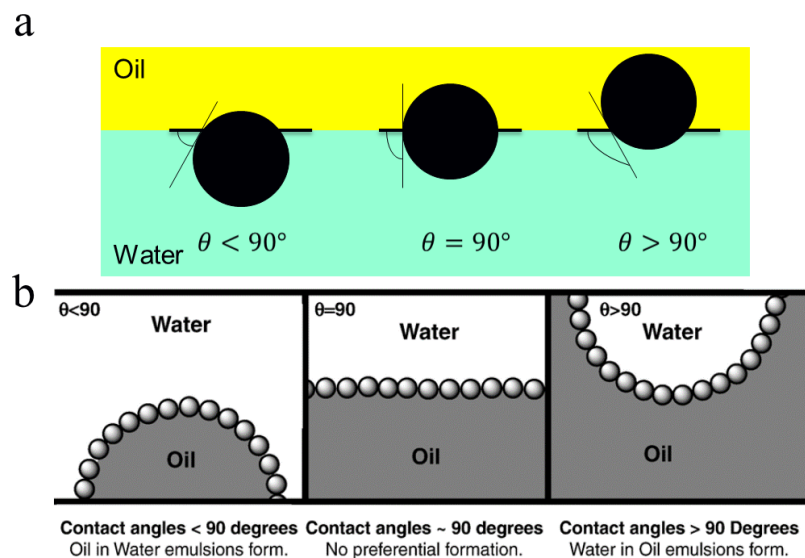


Figure 2.5 (a) Particle location at the oil-water interface depending on the particles contact angle; (b) Deformation of the particle-stabilized film as a consequence of the particles contact angle⁴⁷.

2.2.1.2 Desorption energy of particles. Once a particle is pinned at the liquid (α)-liquid (β) interface, a certain area of the interface is substituted by an equivalent area of the particle (cross-sectional area). Ignoring contributions from gravity, the energy required to remove a particle from the interface is related to the particle contact angle θ , the particle radius r , and the surface tension $\gamma_{\alpha\beta}$, and is given by

$$W_r = \pi r^2 \gamma_{\alpha\beta} (1 \pm \cos\theta)^2 \quad (2.3)$$

where the sign inside the bracket is negative for particle removal into the polar phase, and positive for particle removal into the non-polar phase.¹⁰ For a given particle, assuming that $r = 3.4 \times 10^{-8}$ m (34 nm), $\gamma_{\alpha\beta} = 0.072$ N/m (air-water surface tension), and $\theta = 90^\circ$, then the required detachment energy $W_r \sim 60000$ kT . The enormous desorption energy suggests that the particle adsorption can be considered almost irreversible.

Apart from particle wettability, W_r can also be heavily affected by particle size. Assuming $\gamma_{\alpha\beta} = 0.072$ Nm^{-1} and $\theta = 90^\circ$, the relationship between the desorption energy and particle radius is shown in Figure 2.6. Clearly, the desorption energy of very small particles ($r \leq 0.5$ nm) is in the order of ~ 10 kT , comparable to most surfactant molecules (the dashed line shown in Fig. 2.6). While W_r value increases by 4 orders of magnitude as the particle radius increases from 1 nm to 100 nm. From this perspective, increased foam stability in the presence of Brownian-like particles can be achieved by enhancing particle aggregation at the air-liquid interface, as shown in our recent publication.⁴⁸

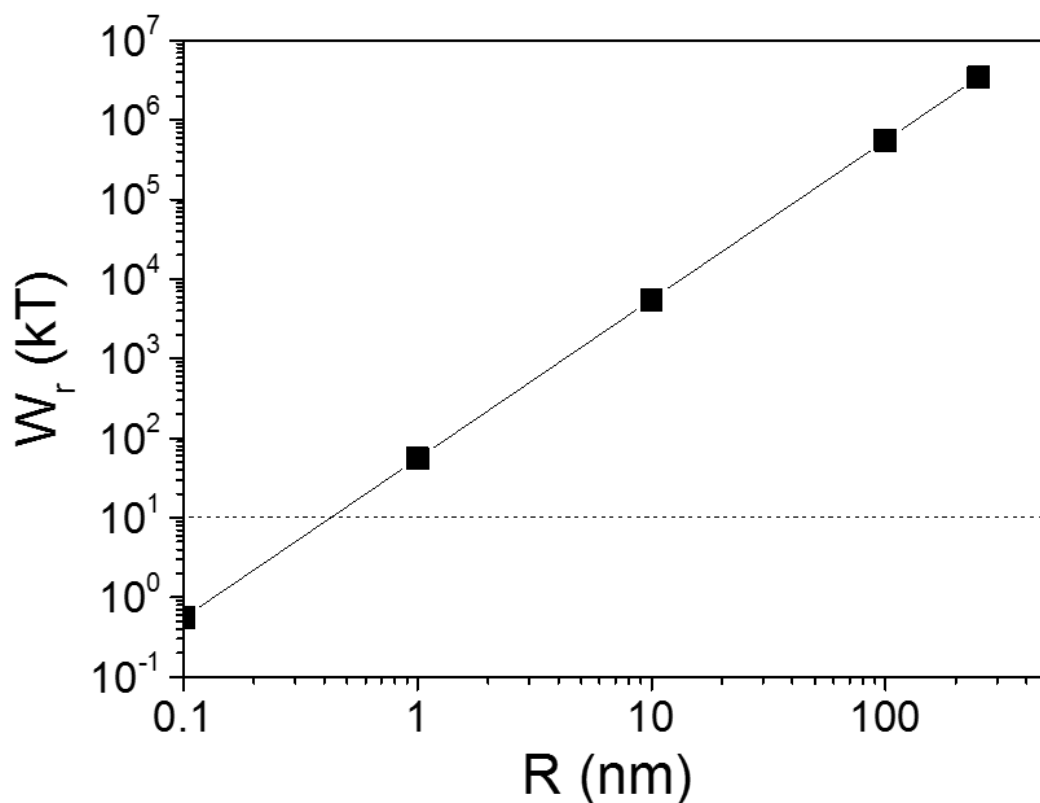


Figure 2.6 Relationship between particle desorption energy and particle radius at the air-water interface, assuming the particle contact angle is 90° . The dashed line shows the desorption energy for most surfactants.

2.2.2 Microgel particles at liquid interfaces

More recently, polymer microgel particles which consist of a highly cross-linked network of high molecular weight polymers was found to be efficient foam and/or emulsion stabilizers.⁴⁹ The microgel particles are considered to be mechanically ‘soft’ since they are intermediates between hard particles and soft polymers, and thus can deform significantly. Therefore, interfacial behaviour of these microgel particles are expected to be different from that of hard spheres.

For instance, PNIPAM microgel particles exhibit a dramatic decrease in particle size around the lower critical solution temperature (LCST, $\sim 32^\circ\text{C}$) as shown in Fig. 2.7a,^{50, 51} whilst remaining sensitive to pH changes (see Fig. 2.7b). Fig. 2.7 suggests

that the hydrophobicity of the PNIPAM microgels can be increased by decreasing the pH and/or raising the liquid temperature.⁵²

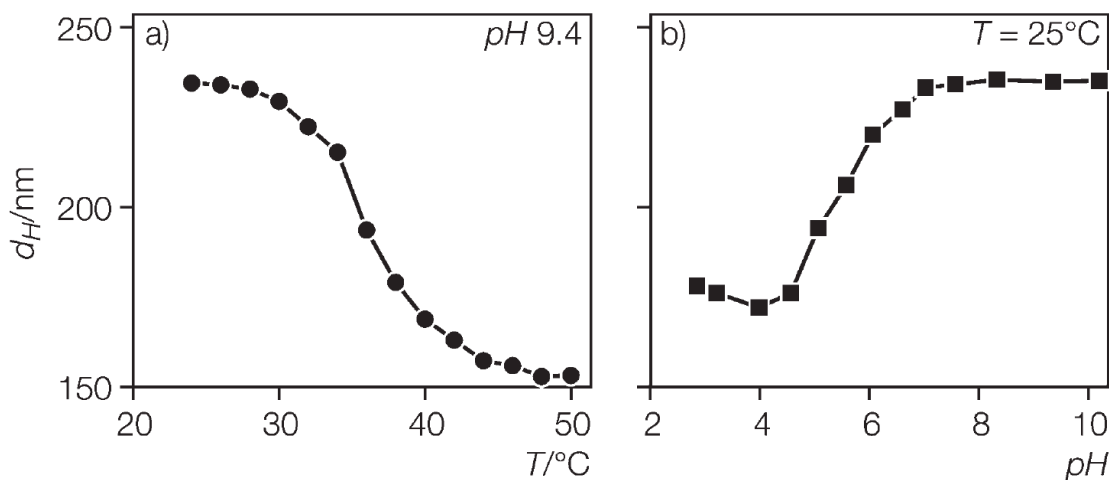


Figure 2.7 Temperature and pH dependence of the mean hydrodynamic diameter of PNIPAM microgel particles in an aqueous dispersion.⁵²

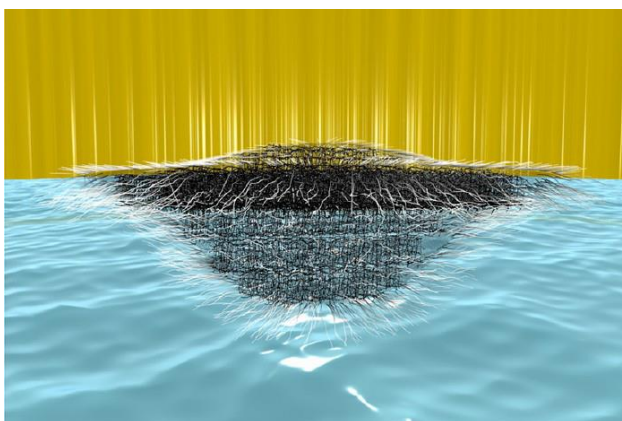


Figure 2.8 Schematic of deformed microgel particles at the oil-water interface.¹⁸

In contrast to solid spheres, deformation of the microgel particles can occur both in a bulk liquid and at liquid-liquid interfaces, although the microgel particles can behave similarly to hard spheres in a bulk liquid when the particle concentration was low, with significant particle deformation not measured until the microgel particles were highly packed (high particle concentration).⁵³ When adsorbed at liquid-liquid

interfaces, however, the microgel particles are able to deform (stretch) at lower particle concentration to minimize the excess (uncovered) interfacial area (Fig. 2.8).⁵⁴ This behaviour confirms that the increased free energy from reducing the interfacial area is higher than the energy costs to deform these particles at liquid interfaces. As the surface coverage increases, the microgel particle deformation can reduce, whilst maintaining coverage of the liquid interface. Deformability of the microgel particles at the interfaces depends on the cross-linking ratio (see Fig. 2.9).⁵⁵ By changing the internal cross-linker density, it was shown that the most deformable microgels were the most effective emulsion stabilizers, producing emulsions with extended lifetime.⁵⁵

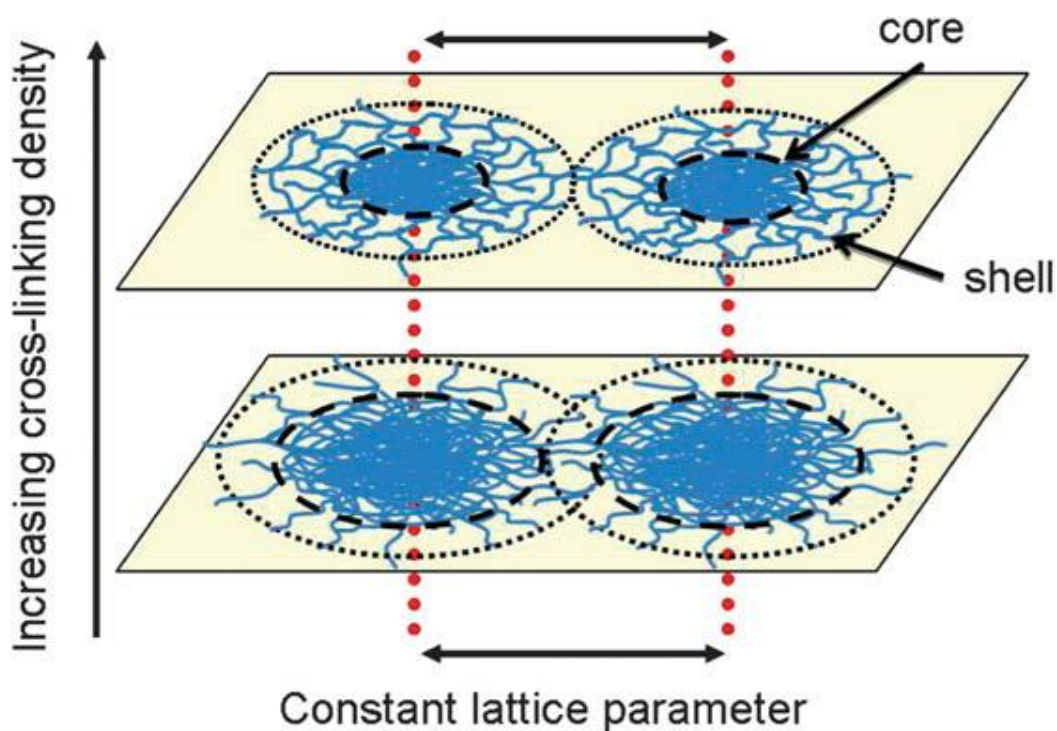


Figure 2.9 Scheme illustrating the effect of cross-linker density on the microgel conformation at the interface. The higher cross-linked microgel particle is less deformable due to the densely cross-linked core.⁵⁶

2.2.3 Pseudo-microgel particles at liquid interfaces

In the current thesis pseudo-microgel particles refer to particles that are decorated by polymers grafted on their surface.⁵⁷ An example is nano-sized PS latexes (core) stabilized by PMMA₁₆-b-PDMAEMA₂₅₄ shell.⁵⁸ With the core-shell structure the particle affinity for the air-water interface was significantly enhanced in basic conditions, due to deprotonation of the PDMAEMA shell. Therefore, particles can adsorb more strongly at the interface at high pH, providing more resistance to lateral compression, see Fig. 2.10. From this perspective, the affinity of polymer-grafted particles at the liquid interface highly depends on the polymers conformation,⁵⁸ where tuning the solvent quality provides a direct route to control particle retention at the liquid-liquid interface.

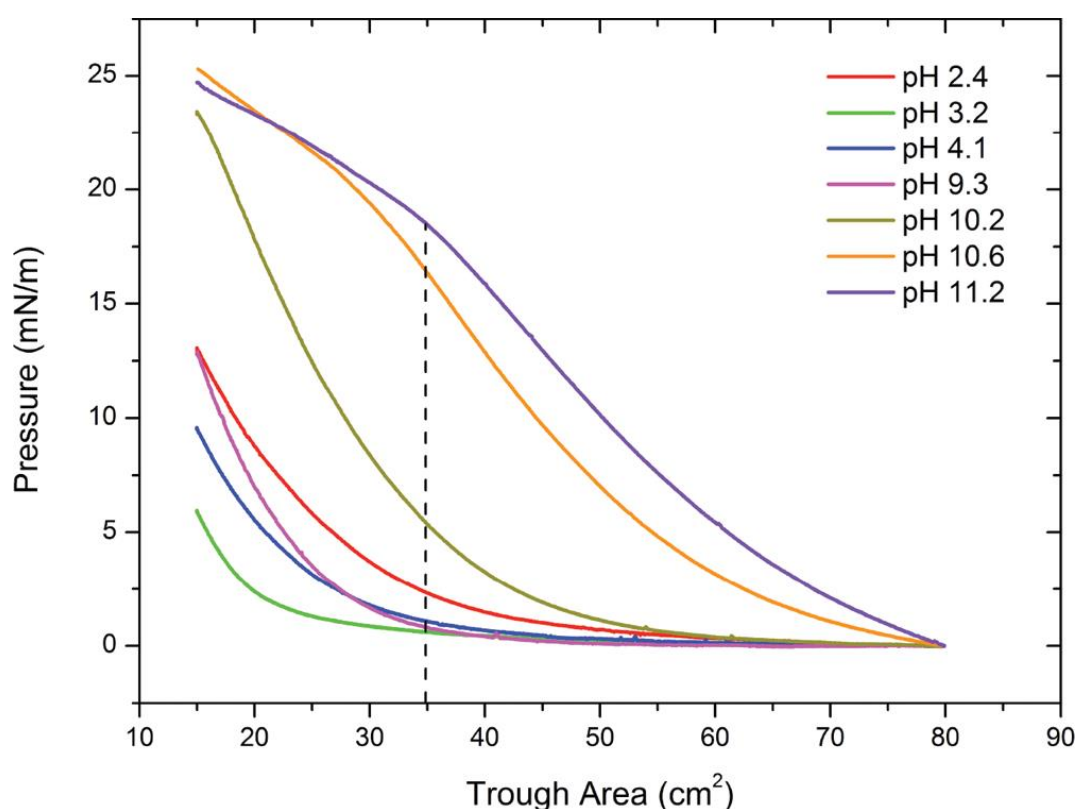


Figure 2.10 *II-A* isotherms of pMMA₁₆-b-pDMAEMA₂₅₄ stabilized PS latexes particles as a function of the sub-phase pH at the air-liquid interface.⁵⁸

2.2.4 Interfacial aggregation of particles

Particle-laden interfaces are of great interest due to their ability to stabilize immiscible fluids, such as foams (gas-liquid) and emulsions (liquid-liquid).⁵⁹ Previous research has demonstrated the importance of interfacial particle aggregation on the overall emulsion stability.⁶⁰ Compared to emulsions stabilized by dispersed particles (repulsion dominated particle-particle interaction), more stable emulsions can be formed under conditions where particles have negligible charge and thus a tendency to aggregate, with the particle surface coverage of the stable emulsion often below the particle close-packing limit.^{61, 62}

For suspensions (3D structures), it has been shown that weakly aggregated suspensions display solid-like properties with yield stress behavior. 2D aggregated suspensions display similar rheological behavior, including an elastic response with small linearity limits, a power law dependence on surface coverage and a dependence on the particle-particle interaction strength.⁶⁰ Our recent publication confirmed that rapid surface aggregations improves particle retention at an interface. The aggregated particle-laden interface becomes strongly elastic which helps to stabilize the interface against bubble-bubble or droplet-droplet coalescence.^{59, 63}

Tailoring aggregate structures is typically achieved by the addition of electrolyte and/or surfactants.^{59, 60, 64, 65} For example, charged polystyrene particles readily form 2D colloidal crystals at a planar water–decane interface due to the repulsive dominant interaction acting between the particles. Addition of sodiumdodecylsulfate (SDS) and sodium chloride (NaCl) to the aqueous sub-phase resulted in a destabilization of these monolayers, forming fractal aggregates at low particle concentrations and a heterogeneous gel structure as the particle surface coverage increased.⁶⁰ Rather dense aggregate structures were observed when only electrolyte was added, whereas more

open structures were obtained in the presence of small amounts of surfactant, confirming that the structure of 2D fractals is dependent on the inter-particle interaction strength.⁶⁶ It has been reported that reaction limited cluster aggregation (RLCA) proceeds when the inter-particle attraction is weak, thus particles have the ability to reorganize on contact leading to the formation of a dense-packed particle layer. For strong inter-particle attraction, diffusion limited cluster aggregation (DLCA) leads to the formation of more porous and heterogeneous structures as particle reorganization is limited (contact and stick).^{48, 60} The aggregation process is also shown to be a function of time, with a typical example demonstrated by octyl-coated silica particles at a planar air-toluene interface. Initially, the structure transitions from (1) a crystalline structure to (2) small clusters + singular particles, to (3) clusters with large size distributions and finally to form (4) one large interconnected particle cluster (particle network).⁶⁷ In the current study, interfacial aggregation was tailored by electrolyte addition. Details regarding interfacial aggregation on foam stability and the rheology of particle-laden interfaces will be discussed in Chapters 4 and 5.

2.3 Aqueous Foams, Foamability and Foam Stability

2.3.1 Foam destabilization

The mechanisms for foam destabilization are considered below, including evaporation, drainage, coarsening, and coalescence.

2.3.1.1 Evaporation. Foams can disappear very quickly due to liquid evaporation. Both environmental humidity and foaming agents can affect the evaporation rates of the liquid film remarkably.⁶⁸ For instance, it was found that the evaporation rate can

be reduced dramatically by forming a highly compressed surfactant layer around bubbles.⁶⁹

2.3.1.2 Drainage. The large density difference between gas and liquid promotes phase separation. Liquid drains out from the foams gradually and thins the liquid films between bubbles,⁷⁰ leading to film rupture.⁷⁰ Foams can be categorized as dry foam, wet foam and bubbly liquid according to their liquid volume fraction ($\phi = V_{liquid}/V_{foam}$). Bubbles in a dry foam ($\phi \leq 0.05$) are polyhedral (see bubbles near the top of the foam in Fig. 2.11). When $\phi = 0.36$, bubbles are no longer deformed, and the foam is called a wet foam (see bubbles near the bottom of the foam in Fig. 2.11). Systems with much higher liquid volume fraction (ϕ) are named bubbly liquid. A schematic demonstrating the transitions from pure air \rightarrow dry foam \rightarrow wet foam \rightarrow bubbly liquid and finally \rightarrow pure water is shown in Fig. 2.12.

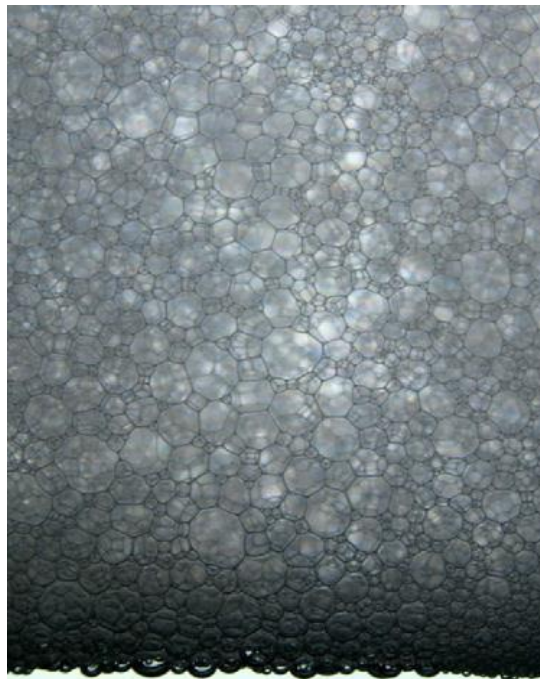


Figure 2.11 Image of a draining foam: bubbles near the top of the foam are considered “dry” and polyhedral, while bubbles near the bottom of the foam are considered “wet” and spherical.⁹

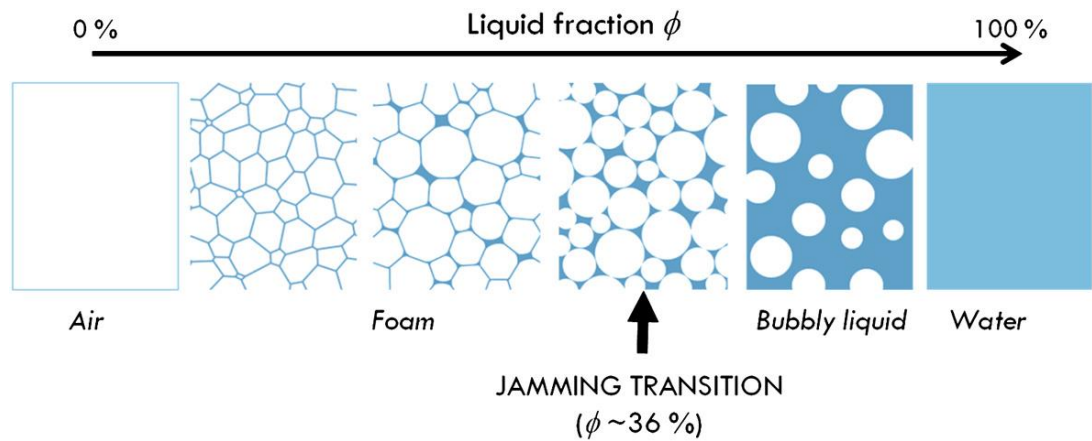


Figure 2.12 Schematic of foam demonstrating for the dependence on the liquid volume fraction.⁷¹

2.3.1.3 Coarsening. The internal and external pressure difference of a bubble is described by the Laplace pressure, which is given by $2\gamma/R$ for an isolated spherical bubble where γ is the gas-liquid surface tension, and R is the bubble radius. For two gas bubbles separated by a thin liquid film, each bubble contributes to the total pressure difference, resulting in an overall Laplace pressure of $4\gamma/R$. Bubble coarsening proceeds when there is a bubble size distribution and the pressure inside the smaller bubbles exceeds that of larger bubbles. Hence, air diffuses from the smaller to larger bubbles, leading to bubble shrinkage (small bubbles), and bubble growth (larger bubbles), with the smaller bubbles eventually disappearing (see Fig. 2.13).⁷²

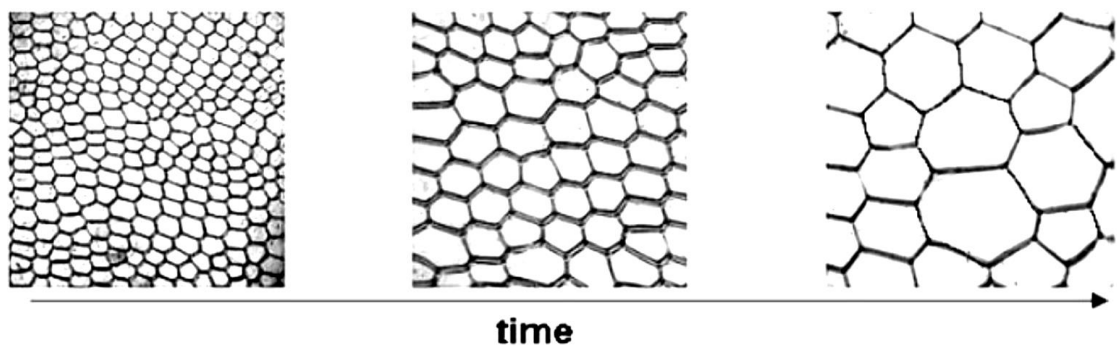


Figure 2.13 Time sequence of a dry foam coarsening.⁷⁰

2.3.1.4 Coalescence. Liquid drainage promotes thinning of the liquid film separating bubbles, which if drained to a critical thickness may promote bubble coalescence. The dominating mechanism for film rupture is still poorly understood.⁹ Some authors report that coalescence occurs once the bubbles have reached a critical size in foams, or once the liquid fraction has reached a critical value, or when the capillary pressure reaches a critical value.⁹ All those mechanisms may seem very different, however, it is very difficult to distinguish them from one another in practice, since capillary pressure, liquid fraction and bubble size are normally connected.⁹ It is likely that the mechanism for film rupture is system dependent with several possibilities shown in Fig. 2.14.

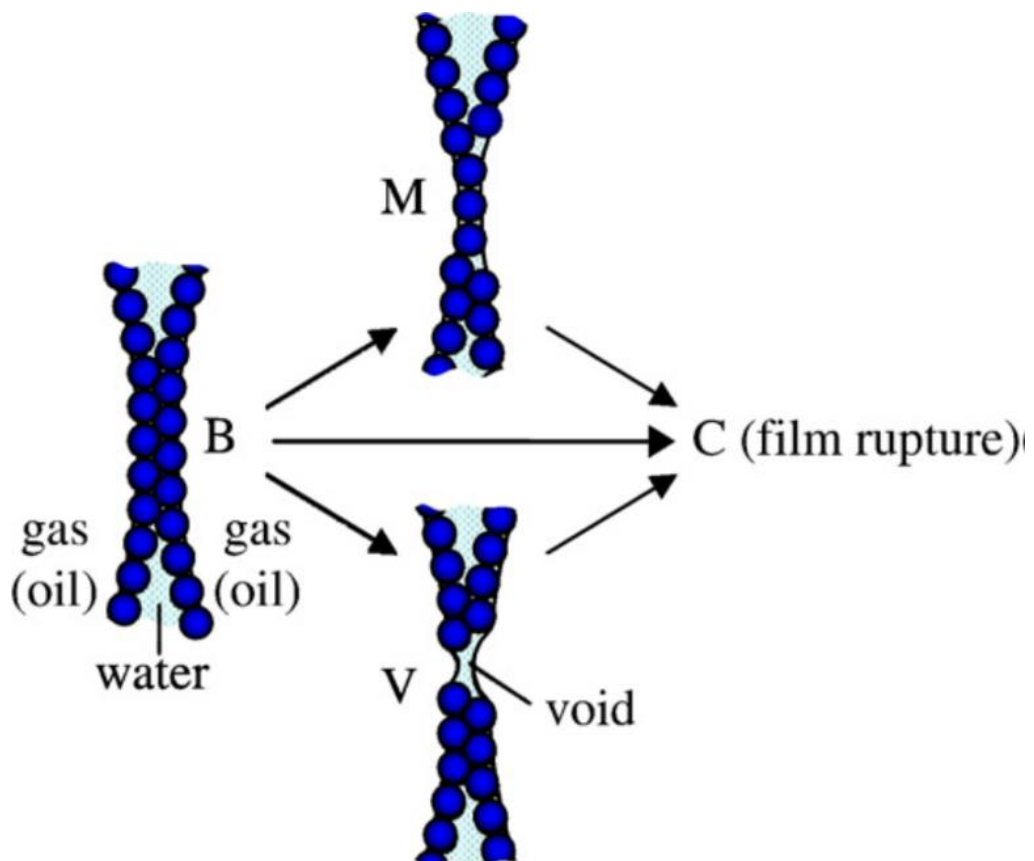


Figure 2.14 Possible mechanisms for film rupture: (B–C) direct rupture, (B–M–C) via bilayer to monolayer transition and (B–V–C) via void formation.⁷³

2.3.2 Aqueous foams stabilized by particles

2.3.2.1 Particle-stabilized foams. It has been demonstrated that foams stabilized by solid particles can be ultra-stable with stabilities reported over several years.⁶ To date, the foaming potential of fumed silica particles has been systematically studied, where the particle contact angle can be easily tuned by chemical modification using a short-chain silane reagent (dichlorodimethylsilane).⁷ Fig. 2.15a shows the foaming behaviour of fumed silica particles with different degrees of silanization (SiOR% content represented along the top axis of the image, $\text{SiOR}\% = 100 - \text{SiOH}\%$), and the measured particle contact angles are shown in Fig 2.15b.⁷ Particles with high SiOR% surface content ($\geq 80\%$) are extremely hydrophobic, producing water-in-air powders or dry water (Figs. 2.16b and c)⁷. By contrast, particles with a low surface SiOR% content ($\leq 34\%$) become extremely hydrophilic resulting in particle dispersion. Between the two extremes, wet foams were readily stabilized by the modified particles. The foams prepared using particles with 68% and 58% SiOR surface coverage were stable to coarsening and coalescence and observed to be stable over a few years (Fig. 2.15a).⁷⁴

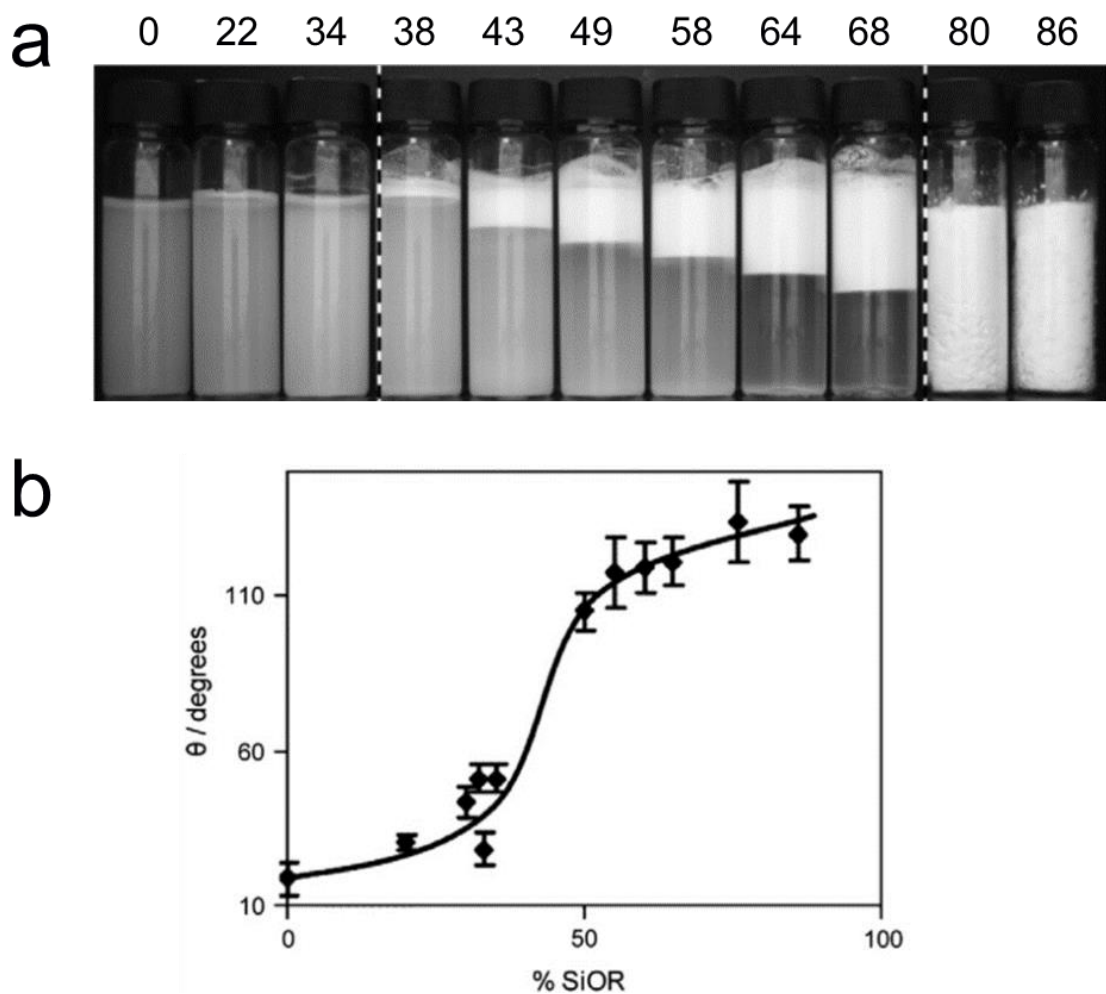


Figure 2.15 (a) Images of particle dispersions in water, particle stabilized wet foams and water-in-air powders. Particles become increasingly hydrophobic from left to right with increasing surface SiOR groups.⁷ (b) Advancing contact angle, θ , of pure water droplets on flat surfaces formed from fumed silica particles of different percentages of surface SiOR groups ($\text{SiOR}\% = 100 - \text{SiOH}\%$).⁹

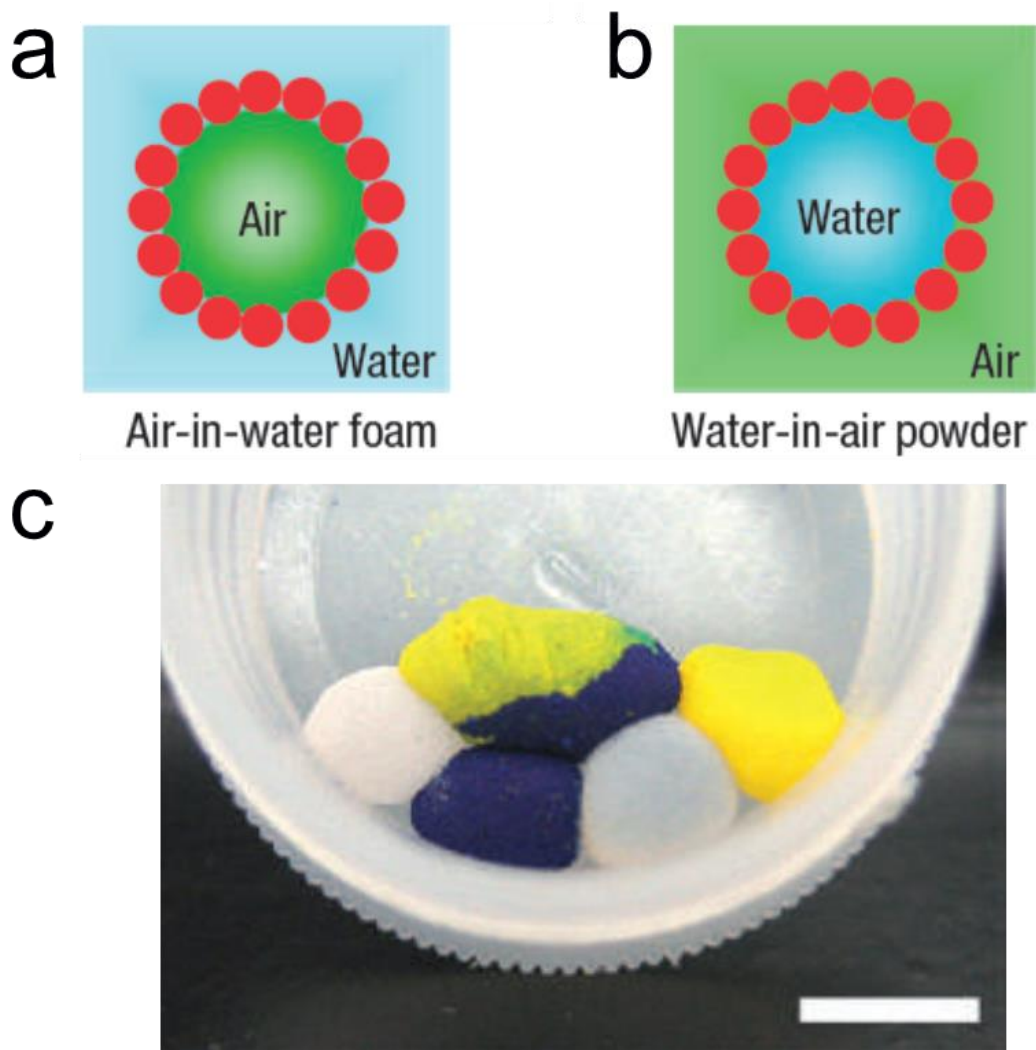


Figure 2.16 Schematic of (a) air-in-water foams and (b) water-in-air powders; (c) Photo of water drops in air stabilized by particles.⁷

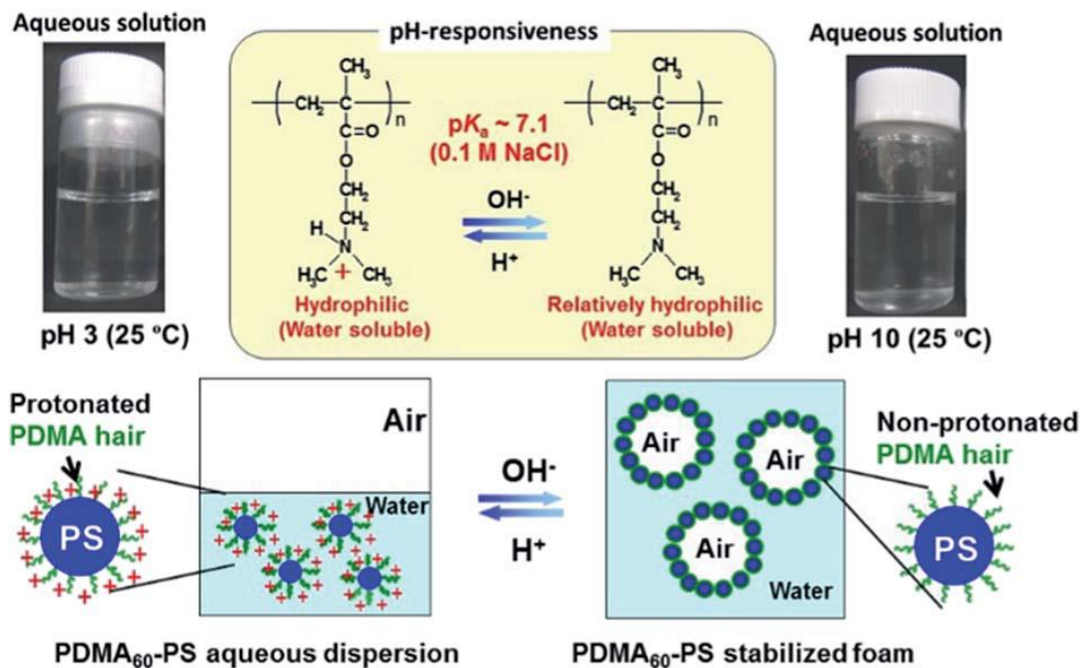
2.3.2.2 Foams stabilized by pseudo-microgel particles. The interfacial behaviour of polymer microgel particles and pseudo-microgel particles has been previously discussed (see earlier text).^{49, 59, 75} Compared with solid spheres, the microgel particles are able to deform at an interface and respond to environmental stimuli.

A good example of this is poly[2-(dimethylamino)ethyl methacrylate] (PDMA) stabilized polystyrene (PS) particles (PDMA-PS particles). The adsorption/desorption behaviour of these “hairy” PDMA-PS particles at the air-water interface was influenced by the pH- and temperature-responsive of the PDMA branches, see Fig.

2.17.⁷⁵ At a pH \geq 6.0 (e.g. pH = 10.0), the PDMA branches were non-protonated or partially protonated. This resulted in relatively hydrophilic PDMA (partially hydrated) branches when the temperature of the fluid was below the lower critical solution temperature, LCST = 34.5 °C. The partially hydrated PDMA branches prevented particles from aggregating, and hence, bubbles were stabilized by particle monolayers. The PDMA branches became hydrophobic (non-hydrated) when the temperature exceeded the LCST at high pH (e.g. pH = 10.0). Particles began to flocculate, and the bubbles were stabilized by particle multilayers (Fig. 2.17). By contrast, the polymer branches were protonated and became hydrophilic at pH \leq 5, and no foam was generated irrespective of the fluid temperature. More interestingly, rapid de-foaming could be achieved by lowering the solution pH to protonate the PDMA branches, and the foaming/de-foaming cycles were repeatable for at least five times.⁷⁵

Poly[2-(diethylamino)ethyl methacrylate] (PDEA) stabilized PS particles (PDEA-PS particles) as a temperature-responsive foam stabilizer were also reported by the same research group.⁴⁹ The LCST of PDEA branches was found to be \sim 41 °C. By adjusting the temperature below and above the LCST, foams stabilized by particle monolayer and particle multilayers were observed respectively, see Fig. 2.18.

pH-responsiveness



Temperature-responsiveness

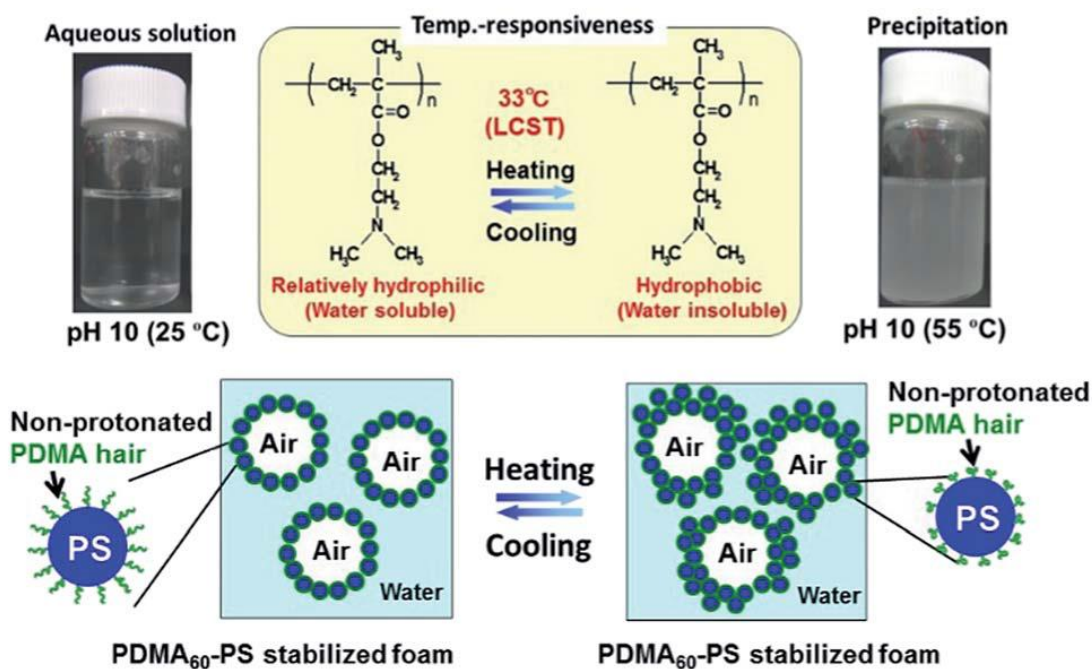


Figure 2.17 Schematic of PDMA-PS particles as a pH- and temperature-responsive foam stabilizer. Images show aqueous solutions of the PDMA homo-polymer at different pH and temperature conditions.⁷⁵

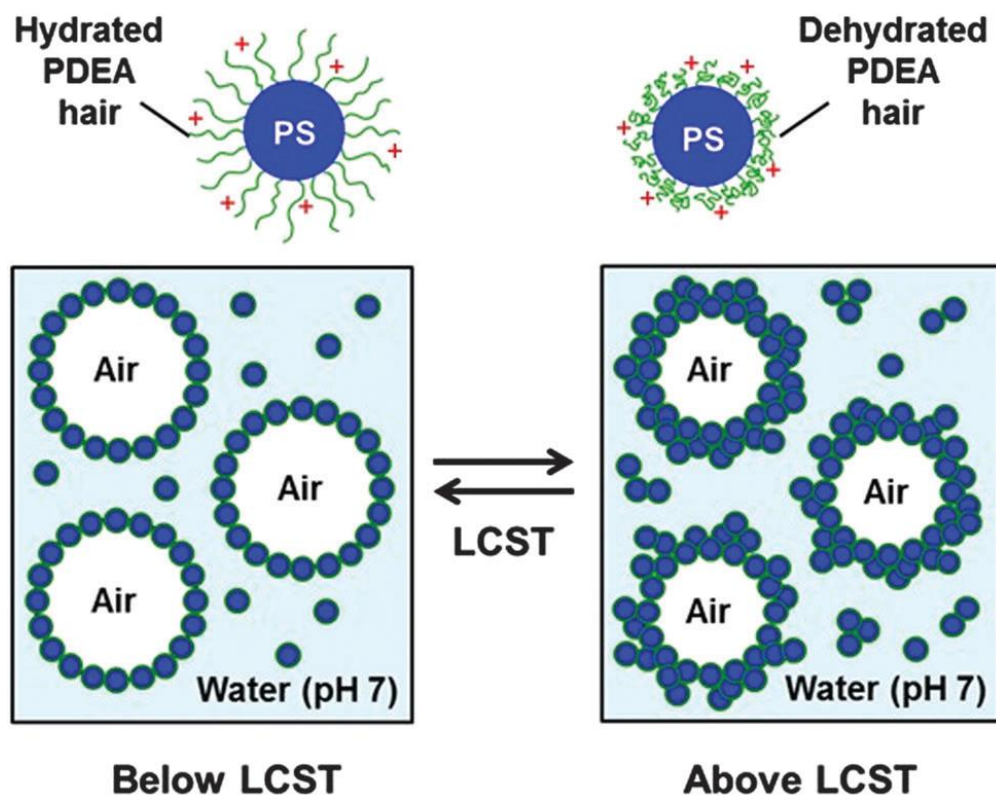


Figure 2.18 Schematic of PDEA-PS particles as a temperature-responsive foam stabilizer.⁴⁹

2.3.3 Long lived foams and foam based light-weight materials

As discussed in Section 2.3.2, evaporation, coarsening, drainage, and coalescence are the different mechanisms for foam destabilization. Thus, in order to produce stable foams, these destabilizing processes should be inhibited or stopped altogether. This is somewhat challenging since these mechanisms can occur concurrently and affect one another to accelerate foam destabilization.

Ultra-stable liquid foams have been demonstrated by Rio et al., some examples are shown in Fig. 2.19.⁹ In brief, liquid drainage can be arrested if the liquid in a foam gels or the drainage channels become blocked by particle aggregates. Coalescence can be retarded by gelified foam films, and it can be arrested if the films surrounding bubbles become very thick and/or rigid.^{9, 59} The reduction in bubble coarsening rate

requires very thick films, and its arrest was observed in cases where the compressional elastic modulus was large.⁹ More details regarding bubble coarsening and coalescence are discussed in Chapter 4.

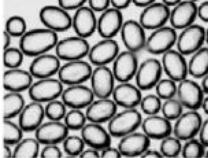
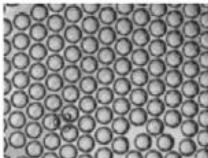
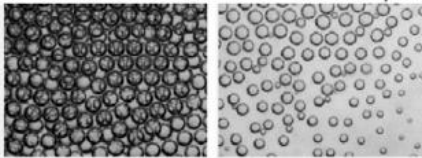
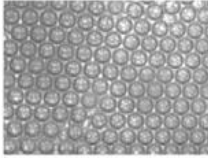

Concent.		Foamability	Foam stability	Regimes
C_p (wt%)	C_a (wt%)			
< 5		COALESCENCE	COALESCENCE	
5	< 1	 LIMITED COALESCENCE	COARSENING	I Limited Coalescence AND Coarsening
10	2	 NO COALESCENCE	 COARSENING (gelled interfaces)	II NO Coalescence BUT Coarsening
10	3	 NO COALESCENCE	 NO COARSENING (here foam after 2 years)	III NO Coalescence NO Coarsening

Figure 2.19 Foamability and foam stability of foams that stabilized by amphiphiles-particle composites (C_a : concentration of n-amylamine, C_p : concentration of particles).⁷⁶

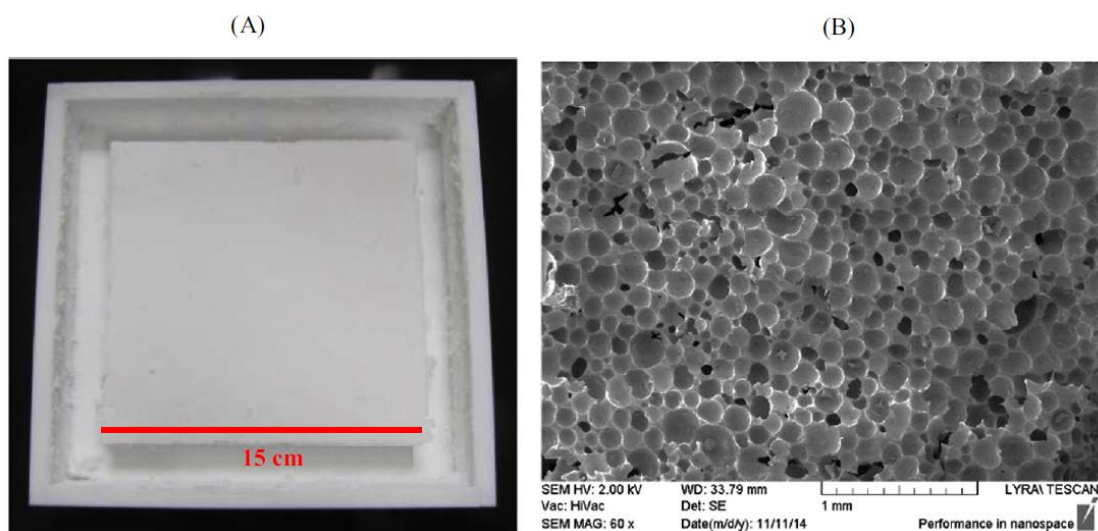


Figure 2.20 (a) Image of foam based porous materials prepared using 15.7 wt% silica particles (d_{50} (agglomerate) $\sim 3.5 \mu\text{m}$, particle density: $\sim 2.1 \text{ g/cm}^3$) and 2.2 wt% tetradecyl trimethyl ammonium bromide (TTAB); (b) SEM image of the formed foam structure.³⁷

Particle-stabilized foams can be used as templates to prepare foam based materials of highly porous structures for a range of applications. Light-weight materials using foaming based methods have already been reported. The solid foams shown in Fig. 2.20 were prepared using silica particles and surfactant mixtures. A key factor for its success is the appropriate selection of surfactants which both modify the particle surface and stabilize the foam.³⁷ Alternatively, solid foams can be prepared by forming capillary foams using particles, bulk fluid (water based) and a small amount of oil, see Fig. 2.21.⁷⁷ Since oils have higher polarity than gases, water dispersible particles tend to have a higher affinity to oil–water interfaces than to gas–water interfaces, and are therefore often more suitable for stabilizing the oil–water interface in Pickering emulsions or the oil-coated bubbles in capillary foams than the air–water interface of aqueous Pickering foams. The addition of a small amount of oil provides a convenient and timesaving alternative to particle surface modification for foam

stabilization and greatly broadens the range of suitable particles.⁷⁷ However, it should be noted that the particle concentration used in both methods was high (> 15wt%) (Fig 2.20 and 2.21), and this is something the current research is trying to address by better understanding the structure - interfacial rheology relationship.

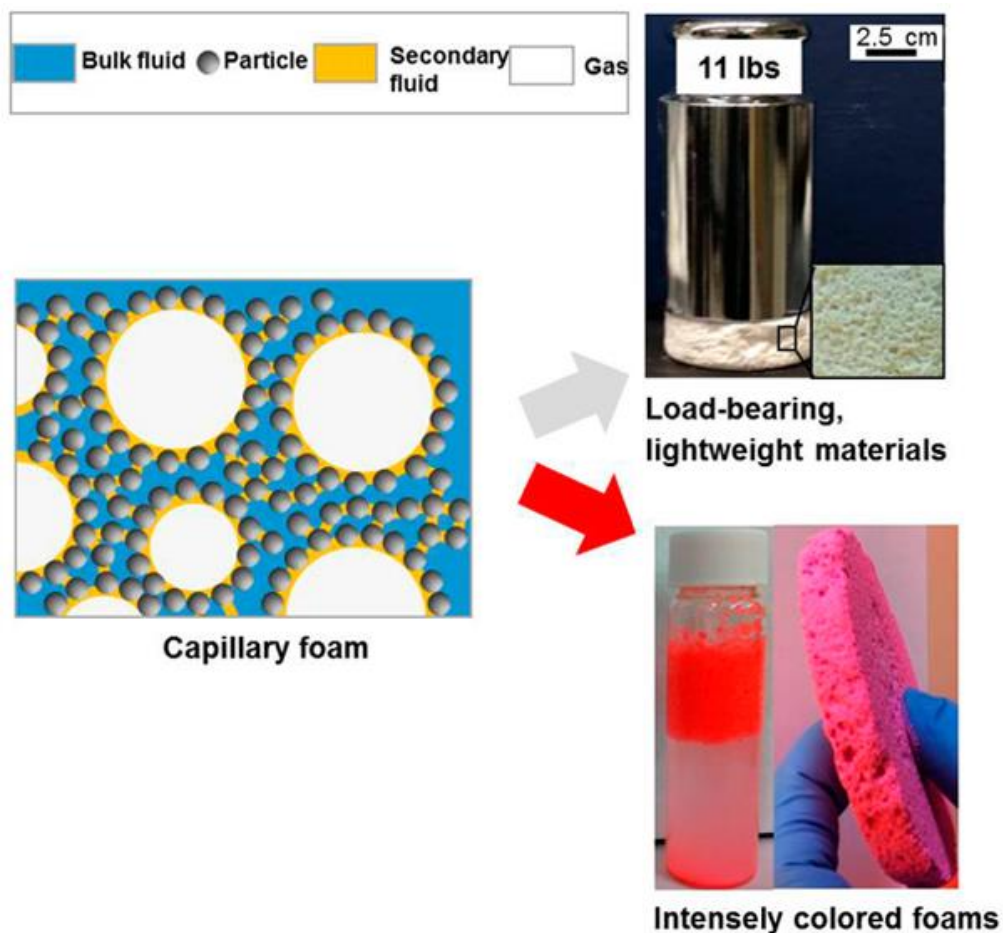


Figure 2.21 Capillary foams prepared using polyvinyl chloride particles ($d_{50} = 14.8 \mu\text{m}$, particle density = 1.41 g/cm^3 , particle concentration > 20 wt%), bulk fluid (water based), and a secondary fluid which is Trimethylolpropane trimethacrylate (TMPTMA).^{77, 78}

Chapter 3: PVP Adsorption on Silica Surface and Lubricating Properties of the Adsorbed PVP Films

3.1 Synopsis

Polymer physisorption is often simpler and less time-consuming than chemical grafting onto surfaces, which can be advantageous when considering routes for large-scale industrial applications. In order to prepare poly(vinylpyrrolidone) (PVP)-coated silica composite particles (composite particles) via polymer physisorption, the knowledge of PVP adsorption on silica surface was essential.

In the current chapter, silica surfaces were modified by the physisorption of PVP from water solution. Four polymer samples with different molecular weights ranging from 8 kDa to 1300 kDa were examined. Optical reflectivity (OR) measurements showed that the saturated surface excess for each PVP sample was around 1 mg/m². The amount of trapped water within the 8 kDa PVP film (~ 10 wt%) was found to be much less than the trapped water (40-55 wt%) in films formed from higher molecular weight PVP (40 kDa, 360 kDa, and 1300 kDa). In addition, QCM-D dissipation values for the 8 kDa PVP films were more than four times smaller than those measured for the higher molecular weight PVPs, suggesting that the 8 kDa PVP conforms to a flat film (predominantly train orientation), while the high molecular weight PVPs slowly reorganize resulting in more lossy films (increased Sauerbrey film thickness). Colloid-probe AFM lateral force measurements showed that 8 kDa PVP films exhibited similar lateral resistance to that seen for uncoated silica surfaces in water, whereas higher molecular weight PVP films showed significantly reduced

lateral forces. This lubrication effect, induced by the adsorbed higher molecular weight PVP samples was explored further by measuring the rheology of concentrated particle suspensions. Suspension yield stress data for PVP-coated particles showed a reduction by a factor of 2 in the yield stress when compared to the uncoated particles for suspension concentrations above 60 vol%, i.e. approaching the close-packed limit of spheres.

3.2 Literature Review

3.2.1 Poly(vinylpyrrolidone) (PVP)

Polymers in solutions and adsorption at solid-liquid interface have been generally reviewed in Chapter 2. In particular, being a biocompatible, water-soluble, and low-cost polymer, PVP has wide applications in food industries, nanoparticle synthesis, cosmetics, medical and pharmaceutical industries.^{11, 79, 80} For instance, owing to its good biocompatibility, PVP has been used as a serum albumin substitute,⁸¹ a component of artificial tears and an ingredient of bactericidal iodine.⁸² The structural formula of a PVP molecule is shown in Fig. 3.1.

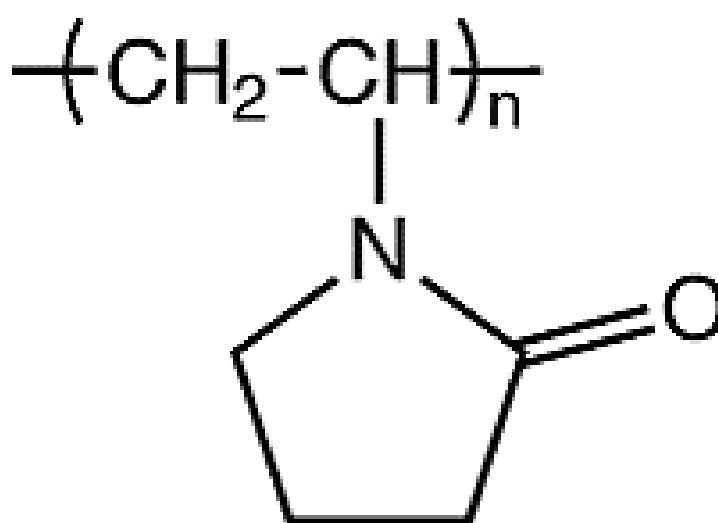


Figure 3.1 Structural formula of a PVP molecule.

It has been reported that PVP molecules strongly (segmental adsorption energy of around 4 kT) adsorb on silica surfaces through hydrogen bonding^{21, 83} between the carbonyl groups of the PVP molecules and the silanol groups on silica, see Fig. 3.2.^{19, 21, 83} PVP adsorption on silica was shown to be pH dependent. At neutral pH, PVP adsorption on silica had been investigated mainly via depletion methods at concentrations $\gg 1$ ppm.^{19, 21, 83, 84, 85, 86, 87, 88} For instance, the saturated surface excess for 540 kDa ($R_g \sim 33$ nm) and 1150 kDa ($R_g \sim 41$ nm) PVPs adsorbing on silica was ~ 1 mg/m², showing a weak dependence on molecular weight. The adsorbed PVP layer thickness was determined from hydrodynamic measurements (particle sizing), showing an increase in PVP layer thickness with increasing surface coverage, although the PVP layer thickness was significantly less than the polymer radius of gyration even at the adsorption plateau, indicating that the polymer adsorbs in a flattened-state.¹⁹ An increase in pH (more basic) reduces the number of PVP adsorption sites due to the dissociation of the surface silanol groups. When the number of surface adsorption sites becomes too low, this leads to a decrease in the amount of PVP that can adsorb on silica (e.g. pH ≥ 8).⁸⁸ The equilibrium between -OH and -O⁻ groups on silica is influenced by the solution pH and the ionic strength. A higher ionic strength screens the negative charges at the silica-solution interface, allowing a higher degree of dissociation of the silanol groups and thus a higher charge density for a given pH. This means that while increasing the pH can lead to a decrease in the amount adsorbed for PVP, an increase in ionic strength may also have the same effect.⁸⁸ In the current chapter, we are interested in the adsorption kinetics of PVP, rearrangement of PVP chains, and layer hydration of adsorbed PVP films, especially at ultra-low concentrations (≤ 1 ppm) in Milli-Q water (pH ~ 6.2). The PVP-coated

silica composite particles that are used in Chapters 4 and 5 were also prepared in Milli-Q water.

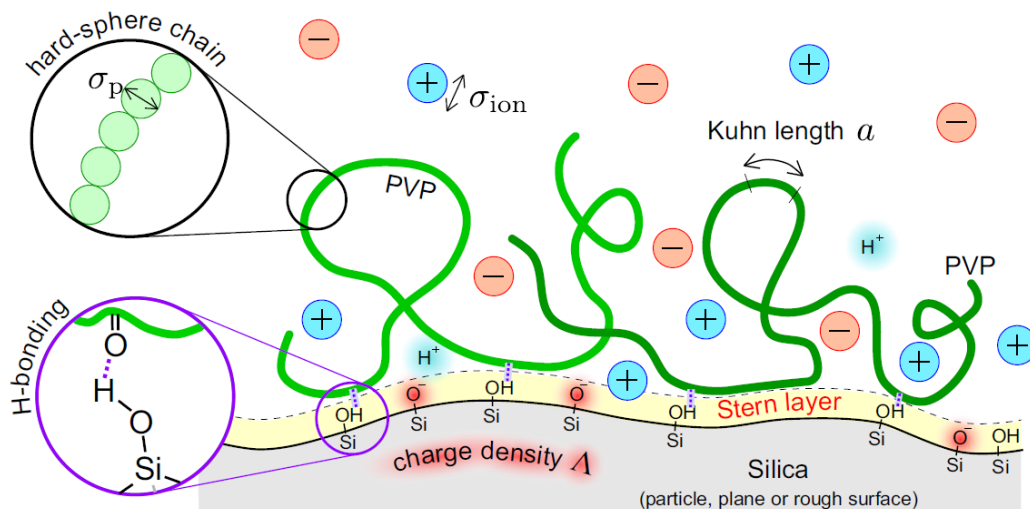


Figure 3.2 Interactions between silica and PVP through hydrogen bond.⁸⁹

3.2.2 Lubricating properties of polymer films

Recently, PVP has been shown to be a promising lubrication additive for artificial joints by significantly reducing the friction coefficient, as well as improving wear resistance of the joint pairs.^{82,90} A 2-fold reduction in the coefficient of friction and a 30% reduction in the wear scar diameter relative to water were measured for PVP solutions under a normal load of 2 kN.⁸² PVP also exhibits high degradation resistance, which is beneficial from a tribology perspective, confirming the polymer stability as a lubricant over extended periods of time.

Friction reduction is important to both traditional industry (e.g. bearing lubrication) and advanced micro- or nano-scale devices such as implants or bio-sensors, from the perspective that reduced friction improves energy utilization and minimizes wear.^{23,91,92} Current opinions of friction have been commonly considered in terms of different energy dissipation pathways as the contacting surfaces move past each other, either by thin fluid films or, for surfaces in contact, by molecular species forming boundary

layers.⁹³ Moreover, lubrication using more environmentally friendly, water-based solvents is increasing in popularity.⁸² Various systems, ranging from micro/nano-electromechanical systems and biomedical devices, to articulating joints or the eye, require surfaces in contact to slide easily past each other in aqueous environments.^{23, 93}

In particular, polymer coatings have been shown to be economic, versatile and convenient approaches to reduce the frictional forces between surfaces in an aqueous system, as they are able to sustain large normal loads while retaining a stable fluid interfacial layer.^{94, 95} The morphology of the adsorbed or grafted polymer layers and the nature of their interactions with the surfaces, with the solvent, and with each other determine the degree of lubrication.^{96, 97, 98} In a good solvent condition, the interactions between two surfaces that are fully coated by polymers (adsorbed or grafted) are usually repulsive due to the osmotic pressure exerted by the confined polymer chains.⁹⁴ Grafted polymer brushes, for example, show negligible mutual interpenetration as they are compressed to $D < 2L_0$ (D is the distance between two surfaces, and L_0 is the mean uncompressed thickness), because of excluded-volume/entropic effects.⁹⁹ Even under moderate compression, the depletion zone where frictional dissipation occurs remains fluid. The combination of a limited mutual interpenetration of the brushes and a fluid interface results in excellent lubrication (also called entropic lubrication).¹⁰⁰ Recent research emphasized the importance of the interfacial fluid film as well as the morphology of polymer layers on the resultant friction forces.¹⁰¹ The interfacial fluid layer may act as a shear plane between polymer brushes (grafted), despite moderate brush collapse, resulting in lower frictional forces. As the solvent quality is further decreased, the brushes undergo significant collapse (see Fig. 3.3), and the fluid film at the interface can no longer be maintained. The shear plane then moves to the entangled polymer layers, leading to higher friction

coefficients. Similar transitional behaviour has also been shown by polymer films that were formed via physisorption: a low boundary friction coefficient was found for highly hydrated viscoelastic surface layers, whereas (very) thin adsorbed rigid polymer films had negligible effect on interfacial lubrication.¹⁰² The lubrication effects of polymer coatings are not only confined to reduce the frictional forces between flat surfaces, but also in bulk systems where the rheology of high volume fraction polymer-coated particles can be manipulated by the degree of lubrication. It has been shown that thick and highly hydrated polymer layers strongly repel each other to provide sufficient lubrication for particles to easily slide past one another, resulting in low suspension viscosities.¹⁰³

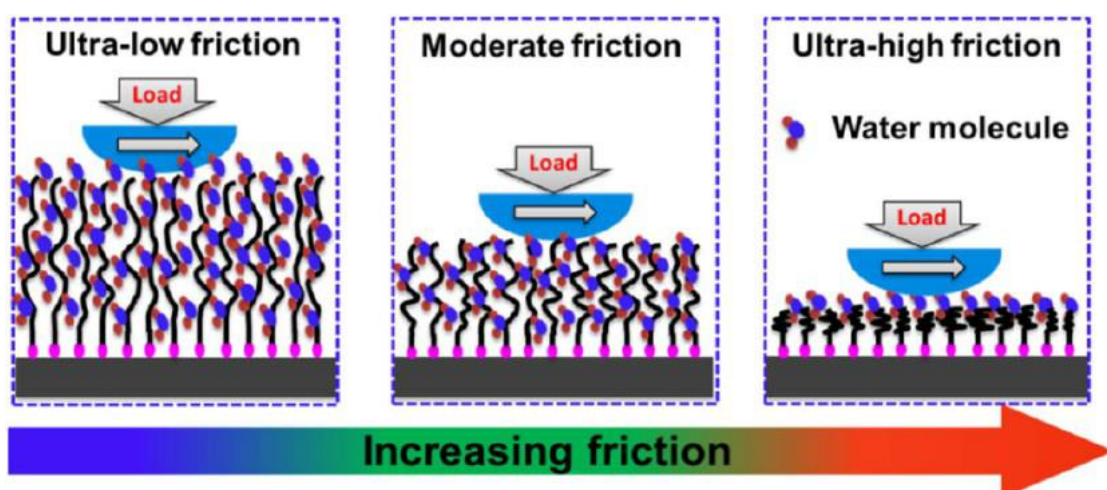


Figure 3.3 Correlation between lubrication and conformation of polymer brushes.¹⁰⁴

To the best of our knowledge, the lubricating properties of ultra-thin PVP films prepared via physisorption has not previously been considered.²² Polymer physisorption is usually simpler than chemical grafting onto surfaces, which can obviously be advantageous when considering routes for efficient and cost effective scale-up. In the current chapter, surface modification was achieved by adsorbing PVP on silica at ultralow concentrations ($\leq 1\text{ppm}$). The adsorption behaviour of PVP was studied by optical reflectometry (OR) and Quartz Crystal Microbalance with

Dissipation monitoring (QCM-D): allowing us to measure or infer the surface excess, adsorption kinetics, polymer rearrangement on the substrate, and PVP film hydration. The lubricating properties of these adsorbed PVP films at the silica-water interface were measured using an atomic force microscope (AFM). The resultant lubrication effect was then highlighted by measuring the suspension rheology of uncoated and PVP-coated silica particles.

3.3 Materials and Experimental Methods

3.3.1 Materials

PVP (8 kDa, 40 kDa, 360 kDa and 1300 kDa) was purchased from Alfa Aesar (UK) and used as received. Silicon wafers with a 100 nm thermally deposited oxide layer were purchased from University Wafer (USA). Hollow silica particles (diameter 9 – 13 μm and density $\sim 1.1 \text{ g/mL}$) were purchased from Sigma-Aldrich (UK). Milli-Q water with a resistivity of 18.2 $\text{M}\Omega\cdot\text{cm}$ was used throughout the study.

3.3.2 Experimental methods

3.3.2.1 Fixed angle optical reflectometry (OR). PVP (8 kDa, 40 kDa, 360 kDa, 1300 kDa) adsorption was studied by a fixed angle optical reflectometry (OR), and the working principle of OR is shown in Fig. 3.4. The OR (purchased from Wageningen University, Netherlands) has a polarized red He-Ne laser (632.8 nm) that is incident onto a silicon wafer close to the Brewster angle. The intensity of the reflected parallel (R_p) and perpendicular (R_s) components of the laser was monitored by a pair of photodetectors mounted at 90° to each other. R_p/R_s produces a value for the measured signal, S and changes to this signal, ΔS , are measured during an experiment. Silicon wafers were cut to the dimensions of $1 \text{ cm} \times 3 \text{ cm}$ and fresh substrates were used for

each experiment. These silicon substrates were UV-Ozone cleaned for 30 min and rinsed with Milli-Q water before positioning the substrate in the flow cell of the OR. Milli-Q water was used as a background liquid to first ensure a stable baseline signal (S_0) before each adsorption experiment, and the change in the measured signal $\Delta S = S - S_0$ was then recorded after PVP solutions were injected.¹⁰⁵ Once a stable surface excess value was obtained, Milli-Q water was re-injected into the OR cell to investigate the rinse-off behaviour of PVP. The adsorbed amount, Γ , can be calculated from, $\Gamma = \frac{\Delta S}{S_0} Q$, where Q is a sensitivity factor, which is determined by a four-layer model (inset in Fig. 3.4) depending on the angle of incidence of the laser light (θ), the refractive indices of the surface and adsorbed materials (n), the thickness of the oxide layer on the silicon wafer (d), and the refractive index increment of the adsorbant (dn/dc). The following values were used: $\theta = 71^\circ$, $n_{SiO_2} = 1.46$, $n_{Si} = 3.85$, $n_{H_2O} = 1.33$, $n_{PVP} = 1.51$, $d_{SiO_2} = 100$ nm, and $dn/dc_{PVP} = 0.175$ mL/g.⁸⁸

After an experiment, the remaining liquid was removed from the OR cell using a 20 mL syringe, before the OR cell was cleaned by continuously rinsing with 2 L of Milli-Q water.

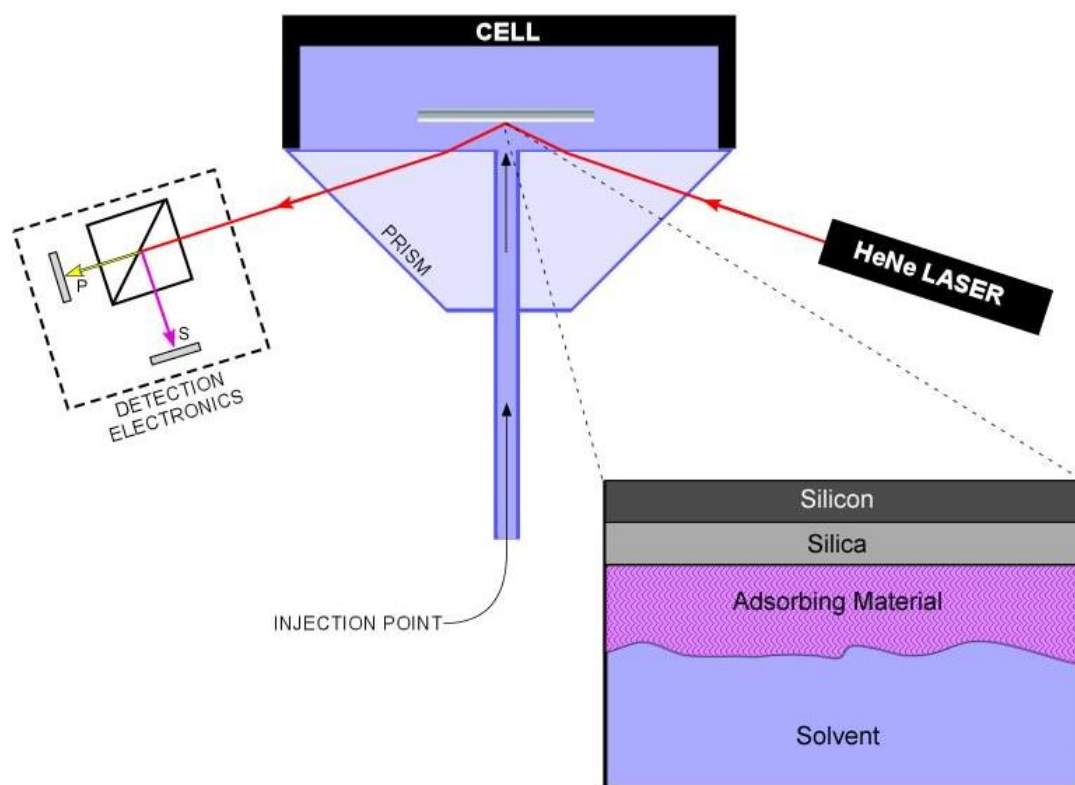


Figure 3.4 Schematic of the OR working principle.

3.3.2.2 Quartz crystal microbalance with dissipation monitoring (QCM-D). The adsorption of PVP (8 kDa, 40 kDa, 360 kDa, 1300 kDa) on silica was also investigated using an E4 QCM-D from Q-Sense (Gothenburg, Sweden), see Fig. 3.5a. The measurement cell (Fig. 3.5b) is mounted on a Peltier element, which can provide an accurate temperature control (25 ± 0.02 °C). The quartz crystal oscillators (sensors) used for the experiments had a diameter of 14 mm and a fundamental shear oscillation frequency of 5 MHz (Fig. 3.5c). The sensors were first cleaned by sonicating in a 2 wt% Decon solution for 30 min followed by 10 min sonication in Milli-Q water, after which the sensors were air dried and left in a UV-Ozone cleaner (Bioforce Nanoscience, USA) for 3 h to eliminate remnant organics.¹⁰⁶ All measurements started by running Milli-Q water as a background fluid, before the PVP solution was pumped into the sensor cell after establishing a stable baseline. The changes in frequency (Δf) and dissipation (ΔD) were measured simultaneously at different overtones. In the

current study, Δf_3 and ΔD_3 were used to present the frequency and dissipation shifts, since the third overtone shows the best signal-to-noise ratio.²⁴

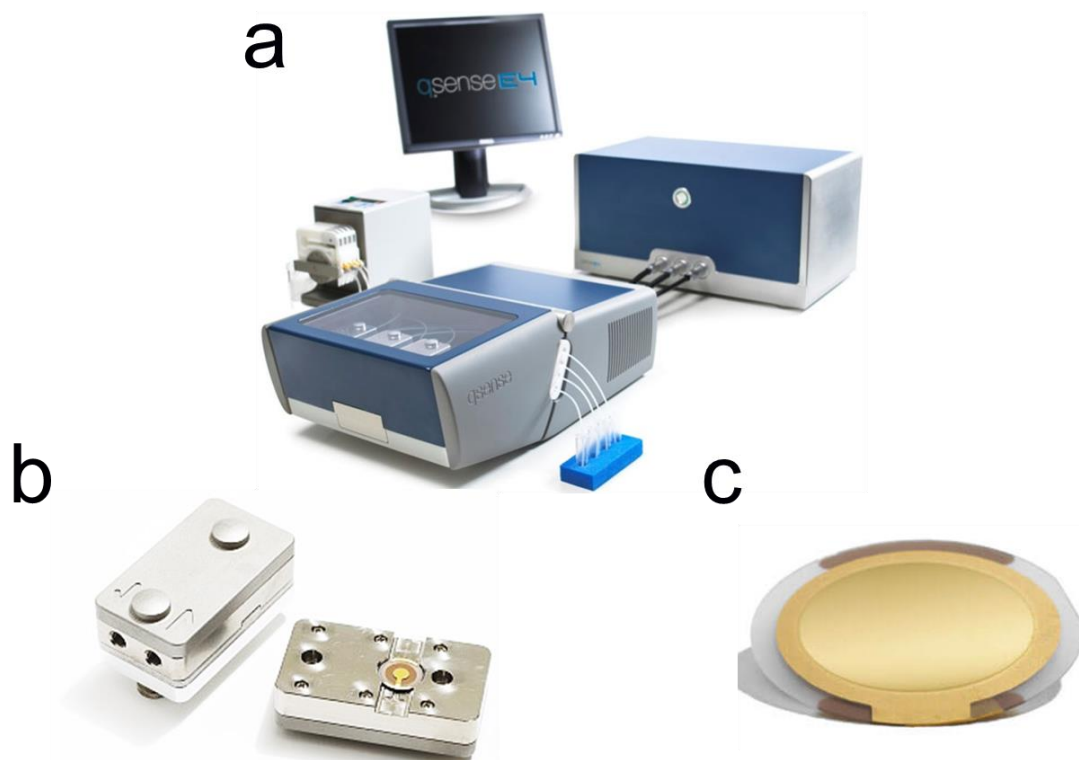


Figure 3.5 Images of the E4 QCM-D system (a), the flow channel (b), and the quartz crystal oscillator (c).

At resonance, an oscillating electric field induces mechanical shear waves in the sensor. Any increase in mass (Δm) on the quartz sensor causes the oscillation frequency of the sensor to decrease, leading to a negative shift in the resonance frequency ($-\Delta f$). According to the Sauerbrey model, $\Delta f = -n \frac{1}{C} \Delta m$, where C is the mass sensitivity constant ($C = 17.7 \text{ ng cm}^{-2} \cdot \text{Hz}^{-1}$ at 5 MHz), and n is the overtone number ($n = 1, 3, \dots$).³¹ The Sauerbrey equation is entirely valid when the adsorbed film couples perfectly to the shear oscillator to form a thin, rigid film. Under such circumstances the deposited mass is directly related to the sensor frequency shift. However, in many systems such criteria may not be realized, in particular when the adsorbed film is more viscous, displaying fluid-like behaviour (softer layer properties

– viscoelastic). The frequency response of the oscillator is influenced by the viscoelastic properties of the deposited layer which influences the oscillator dissipation (D) (considered to be zero for a true Sauerbrey film). With a substantial change in the sensor dissipation, usually considered to be >5% of the frequency shift, the apparent mass of the deposited viscoelastic film can be modeled using the Voigt–Voinova equation, by considering the shift in both the sensor frequency and dissipation. In the following equations, subscripts 0, 1, and 2 represent the quartz sensor, the adsorbed viscoelastic layer, and the Newtonian fluid, respectively.¹⁰⁷

$$\Delta f = -\frac{1}{2\pi\rho_0 h_0} \left\{ \frac{\eta_2}{\delta_2} + \left[h_1 \rho_1 \omega - 2h_1 \left(\frac{\eta_2}{\delta_2} \right)^2 \frac{\eta_1 \omega^2}{\mu_1^2 + \omega^2 \eta_1^2} \right] \right\} \quad (3.1)$$

$$\Delta D = \frac{1}{2\pi f \rho_0 h_0} \left\{ \frac{\eta_2}{\delta_2} + \left[2h_1 \left(\frac{\eta_2}{\delta_2} \right)^2 \frac{\eta_1 \omega^2}{\mu_1^2 + \omega^2 \eta_1^2} \right] \right\} \quad (3.2)$$

$$\delta_2 = \sqrt{\frac{2\eta_2}{\rho_2 \omega}} \quad (3.3)$$

where h is the thickness, ρ is the density, η is the viscosity, μ is the shear modulus, and ω is the angular frequency. To calculate the adsorbed film thickness from the frequency and dissipation responses a couple of assumptions must be made in regards to the layer density, fluid density and fluid viscosity. In the current study the layer density, fluid density and fluid viscosity were set to $1 \times 10^3 \text{ kg/m}^3$, $1 \times 10^3 \text{ kg/m}^3$ and $1 \times 10^{-3} \text{ Pa}\cdot\text{s}$, respectively.^{31, 108} For comparison, both the Sauerbrey and the Voigt models were used to estimate the surface excess of the adsorbed PVP films.

3.3.2.3 Lateral force measurements using an atomic force microscopy (AFM).

A Bioscope II AFM (Bruker, USA) was used to measure the lateral forces between silica-silica surfaces and PVP-PVP coated silica surfaces using the colloid probe technique, see Fig. 3.6. Tipless silicon nitride cantilever (DNP-020, Bruker AFM Probes International Inc., USA) with a spring constant of 0.6 N/m, determined by the thermal resonance method, was used to create colloid probes. Silica particles (Duke

Scientific, USA) of 30 μm diameter were attached to the cantilevers using a two-part epoxy glue (Araldite 2012, UK) which was allowed to cure overnight. These colloidal probes were then examined by SEM (Hitachi TM3030, UK) to ensure that the particle was well centred and cleanly attached to the cantilever. Four pieces of silicon wafer were cut and cleaned as aforementioned and were soaked in 1 ppm PVP solutions of different molecular weight (8 kDa, 40 kDa, 360 kDa, and 1300 kDa) for 30 min to ensure the silica surfaces were completely saturated with PVP molecules, after which the silicon wafers were rinsed with Milli-Q water to remove excess PVP. In the same way, four different PVP-coated colloid probes were also prepared. Lateral force measurements were obtained immediately after the PVP surface preparation to ensure that both PVP surfaces remained fully hydrated. These experiments involved depositing two or three drops of Milli-Q water onto the PVP coated substrate before immersing the colloid probe into the solution. Friction loops were obtained as a function of the normal load (0.44 μN to 2.22 μN) at a scan length of 1 μm and a scan rate of 1 $\mu\text{m/s}$. All force curves were collected at 0.5 Hz at a minimum of three different surface sites to ensure representative behaviour.

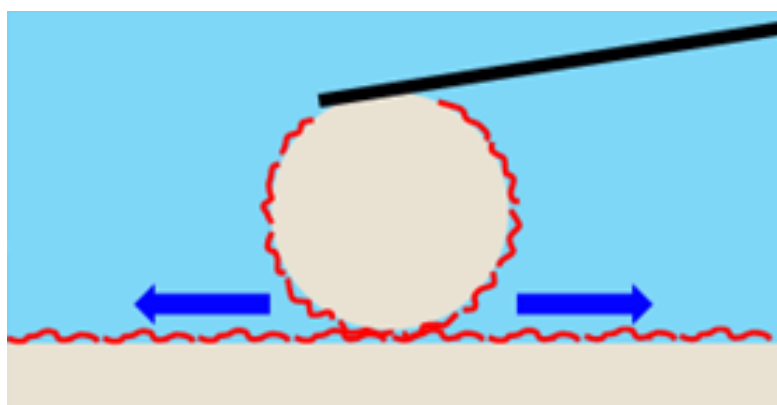


Figure 3.6 Schematic of the lateral force measurement using colloid probe technique.

3.3.2.4 Suspension preparation and bulk rheology. Particle pastes were prepared for bulk rheology measurements. To prepare the uncoated silica particle paste, 50 g of

silica (9-13 μm) was added to 50 g of Milli-Q water very slowly under gentle agitation, creating a 50 wt% paste. The paste concentration was then increased by gradually removing the supernatant by centrifuging the sample at 10000 rpm. To prepare PVP-coated particle pastes, 0.2 wt% solutions of either 8 kDa or 40 kDa PVP were used instead of pure Milli-Q water, to create a 50 wt% paste. The adsorption data (will be shown in this chapter) showed that a PVP to silica surface area ratio of 5 mg/m^2 is sufficient to saturate the silica particle surface with PVP.⁵⁹ The PVP–silica paste was continually mixed for 12 h to ensure uniform PVP coverage throughout the paste, before centrifugation and then removing the supernatant.⁵⁹ These pastes were then re-dispersed in Milli-Q water, readjusting the paste concentration to 50 wt%. This washing process was repeated several times to ensure that any excess PVP was removed.⁵⁹ Once the 50 wt% paste containing PVP-coated particles was created, the paste concentration could be increased using the same centrifugation method as for the uncoated particle pastes.

Flow curves of pastes made with silica particles and PVP-coated particles were measured using a stress-controlled Discovery Hybrid Rheometer (DHR-2, TA Instruments, UK) equipped with a cross-hatched plate geometry.¹⁰⁹ Prior to each measurement the plate geometry was cleaned in acetone and washed with excess Milli-Q water. Sand paper of Grade 40 was fixed to the center of the base plate to prevent paste slippage, and a solvent trap was used to minimize the evaporation of the paste liquid. For the flow curve measurements, ~ 2 mL of the paste was placed on the Peltier plate and the plate geometry lowered to a 1 mm gap setting. Once positioned, the paste rheology was measured by varying the shear rate between 0.1 and 200 s^{-1} . The measured flow curves were analyzed using the Herschel-Bulkley model to obtain

values of yield stress at each paste concentration. All the measurements were conducted at a constant temperature of 25 °C.

3.4 Results and Discussion

3.4.1 PVP adsorption measured by OR

3.4.1.1 PVP surface excess. According to Fig. 3.7a, the adsorption isotherm for 40 kDa PVP at 25°C obtained using the OR can be described by two phases (i) increasing surface excess up to a PVP concentration of 0.1 ppm, and (ii) a plateau surface excess of $\sim 0.9 \text{ mg/m}^2$ ($1.35 \times 10^{-2} \text{ molecules/nm}^2$) for PVP concentrations $\geq 0.1 \text{ ppm}$, correlating well with previously published data.^{19, 21, 59, 110} Isotherms for 8 kDa, 40 kDa, 360 kDa and 1300 kDa PVP are presented in Fig. 3.7b and show similar behavior, although the plateau surface excess values are partly dependent on the molecular weight, which is commonly observed for linear polymers.²⁵

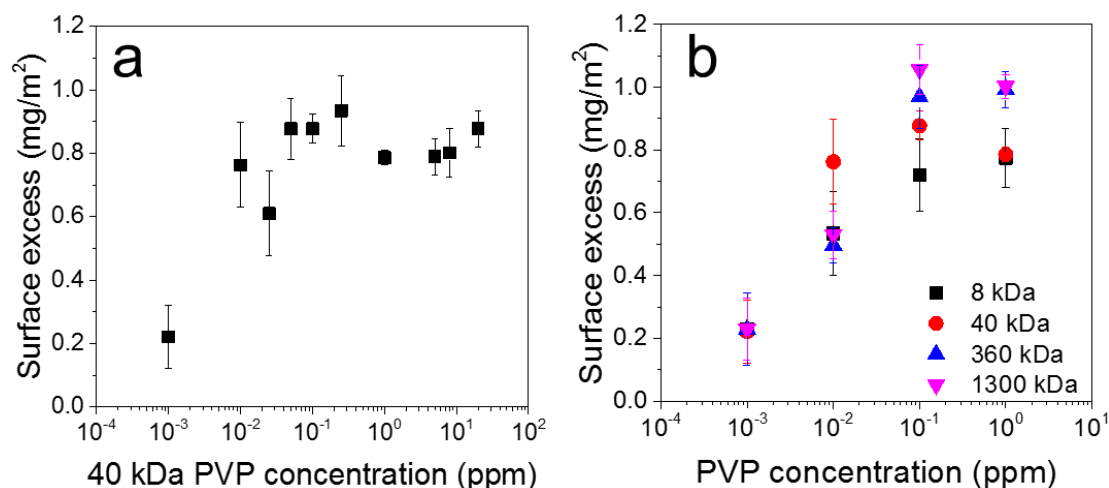


Figure 3.7 Surface excess isotherms for (a) 40 kDa PVP and (b) comparison of isotherms for 8 kDa, 40 kDa, 360 kDa and 1300 kDa PVP measured by OR at 25 °C.

3.4.1.2 PVP adsorption kinetics. Fig. 3.8 shows the adsorption kinetics of 8 kDa PVP for a variety of PVP concentrations. Each OR experiment begins with

establishing a baseline (approximately 10 min) in Milli-Q water before the PVP solution is injected into the measurement cell. A clear concentration dependence on the PVP adsorption rate exists, with the equilibrium surface excess values being achieved after 5 min for 1 ppm PVP but more than 1 h is required to reach equilibrium for 0.01 ppm PVP. The adsorption rate for 0.001 ppm PVP has the largest uncertainty due to the poor signal-to-noise ratio at this ultra-low concentration, although a repeatable equilibrium surface excess of around 0.2 mg/m^2 was measured. Once the equilibrium surface excess was obtained, Milli-Q water was re-introduced into the OR cell at the positions indicated by the arrows in Fig. 3.8. Negligible rinse-off of the adsorbed PVP was observed at all concentrations, indicating that the PVP molecules are strongly bound to the silica surface, hence the adsorption of PVP onto silica can be regarded as irreversible (over the timescales of interest).⁸⁶

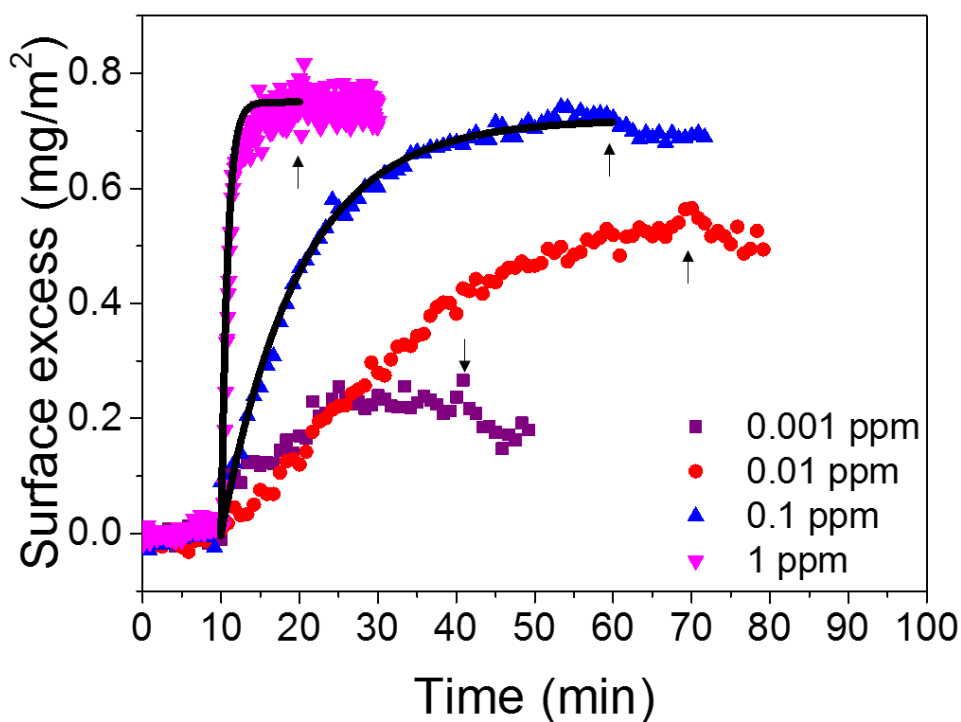


Figure 3.8 Adsorption kinetics for 8 kDa PVP as a function of the PVP concentration measured by OR. Adsorption kinetics described by Eq. 3.3 are shown as solid lines. Arrows indicate the injection time of Milli-Q water (rinse-off).

Since PVP adsorption on silica has been found to be irreversible, the adsorption kinetics of PVP can be described by relating the changing rate of the surface excess as a function of time t and the initial concentration c of PVP in solution as²⁵

$$\frac{d\Gamma}{dt} = k_a c B(\Gamma) \quad (3.4)$$

where k_a is the adsorption rate coefficient of PVP and $B(\Gamma)$ is the blocking function, which is suggested by the Langmuir model to be²⁵

$$B(\Gamma) = \begin{cases} 1 - \Gamma/\Gamma_0, & \Gamma < \Gamma_0 \\ 0, & \Gamma \geq \Gamma_0 \end{cases} \quad (3.5)$$

where Γ and Γ_0 are the surface excess at time t and at saturation respectively.²⁵ The relationship between Γ and the adsorption time can then be calculated by integrating Eq. 3.4 to give

$$\Gamma = \Gamma_0 - \exp\left(-\frac{k_a c t}{\Gamma_0}\right) \Gamma_0 \quad (3.6)$$

Comparisons between the experimental data and the kinetic model fitting is shown in Fig. 3.8 for the 8 kDa PVP. Excellent agreement is obtained for the 0.1 and 1 ppm PVP with an optimal fitting parameter of $k_a = 1.2 \times 10^{-5}$ m/s. However, poor agreement between the experimental data and the kinetic model was observed at lower PVP concentrations due to insufficient polymer concentration, i.e. sub-monolayer coverage.²⁵

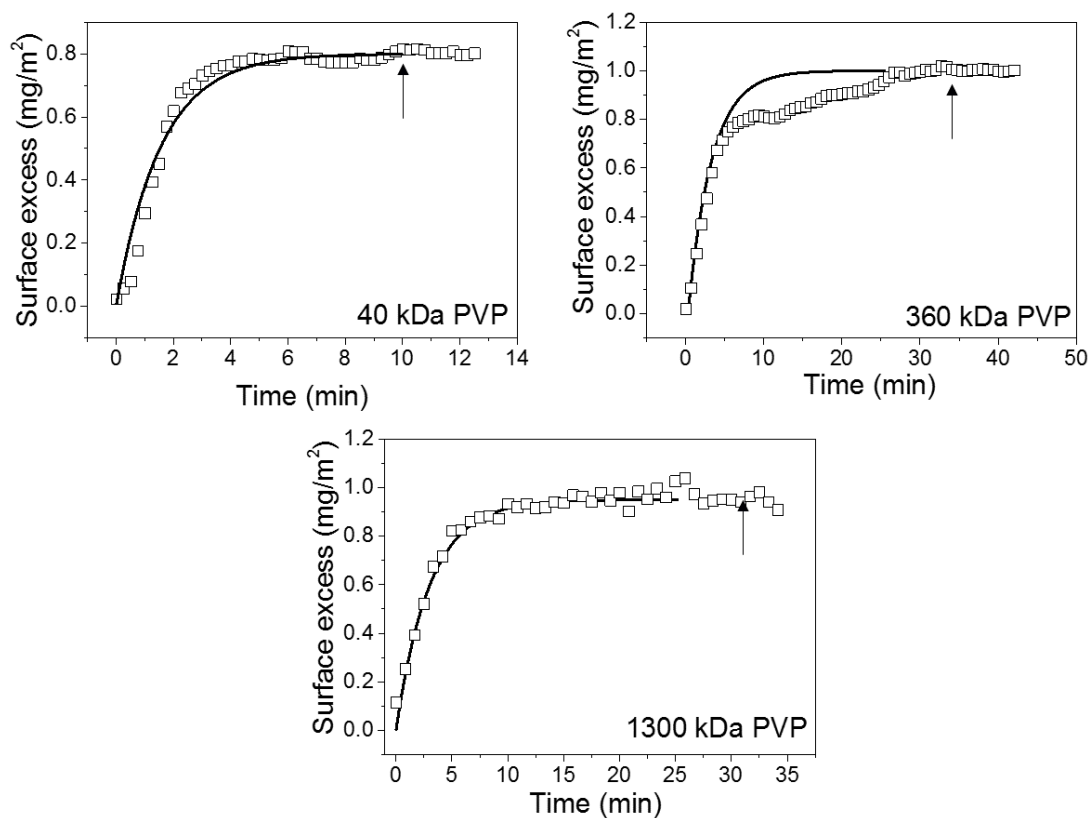


Figure 3.9 Adsorption kinetics for 40, 360 and 1300 kDa PVP measured by OR at 1 ppm. Adsorption kinetics described by Eq. 3.3 are shown as solid lines. Arrows indicate the injection time of Milli-Q water (rinse-off).

The adsorption kinetics of 40, 360 and 1300 kDa PVP at 1 ppm was also measured by OR, and again, good kinetic model fitting was observed (Fig. 3.9). The fitting parameters (k_a) for the 40 kDa, 360 kDa, and 1300 kDa PVP are 8.6×10^{-6} m/s, 5.5×10^{-6} m/s, and 5.0×10^{-6} m/s respectively, similar in magnitude to other linear polymers.²⁵

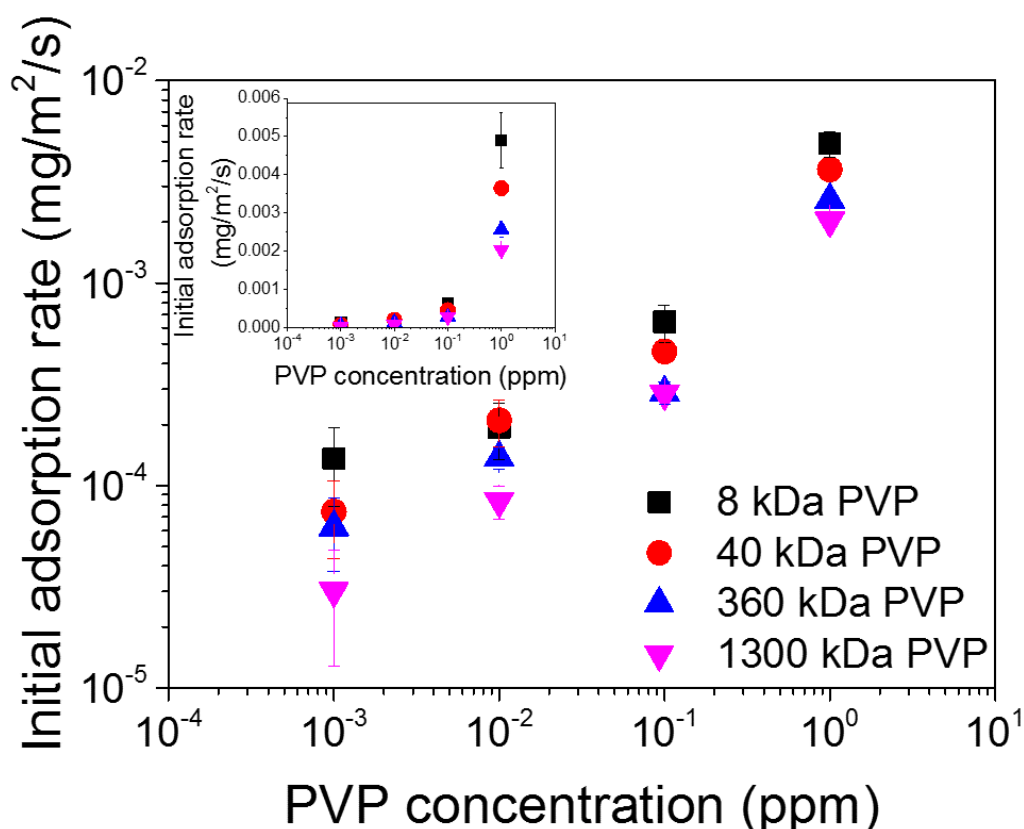


Figure 3.10 Initial PVP adsorption rate dependence on the PVP concentration and molecular weight. Semi-log data shown inset.

Fig. 3.10 compares the initial PVP adsorption rates as a function of the polymer concentration and molecular weight. The initial adsorption rates of PVP increased with increasing PVP concentration and decreasing PVP molecular weight.

3.4.2 PVP film hydration

Complementing the OR data, surface adsorption was also studied using QCM-D at equivalent PVP concentrations and molecular weights. The main difference between the two techniques is that the QCM-D is sensitive to both the adsorbed PVP and any solvent trapped within the adsorbed film (i.e. an apparent film mass), whereas the OR is sensitive to the adsorbed PVP while the trapped solvent within the polymer film remains absent (i.e. the real film mass). Therefore, by comparing the QCM-D and OR data it is possible to estimate the degree of adsorbed film hydration.¹¹¹

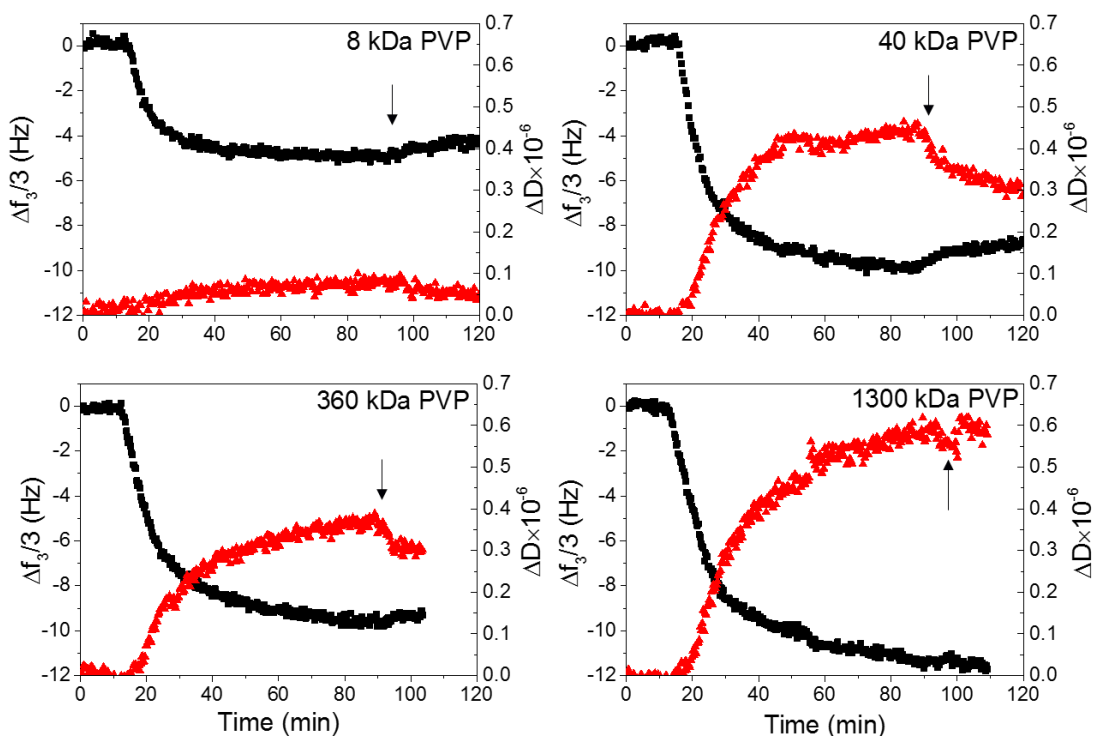


Figure 3.11 Time dependent resonance frequency (black filled squares) and dissipation (red filled triangles) for 8 kDa, 40 kDa, 360 kDa, and 1300 kDa PVP at 1 ppm. Arrows indicate the injection time of Milli-Q water (rinse-off).

The raw QCM-D data (Δf - time and ΔD - time) is shown in Fig. 3.11. For each QCM-D experiment, a stable baseline (approximately 10 min) was first established in Milli-Q water first before injecting the PVP solution. Milli-Q water was re-introduced once equilibrium surface excess obtained, see arrows in Fig. 3.11.

The raw QCM-D data was converted to adsorbed surface excess using two different models i) Sauerbrey¹¹² and ii) Voigt¹¹³, see Fig. 3.12.³¹ In both models the background fluid is Newtonian with only the thin adsorbed film modelled differently. It can be seen that both the viscoelastic Voigt model and the elastic Sauerbrey model differ from each other by around 10%, indicating that the adsorbed PVP films mainly behave as an elastic film. Hence the Sauerbrey model is adequate, and is used for the following analysis.³¹

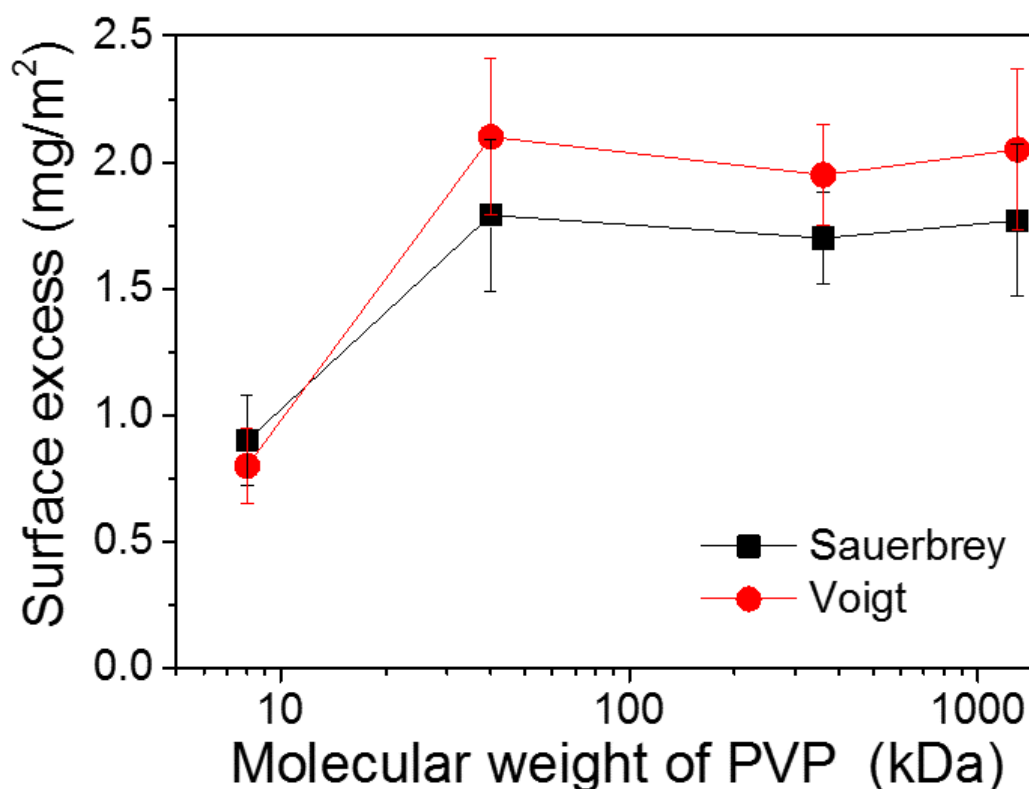


Figure 3.12 PVP molecular weight dependent equilibrium surface excess as determined by Sauerbrey and Voigt models, PVP concentration = 1 ppm.

Adsorption of 1 ppm PVP on silica using OR and QCM-D is directly compared in Fig. 3.13. 1 ppm was chosen since the adsorption isotherms in Fig. 3.7 confirmed complete surface saturation at PVP concentrations ≥ 0.1 ppm. Fig. 3.13 shows that for all QCM-D data, the equilibration time was much longer than was observed for the equivalent OR data due to the conformational rearrangement/reorganization of the polymer chains at the solid-liquid interface, which the OR is less sensitive to. The QCM-D data also showed little or no rinse-off (Milli-Q water wash identified by the arrows), confirming the results from the OR data where irreversible PVP adsorption was also shown.

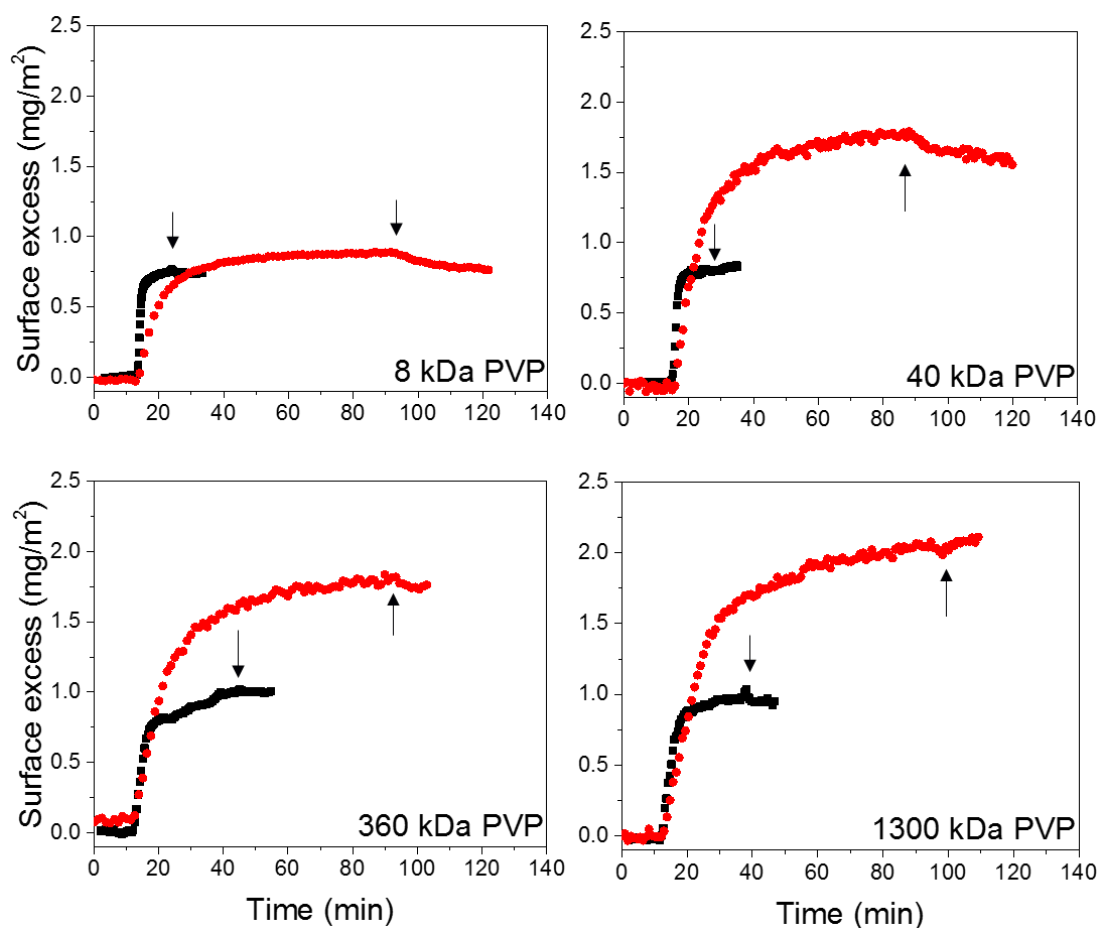


Figure 3.13 Adsorption kinetics for 1 ppm PVP of different molecular weights measured by both OR (black squares) and QCM-D (red circles). Arrows indicate the injection time of Milli-Q water (rinse-off).

Equilibrium surface excess values as a function of the PVP molecular weight are compared for the OR and QCM-D data, see Fig. 3.14. The equilibrium PVP surface excess measured by QCM-D (apparent film mass) is shown to be greater than the surfaces excess determined by OR, albeit the 8 kDa PVP data is in good agreement for both techniques. Since the PVP concentration is too low to change the density and viscosity of the bulk liquid,¹¹⁴ the QCM-D data indicates that the 8 kDa PVP forms a film with little water trapped, while the higher molecular weight polymers form more hydrated films. Based on the differences in surface excess between the OR and QCM-D data, we may therefore estimate that the amount of water retained in the PVP films

for 8 kDa PVP is around 10 wt%, and for the higher molecular weight PVPs (40 kDa, 360 kDa, and 1300 kDa) is approximately 40-55 wt%.

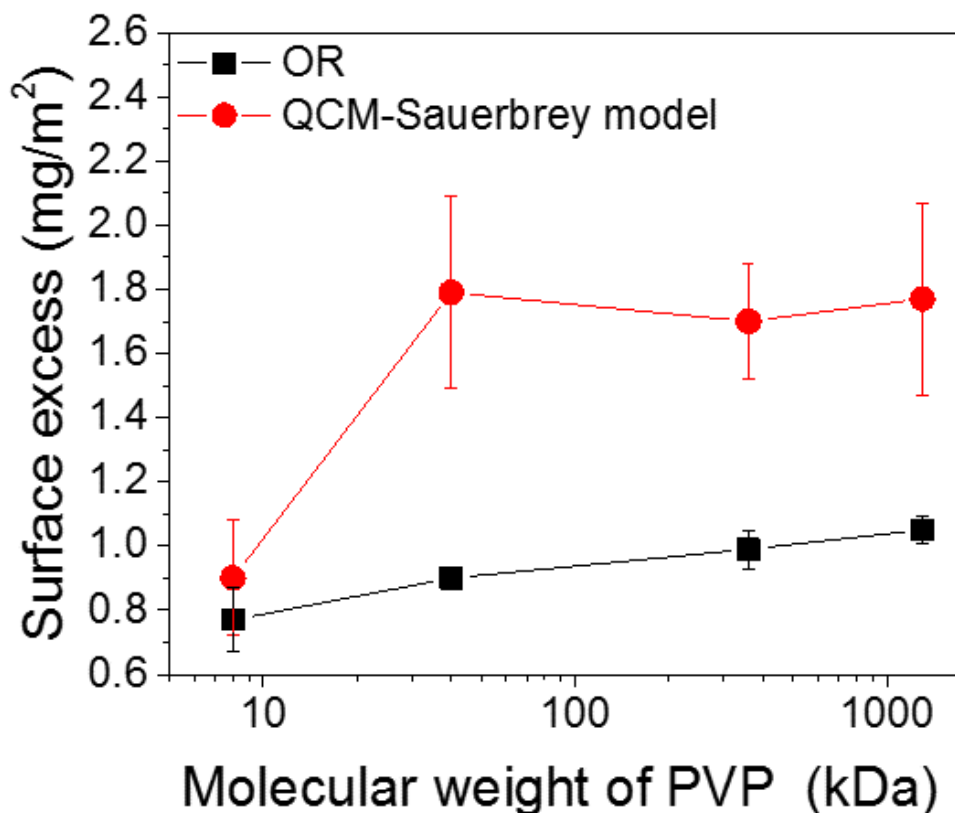


Figure 3.14 Equilibrium surface excess as a function of the PVP molecular weight measured by OR and QCM-D.

3.4.3 PVP Sauerbrey film thickness and conformation

In addition to the frequency shift (Δf), the dissipation shift, ΔD , is also recorded by the QCM-D, see Fig. 3.11. Since the polymer concentration (1 ppm) used here is too low to change the properties of the background liquid,¹¹⁴ the sensor dissipation should mainly result from the viscous losses of the adsorbed PVP film itself, including any trapped water inside the PVP film.¹⁰⁸

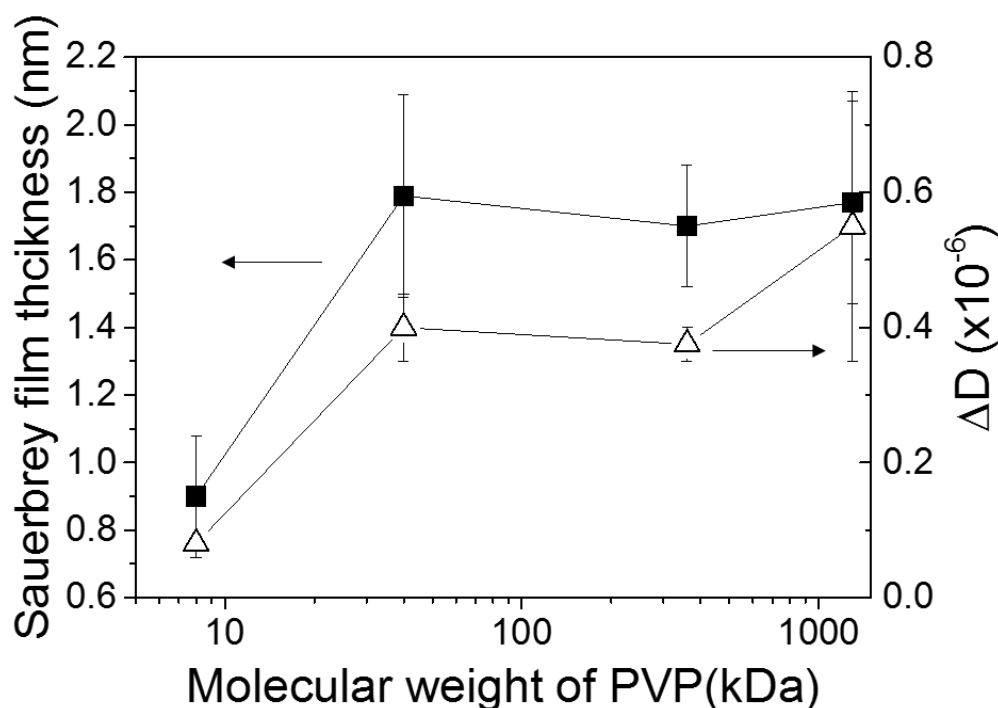


Figure 3.15 Comparison of the PVP Sauerbrey film thickness and the QCM-D equilibrium dissipation as a function of the PVP molecular weight at 1 ppm.

Fig. 3.15 shows the relative changes in Sauerbrey film thickness and dissipation for PVP films as a function of the PVP molecular weight and at a fixed PVP concentration of 1 ppm. The average hydrated film thickness from the QCM-D data was 0.9 nm for the 8 kDa PVP film and 1.8 nm for the higher molecular weight PVP films according to the Sauerbrey model. While the calculated film thickness of the 8 kDa PVP is in good agreement with the average film thickness determined from the OR data (~ 0.8 nm), when compared for the higher molecular weight PVPs there is significant divergence of the resulting film thicknesses (OR data ~ 1 nm for the 40 kDa, 360 kDa and 1300 kDa PVP films), again confirming that the difference likely results from the degree of PVP film hydration. Considering that the radius of gyration (R_g) of these polymers in solution are ~ 4 nm, ~ 7 nm, ~ 27 nm and ~ 51 nm for 8, 40, 360 and 1300 kDa PVP respectively¹¹⁵, the film thickness data shown in Fig. 3.15 most likely corresponds to the PVP chains lying flat or nearly flat on the substrate

(PVP chain width previously reported to be ~ 1 nm).⁸⁹ This likely polymer orientation on the substrate is also justified by the low dissipation values, although it is worth noting that the dissipation of the 8 kDa PVP film is four times smaller than the higher molecular weight PVPs. Once again signifying increased film stiffness by the lowest molecular weight PVP.

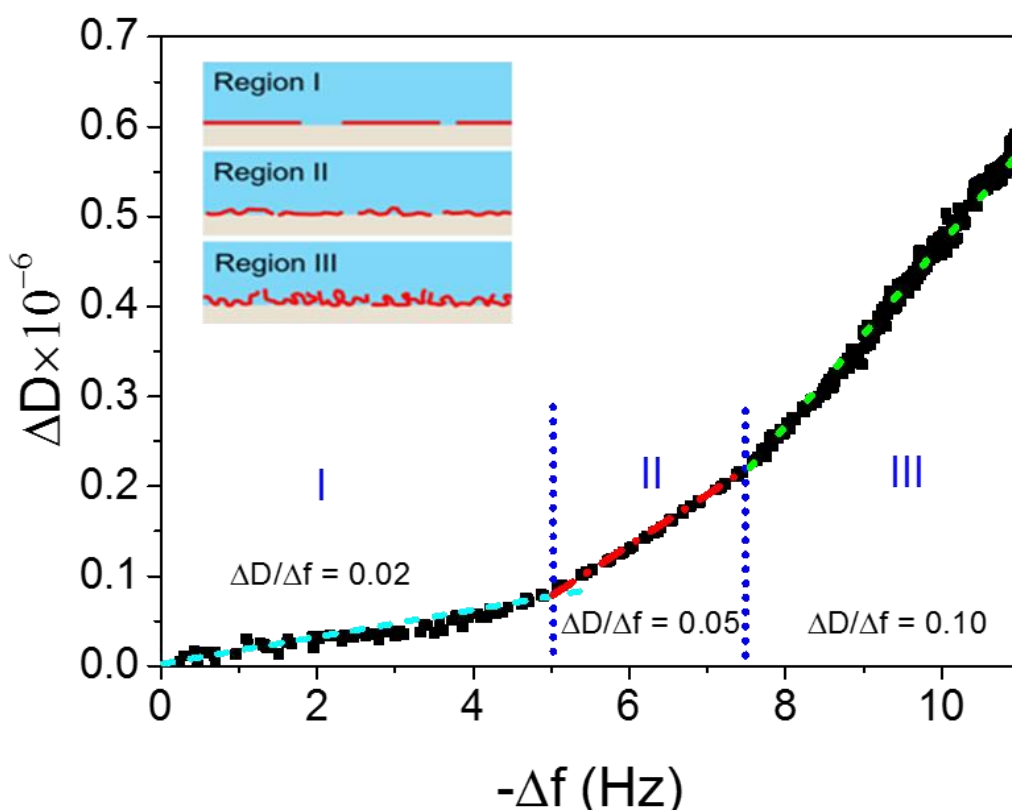


Figure 3.16 ΔD as a function of Δf for the 1300 kDa PVP at 1 ppm. All the $\Delta D/\Delta f$ values shown should be multiplied by a factor of 10^{-6} . Schematic to show the likely polymer orientation to reach the equilibrium state.

Fig. 3.16 shows ΔD as a function of Δf for the 1300 kDa PVP adsorption, highlighting potential conformational changes of the PVP molecules on silica during the adsorption process (rinse-off data not included). The experiment was allowed to reach equilibrium and the raw data is shown in Fig. 3.11. In Fig. 3.16 the QCM-D response for the 1300 kDa PVP can be divided into three stages, labelled as regions I,

II and III, according to the mean slope of each region.³¹ Region I shows a very small increase in dissipation (up to 0.08×10^{-6}) with a faster increase in frequency, up to 5 Hz, which is approximately half of the equilibrium plateau value of 11 Hz (see Fig. 3.11), suggesting that during the initial stages of adsorption, the 1300 kDa PVP molecules lie flat on the silica surface. In regions II and III the slope ($\Delta D/\Delta f$) increases to 0.05×10^{-6} and 0.1×10^{-6} respectively, representing a larger and larger contribution from the sensor dissipation, with relatively small changes in the frequency. These latter stages (regions II and III) represent the gradual rearrangement/reorganization of the 1300 kDa PVP film resulting in a 40-55 wt% hydration of the adsorbed polymer film. The increased contribution from the dissipation is further confirmation of gradual film softening (increased hydration) due to the longer time conformational changes of the adsorbed polymer film (inset Fig. 3.16). These slower dynamics have previously been reported using AFM, where the authors studying the adsorption of 1 ppm PVP on graphite observed that the polymer first adsorbs in an expanded chain conformation before reconfiguring over several hours to reach an equilibrium state that is slightly more globular and rougher.¹¹⁶ Similar softening behaviour was also observed for the 40 kDa and 360 kDa PVP films, see Fig. 3.17.

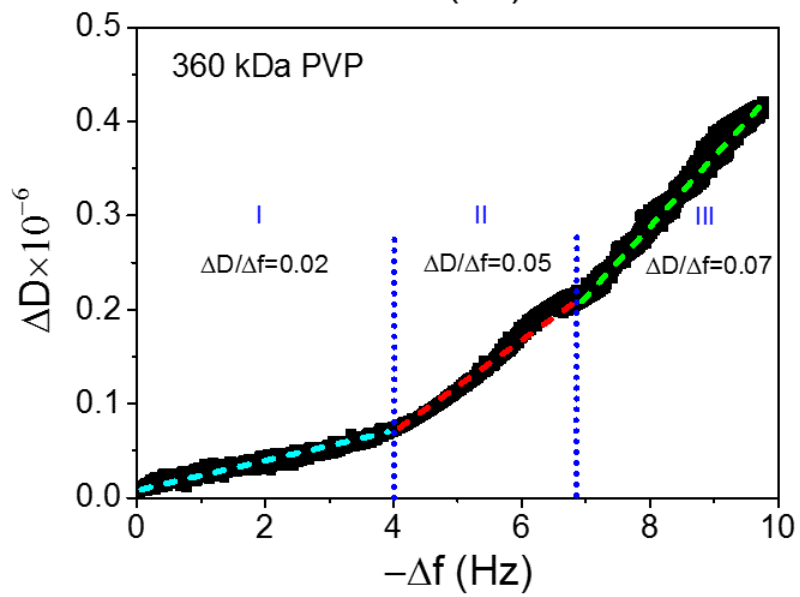
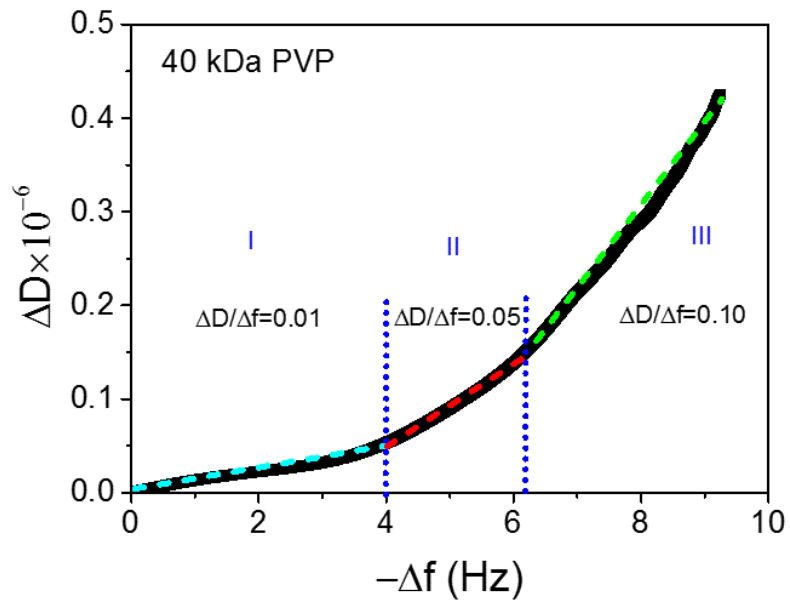
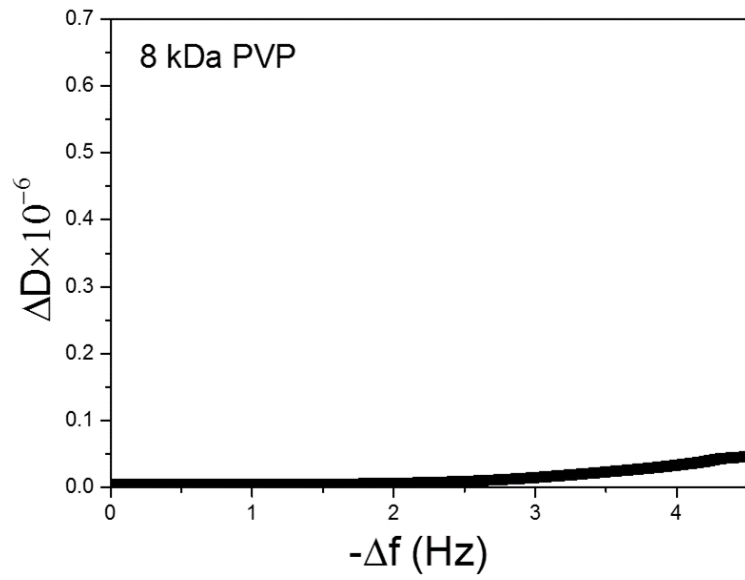


Figure 3.17 ΔD as a function of Δf for the 8 kDa 40 kDa and 360 kDa PVP at 1 ppm. All the $\Delta D/\Delta f$ values shown should be multiplied by a factor of 10^{-6} .

By comparison, the entire adsorption process of the 8 kDa PVP (Fig. 3.17) reasonably compares to region I of the 1300 kDa PVP data. Very small equilibrium values of Δf and ΔD of 5 Hz and 0.1×10^{-6} respectively were measured for the 8 kDa PVP film. The fact that the equilibrium Δf for the 8 kDa PVP film was about half that of the 1300 kDa film, whereas the ΔD value was more than 4 times smaller, confirms that negligible softening of the 8 kDa film occurs. From the QCM-D data we would expect the 8 kDa PVP film to be more rigid than the higher molecular weight PVP films.

3.4.4 Lubrication effects

3.4.4.1 Particle-substrate lateral force. The lateral forces between silica-silica surfaces, and PVP coated silica surfaces were measured under different normal loads using the AFM colloid probe technique.⁹⁶ The lateral forces between uncoated silica surfaces (Fig. 3.18) increased almost linearly with increasing normal load (over the range considered), as expected by Amonton's law.¹¹⁷ Interestingly, the measured lateral forces between 8 kDa PVP-PVP surfaces closely matched the uncoated silica data at all loads. By contrast, the 40 kDa PVP-PVP, 360 kDa PVP-PVP, and 1300 kDa PVP-PVP surfaces showed significantly smaller lateral forces, and each of these three longer chain PVP polymers showed a similar response independent of the polymer molecular weight. This suggests that above a critical chain length, PVP can reduce the friction between silica surfaces by approximately a factor of 2.

Qualitatively these results complement the adsorption data, where it was shown that the 8 kDa PVP forms a comparatively more “rigid” film than the more “lossy” higher molecular weight PVP films. The ability to reconfigure and essentially hydrate to produce an interfacial film of increased softness is favorable for lubrication. Under compression the “soft” interfacial film is able to accommodate the normal load and inhibit hard surface contact, something that is less achievable for the lowest molecular weight PVP, which essentially adsorbs in a flat configuration with little retained water in the polymer film.^{93, 101}

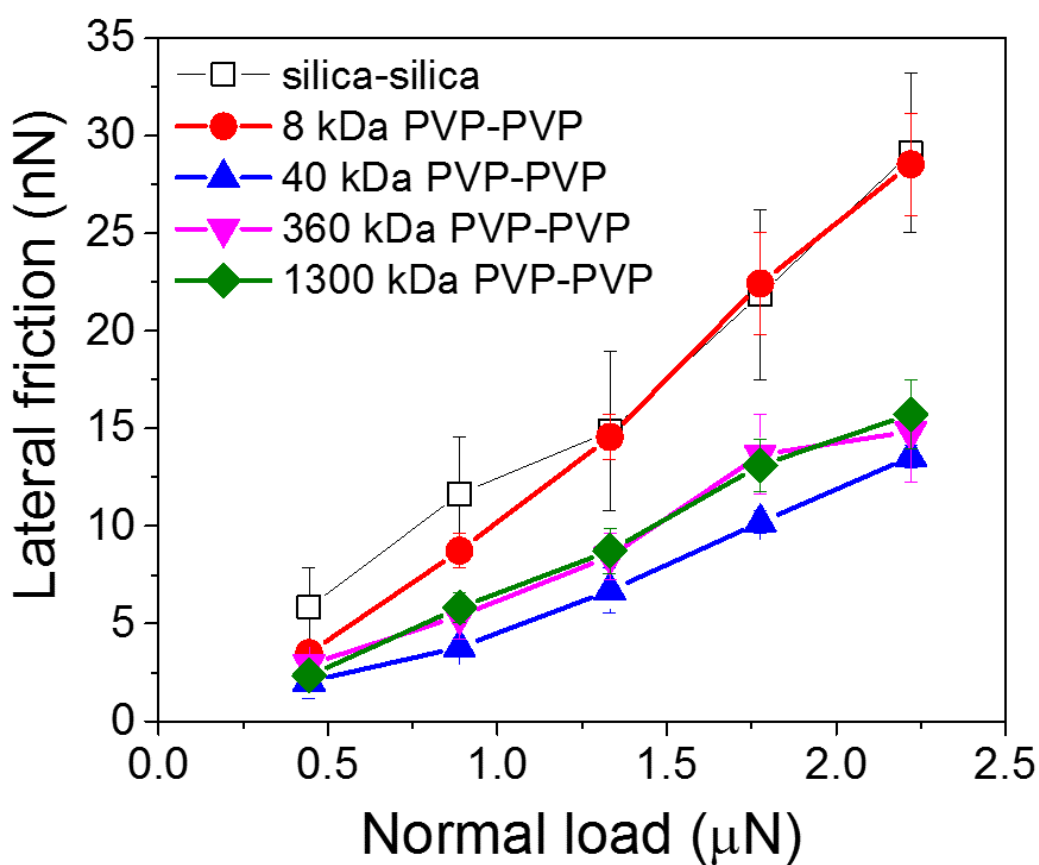


Figure 3.18 Lateral forces measured between silica-silica, 8 kDa PVP-PVP, 40 kDa PVP-PVP, 360 kDa PVP-PVP, and 1300 kDa PVP-PVP surfaces by a colloid AFM probe.

In summary, we have determined a critical PVP molecular weight (~ 40 kDa) exists, around which the friction may be reduced by ~50% compared with uncoated silica surfaces.

3.4.4.2 Yield stress of suspensions. High concentration (50 to 63 vol%) suspensions were prepared using uncoated silica particles in water, as well as 8 kDa PVP and 40 kDa PVP coated silica particles in water. The Herschel-Bulkley equation, $\tau = \tau_0 + k(\dot{\gamma})^n$, where τ is the shear stress, τ_0 the suspension yield stress, $\dot{\gamma}$ the shear rate, k and n the consistency and flow indices, respectively, was used to determine the suspension yield stress, with an example fitting shown in Fig. 3.19. The fitting parameters (k and n) are summarized in Table 3.1. As shown, for the uncoated and 8 kDa PVP-coated silica particles the apparent suspension viscosity (k) was observed to increase with increasing solids concentration, while the extent of suspension shear thinning (n) also increased ($n < 1$, shear thinning). However, the 40 kDa PVP-coated silica particles showed minimal variation in n (exhibiting Newtonian-like fluid behavior), even though the suspension viscosity increased with increasing solids concentration.¹¹⁸

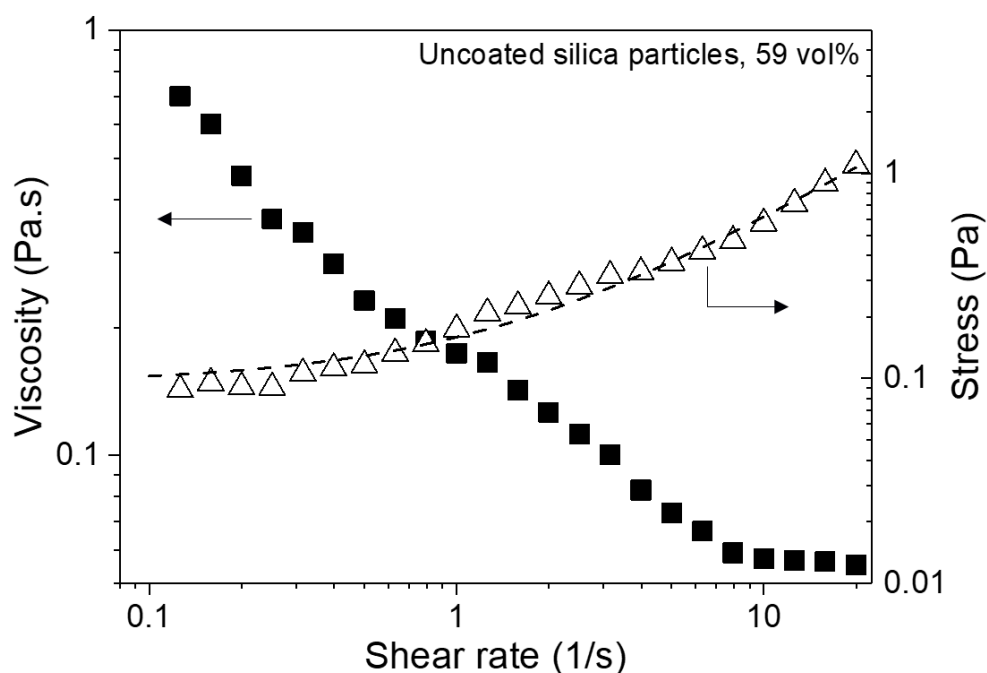


Figure 3.19 Suspension viscosity (closed symbols) and shear stress (open symbols) as a function of the applied shear rate for a 59 vol% uncoated silica suspension. Dashed line represents the Herschel-Bulkley model used to determine the suspension yield stress (τ), consistency index (k) and flow index (n), see Table 3.1.

Table 3.1 Fitting parameters k and n of the Herschel-Bulkley equation.

Solids conc. (vol%)	Uncoated silica particles		8 kDa PVP-coated silica particles		40 kDa PVP-coated silica particles	
	k (Pa·s)	n	k (Pa·s)	n	k (Pa·s)	n
53	5.0×10^{-3}	0.99			5.0×10^{-3}	0.99
56	1.0×10^{-2}	0.95			6.0×10^{-3}	0.99
59	6.4×10^{-2}	0.91	3.0×10^{-2}	0.95	1.0×10^{-2}	0.99
61	8.9×10^{-2}	0.90	6.0×10^{-2}	0.91	7.0×10^{-2}	0.95
63	3.0×10^{-1}	0.86	2.2×10^{-1}	0.85	9.0×10^{-2}	0.99

Suspension yield stress as a function of the apparent particle volume fractions were shown in Fig. 3.20. The Sauerbrey thickness of the PVP film (Fig. 3.15) was taken into account to shift the ‘apparent’ volume fraction of the composite particle suspension to a slightly higher value (Fig. 3.20) compared with the uncoated particles.

The yield stress of the 40 kDa PVP-coated particle suspension was shown to be significantly reduced above 60 vol% compared with the uncoated silica particle suspension. This result is in broad agreement with the lateral force data (Fig. 3.18) where it was shown that the 40 kDa PVP films had significantly lower lateral forces than the uncoated silica surfaces. The lubrication effect from a softer polymer film would assist particles to slide past each other more easily when the particles are highly packed (high contact loading).¹⁰³ By contrast, the suspensions prepared using 8 kDa PVP-coated particles behaved similarly to uncoated silica particles, most likely a result of the thin, dehydrated PVP film adsorbed on the particle, as evidenced by OR and QCM-D techniques. This thin and rigid film has much less retained water, resulting in a greater degree of friction between each particle, and therefore, a larger shear force is needed to induce yielding of the high volume fraction suspension.

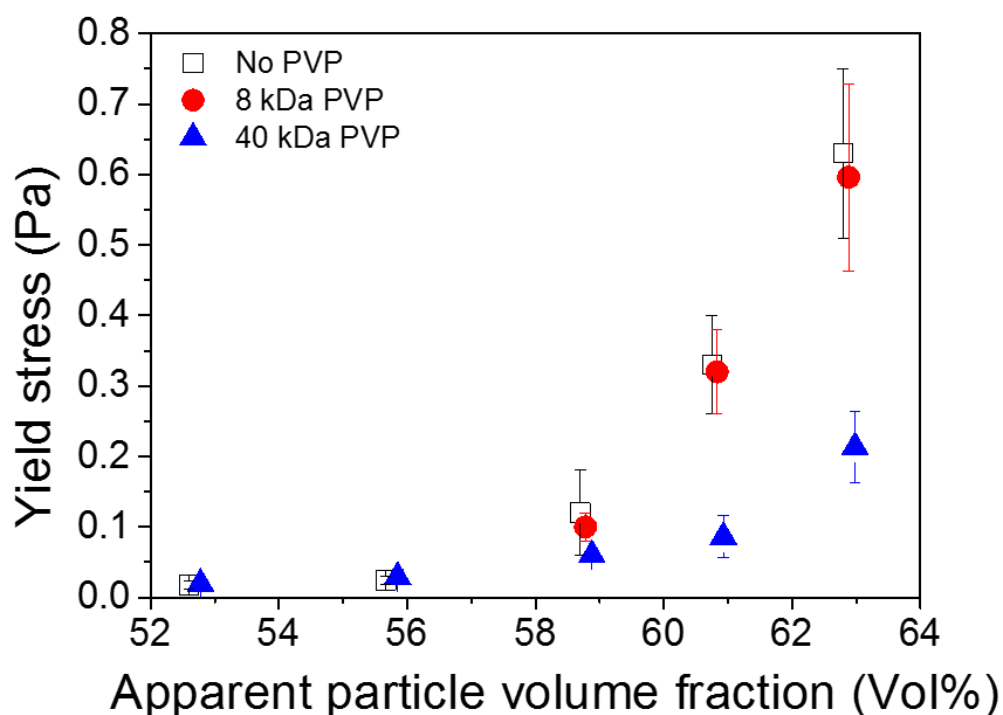


Figure 3.20 Suspension yield stress as a function of the apparent particle volume fraction for uncoated silica particles (No PVP), 8 kDa and 40 kDa PVP coated silica particles in water.

3.5 Conclusion

In the current study, silica surfaces were modified by adsorbing poly(vinylpyrrolidone) (PVP) at ultra-low concentrations (< 1 ppm). Different PVP molecular weights between 8 kDa and 1300 kDa were used to investigate both the adsorbed mass and the frictional properties of the resultant polymer coating. The surface excess measurements obtained by OR only showed a very weak molecular weight dependence, whereas QCM-D data on the same PVP films showed that the amount of retained water in the 8 kDa PVP film was much less (~ 10 wt%) than the retained water in films formed using higher molecular weight PVP (trapped water ~ 40 -55 wt%). Lateral forces measured by AFM between 8 kDa PVP-PVP surfaces very closely matched the uncoated silica lateral forces at all normal loads tested. By contrast, the lateral forces measured between 40 kDa PVP-PVP, 360 kDa PVP-PVP, and 1300 kDa PVP-PVP surfaces were significantly smaller, indicating that above a critical chain length (~ 40 kDa), PVP can significantly reduce the friction between silica surfaces by approximately a factor of 2. This lubrication effect of PVP has been verified by observing a reduction in the yield stress of high concentration silica suspensions when the particles were coated with 40 kDa PVP. The 8 kDa PVP-coated particles showed negligible variance from the uncoated particles, further validating the lubricating effect of higher molecular weight PVP at ultra-low polymer concentrations.

Chapter 4: Foaming Behaviour of PVP-coated Silica Particles

4.1 Synopsis

PVP adsorption on silica has been studied in the previous chapter. Since the adsorption of PVP on silica was shown to be irreversible, PVP-coated silica particles (composite particles) were considered as a means of stabilizing foams.

The current chapter examines the foaming behaviour of composite particles. Individually, the two components, PVP and silica nanoparticles, exhibit very little potential to partition at the air-water interface and, as such stable foams cannot be generated. In contrast, combining the two components to form silica-PVP core-shell nanocomposites leads to good ‘foamability’ of long-term foam stability. Addition of an electrolyte (Na_2SO_4) was shown to have a marked effect on the foam stability. By varying the concentration of electrolyte between 0 and 0.55 M, three regions of foam stability were observed: transitioning from rapid foam collapse at low electrolyte concentrations, through delayed foam collapse at intermediate concentrations, and finally long-term stability (~ 10 days) at the highest electrolyte concentration. The observed transitions in foam stability were better understood by studying the microstructure and physical and mechanical properties of the particle-laden interface. For rapidly collapsing foams the nanocomposite particles were weakly retained at the air-water interface. The interfaces in this case were characterized as being “liquid-like” and the foams collapsed within 100 min. At an intermediate electrolyte concentration (0.1 M), delayed foam collapse over ~16 h was observed. The particle-laden interface

was shown to be pseudo solid-like as measured under shear and compression. The increased interfacial rigidity was attributed to adhesion between interpenetrating polymer layers. For the most stable foam (prepared in 0.55 M Na₂SO₄), the ratio of the viscoelastic moduli, G'/G'' was found to be equal to ~ 3 , confirming a strongly elastic interfacial layer. Using optical microscopy, the enhanced foam stability was assessed and attributed to a change in the mechanism of foam collapse. The bubble-bubble coalescence was found to be significantly retarded by the aggregation of nanocomposite particles, with the long term destabilization being recognized to result from bubble coarsening. For rapidly destabilizing foams the contribution from bubble-bubble coalescence was shown to be more significant.

4.2 Literature Review

Assembly of colloidal particles at fluid interfaces (Fig. 4.1) is a promising technique for synthesizing novel materials which can be potentially used in biomedicine, materials science, and formulated products.^{3, 4, 32, 33, 34, 35} In many products, colloid particles and a wide range of chemical additives such as surfactants and polymers often co-exist to provide desirable properties, which usually include immiscible fluids (liquid-liquid or gas-liquid). Upon mixing in these systems, interfaces generated are stabilized by the chemical additives. While the amphiphilicity of surfactants governs their interfacial activity, the surface chemical uniformity of a particle means that contrasting affinities for both the polar/non-polar fluids is not readily achieved, although the use of Janus particles is a route to provide such amphiphilicity.¹¹⁹

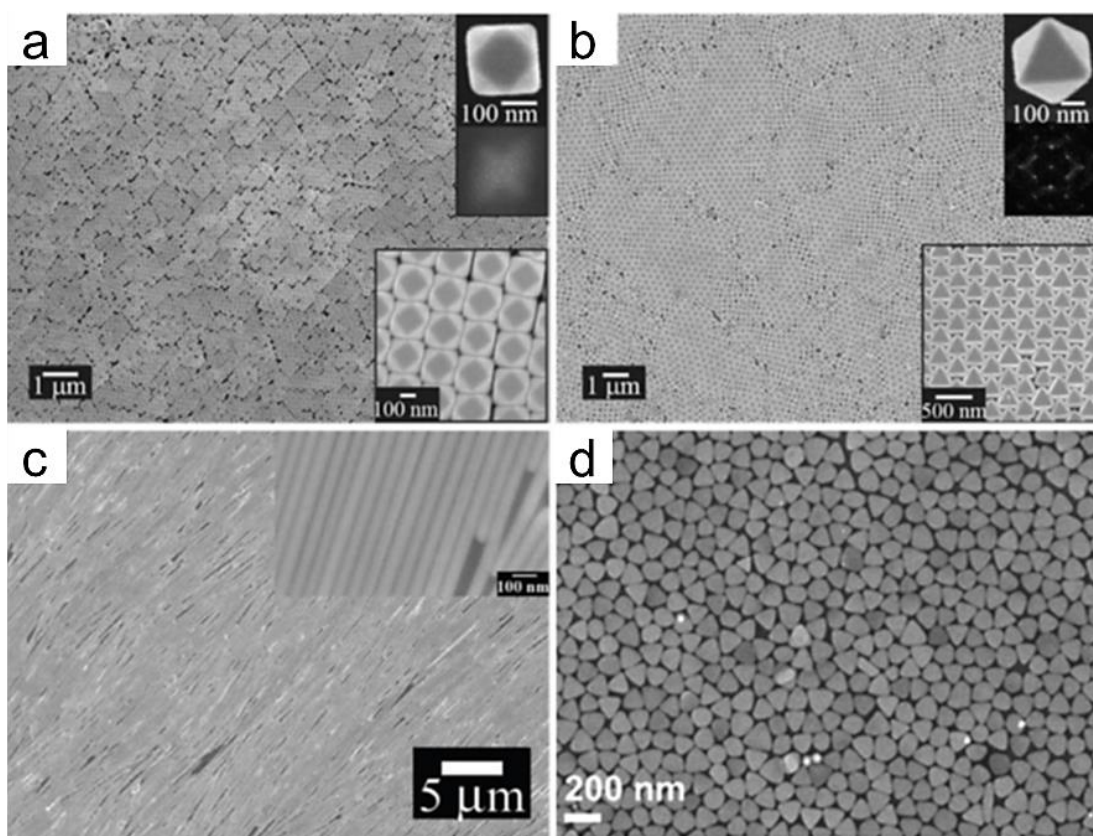


Figure 4.1 Self-assembled PVP coated (a) Ag nano-cubes, (b) Ag octahedra, (c) Ag nanowires and (d) Au nanoprisms films at the air-water interface.^{120, 121, 122}

The potential for a particle to reside at an interface is influenced by the particle wettability, represented by the three phase contact angle (θ).¹⁰ Previous studies showed that good emulsion stabilizing particles exhibit contact angles close to 90° . For foams, this critical contact angle is lower than 90° , with optimum stabilizing conditions reported for contact angles close to 70° .⁹ Relatively small deviations away from this optimum contact angle can lead to dramatic changes in foam stability, with particles behaving as de-stabilizers rather than stabilizers. Various routes to modify particle wettability have been demonstrated, which include silanization,^{10, 72} surfactant adsorption,¹² addition of electrolyte,¹²³ polymer grafting,^{14, 57} surface roughness modification,¹²⁴ and more recently switching of physical conditions of the system such as temperature, pH, light, or CO_2 addition/removal.

4.2.1 Foaming potential of surfactant-particle composites and interfacial rheology

For foams stabilized by surfactant, the behavior and mechanisms of foam collapse have recently been reviewed by Briceno-Ahumada and Langevin. They showed that the rate of bubble coarsening was proportional to the permeability of the interfacial layer, which was dependent on the layer thickness and the surfactant packing density, a factor that can be controlled by introducing surfactant mixtures.¹²⁵ The added benefit of using composite surfactant-particles to arrest bubble coarsening has been demonstrated in several recent studies.^{12, 126, 127} Through the electrostatic attraction between cetyltrimethyl ammonium bromide (CTAB) and silica particles, foams stabilized by composite particles were shown to exhibit substantially longer foam lifetimes than surfactant-only stabilized foams.¹²⁶ The enhanced foam stability was shown as a reduction in the rate of bubble coarsening once the particle concentration at the interface was sufficiently high to effectively “jam” the foam network.¹²⁶ The critical condition to minimize bubble coarsening was influenced by the particle number density at the interface, which was directly related to the surfactant concentration.^{12, 127} During bubble coarsening, smaller bubbles were observed to reduce in size before the interface eventually buckled.¹²⁶ Interfacial buckling (see Fig. 4.2) confirmed the strong retention of the surfactant-particle composites at the gas-liquid interface, with the energy for particle detachment affected by the wetting angle. The critical wetting angle has been shown to vary between 50° and 70°, depending on the surfactant concentration when below the critical micelle concentration (CMC).¹²⁷

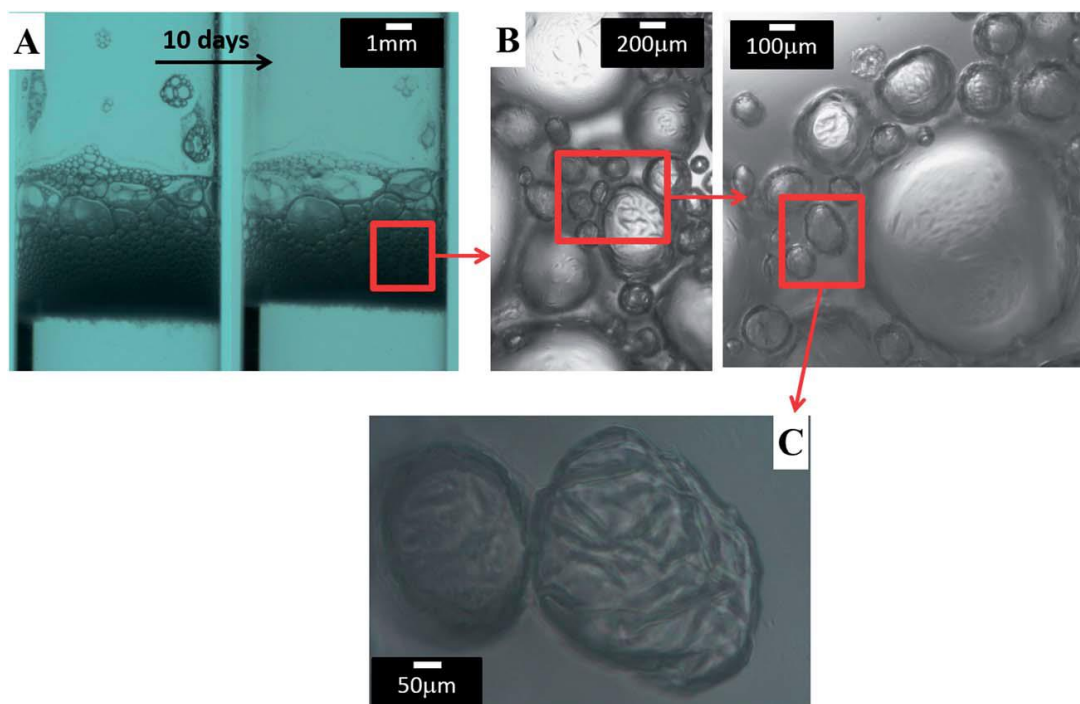


Figure 4.2 Crumpled bubbles stabilized by surfactant-particle composites.¹²⁶

For an interface to buckle Erni et al.¹²⁸ confirmed that the two interfacial rheological contributions, shear and dilatational, should be non-zero, and the interface should behave as an elastic solid, i.e. G' (storage modulus) $>$ G'' (loss modulus). With continued bubble shrinking, the irreversibly adsorbed chemical species eventually ‘jam’ and resist any further surface area reduction, until a critical compressive strain is surpassed to buckle the interface. The ability for an interface to resist in-plane shear has recently been shown as a key contributing factor in stabilizing droplets. At the liquid-like state ($G'' > G'$) the interfacial layer provides little resistance to droplet-droplet coalescence. However, when the condition for interfacial buckling is satisfied and the interface is described as being solid-like, two interacting droplets do not coalesce.⁶³ The stabilizing mechanism is attributed to the interfacial shear yield stress which must be exceeded in order for the interfacial layer to flow away from the contact area and initiate droplet coalescence. For foams stabilized by surfactant-only,

the conservation of the surfactant surface coverage through the reversible adsorption of surfactant molecules mitigates the buckling.

Langevin and co-workers recently demonstrated that the shear rheology of a surfactant-particle-laden interface satisfies the soft glassy rheological response, with the elastic contribution of the layer being dependent on the surfactant concentration.¹² The data qualitatively verify previous observations of foam lifetime. However, the contribution of interfacial shear rheology to foam destabilization may be more relevant to bubble coalescence than bubble coarsening, as the arrest of bubble coarsening has frequently been discussed in terms of the dilatational elasticity.¹²⁵ For a single bubble, coarsening can be stopped if the elastic compression modulus E of the interfacial layer is at least twice the gas-liquid surface tension (γ). Following the derivation by Gibbs,^{9, 72, 125} bubble coarsening ceases when the Laplace pressure approaches zero. While numerous practical foam studies have verified this criterion, contradictions have also been reported, which were often justified by the formation of multilayers.⁷²

4.2.2 Foaming potential of polymers and polymer-surfactant mixtures

The application of polymers to stabilize foams has received little scientific attention due to weak adsorption of polymers at the gas-liquid interface.^{11, 16} However, polymer-surfactant mixtures have been shown to extend the lifetime of thin liquid films by promoting the formation of surface complexes below the critical aggregation concentration (CAC). The presence of surface complexes leads to an increase in the surface viscosity and steric repulsion between two approaching fluid interfaces, as shown in Fig. 4.3.^{11, 17} Above the CAC the polymer-surfactant complexes gel, significantly increasing the bulk fluid viscosity and extending film lifetime. In this

case the maximum foam stability was observed at the onset of surfactant-polymer precipitation.^{17, 129}

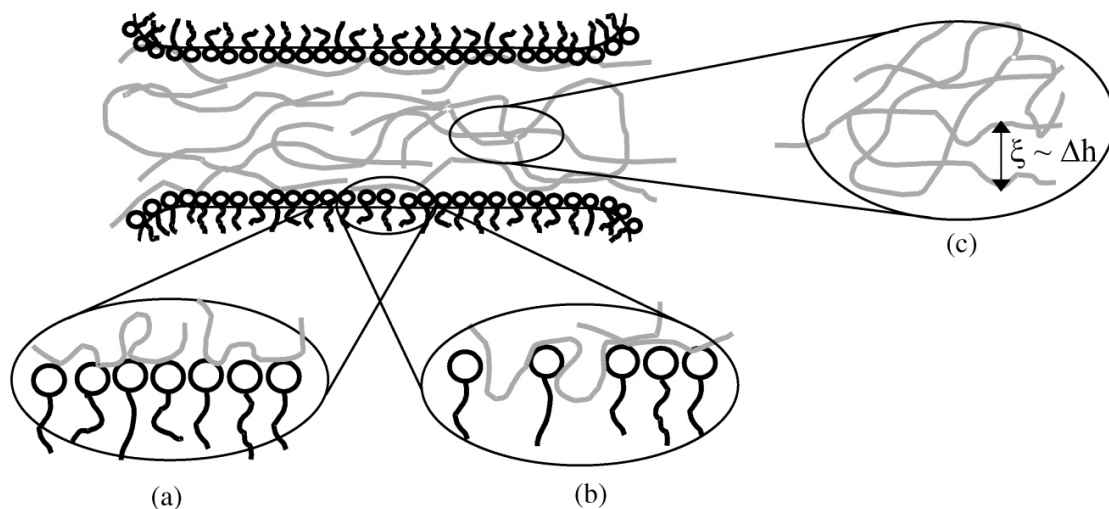


Figure 4.3 Schematic of a thin liquid film stabilized by polymer-surfactant complexes, Δh indicates the distance between two neighbouring polymer branches.¹⁷

4.2.3 Foaming potential of microgel particles and pseudo-microgel particles

More recently, emulsions and foams stabilized by polymer microgel particles have demonstrated tuneable functionality in two-phase systems by the use of thermal-responsive or pH-responsive polymers.^{13, 130} The co-polymer ratio in microgel particles has been shown to affect the emulsifying potential of particles. Compared with rigid microgel particles, ‘softer’ and more responsive particles produce emulsions of extended lifetime.¹³¹ Pseudo-microgel particles formed by grafting polymer onto the surface of nanoparticles have also been proven to be good emulsifying agents, stabilizing emulsions for several months. Tilton and co-workers reported that the best nanoparticles for emulsification had a low concentration of polymer chains adsorbed on their surface (0.077 chains/nm²), stabilizing emulsions with only 0.05 wt% polymer-grafted nanoparticles. This concentration of particles is

much lower than that usually required to stabilize Pickering emulsions.¹⁴ Compared with hard spheres, core-shell particles were shown to be good foaming/emulsifying agents and stabilizers since they are capable of reducing the surface tension,⁵⁷ facilitate the adsorption of particles at the fluid-fluid interface,^{50, 57, 132} and provide a route to control the particle-particle separation distance to adjust the structure and mechanical strength of interfacial layers.^{133, 134, 135}

To the best of our knowledge, foaming ability of polymer-particle composites formed via polymer physisorption has not been considered in detail. In the current chapter, we focus on the interfacial properties of PVP-coated silica composite particles. The role of electrolyte concentration on the mechanical response of deposited particle layers was investigated and correlated to the observed transitions in foam stability.

4.3 Materials and Experimental Methods

4.3.1 Materials

PVP with a molecular weight of 40 kDa was purchased from Alfa Aesar (UK) and used as received. Ludox AS40 silica nanoparticles were purchased from Sigma-Aldrich (UK) as a 40 wt% aqueous suspension. Prior to its use the silica particle suspension was diluted to 10 wt% using Milli-Q water and then ion exchanged using Amberlite IRN 50 resin (Alfa Aesar, UK) to remove excess SO_4^{2-} counter-ions. The removal of excess counter-ions was verified by conductivity measurements of the diluted suspensions (reduced from $\sim 225 \pm 30 \mu\text{S}/\text{cm}$ to $\sim 53 \pm 10 \mu\text{S}/\text{cm}$). The particle hydrodynamic diameter was determined using a Malvern ZetaSizer Nano ZS (Malvern Instruments, UK) to be $\sim 34 \text{ nm}$ with a PDI of 0.14. Milli-Q water with a resistivity of $18.2 \text{ M}\Omega\cdot\text{cm}$ was used throughout the study and sodium sulphate (99+%, A.C.S. R,

Sigma Aldrich, UK) was used as received without further purification for changing the electrolyte concentration.

4.3.2 Experimental methods

4.3.2.1 Preparation of PVP coated silica composite particles. To prepare the PVP (40 kDa) coated silica nanoparticles, henceforth referred to as composite particles, 30 mL of 10 wt% silica nanoparticle suspension was added dropwise to 5 wt% PVP solution (40 mL) under gentle agitation. The PVP-silica suspension was continually mixed for 12 h to ensure PVP adsorption. Excess or weakly adsorbed PVP was removed from the silica particle suspension by centrifuging the sample at 13,000 rpm (18549g) for 4 h. The supernatant was removed using a wide bore pipette before re-dispersing the centrifuged particles in Milli-Q water using mild sonication. The wash process was repeated several times and complete removal of any unadsorbed PVP was verified by measuring the surface tension of the removed supernatant after each wash cycle. Complete PVP removal was assumed when $\gamma_{a/w}$ of the removed supernatant reached ~ 72.3 mN/m, at 25 °C. A schematic of the method designed to form the composite particles is shown in Fig. 4.4.

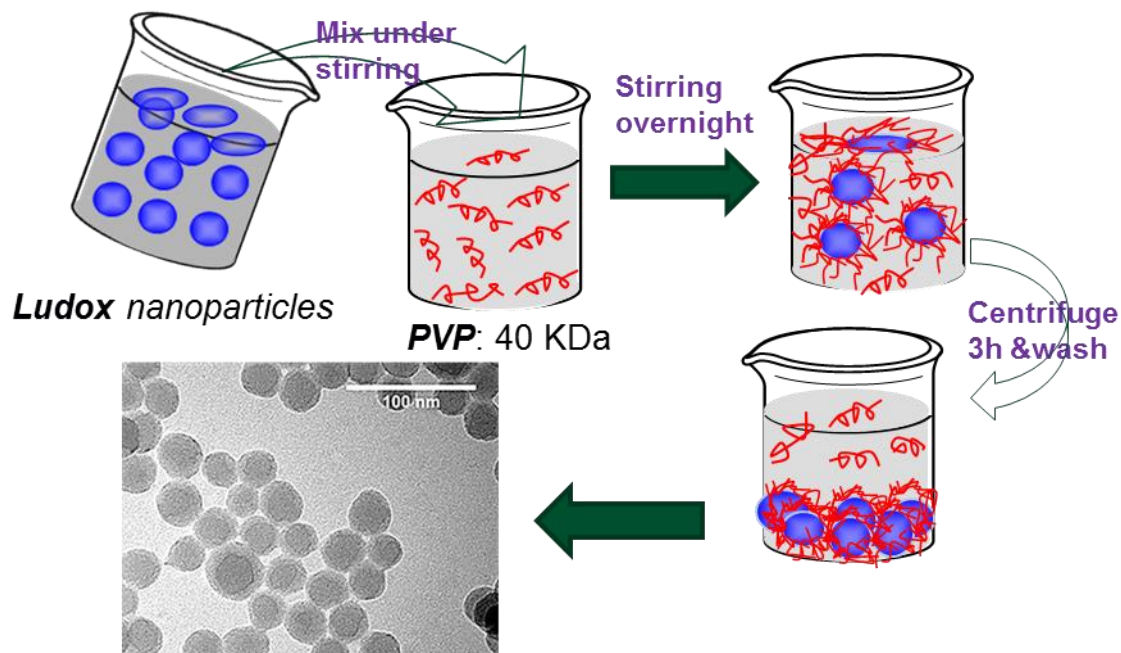


Figure 4.4 Schematic of composite particle preparation.

PVP adsorption on the silica nanoparticles was confirmed by transmission electron microscopy (TEM), see Fig. 4.4, and the amount of adsorbed PVP determined using thermo-gravimetric analysis (TGA) (Q-500- TA, USA). For TGA, 5-10 mg of the composite particles was heated from 30 °C to 900 °C (the thermal degradation temperature of PVP is around 400 °C²⁶) at a 10 °C/min heat rate under N₂ flow (50 mL/min). Here, silica only, PVP only and the empty aluminum pan were used as reference samples measured at identical conditions. Since all the trapped water should have evaporated around 100 °C, the remaining mass of the composite particles at 100 °C was used as a starting value for the analysis. Assuming that the PVP and SiO₂ mass loss from the composite particles up to 600 °C are 100% and 0%, respectively, the mass of adsorbed PVP with respect to the mass of silica nanoparticles was determined using the following equation

$$\frac{W_{PVP}}{W_{SiO_2}} = \frac{(W_{total,100\text{ }^\circ\text{C}} - W_{total,600\text{ }^\circ\text{C}})}{W_{total,100\text{ }^\circ\text{C}} - (W_{total,100\text{ }^\circ\text{C}} - W_{total,600\text{ }^\circ\text{C}})} \quad (4.1)$$

where $W_{total,100\text{ }^{\circ}\text{C}}$ and $W_{total,600\text{ }^{\circ}\text{C}}$ are the remaining masses of the composite particles at 100 °C and 600 °C, respectively. W_{PVP} and W_{SiO_2} represent the mass of PVP and silica in the composite particles, respectively. Based on Eq. 4.1, the adsorbed amount (Γ) of PVP on the silica nanoparticles is given by

$$\Gamma = \frac{W_{PVP}}{S_{spe} \times W_{SiO_2}} \quad (4.2)$$

where S_{spe} is the specific surface area of silica nanoparticles (~135 m²/g for Ludox AS40).

4.3.2.2 Foam studies. After several washes the composite particles were re-dispersed in Milli-Q water to 10 wt% (particle to suspension mass). The suspension was refrigerated during storage. For foam testing, 10 mL of 1 wt% composite particles was prepared in 40 mL glass vial to an appropriate electrolyte concentration (between 0 and 0.55 M Na₂SO₄). The composite particle suspension was gently agitated using a laboratory carousel before 1 min of vigorous handshaking to generate the foam. The foamability and foam stability were visually measured by tracking foam heights at regular time intervals.

More detailed analysis of the foam destabilization mechanism was undertaken by studying bubble-bubble interactions using an optical microscope (Olympus BX51). Immediately following foaming, a small volume sample of the stable foam was extracted using a flat edged capillary tube (CM Scientific Ltd, 0.5 × 5 mm). The capillary tube was positioned below the air-foam interface and the sample gently drawn into the capillary tube with minimal disturbance. The dimensions of the capillary tube were chosen to minimize the deformation (i.e. flattening) of the foam bubbles. To prevent foam drying, both ends of the capillary tube were sealed using Parafilm M®, and the sealed sample left un-disturbed on the optical microscope stage.

The bubble size distribution as a function of foam aging was determined by measuring the diameter of individual bubbles using ImageJ software. All foam stability experiments were conducted at $T = 25\text{ }^{\circ}\text{C}$.

4.3.2.3 Π -A isotherms. Surface pressure–area (Π -A) isotherms of deposited particle layers at the air-water interface were measured using a Langmuir trough (Biolin Scientific, Sweden), with a maximum trough area of 85 cm^2 . Surface pressure was measured using a paper Wilhelmy balance of dimensions $10 \times 30\text{ mm}$ ($w \times l$). Prior to each measurement the Delrin trough and baffles were thoroughly cleaned using 2 wt% Decon solution and rinsed with excess Milli-Q water and acetone. Any contaminants residing at the air-aqueous interface were first removed by compressing the barriers to the minimum trough area (20 cm^2), before aspirating the liquid surface under gentle suction. The “cleanliness” of the air-aqueous interface was verified by subsequent compressional isotherms. The trough was considered clean when the maximum deviation of the surface pressure under the maximum compression was less than 0.3 mN/m . Surface pressure Π is given by: $\Pi = \gamma_0 - \gamma$, where γ_0 is the surface tension of a pure interface and γ is the surface tension of a contaminated interface.¹³⁶

The prepared particles (uncoated or composite) were first dispersed in the spreading solvent (mixture of water and isopropanol alcohol at a 1:1 vol/vol ratio), to a concentration of 0.5 wt% (based on the total suspension mass). Spread at the air-aqueous interface was $40\text{ }\mu\text{L}$ of 0.5 wt% particle suspension, ensuring that droplets were evenly distributed across the trough area and added without disturbing the interface (i.e., no droplet splashing). To evaporate the spreading solvent, the interface was left undisturbed for 30 min prior to collecting the Π -A isotherms. The surface pressure of the particle layer under compression was continuously measured as the interfacial area was reduced from 76 cm^2 to 20 cm^2 at a speed of $5\text{ cm}^2/\text{min}$. All the

measurements were repeated in triplicate with the results demonstrating a good repeatability (surface pressures at equivalent areas within $\pm 5\%$).

4.3.2.4 Microstructure of particle layer. The micron-scale structure of the composite particles layer at the air-water interface was studied under several states of compression (low \rightarrow high compression). Following the layer preparation using the method described above, the composite particles layer was compressed to the desired surface pressure and held at a constant pressure for 5 min. The particle layer was then transferred from the air-aqueous interface to molecularly smooth mica basal planes using the Langmuir-Blodgett (LB) deposition technique.¹³⁷ The freshly cleaved mica substrate (Agar SCIENTIFIC, UK) was withdrawn through the air-aqueous interface at 90 mm/min whilst maintaining the surface pressure to ensure that the transfer ratio (deposited area to compressed area) remained constant at ~ 1 , see Fig. 4.5. The deposited particle layers were carefully dried at slightly elevated temperature to minimize any drying effects, and stored in a ZONESEM sample cleaner before imaging using a scanning electron microscope (Hitachi SU8230, UK).

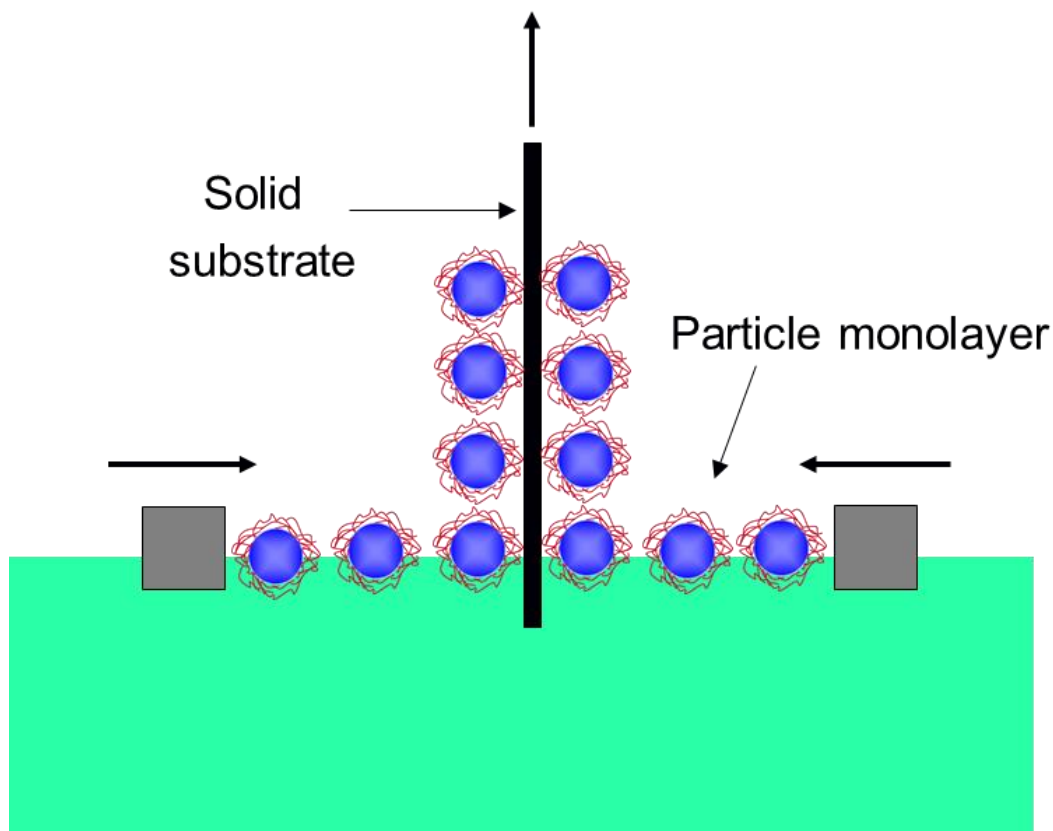


Figure 4.5 Schematic of the Langmuir-Blodgett deposition method.

4.3.2.5 Interfacial shear rheology. The shear viscoelasticity of the composite particles interfacial layer was studied using a stress-controlled Discovery Hybrid Rheometer (DHR-2, TA Instruments, UK) equipped with a double wall ring (DWR) geometry (see Fig. 4.6).¹⁰⁹ To ensure maximum measurement sensitivity, the rheometer was calibrated using precision mapping with the transducer bearing mode set to soft. For the interfacial shear rheology measurements, 19.2 mL of the electrolyte solution was pipetted into the circular Delrin trough to ensure that the air-aqueous interface was pinned at the inner ridge of the trough. Spread at the air-aqueous interface was 10 μL of the composite particle suspension of 0.5 wt% solid content in a mixture of water/IPA (1:1 v/v). Prior to each measurement the DWR geometry was cleaned in acetone and washed with excess Milli-Q water and then flamed to remove any organic contaminants. With the particle layer formed at the air-aqueous interface,

and the spreading solvent being evaporated (evaporation time ~ 30 min), the DWR geometry was gently lowered and positioned to pin the air-aqueous interface. Once positioned, the viscoelasticity of the interfacial layer was determined from data collected whilst oscillating the DWR geometry at a constant frequency of 0.5 rad/s and varying strain between 10^{-2} % and 10^3 %. All the measurements were conducted at a constant temperature of 25 °C. More details describing the experimental technique and procedures can be found elsewhere.^{63, 109, 132}



Figure 4.6 Image of a stress-controlled Discovery Hybrid Rheometer equipped with a double wall ring (DWR) geometry.

4.3.2.6 Adhesion force measurements between two PVP coated surfaces using colloid probe technique. A Bioscope II AFM (Bruker, USA) was used to measure the interaction forces between two PVP coated surfaces using the colloid probe technique. The tipless silicon nitride cantilever (DNP-020, Bruker AFM Probes International Inc.,

USA), with a spring constant of 0.6 N/m determined by the thermal resonance method, was used to create colloid probes. Silica particles (Sigma Aldrich, UK) between 9 and 13 μm were attached to the cantilevers using a two-part epoxy glue (Araldite 2012) which was allowed to cure overnight. These probes were then examined by SEM (Hitachi TM3030, UK) to ensure that the particle was well centred and cleanly attached to the cantilever (see Fig. 4.7). A 1 cm^2 piece of silicon wafer (University Wafer Inc., Boston, USA) with a 100 nm top layer of silicon dioxide was placed into a UV/Ozone cleaner (Bioforce Nanosciences, Iowa, USA) for 30 min and then rinsed with Milli-Q water. Both the silicon wafer and the colloid probe were dipped into two trays each containing 10 ppm 40 kDa PVP for 10 min, after which the silicon wafer was rinsed with Milli-Q water and the colloid probe was dipped into a tray of Milli-Q water. Optical reflectometry data confirmed rapid adsorption of PVP on silica, reaching steady state conditions within 10 min, see data in Chapter 3.

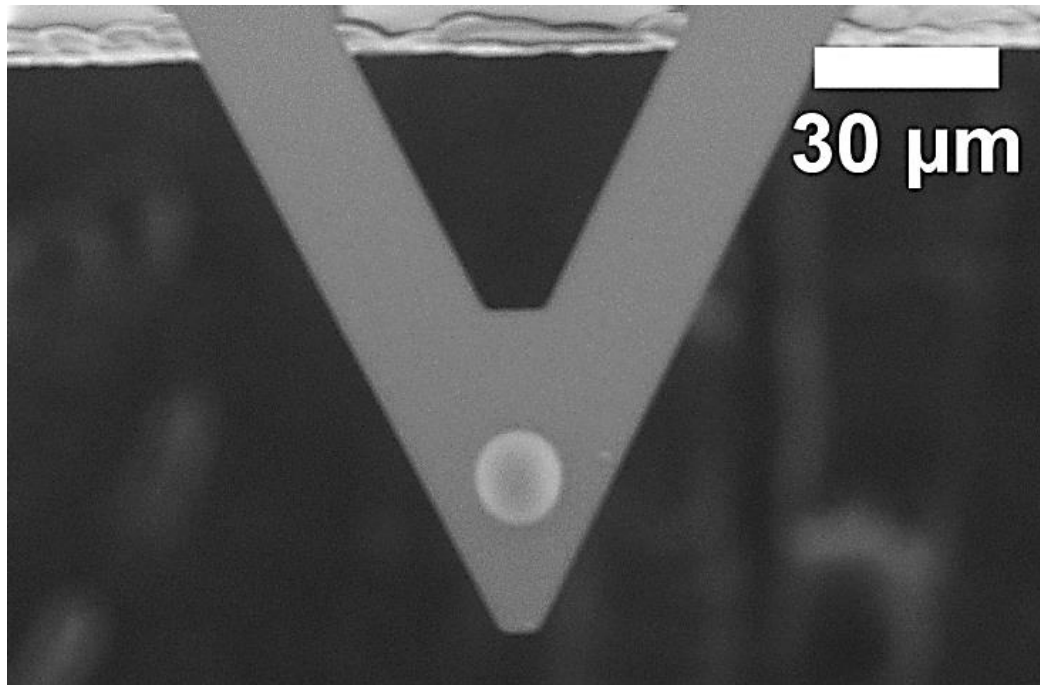


Figure 4.7 SEM image of the silica colloid mounted on a tipless silicon nitride AFM cantilever.

Force curves were obtained immediately after the PVP surface preparation to ensure that both PVP surfaces remained fully hydrated. Two or three drops of liquid (either Milli-Q water or Na₂SO₄ solution) were deposited onto the PVP coated wafer surface before immersing the colloid probe into this solution. All force curves were collected at 0.5 Hz at a minimum of 3 different surface sites. A minimum of 10 force curves per area were obtained.

4.4 Results and Discussion

4.4.1 Characterization of composite particles

4.4.1.1 PVP surface coverage and polymer film thickness. The Ludox particles used to form the composite particles had a hydrodynamic diameter (D_h) of ~ 34 nm (determined using a Malvern ZetaSizer). By comparison, the radius of gyration (R_g) of the PVPs in water was ~ 4 nm, ~ 7 nm, ~ 27 nm and ~ 51 nm for the 8, 40, 360 and 1300 kDa PVP, respectively.¹¹⁵ The selection of PVP to form the composite particles was first based on the R_g/D_h ratio. Neither the 360 nor the 1300 kDa PVP was suitable to form the composite particles because of the large R_g/D_h value, which may result in significant particle bridging. The 8 kDa PVP was deemed unsuitable due to the little difference from silica only (Chapter 3). Hence, 40 kDa PVP was chosen to synthesize the composite particles via polymer physisorption. The irreversibly adsorbed 40 kDa PVP films were highly hydrated (Chapter 3), which assisted in stabilizing the particles by steric forces.

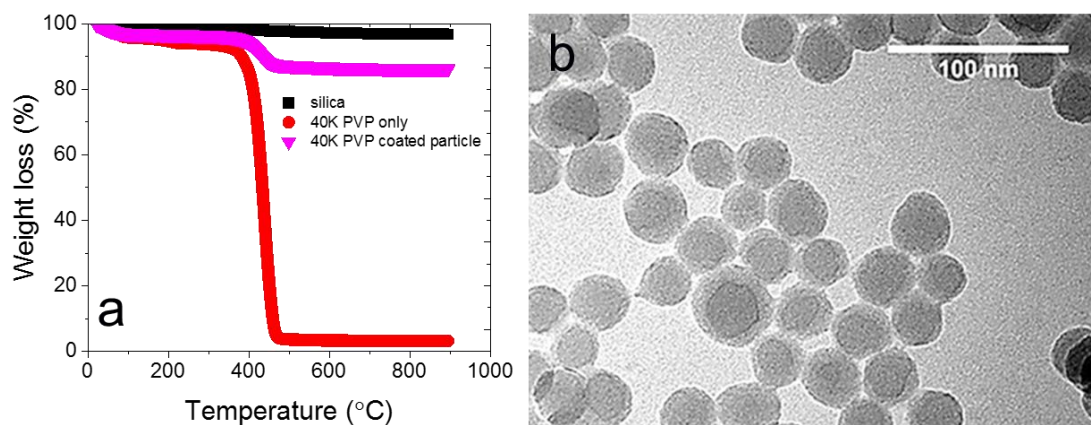


Figure 4.8 (a) TGA data for silica nanoparticles, PVP, and composite particles; (b) TEM image of the formed composite particles.

With the composite particles prepared (PVP-coated silica particles), the PVP surface coverage was confirmed by TGA (Fig. 4.8a) and found to be $\sim 0.9 \text{ mg/m}^2$ ($1.35 \times 10^{-2} \text{ molecules/nm}^2$, 5 molecules/particle) based on Eq. 4.2, which is in good agreement with the OR results presented in the previous chapter. Since these two results are similar it might indicate that the surface morphology (planar or high curvature) has little effect on the adsorbed state of the polymer. Using dynamic light scattering, the mean hydrodynamic diameter (D_h) of the composite particles was found to be $\sim 52 \text{ nm}$, confirming an approximate hydrated polymer shell thickness of $\sim 9 \text{ nm}$. The core-shell structure of the composite particles is clearly visible in the TEM images shown in Fig. 4.8b with the average thickness of the dried polymer shell being $\sim 3\text{-}5 \text{ nm}$ (images were analyzed using ImageJ). When considering the associated PVP layer thickness (planar and particle), it becomes apparent that the curvature restricts polymers from adsorbing almost flat on the substrate, something which has been observed for planar substrates. The thicker PVP film surrounding the nanoparticles confirms the inability for the polymer chains to fully relax and adsorb almost flat (train orientation) on the curved substrate. Hence, the polymer chains remain partially

extended, with the polymer adsorption density severely restricted by their closest neighbors.

4.4.1.2 Electrolyte concentration effects on the stability of the composite particles. The effect of electrolyte concentration on the stability of the composite particles was studied prior to assessing the particles foaming potential. Fig. 4.9 shows the dependence of the particle electrophoretic mobility and the mean particle size on the electrolyte concentration (0 to 0.1 M Na₂SO₄). At low electrolyte concentrations (≤ 0.01 M) the particle electrophoretic mobility was relatively high (~ -2.0 cm²/Vs) with particles sizes in the range of 47 – 52 nm. The particles can therefore be considered as non-interacting and dispersed. The observed decrease in the measured particle size between water and 0.01 M Na₂SO₄ resulted from the change in the polymer conformation, shrinking back to the particle surface as the solvency of the polymer reduced in the divalent electrolyte solution. At 0.1 M electrolyte concentration the composite particles electrophoretic mobility decreased and the mean particle size increased. The onset of particle aggregation at 0.1 M was confirmed, with particle aggregation more pronounced with increasing electrolyte concentration. At the highest electrolyte concentration (0.55 M), the particle/aggregate size could not be accurately measured using the Nano ZS instrument due to fast sedimentation of the formed aggregates.

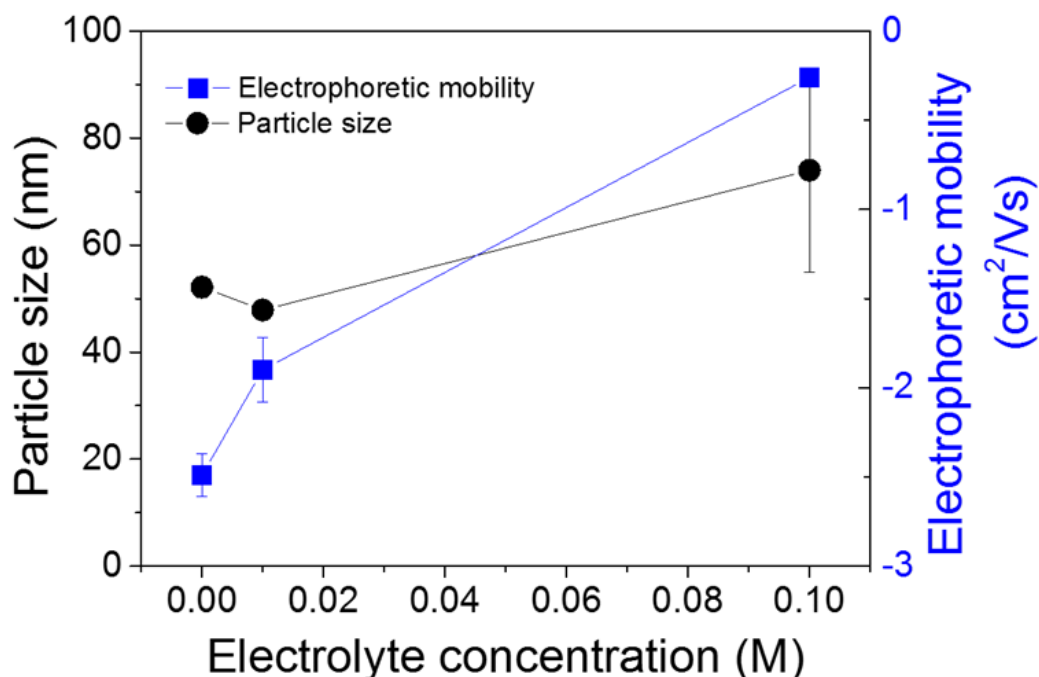


Figure 4.9 Measured hydrodynamic diameter of composite particles (symbol: circle), and particle electrophoretic mobility (symbol: square) as a function of the electrolyte concentration. Lines to guide the eye.

4.4.2 Foamability and foam stability

4.4.2.1 Contact angle measurements. For particles to act as foaming agents they must demonstrate the ability to partition from the solvent and reside at the air-water interface. The particle desorption energy from an interface has been discussed, with the desorption energy (W_r) given as a function of the air-water interfacial tension ($\gamma_{a/w}$), the particle radius (R), and the particle wettability which is described by the three-phase contact angle (θ). Increased foam stability in the presence of Brownian-like particles can be achieved by enhancing particle aggregation at the air-water interface, as shown in our recent publication,⁴⁸ increasing the particle wettability, or both. While increasing the electrolyte concentration enhances particle aggregation (Fig. 4.9), measuring changes in the particle contact angle at an air-water interface can

be challenging. However, a useful approximation can be made by measuring the three-phase contact angle of a sessile droplet on a PVP coated silica substrate.^{123, 138}

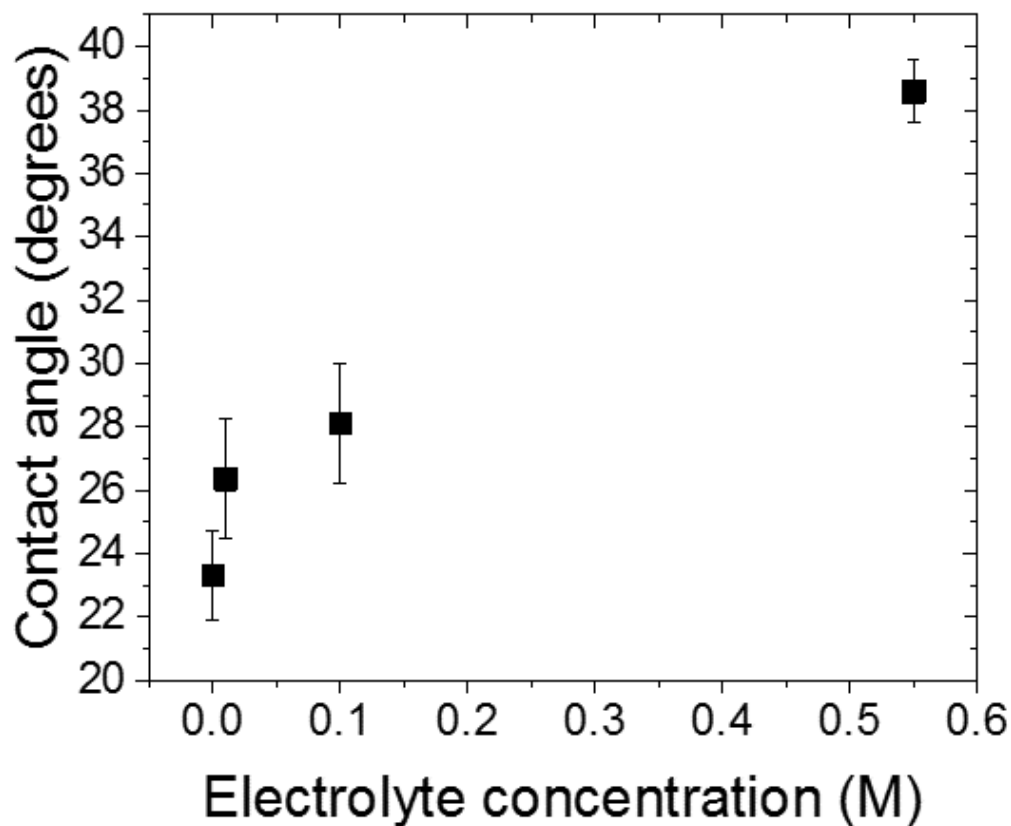


Figure 4.10 Contact angle of a sessile drop at rest on PVP coated silicon wafer as a function of the electrolyte concentration.

The three-phase contact angle of the composite particle residing at the air-aqueous interface was approximated by the sessile droplet technique. The substrates were prepared by immersing $1.5 \times 1.5 \text{ cm}^2$ pieces of silicon wafer in 10 ppm 40 kDa PVP solution for 10 min (ensuring a saturated PVP coverage on the silicon substrate based upon the OR data), before rinsing the surfaces with Milli-Q water. Fig. 4.10 confirms that increasing the electrolyte concentration from 0 to 0.55 M Na_2SO_4 increased slightly the three-phase contact angle from 23° to 39° . A slight increase in the three-phase contact angle, coupled with an increase in the aggregate size (with increasing

electrolyte concentration) will ultimately improve particle retention at the air-aqueous interface.

4.4.2.2 Foaming behavior of the composite particles. Foams were prepared using three potential foaming agents i) PVP, ii) hydrophilic silica nanoparticles and iii) composite particles, in four liquid environments of increasing electrolyte concentration. As expected, for the untreated hydrophilic silica nanoparticles, no foaming was observed even at the highest electrolyte concentration (0.55 M), and this was attributed to poor interfacial partitioning. Compared with hydrophilic silica nanoparticles, PVP exhibited greater surface activity, reducing the air-aqueous surface tension to ~ 61 mN/m at the highest electrolyte concentration (Fig. 4.11). Upon shaking, foams were readily formed confirming good ‘foamability’, but the foams rapidly collapsed within a few seconds once the shaking had ceased. Poor foam stability in the presence of polymers has been widely reported with rapid foam collapse being attributed to the low elasticity and viscosity of the interfacial layer.¹³⁹

140

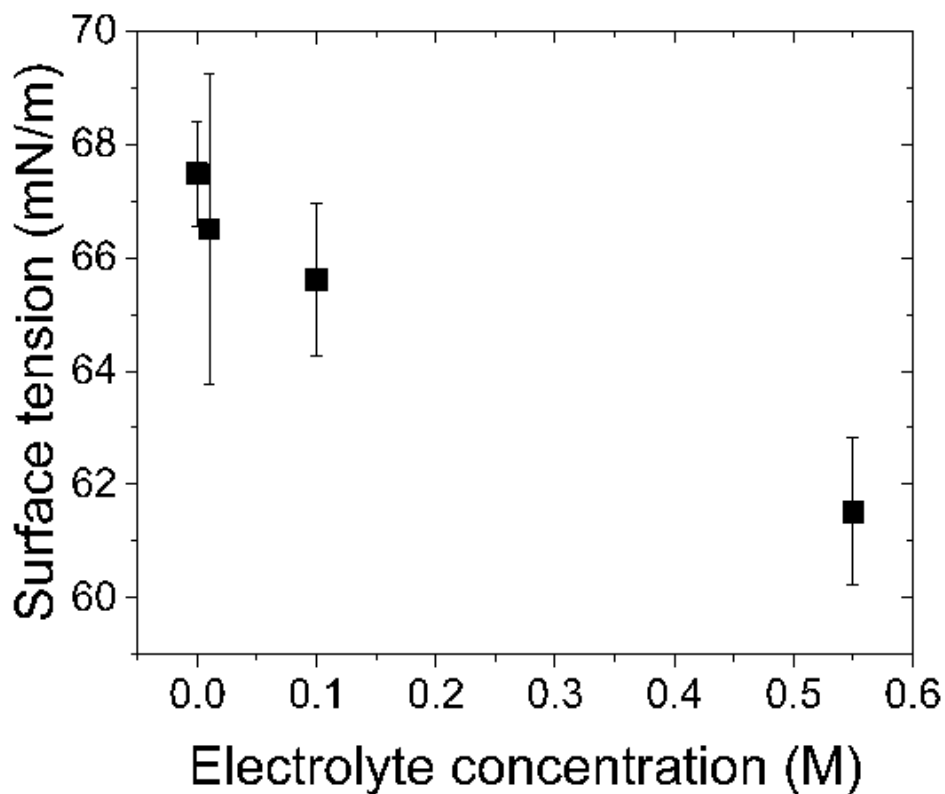
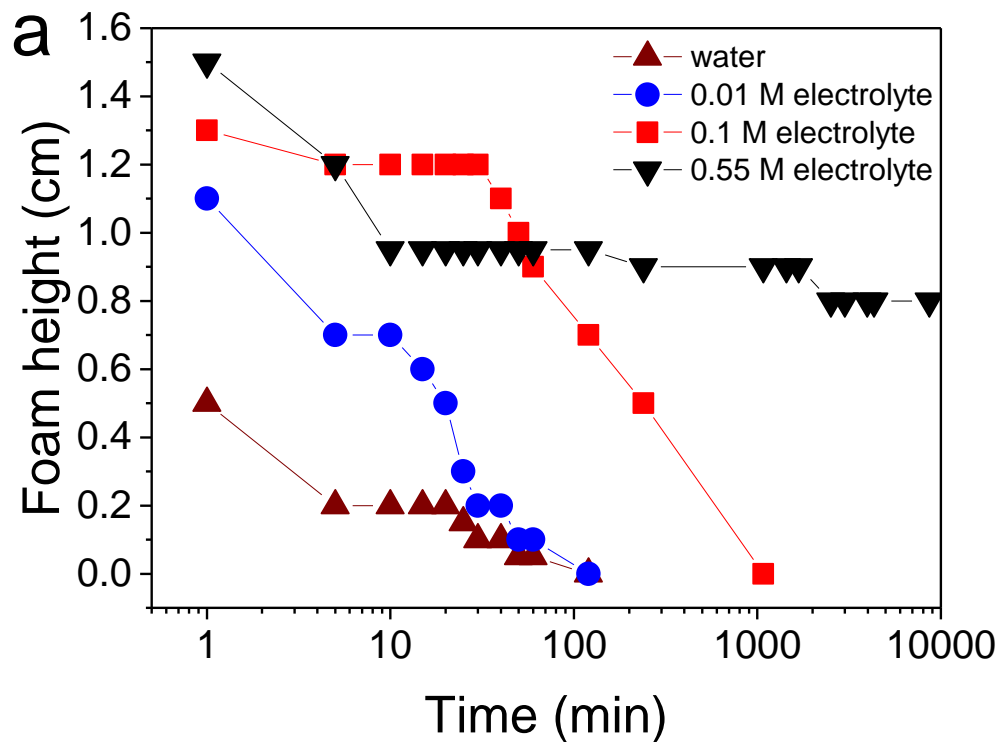


Figure 4.11 Air-aqueous surface tension in the presence of 0.5 wt% PVP as a function of the electrolyte concentration.



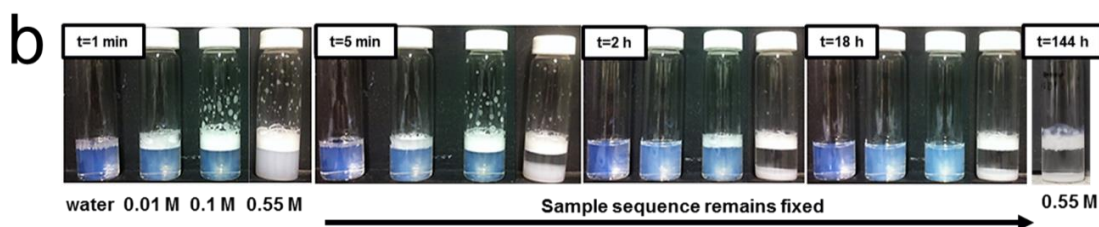


Figure 4.12 (a) Time-dependent stability of foams prepared using composite particles as a function of the electrolyte concentration (lines to guide the eye); (b) Images showing changes in foam height with aging time. The electrolyte concentrations are shown below each glass vial depicted at $t = 1$ min. Height of glass vial = 9 cm.

Using composite particles as the foaming agent, the effect of electrolyte concentration was shown to have a marked effect on the foam stability, see Fig 4.12. At all electrolyte concentrations the composite particles exhibited good foaming potential. However, the rate of foam collapse was shown to be sensitive to the electrolyte concentration. In the absence of any electrolyte, the initial foam height was substantially less than foams formed in the presence of electrolyte. At low electrolyte concentrations (≤ 0.01 M), the foams were observed to steadily collapse, with the foam height diminishing completely within 1 h. At intermediate electrolyte concentration (0.1 M), the foam collapse trend appeared different from the steady foam collapse observed at lower electrolyte concentrations: immediately following shaking (< 5 min), the foam height reduced by $\sim 8\%$ and then remained constant for the next 30 min. Subsequent collapse of the foam over the next 18 h followed an exponential decay, a typical decay profile for collapsing foams.^{141, 142, 143} At the highest electrolyte concentration (0.55 M), partial foam collapse was observed immediately following shaking (< 10 min), most likely associated with liquid drainage from the foam.¹⁴³ However, unlike all other foams which eventually collapsed within several hours, the foam remained stable over a prolonged period of time. Fig. 4.12a

shows a gradual reduction in the foam height ($\sim 15\%$) over a period of six days, with complete foam collapse observed after two weeks (data point not shown). These simple experiments highlight the importance of solvent composition on the ‘foamability’ and stability of foams stabilized by composite particles. However, the mechanism that governs foam stability is not readily apparent.

Fig. 4.12b shows the general appearance of the foams and composite particle suspensions used in the foaming experiments. At low electrolyte concentrations (≤ 0.1 M), a blue haze was observed in the aqueous sub-phase below the foam surface, thus confirming good dispersion of the composite particles. In contrast, the aqueous sub-phase containing 0.55 M electrolyte appeared white, resulting from increased scattering of visible light by the larger aggregates, which eventually settled to form a sediment bed on the base of the glass vial. These visual observations were in good agreement with the particle size data shown in Fig. 4.9.

Particle retention in the 0.55 M Na_2SO_4 foams (after vigorous shaking) was found to be ~ 10 wt%, determined from the dry mass of the sediment (electrolyte removal and repeat suspension washing). The particle content was in good agreement with the data published by Hunter et al.¹⁴⁴ The low particle retention was likely due to the hydrophilic nature of the composite particles. As the electrolyte concentration decreased (0.1 and 0.01 M Na_2SO_4) the particle wetting angle also decreased (Fig. 4.10) i.e. more hydrophilic. Hence, it is anticipated that the proportion of particles partitioned in the 0.1 and 0.01 M Na_2SO_4 foams would be < 10 wt%.

4.4.2.3 Liquid volume fractions in foams. The liquid volume fraction in the foams has been estimated by measuring the changes in both the liquid ($V_{L1}-V_{L2}$) and foam (V_F) volumes with aging time (see Fig. 4.13). Fig. 4.13 confirms that the 0.55 M foam remains considerably water-wet, with a liquid volume fraction of ~ 45 vol% after 6

days aging. High water retention in foams prepared using strongly aggregating particles is in good agreement with previously reported data.^{145, 146} The water-wet foam (0.55 M) is in contrast to the 0.1 M Na₂SO₄ foam, which during aging gradually de-watered leading to a relatively dry foam (~ 15 vol% water) after 2 h aging.

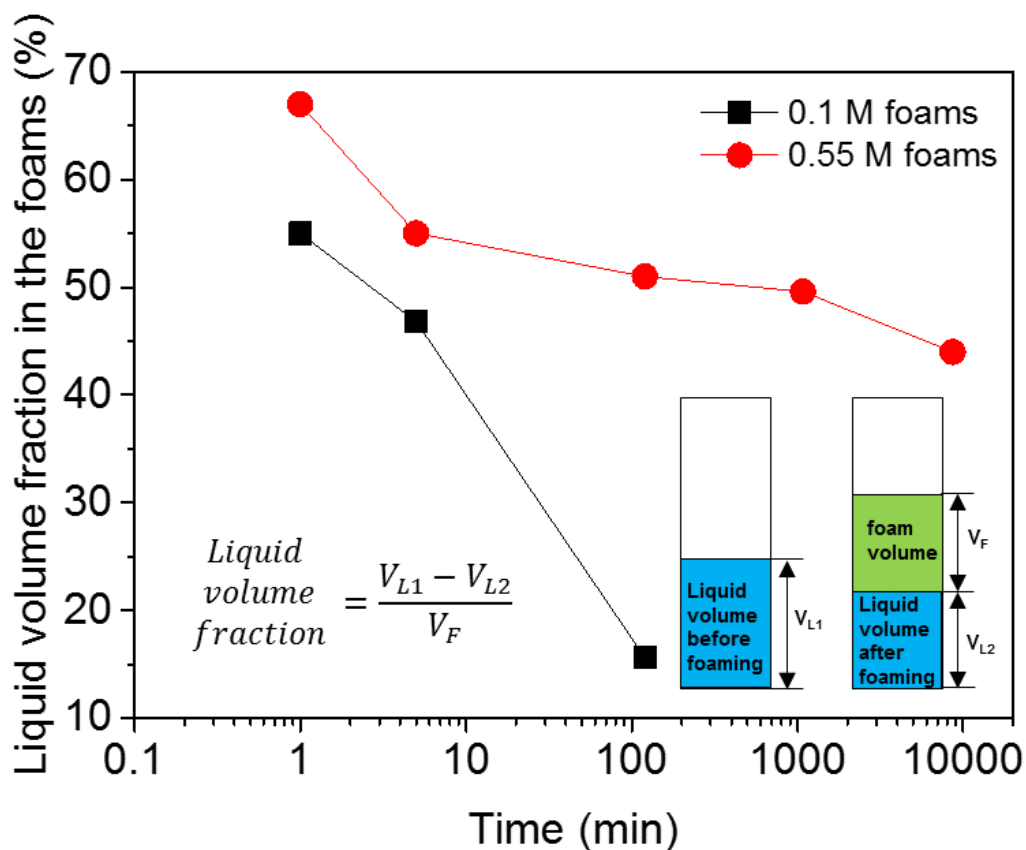


Figure 4.13 Time-dependent liquid volume fractions for 0.1 M and 0.55 M Na₂SO₄ foams. Data calculated from foam heights in Fig. 4.12b.

4.4.3 Compression, microstructure and relaxation of the particle-laden interfaces

4.4.3.1 Π -A isotherms. To better understand the observed transitions in foam stability: rapid collapse, delayed collapse and long-term stability, the compressional and relaxation properties of the deposited composite particle layers were studied using an air-liquid Langmuir trough. Fig. 4.14 compares the Π -A isotherms for all particle systems used in the current study. As expected, hydrophilic silica nanoparticles

provided no resistance to lateral compression, depositing into the water. As a result, the surface pressure remained extremely low (~ 0 mN/m) over the full compression range. When the composite particles were spread at the air-water interface the surface pressure at maximum compression increased to 2.8 mN/m, although exhibited little resistance to compression. It was evident that the presence of PVP improved particle retention at the air-water interface.

Spreading a fixed volume of the composite particles on to a sub-phase of increasing electrolyte concentration (0.01 M, 0.1 M and 0.55 M), resulted in a progressive increase in the maximum measurable surface pressure, thus confirming the electrolyte concentration effect previously described. The effect of electrolyte concentration on particle retention at the air-aqueous interface was clearly evident at the maximum trough area (low compression), where the surface pressure of the particle layer increased from 0.4 mN/m to 2.0 mN/m when deposited on water and 0.55 M electrolyte solution, respectively.

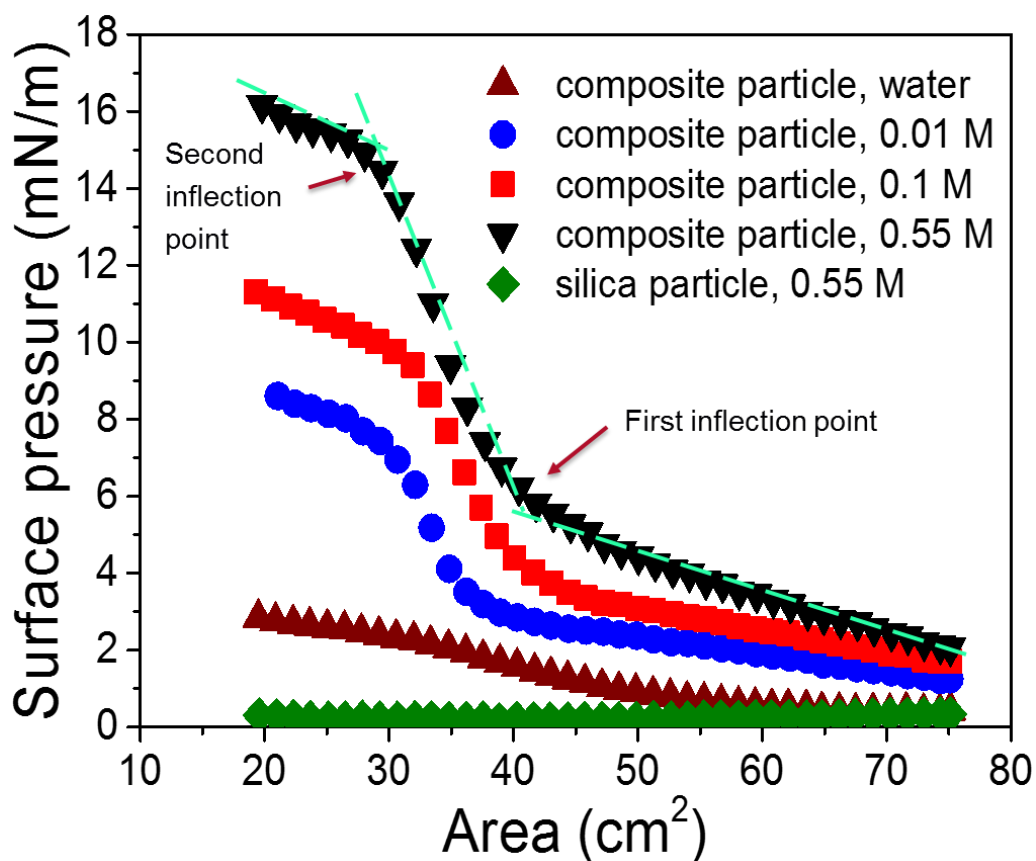


Figure 4.14 Π - A isotherms for silica and composite particles spread at the air-aqueous interface. The particle concentration and spreading volume were fixed at 0.5 wt% and 40 μL , respectively. The inflection points were identified by the changing of the isotherm slope.

Based on the Π - A isotherm data in Fig. 4.14, the compression elastic modulus (E) of the composite particle-laden films (0.01 M, 0.1 M and 0.55 M Na_2SO_4) can be determined by:

$$E = -Ad\Pi/dA \quad (4.3)$$

where Π is the surface pressure (mN/m) and A (m^2) is the trough area. The compression elastic modulus (E) in Fig. 4.15 will be discussed further when considering the foam destabilization mechanism in Section 4.4.7.

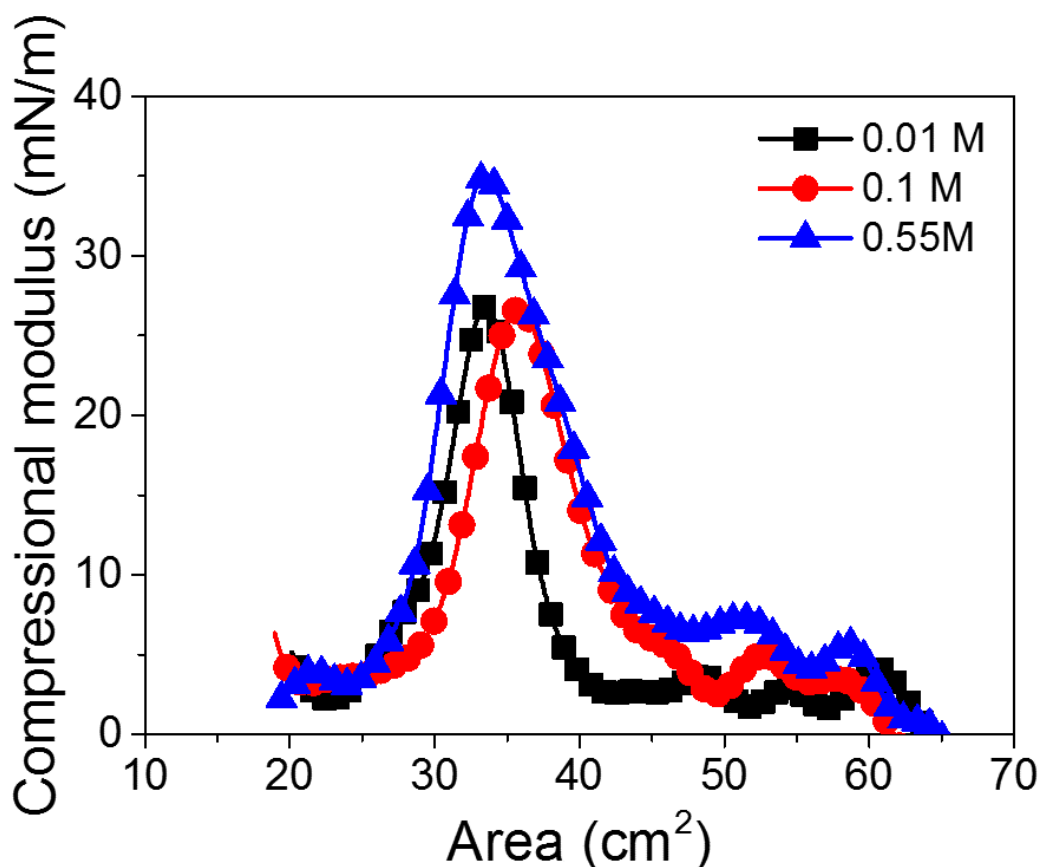


Figure 4.15 Compressional elasticity of composite particle layers deposited on aqueous sub-phases of increasing electrolyte concentration 0.01 M, 0.1 M and 0.55 M Na_2SO_4 .

4.4.3.2 Micron-scale structure of particle-laden interfaces. The composite particles network was assessed by scanning electron microscopy (SEM) close to the inflection points, as well as the maximum interfacial layer compression (minimum trough area). The interfacial particle layers were transferred onto solid substrates (mica) using the LB deposition technique.

With no electrolyte addition, the surface pressure of the composite particle layer remained low, and the corresponding SEM images (Fig. 4.16a-1) confirmed a lack of particle networking and the absence of a close-packed particle monolayer at the minimum trough area (Fig. 4.16a-2). At 0.01 M Na_2SO_4 , the deposited particle layer

was more interconnected but showed significant voids at the first inflection point (see Fig. 4.16b-1). With further compression ($II = 5$ mN/m) the void domain size decreased to form an almost complete particle monolayer (Fig. 4.16b-2). Close to the second inflection point ($II = 7$ mN/m), the particle network became sufficiently compressed that particle aggregates were displaced and formed a patchy multi-layer network (displaced particles identified as bright spots in the particle layer, see inset Fig. 4.16b-3). At maximum compression ($II = 8.6$ mN/m), substantial displacement of particles resulted in the formation of a multi-layer network, with the second particle layer showing finger-like structures (see Fig. 4.16b-4). At 0.1 M Na₂SO₄, the surface pressures of the particle layer at equivalent trough areas (32 cm² and 20 cm²) were approximately 40% higher than that at 0.01 M Na₂SO₄ electrolyte concentration. A multi-layer particle network was once again observed near the second inflection point (see Fig. 4.16c-1). However, under maximum compression substantial crumpling of the particle layer was observed, confirming buckling of the interfacial particle layer under high lateral compression force (see Fig. 4.16c-2). Interfacial buckling of the particle-laden interface has previously been reported.¹⁴⁷ Instead of being expelled from the air-water interface, which requires a large amount of energy as highlighted by the particle detachment theory (Eq. 2.3), particle-laden interfaces buckle under sufficient static compressive loading. For an interface to buckle, previous work confirmed that the two interfacial rheological contributions, shear and dilatational, should be non-zero, and the interface should behave as an elastic solid, i.e. G' (storage modulus) $>$ G'' (loss modulus).¹⁴⁷ An attempt was made to repeat the deposition and imaging protocol for the highest electrolyte concentration (0.55 M), however, significant salting on the mica substrate interfered with the sample imaging.

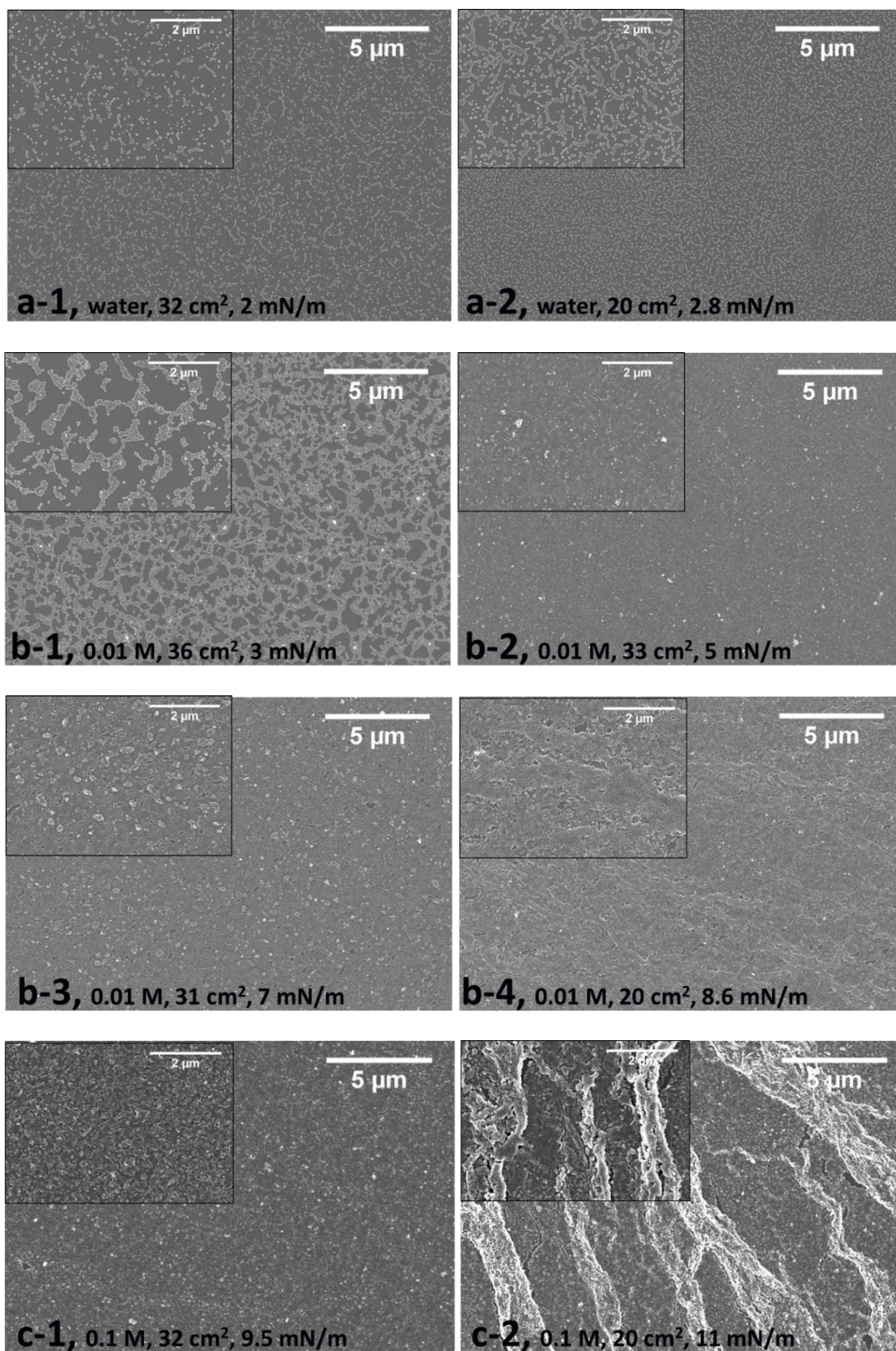


Figure 4.16 SEM images showing the surface pressure dependent micron-scale structure of deposited composite particle layers transferred from the air-aqueous

interface. Sub-phase electrolyte concentration equal to 0 M, 0.01 M, and 0.1 M, as labelled. Trough area and film surface pressure provided for each micrograph.

The LB deposition technique was also used to recover the hydrophilic silica particle-laden films from the air-aqueous interface for SEM observation at the minimum trough area (20 cm^2). Fig. 4.17a shows that only a few silica particles were retained at the interface when the sub-phase electrolyte concentration was 0.01 M, although particles retention was only slightly increased when increasing electrolyte concentration to 0.1 M (Fig. 4.17b). Still the particle surface coverage remained too low to influence the surface pressure. Fig. 4.17 verifies that the extremely low surface pressure ($\sim 0 \text{ mN/m}$) recorded for the silica only particle-laden interfaces results from poor particle retention.

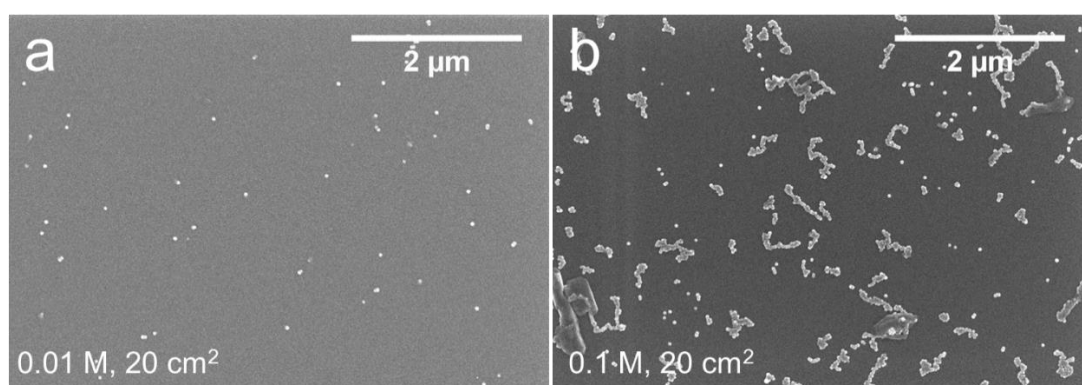


Figure 4.17 SEM images showing the micron-scale structure of deposited silica particle layers transferred from the air-aqueous interface at minimum trough area. Sub-phase electrolyte concentrations as labelled.

4.4.3.3 Particle layer relaxation. Relaxation/reorganization of the composite particle layers at the air-aqueous interface was studied at constant surface pressures, 3 mN/m and 7 mN/m. A constant surface pressure experiment was conducted to elucidate the mobility of the particle layers as a function of the sub-phase electrolyte concentration under equivalent compressional force, albeit the compression areas were

slightly different. Firstly, a surface pressure of 7 mN/m was chosen to ensure that the particle layers were in a close-packed state, proved by Fig. 4.16. With the target surface pressure reached, the barriers of the Langmuir trough were operated in feedback mode to ensure that the surface pressure remained fixed, and the trough area recorded over 600 s. Fig. 4.18a shows the time-dependent changes in the normalized trough area required to maintain a constant surface pressure. The trough area was normalized by the starting trough area which was a function of the sub-phase electrolyte concentration: 0.01 M = 32 cm², 0.1 M = 36 cm², and 0.55 M = 38 cm².

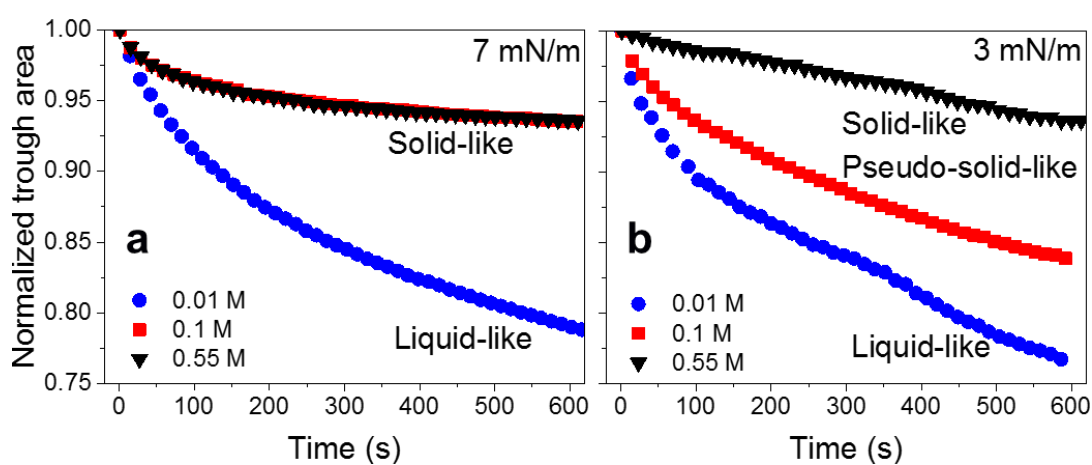


Figure 4.18 Relaxation/reorganization of particle layers compressed to a constant surface pressure of (a) 7 mN/m and (b) 3 mN/m.

Quite interestingly there was a distinct division in the behaviour of the particle layers with the response clearly dependent on the sub-phase electrolyte concentration. At 0.01 M the trough area was shown to continually decrease such that the surface pressure of the composite particle-laden film could be maintained. This behaviour was characteristic of a liquid-like system where neighbouring particles are able to reorganize to an apparent lower energy state when under an applied load. At 600 s the trough area had reduced by 22%. At higher electrolyte concentrations (0.1 M and 0.55 M) the response was more solid-like, with only a 6% reduction in the trough area after

600s. The time-dependent response would indicate that following compression, the interfacial particle layer (0.1 M and 0.55 M) was effectively “locked in place” and could not reorganize under lateral compression to alleviate the applied pressure.

At a lower surface pressure, 3 mN/m (Fig. 4.18b), where all three particle layers were in a non-close-packed state, the time-dependent response of the particle layers differed only slightly. For the case of 0.01 M and 0.55 M electrolyte solution, the response of the compressed particle layers showed similar behaviors to those observed at higher surface pressure, i.e. liquid-like and solid-like states. However, for the 0.1 M electrolyte solution the particle layer showed a different time-dependent response, as shown by the continued reduction in the trough area to maintain the constant surface pressure (3 mN/m). Since the response was between the two extremes (liquid-like and solid-like states), we have termed this particle layer to be “pseudo solid-like” at low surface pressure.

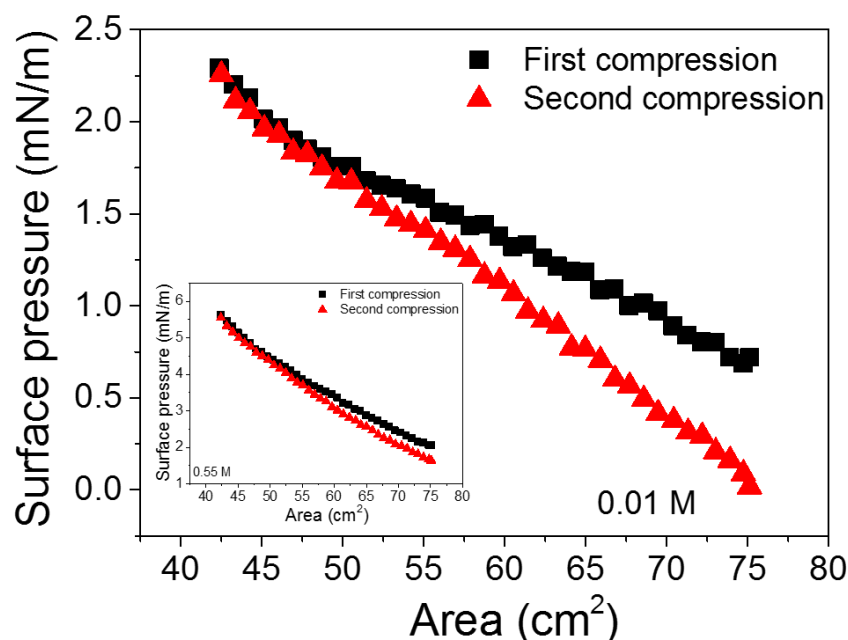


Figure 4.19 First and second compression isotherms for a composite particle film deposited on 0.01 M Na₂SO₄. Inset: equivalent data for a composite particle film deposited on 0.55 M Na₂SO₄.

A multi-compression isotherm (first and second cycle) was conducted to examine the influence of composite particle desorption under compression for the 0.01 M film. Fig. 4.19 shows little difference between the first and second compression cycles, with the two isotherms overlapping when the surface pressure was between 1.75 mN/m and 2.25 mN/m. The small differences between consecutive isotherms at low surface pressures most likely result from clustering of particles rather than particle desorption.⁵⁸ Similar multiple compression isotherms were observed for a composite particle film deposited on 0.55 M Na₂SO₄ (inset of Fig. 4.19). At higher electrolyte concentrations (0.1 M and 0.55 M), particle retention at the air-aqueous interface increases due to increased particle (aggregate) size and apparent wettability (slight increase, see Fig. 4.10). Hence, the possibility of particle desorption is more unlikely, and the time-dependent behaviour shown in Fig. 4.18 should only be due to relaxation/reorganization of particle layers rather than particle desorption.

4.4.4 Interfacial rheology of deposited particle layers

Interfacial mobility of the particle layers was measured using the interfacial DWR geometry. Recent studies have highlighted the importance of interfacial shear elasticity to stabilize liquid droplets.^{57, 63, 131, 148} For strongly elastic interfacial layers the shear strength is a major contributing factor inhibiting droplet coalescence. If the applied load is sufficient to exceed the shear yield stress, the interfacial layer will rupture to cause droplet coalescence. It is important to note that the shear interfacial viscoelasticity correlates to the likelihood of droplet coalescence but has not been considered in terms of hindrance to droplet coarsening. Droplet coarsening is frequently correlated to the dilatational elasticity, which will be discussed later in the Chapter.^{72, 125}

To replicate the condition of low surface pressure (equivalent to the particle surface coverage at the maximum Langmuir trough area), the spreading volume was adjusted in such a way that the expected surface pressure for the interfacial shear rheology measurements was in the region of 3 mN/m. Following particle deposition, the viscoelasticity of the composite particle layers was measured at constant oscillation frequency of 0.5 rad/s and increasing strain between 10^{-2} % and 10^3 %.

The open and closed symbols in Fig. 4.20 represent the elastic (G') and viscous (G'') contributions, respectively. When oscillating in the linear viscoelastic region, at the lowest electrolyte concentration (0.01 M) the viscoelastic moduli (G' and G'') are almost equal (2.7 to 5.9×10^{-5} N/m). The rheology of the deposited particle layer can therefore be described as “weakly elastic”. At 0.1 M Na_2SO_4 , the viscoelasticity of the particle layer increased, exhibiting a higher elasticity with $G' = 2.2 \times 10^{-3}$ N/m and the G'/G'' ratio equal to ~ 3 . The viscous to elastic ratio remained unchanged at the highest electrolyte concentration (0.55 M), although the elasticity of the particle layer increased by almost an order of magnitude as compared with the case of 0.1 M. This substantial increase in elasticity of the particle layer was in good agreement with the relaxation data shown in Fig. 4.18b, and supports the general observation of a more rigid interfacial particle layer at higher electrolyte concentrations.

With increasing oscillation strain the linear viscoelastic region was exceeded as the mechanical structure of the composite particle layer fractured under larger deformations. Increasing the oscillation strain led to a reduction in both the G' and G'' contributions as the particle aggregates begin to flow. Eventually a critical strain is surpassed when the film transitions from solid-like ($G' > G''$) to liquid-like ($G' < G''$) response.^{63, 131} In an oscillation stress ramp test (data not shown) the yield point (τ_y) of the three particle layers, identified as the crossover in G' and G'' (i.e. $G'' = G'$), was

observed to increase from 4.3×10^{-6} N/m to, 2.4×10^{-5} N/m and 5.9×10^{-5} N/m with increasing Na_2SO_4 concentration from 0.01 M to 0.1 M and 0.55 M, respectively. Interestingly, the yielding dynamics of the composite particle film is somewhat different to the more conventional yielding of a solid particle film (i.e. silica particles). In the absence of polymer, the rigid-body interaction between neighbouring particles leads to a strongly elastic film ($G' \gg G''$) which often yields in stages, i.e. two-step yielding dynamics, observed as a ‘hump’ in G'' prior to the power-law decay.⁴⁸ In the presence of polymer, the particle-particle interaction is ‘softened’ by the interacting polymer layers, which has been shown to lubricate the particle-particle interaction (Chapter 3). This lubrication weakens the overall network strength ($G' \approx G''$) and the film yields via a one-step mechanism.

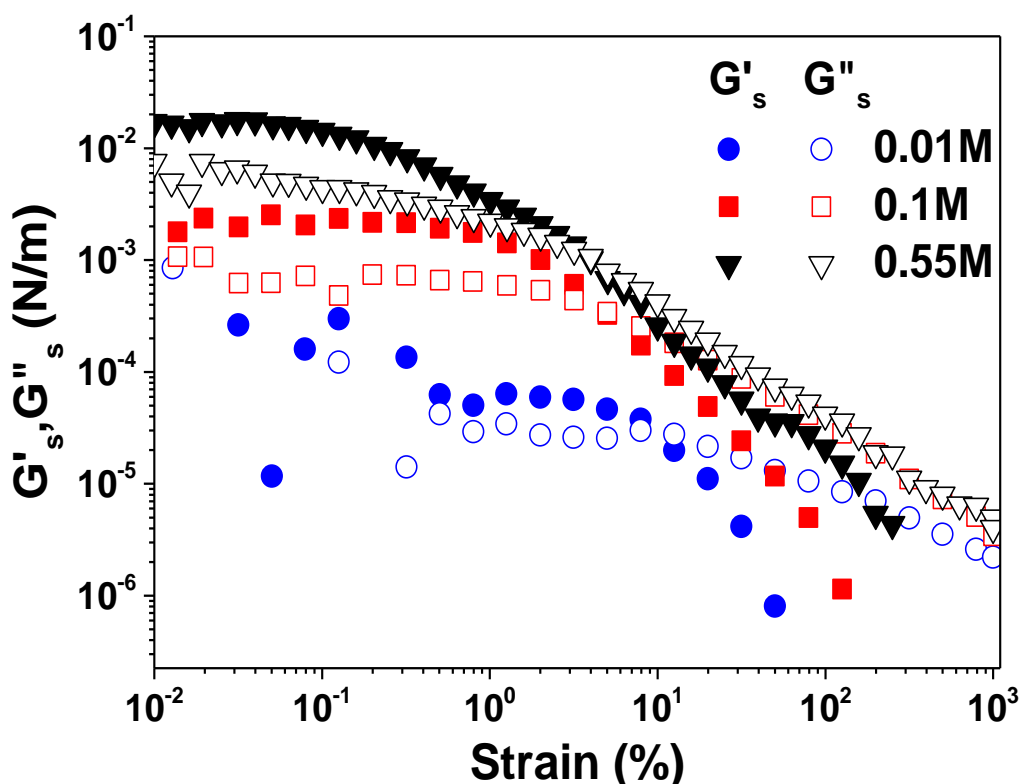


Figure 4.20 Strain dependent viscoelasticity of the composite particle layers spread at the air-aqueous interface. Sub-phase electrolyte concentration: 0.01 M, 0.1 M and 0.55 M Na_2SO_4 ; particle spreading concentration = 0.5 wt%; spreading volume = 10 μL .

4.4.5 Interaction forces between PVP coated surfaces

The influence of electrolyte concentration on the interactions between PVP polymer coated silica surfaces was investigated using the AFM colloid probe technique. Fig. 4.21 shows the results of interaction forces as two PVP coated surfaces approach each other in aqueous electrolyte solutions. In 0.01 M Na₂SO₄ solution, the forces are monotonically repulsive, with the long-range interaction taking the form of an exponential decay. Although only the first few nm of the observed repulsion (i.e. from 40 to approximately 30 nm) is anticipated from the electrostatic component of the interaction, since the Debye length is only ~ 1.8 nm for 0.01 M divalent electrolyte solution, this repulsion was sufficiently strong that it was detected at separations of 2 or 3 times the Debye length.¹⁴⁹ At separations closer than 30 nm the measured repulsive force was from direct chain-chain interactions (steric forces). Gentle compression of these layers under the applied force of the AFM cantilever was measured with no obvious overlapping, indicating a soft layer on silica surfaces. Steric repulsion between the two interacting polymer layers can be pseudo-quantitatively described by the Alexander-de Gennes (AdG) theory. When two polymer brush layers approach each other, a critical distance is eventually reached when the loops and tails of the polymer overlap, leading to an increase in the local density of “polymer segments”. The resulting polymer overlap leads to an increase in osmotic pressure and repulsive interaction energy. Applying the Derjaguin approximation, the total interaction force is given by¹⁵⁰

$$\frac{F(D)}{R} = \frac{16\pi kTL}{35s^3} \left[7 \left(\frac{2L}{D} \right)^{5/4} + 5 \left(\frac{D}{2L} \right)^{7/4} - 12 \right] \quad (4.4)$$

where k is the Boltzmann constant, T is the temperature, D is the surface separation distance, s is the mean distance between anchoring sites on the surface, and L is the

uncompressed brush layer thickness. Since the absolute surface separation distance is unknown, the fully compressed layer thickness was estimated and used to offset the data. The AdG model fitting for interacting PVP polymer surfaces in 0.01 M Na_2SO_4 is shown in Fig. 4.21b. The fitting parameters s and L are 1.69 nm and 31 nm, respectively. With the uncompressed brush layer thickness exceeding the room temperature R_g (radius of gyration) for 40 kDa PVP ($R_g \sim 7$ nm),¹⁹ the likely configuration for the PVP polymer is consistent with a high adsorption density, and the polymer brush extending slightly into solution beyond a compact PVP layer.

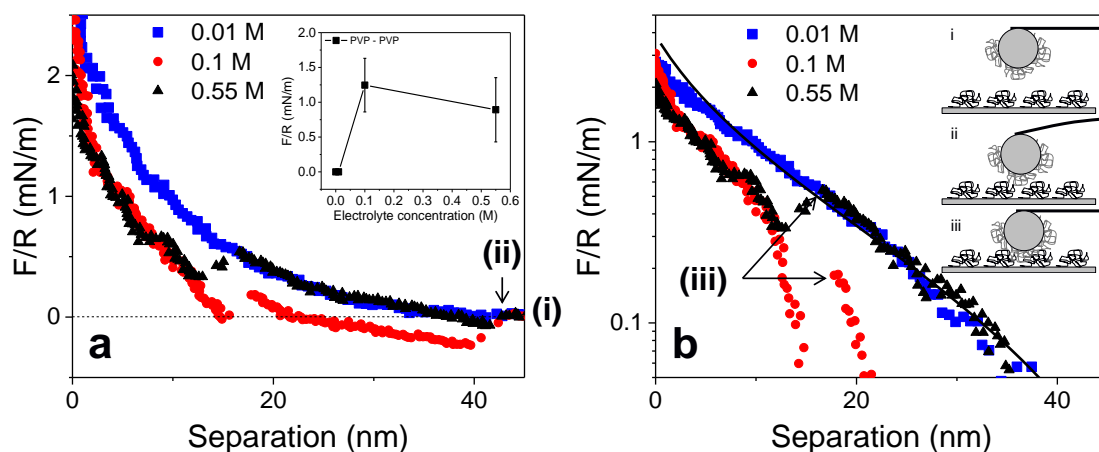


Figure 4.21 AFM force curves showing the influence of Na_2SO_4 concentration on the interactions between two approaching PVP coated silica surfaces using the colloid probe method. (a) Approach force curves shown on a linear scale; inset shows the adhesion data obtained between PVP polymer coated silica surfaces. (b) Approach force curves shown on a semi-log scale including the AdG theory (solid line) with fitting parameters $s = 1.69$ nm and $L = 31$ nm; inset highlighting the likely interactions between the approaching polymer layers in a poor solvent. (i) out of contact, (ii) jump-in due to intersegment attraction, (iii) push-through associated with the fusion of polymer layers.

For the force curves obtained in 0.1 M and 0.55 M Na₂SO₄ aqueous solutions, we expect minimal electrostatic interactions due to significant compression of electrical double layers. Instead, a jump of the colloid probe towards the surface was observed at separation distances equal to 40 nm, followed by a second jump at distances less than 20 nm under further compression. The measured jump-in at long range was attributed to intersegment attraction between the outermost polymer segments. The fact that the observed interaction force for the two PVP surfaces interacting at ~ 40 nm was weakly attractive suggests that aggregation of composite particles under these conditions should be favoured. The second jump-in is thought to be associated with a push-through event and fusion of the opposing polymer layers, see schematic in Fig. 4.21b.

The inset in Fig. 4.21a shows that no adhesion was measured between PVP coated surfaces in 0.01 M Na₂SO₄. Weak adhesion of the polymer coated surfaces was only measured at higher electrolyte concentrations, with similar values being recorded for both 0.1 M and 0.55 M Na₂SO₄. The measured adhesion can be attributed to interpenetration and attraction between polymer segments on opposing surfaces.

4.4.6 Optical microscope observations

Following liquid drainage, foam destabilization was attributed to either bubble coalescence and/or bubble coarsening (i.e. Ostwald ripening driven by a gradient of Laplace pressures). To better understand the governing mechanism for foam collapse, as shown in Fig. 4.12, an optical microscope study was conducted focusing on a few foam bubbles, with the bubble size distributions determined by analysing a sequence of images using ImageJ software. To ensure reasonable statistical certainty each bubble size distribution was determined from analysing a minimum of 15 - 20 bubbles.

4.4.6.1 0.1 M foams. Unfortunately, foam bubbles generated in 0.01 M electrolyte solution collapsed during foam transfer and could not be analysed, thus confirming the fragility of the particle-laden interface. Close-packed bubbles were observed in 0.1 M Na_2SO_4 foam (inset image in Fig. 4.22). The number of bubbles within the glass capillary was observed to decrease during the 230-min aging time, which corresponded to an increase in the average bubble size and a broadening of the bubble size distribution (indicated by the “error” bars in Fig. 4.22). An increase in bubble size and polydispersity was also evidenced in the images taken at 1, 29 and 72 min aging, see Fig. 4.23. While it was difficult to determine the dominant mechanism for bubble growth, bubble-bubble coalescence was clearly observed in the 0.1 M Na_2SO_4 foam, as evidenced by the periodic ‘jumps’ in the bubble size, thus suggesting the occurrence of bubble coalescence leading to rapid bubble growth (Fig. 4.22, symbols: open circles).

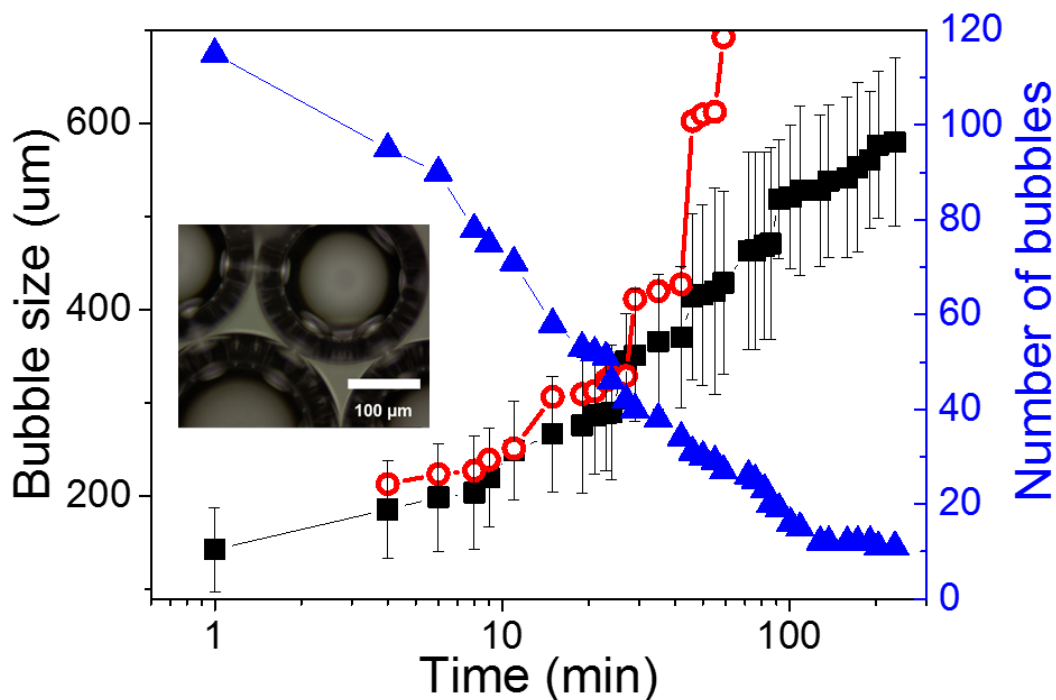


Figure 4.22 Average bubble size (symbol: closed squares) and number of bubbles (symbol: closed triangles) as a function of the foam aging time. Open symbols (circle)

correspond to the time-dependent growth of a typical bubble (electrolyte concentration = 0.1 M Na₂SO₄). The inset shows an optical microscope image of fresh foam bubbles prepared in 0.1 M Na₂SO₄.

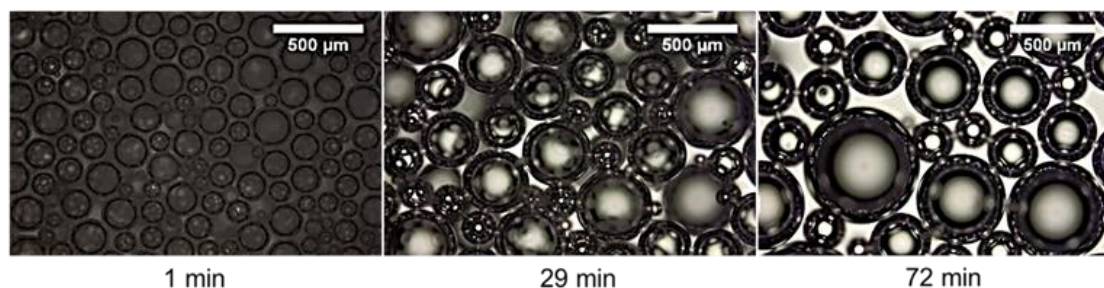


Figure 4.23 Image time sequence demonstrating an increase in bubble size and polydispersity in a foam prepared in 0.1 M Na₂SO₄ electrolyte solution.

4.4.6.2 0.55 M foams. The optical microscope image in Fig. 4.24 showed that the 0.55 M bubbles were well separated by micron-sized particle aggregates (highlighted by the dashed red box). This is distinctly different from the closely packed 0.1 M foams. The time-dependent average bubble size was observed to increase, gradually reaching steady state after ~200 min aging. At the same time the bubble polydispersity decreased as indicated by the ‘error’ bars. Growth of the large bubbles resulted from the volume reduction and disappearance of some smaller bubbles, hence the number of bubbles in the measured sample decreased from 15 to 8. No bubble coalescence was observed during the measurement.

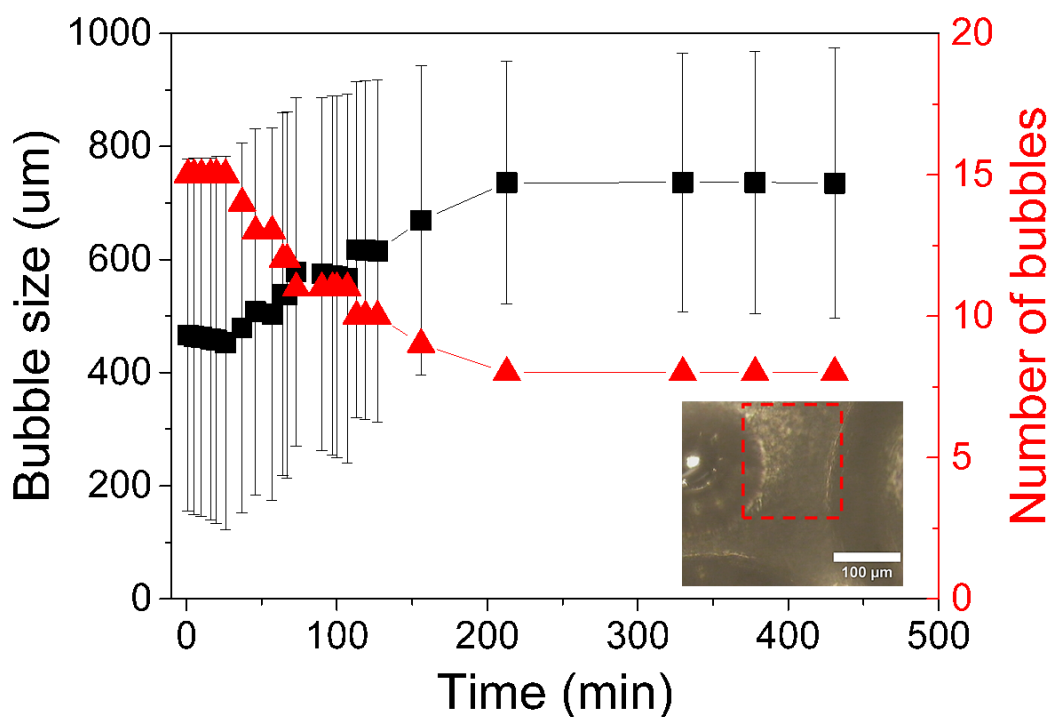


Figure 4.24 Average bubble size (symbol: closed squares) and number of bubbles (symbol: closed triangles) as a function of foam aging time. Electrolyte concentration = 0.55 M Na_2SO_4 . The inset shows an optical microscope image of fresh foam bubbles prepared in 0.55 M Na_2SO_4 .

Fig. 4.25 shows a sequence of images which depict the time-dependent shrinkage of an isolated bubble in the 0.55 M Na_2SO_4 foam. At $t = 1$ min the bubble size was approximately $100 \mu\text{m}$ before decreasing in size and eventually disappearing below the resolution of the optical microscope at $t = 45$ min. As the bubble size reduced the particle layer was observed to detach from the air-aqueous interface, forming a crumpled particle layer on the surface of the glass capillary. This finding indicated that the particle layer was not able to resist bubble coarsening. Since bubble coalescence was not observed during foam aging, the dominant mechanism for foam collapse was anticipated to be bubble coarsening. Hence, while bubble coarsening was

expected to occur in all foam systems, the extent of droplet coalescence has been demonstrated to reduce with increasing electrolyte concentration.

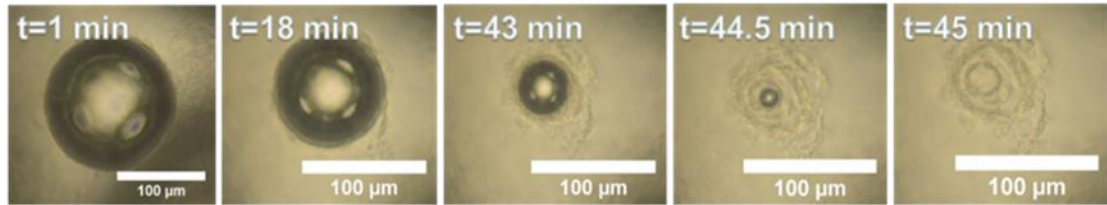


Figure 4.25 Optical microscope images of an isolated bubble aging in 0.55 M electrolyte solution.

To verify bubble coarsening in the 0.55 M Na_2SO_4 foam, the time-dependent sizes of several small ($< 300 \mu\text{m}$) and several large ($> 700 \mu\text{m}$) bubbles were measured. For the large bubbles shown in Fig. 4.26b, the bubble sizes increased slightly over the duration of the measurement (ca. 500 min). This was in contrast to the smaller bubbles shown in Fig. 4.26a, which were observed to decrease in size and eventually disappear. The time for complete bubble disappearance depended on the initial bubble size, i.e. smaller bubbles are inherently more unstable to disproportionation due to their higher Laplace pressure. For bubbles of intermediate sizes ($\sim 350 - 450 \mu\text{m}$), the bubble size was observed to remain almost independent of aging time. The rate of bubble shrinkage via coarsening can be characterized by¹⁵¹:

$$R^3(t) = R_0^3 - \left(\frac{t}{\tau}\right) \quad (4.5)$$

where $R(t)$ and R_0 are the bubble radius at time t and t_0 , and τ is the coarsening time.

Normalizing the bubble coarsening time ($\frac{t_i}{t_\infty}$) and bubble size ($\frac{b_i}{b_0}$) (where subscript i represents intervals of time, and subscripts 0 and ∞ represent the initial and final measurable conditions), the shrinkage dynamics of the smaller bubbles were in excellent agreement with the bubble shrinkage theory (see Fig. 4.26c).

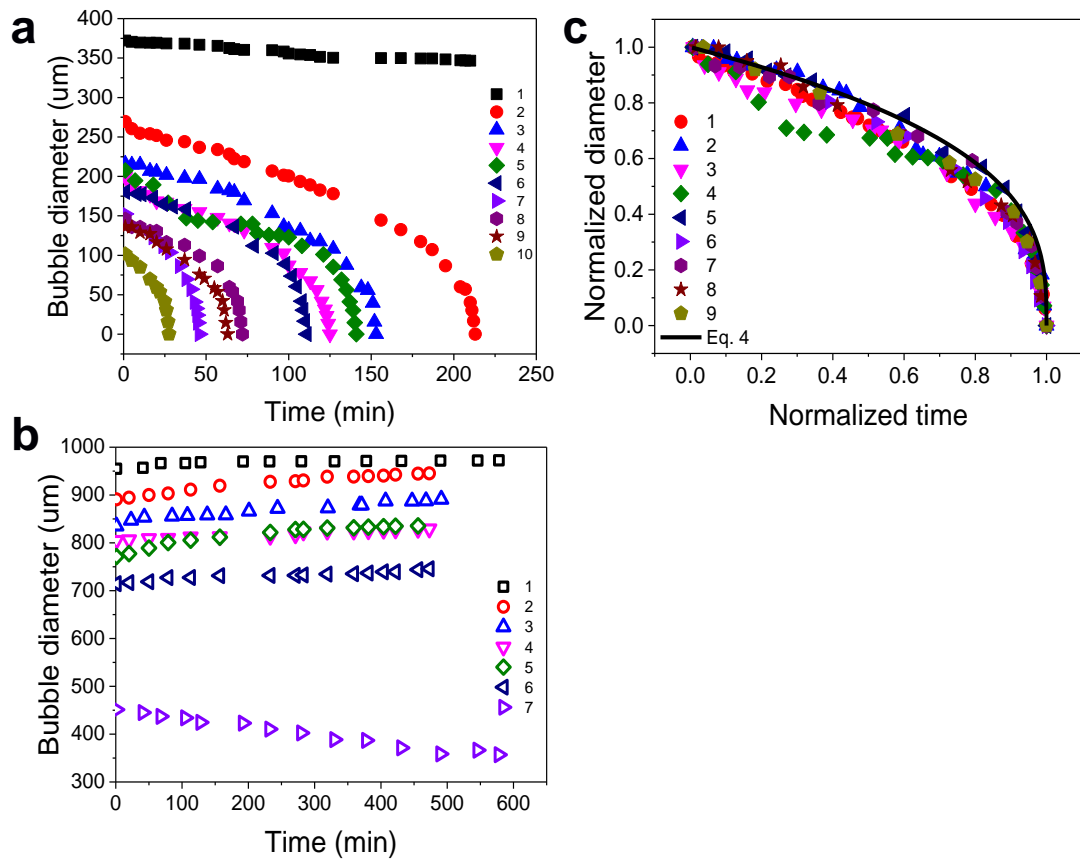


Figure 4.26 Time-dependent changes in the size of individual bubbles: (a) small bubbles, and (b) large bubbles. (c) Normalized bubble size (b_i/b_0) and coarsening time (t_i/t_∞) for nine selected bubbles. Empirical fitting is described by Eq. 4.5. Foams prepared by dispersing composite particles in 0.55 M Na_2SO_4 .

4.4.7 Discussion of foam destabilization mechanism

Following initial liquid drainage, long-term foam stability becomes mainly a function of the rates of bubble coalescence and coarsening. In the current study, foam stability has been shown to be a function of the electrolyte concentration, with poor foam stability observed at the lowest electrolyte concentration (0.01 M Na_2SO_4), and attributed to a high rate of bubble coalescence due to the increased mobility of the particle-laden layer. Upon bubble-bubble contact the repulsive interaction between neighbouring composite particles facilitates particle migration away from the contact

region, resulting in thin liquid film rupture and bubble coalescence. At higher electrolyte concentrations (0.1 M and 0.55 M Na₂SO₄), the interaction between composite particles was weakly attractive, and we observed the formation of more solid-like particle-laden interfaces of increased rigidity. The interfacial rigidity was partly influenced by the reduced solvation of polymer layers on silica particles with increasing electrolyte concentration. The reduction in solvation will modify the conformation of polymers from an expanded coil when dispersed in pure water (a very good solvent) to a tightly packed globule beyond the theta condition (i.e. poor solvent). Between these two extremes, the coil dimensions will steadily decrease with the reducing solvation of polymer. Evidence for such collapse was seen in the change of particle size shown in Fig. 4.9 (the observed decrease in the measured particle size between water and 0.01 M Na₂SO₄). The gradual collapse of the polymer is, in effect moving it from a strongly hydrophilic state towards a more hydrophobic state. This change leads to strengthening of the particle-laden interface, with both a growth of particle aggregates and their increased retention at the air-aqueous interface driven by this decreased solvation of the polymer layers.

4.4.7.1 Bubble coarsening. Bubble coarsening was evidenced in all foam systems. While the particle-laden interfaces exhibited mechanical strength they were unable to cease bubble coarsening. Foam coarsening occurs when $\frac{dP}{dR} = -\frac{2\gamma}{R^2} + \frac{4E}{R^2} < 0$,⁷² hence bubbles become stable to coarsening when $E > \frac{\gamma}{2}$. From the compressional isotherm data shown in Fig. 4.14, the compression elastic modulus can be calculated from the changes in surface pressure and trough area ($E = -A \frac{d\pi}{dA}$). The dynamic compression elastic modulus (E) as a function of trough area is shown in Fig. 4.15. For composite particles deposited on 0.01 M and 0.1 M Na₂SO₄, the maximum compression modulus

was found to be, $E_{max,0.01 M} \approx E_{max,0.1 M} < \gamma/2$, while for 0.55 M Na₂SO₄ the maximum compressional elastic modulus was $E_{max,0.55 M} \approx \gamma/2$ (γ determined from the data presented in Fig. 4.11). For all foam systems $E > \frac{\gamma}{2}$ was not satisfied, hence, bubble coarsening contributed to the destabilization of prepared foams.

4.4.7.2 Bubble coalescence. Although both particle-laden interfaces prepared using 0.1 M and 0.55 M Na₂SO₄ solutions were elastically dominant ($G' > G''$), bubble coalescence was observed only in the case of 0.1 M Na₂SO₄ foam. Previous research confirmed that coalescence is feasible when the interfacial shear yield strength of the particle layer is exceeded.^{48, 63, 131} In an attempt to understand why bubble coalescence was possible when the particle-laden interfaces were elastically dominant, we considered the relationship between the compressive stress ($P_c = \frac{4\gamma}{R}$) acting on the thin liquid film separating two bubbles intimately in contact,⁷² and the yield stress of the particle-laden interface. Assuming an average bubble diameter ($2R$) of 400 μm and the surface tensions (γ) taken from the data presented in Fig. 4.11, the compressive stress exerted on the interacting particle layers was approximately $1.3 \times 10^3 \text{ N/m}^2$ for composite particle foams formed in 0.1 M and 0.55 M electrolyte solutions. Based on the yield points (τ_y) for the two particle layers (0.1 M Na₂SO₄, $\tau_y = 2.4 \times 10^{-5} \text{ N/m}$; 0.55 M Na₂SO₄, $\tau_y = 5.9 \times 10^{-5} \text{ N/m}$), an apparent yield stress can be calculated by introducing a second dimension, which is taken to be the thickness of the interfacial particle layer. Since we did not measure the particle layer thickness, we can reasonably assume that the thickness is equivalent to the hydrodynamic diameter of the composite particles/aggregates. The apparent yield stress (τ'_y) for both the 0.1 M and 0.55 M interfacial particle layers was in the region of $3.0 \times 10^2 \text{ N/m}^2$, and approximately an order of magnitude lower than P_c . Hence, when bubbles are closely

packed within a foam, and $P_c \geq \tau'_y$, it is reasonable that the particle-laden interfaces will rupture leading to bridging and bubble coalescence. The absence of bubble-bubble coalescence in foams prepared using composite particles dispersed in 0.55 M Na_2SO_4 can be attributed to the lack of thin liquid film formation. With strong attraction between composite particles, the resulting large aggregates appear as a network within the continuous aqueous phase, as highlighted by the dashed red box in Fig. 4.24 (inset image). The network impedes liquid drainage therefore inhibiting the formation of thin liquid films between neighbouring bubbles.^{145, 146} In the highest electrolyte solution the dominant mechanism for foam collapse was attributed to bubble coarsening.

4.5 Conclusion

A simple method to form polymer-coated silica nanoparticles (composite particles) has been demonstrated, with the stabilizing potential of the composite particles studied as a function of the aqueous electrolyte concentration (Na_2SO_4). Individually, the two components, polymer and silica nanoparticles, exhibit no or poor foaming ability. However, with minimal energy input, the composite particles were observed to stabilize foams over several days. Foam lifetimes were shown to increase with increasing electrolyte concentration, and the enhanced foam stability was attributed to the formation of solid-like (elastic dominant) interfacial particle layers surrounding bubbles, with high interfacial layer elasticity resulting from greater particle retention at the air–aqueous interface and strong attraction between neighbouring composite particles. The absence of bubble coalescence in foams prepared using 0.55 M Na_2SO_4 was linked to the formation of large particle aggregates, preventing the formation of

thin liquid films (plateau borders) between neighbouring bubbles. Bubble coarsening was identified to be the dominant foam destabilization mechanism.

Chapter 5: Interfacial Rheology of Composite Particle-laden Planar and Curved Interfaces

5.1 Synopsis

Particle-stabilized emulsions and foams are widely encountered, yet few studies have considered the structure-rheology relationship for particle-laden interfaces surrounding bubbles. The composite particles were shown to be effective foam stabilizers in the last chapter, with the foam stability depending on the aqueous phase electrolyte concentration. In the current chapter, the interfacial shear rheology of the composite particle-laden planar interfaces was measured as a function of both the sub-phase electrolyte concentration and surface pressure using the Interfacial Shear Rheometer (ISR 400). All particle-laden interfaces exhibited a liquid-like to solid-like transition with increasing surface pressure. The surface pressure-dependent rheology was correlated to the micron-scale structure of the particle-laden interfaces imaged using Brewster angle microscope (BAM). These structures were further studied using cryo-SEM of particle-stabilized bubbles in foams. Combining different techniques such as the ISR, BAM and cryo-SEM, attempts were made to elucidate the interfacial shear rheology of particle-stabilized bubbles and its relation to foam stability. Independent of the sub-phase electrolyte concentration, the resultant rheology of the particle-laden interface stabilizing bubbles is elastic dominant at a compression state in the region of the L-S phase transition.

5.2 Literature Review

2D colloid assemblies at gas-liquid or liquid-liquid interfaces of particle-stabilized foams and emulsions have been progressively utilized to produce novel, functional products and materials.^{7, 32, 152, 153} An expansion in the number of applications has resulted from the significant research interests in particle assemblies over the past few decades. We now have a sufficiently detailed understanding of these systems to allow us to fine tune their properties.^{10, 154} This precise control of particle assemblies at interfaces can now be used to design-in performance characteristics, i.e. structure – property relationship control.^{60, 155} In the simplest case the range of particle assemblies (structure) can be bound by the degree of dispersion, with interfacial and bulk properties significantly different when considering particle-laden interfaces of highly dispersed and close packed assemblies.¹⁵⁶

The potential for a particle to reside at a liquid-liquid interface is highly dependent on the interaction forces between the particle and interface, and the particle wettability.^{157, 158} While particle interactions in a single phase are well characterized, the asymmetric alignment of particles at an interface between two immiscible liquids of contrasting polarity introduces added complexity which contributes to the overall arrangement of the particle assembly.¹⁵⁹ The main forces contributing to the particle assembly include colloidal (DLVO), capillary, hydrophobic, monopolar and dipolar interactions. Since the dipolar and dispersion forces are a function of the total surface area exposed to the non-aqueous and aqueous phases, respectively, the overall interaction energy becomes very sensitive to the particle hydrophobicity, i.e. wettability.^{160, 161}

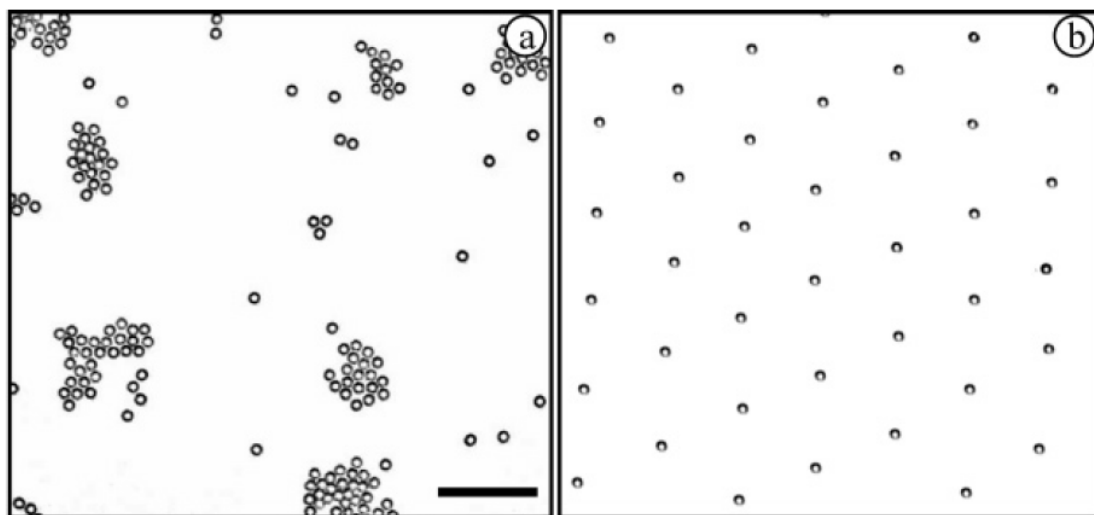


Figure 5.1 Structure of silica particle monolayer at the octane-water interface, the particle contact angle in (a) and (b) is 65° and 152° respectively.¹⁶⁰

The control on particle assemblies offered by particle wettability has been demonstrated in several recent studies.^{156, 157, 160} For hydrophilic particles, particle assemblies are governed by the interaction forces mediated through the aqueous phase. Since the particle repulsion is weak, hydrophilic particles have a tendency to form particle clusters (Fig. 5.1) which have been observed to densify through the addition of electrolyte, and as a function of time, see Fig. 5.2.¹⁶⁰ Similar to the particle aggregation kinetics observed in the bulk, particle aggregation at the liquid-liquid interface follows the diffusion-limited (DLCA), or reaction-limited cluster aggregation (RLCA) kinetics to form low density or high density gel-like networks, respectively (see Fig. 5.3).^{48, 60} Well ordered, crystalline structures have been observed when strongly hydrophobic particles are deposited at a liquid-liquid interface (see Fig. 5.1b).⁶⁷ Since the interaction force mediated through the non-polar phase becomes significant, the long-range Coulomb interaction dominates the particle-particle repulsion, leading to well-ordered and dispersed particles at the interface.

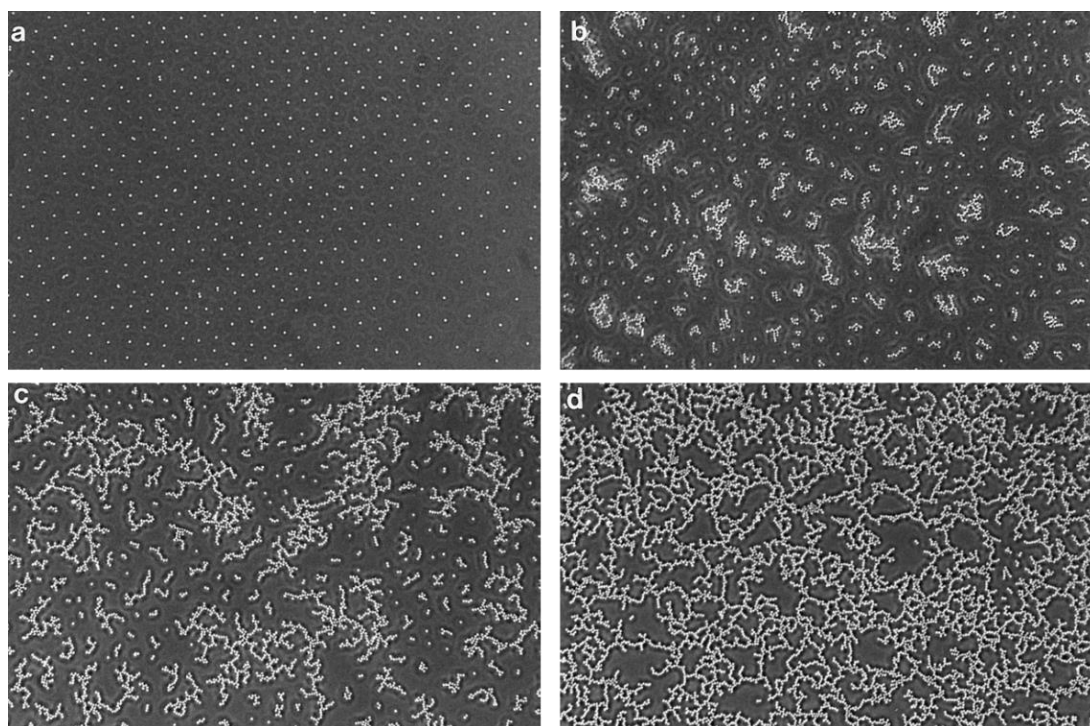


Figure 5.2 Time-dependant aggregation of octyl-coated silica particles at the air–toluene interface (a) $t = 4$ min, (b) $t = 90$ min, (c) $t = 270$ min, and (d) $t = 400$ min.⁶⁷

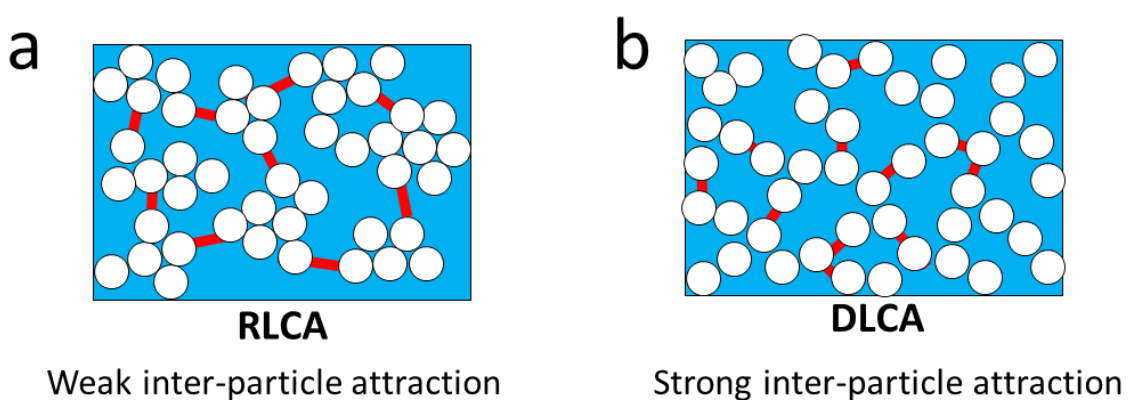


Figure 5.3 Schematic to represent the likely particle-laden structures formed via the (a) RLCA and (b) DLCA processes, the red lines denote the “bond” between particle clusters.⁴⁸

Particle assemblies can also be influenced by the number of particles residing at the liquid-liquid interface.¹⁵⁵ The contribution of particle assemblies to the properties of the liquid-liquid interface is significant, with the lateral mobility of particles and

particle domains contributing to the interfacial rheology, a governing property in the stabilization of droplets and bubbles.^{59, 63, 162} The mobility of the particle-laden interface has been shown to be a function of the particle coverage and the applied shear at the interface, see Fig. 5.4.¹⁶³ At relatively low particle concentrations the lateral displacement force is low and the particles migrate in slip layers. At slightly higher particle concentrations the lateral displacement force also remains low, but mobility is frequently observed through the rotation of particle domains due to the influence of neighbouring particles. The force required to laterally displace particles at an interface increases dramatically as the 2D close-packed assembly is approached ($\phi \sim 75\%$), Fig. 5.5.¹⁶⁴ This increase in the lateral displacement force correlates to a sudden increase in the interfacial shear rheology.¹⁵⁵ At very high particle concentrations the shear deformation of the interface is highly constrained, leading to ‘jamming’ of the particle domains and restricting mobility as the interface response becomes more solid-like.¹⁵⁵ As a result, the rigid particle network remains intact to inhibit droplet coalescence when the two liquid interfaces (droplets or bubbles) approach.⁶³ The critical particle concentration for network jamming is dependent on the attractive potential, with strong attraction between particles leading to the formation of a space-spanning, contiguous particle assembly of increased shear viscosity at significantly lower particle surface coverages ($\phi \sim 40\%$).^{48, 60} Such transitions from liquid-like to solid-like responses have been shown to strongly correlate to the decreased probability of droplet coalescence.⁶³ In a solid-like state, mobility of the particle assembly can only be achieved once the particle assembly is ruptured after the sustained stress exceeds the interfacial shear yield stress of the particle-laden interface.⁵⁹

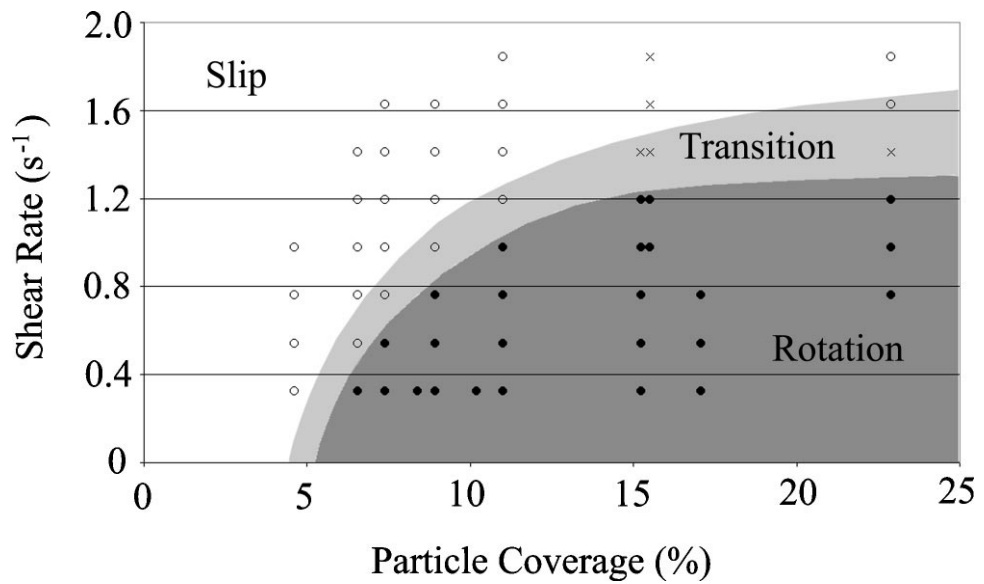


Figure 5.4 Phase diagram illustrating two regimes of interfacial particle dynamics as a function of particle concentration and shear rate.¹⁶³

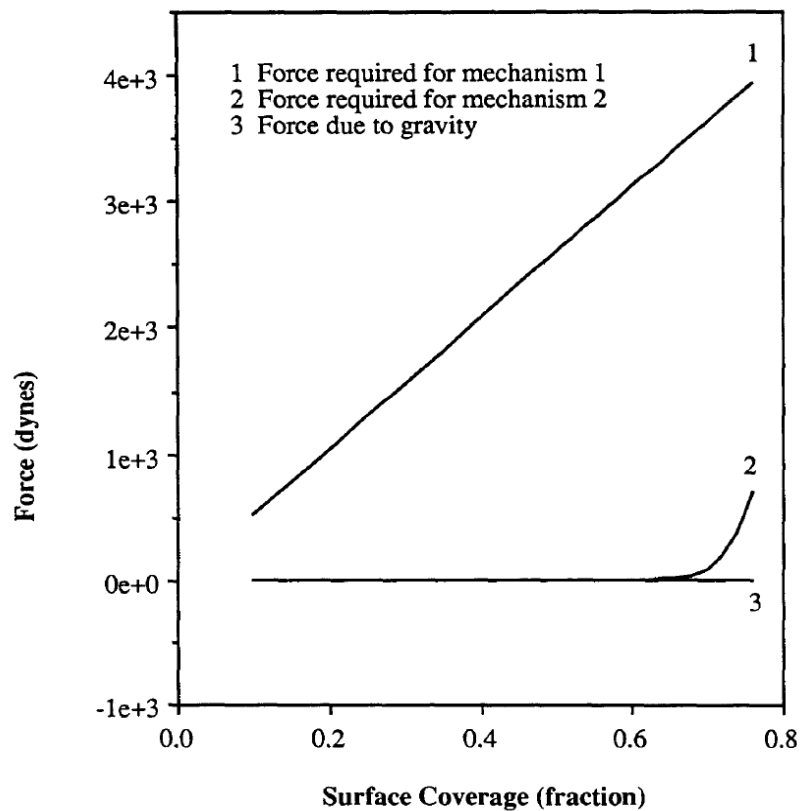


Figure 5.5 Summary of the interfacial particle forces: (1) force required to push particles into the bulk; (2) force required to displace particles laterally along the interface; (3) force due to gravity.¹⁶⁴

In the previous chapter, polymer-coated nanoparticles were shown to be effective foam stabilizers.⁵⁹ The current chapter develops those initial findings to elucidate the structure-rheology relationship for polymer-coated nanoparticles deposited at the planar air-water interface. Using techniques such as Brewster Angle Microscopy (BAM) and pressure-modulated interfacial shear rheology, we are able to directly correlate the mechanical properties of the particle-laden interface to its structure. We extend our observations to make some initial assessment about the rheology of particle-laden interfaces surrounding foam bubbles, by identifying equivalent structures of a 2D planar interface and a curved air-aqueous interface.

5.3 Materials and Experimental Methods

The particle types used in the current chapter are equivalent to those presented in Chapter 4 (Sections 4.3.1 and 4.3.2.1). Experimental methods are introduced below.

5.3.1 Characterization of particle-laden interfaces

5.3.1.1 *II-A* Isotherms. Surface pressure–area (*II-A*) isotherms of deposited particle layers were investigated using an air-liquid Langmuir trough (Biolin Scientific, Sweden), with a maximum trough area of 280 cm². Details of the trough cleaning procedure can be found in Chapter 4.⁵⁹ The particles were first dispersed in the spreading solvent (mixture of water and isopropanol alcohol at a 1:1 vol. ratio) to a concentration of 0.5 wt%. 80 μL of the 0.5 wt% particle suspension was spread carefully at the air-liquid interface. The deposited film was left undisturbed for 30 min to evaporate the spreading solvent. The surface pressure of the particle-laden interface was continuously measured as the trough area was reduced from 280 cm² to 20 cm² at a compression rate of 50 cm²/min. All measurements were repeated in triplicate and

the results demonstrated good reproducibility (surface pressures at equivalent trough areas were within $\pm 5\%$).⁵⁹

5.3.1.2 Particle-laden interface structure. The structure of the particle-laden interface was studied under several states of compression (low \rightarrow high surface pressures) using a Brewster Angle Microscope (BAM, Model EP3, Accurion GmbH, Germany) combined with a Langmuir trough, see Fig. 5.6. One advantage of combined Langmuir trough + BAM is that the structural changes associated with compression of the particle-laden interface can be measured in-situ without the need for ex-situ analysis of a Langmuir-Blodgett film.¹⁶⁵ In the current chapter the BAM was equipped with light guides and a CCD camera used to image the particle-laden interface at $\times 10$ magnification. Both the microscope and polarized light were initially aligned to the air-water Brewster angle, $\theta_B \approx 53.22^\circ$. With no p-polarized reflection (i.e. parallel light to the incident plane) from a clean air-water interface, reflected light was only measured following deposition of the particle-laden interface (Fig. 5.7), with the reflected light intensity being a function of the particle surface coverage and film thickness.¹⁶⁶

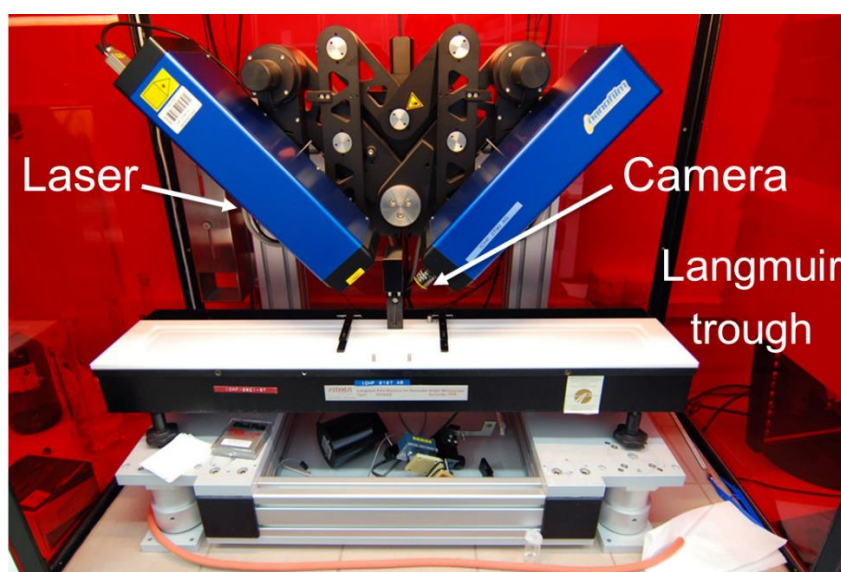
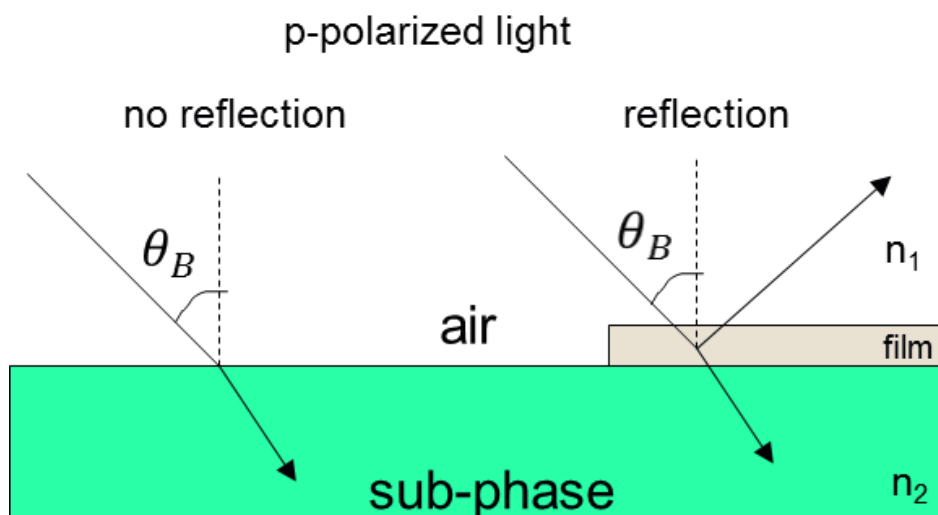


Figure 5.6 Image of the Brewster angle microscope combined with Langmuir trough.



$$\tan\theta_B = n_2/n_1$$

Figure 5.7 Working principle of the Brewster angle microscopy.

Three electrolyte concentrations (0.01 M, 0.1 M and 0.55 M Na₂SO₄) in the aqueous sub-phase were considered. The Brewster angle was calibrated for each electrolyte concentration (0.01 M ~53.23°, 0.1 M ~53.27° and 0.55 M ~53.45°) to achieve the best image quality (i.e. maximize the contrast between the aqueous sub-phase and the particle layer). Following calibration 80 μL of the 0.5 wt% composite particle suspension was deposited at the air-aqueous interface in the spreading solvent. The deposited particle-laden interface was left undisturbed for 30 min prior to imaging. The particle-laden interfaces were compressed to several target surface pressures (0.5, 1, 2, 3, and 4 mN/m) from a maximum trough area of 320 cm². The compressed particle-laden interfaces were allowed to relax for 1 min before imaging by BAM at constant pressure. The polarizer and analyzer were set to 2° and 10°, respectively. Images were collected using the EP3View2.x software (Accurion).

5.3.1.3 Interfacial shear rheology. The viscoelasticity of the particle-laden interfaces was studied under shear using an Interfacial Shear Rheometer (ISR400,

Biolin Scientific,) combined with a KSV NIMA Langmuir trough (Biolin Scientific), as shown in Fig. 5.8a. The measurement region is enveloped by a pair of Helmholtz coils with one coil used to fix the orientation of the magnetic needle and the second coil producing a magnetic field gradient to drive the magnetic needle in motion. The needle had dimensions of radius (a) = 0.27 mm and length (L) = 55 mm, and mass (m) = 72 mg. To conduct the rheology measurements a hydrophobically modified magnetic needle was pinned at the air-aqueous interface and positioned within a roughened glass channel (Fig. 5.8b). A slight meniscus was generated by the glass channel to ensure that the magnetic needle was self-centred. An overhead CCD camera (Basler Electric Company) was focused on the needle such that one edge of the needle could be precisely tracked during oscillatory motion.¹⁵⁵ Edge detection was projected onto a linear image sensor with a 512-pixel photodiode array and pixel resolution of 3.58 μm .

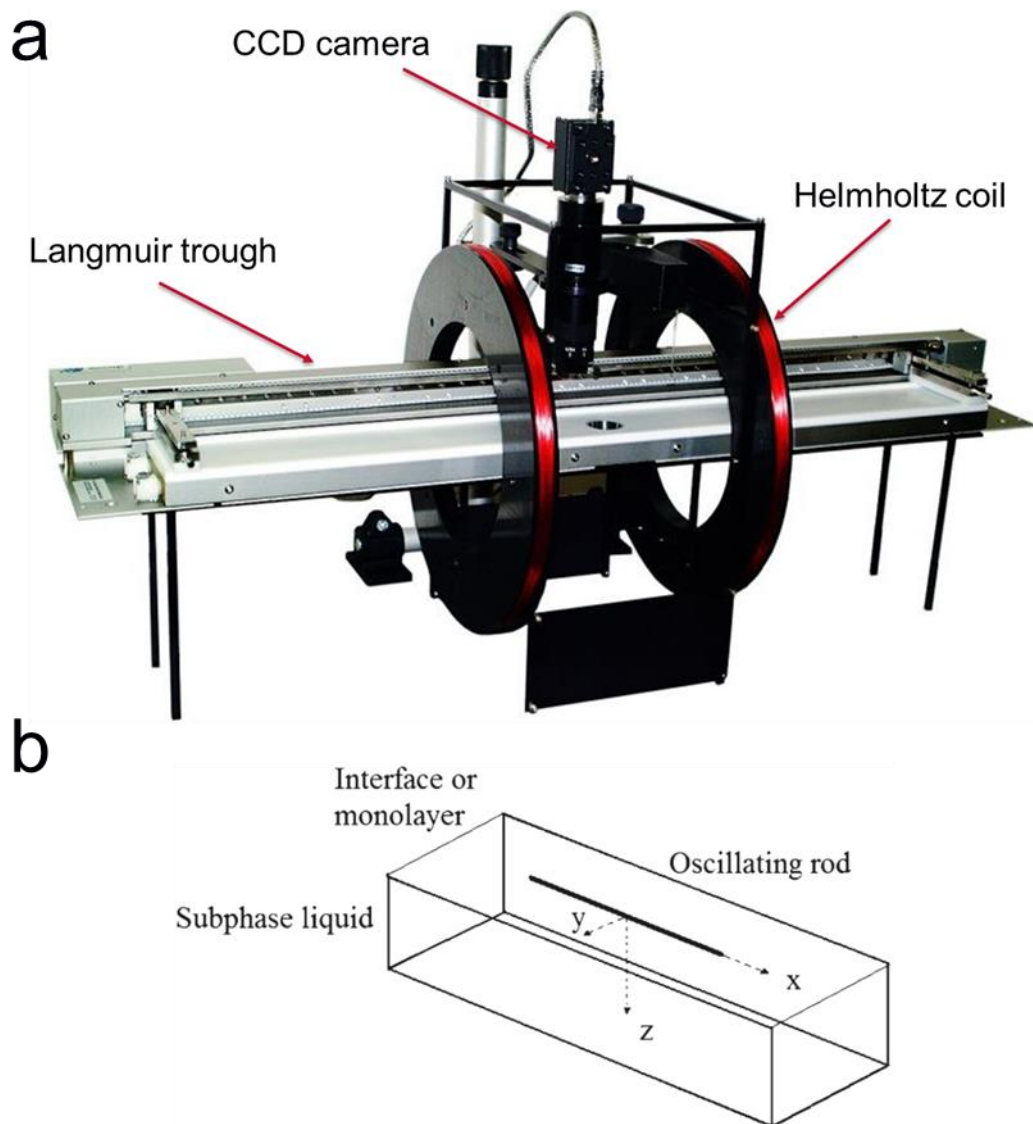


Figure 5.8 Image of (a) the Interfacial Shear Rheometer (ISR400) with Langmuir trough and (b) schematic of the magnetic needle positioned in the glass channel at the air-water interface.¹⁶⁷

With the magnetic needle oscillating sinusoidally (induced by the Helmholtz coils), an amplitude ratio, AR , can be defined as the ratio of the amplitude of the rod displacement (strain, γ) to the forcing amplitude (stress, σ), with the strain and stress offset being the phase difference (δ). The dynamic surface modulus, G^* , which is given by $G^*(\omega) = G'(\omega) + iG''(\omega)$, can be determined from AR and δ ^{168, 169}

$$G^*(\omega) = \frac{1}{AR} e^{i\delta} = G'(\omega) + iG''(\omega) \quad (5.1)$$

where G' and G'' describe the storage and loss moduli of the interfacial film, respectively. One of the sensitivities of the ISR technique is to ensure that the surface stresses dominate the underlying sub-phase stresses. The requirement to decouple the surface stresses from the sub-phase bulk contribution can be assessed by the dimensionless Boussinesq number (Bo), which is defined as the ratio of surface to bulk stresses.¹⁷⁰ For all particle-laden interfaces considered in the current study $Bo \geq 20$, indicating no requirement to decouple the sub-phase contribution. For this reason, all experimental data are presented without further processing.⁴⁸

In a typical ISR measurement, 400 mL of the aqueous sub-phase was first pipetted into the Langmuir trough. Prior to each measurement the needle was magnetized and positioned at the air-aqueous interface within the glass channel. A calibration of the magnetic needle was first conducted on a particle-free interface such that the influence of sub-phase viscosity, rod dimensions and inertia could be subtracted from the measured needle response. 80 μ L of the 0.5 wt% particle suspension was then deposited at the air-aqueous interface following the film preparation procedure previously described. The particle-laden interface was left undisturbed for 30 min to evaporate the spreading solvent and then compressed at a rate of 10 cm^2/min to several target surface pressures (0.5, 1, 2, 3, 4, 5 and 6 mN/m). To maintain a constant surface pressure the operational mode of the Langmuir trough was switched to pressure control mode during the rheological measurement.

Table 5.1 Strain sweep settings for the ISR measurements.

Surface pressure (mN/m)	0.01 M Na ₂ SO ₄		0.1 M Na ₂ SO ₄		0.55 M Na ₂ SO ₄	
	Frequency (Hz)	Voltage range (V)	Frequency (Hz)	Voltage range (V)	Frequency (Hz)	Voltage range (V)
0.5	0.5	0.05-0.8	0.5	0.05-0.8	0.5	0.05-1
1	0.5	0.05-0.8	0.5	0.05-0.8	0.5	0.05-3
2	0.5	0.05-0.8	0.5	0.05-1.5	0.5	0.5-5
3	0.5	0.1-1.5	0.5	0.5-5	0.5	0.5-8
4	0.5	0.5-7	0.5	0.5-7	0.5	1-9
5	0.5	1-8	0.5	2-9	0.5	2-10
6	0.5	1-10	0.5	3-10	0.5	4-10
7	0.5	1-10				
8	0.5	1-10				

For all particle-laden interfaces a dynamic strain sweep (amplitude sweep) was first conducted at a fixed frequency of 0.5 Hz (3.14 rad/s) to determine the linear viscoelastic region. Such measurements also provided guidance on the input voltages required to drive the magnetic needle into oscillation with sufficient forward and backward motion. For example, for weak particle-laden interfaces (i.e. low surface pressures \sim 0.5 mN/m) the optimal input voltage was in the range 0.05 to 0.8 V, while for more compressed interfaces (i.e. higher surface pressures \sim 3 mN/m) the input voltage varied between 0.1 and 1.5 V. Details of the input voltages used in the current study are summarized in Table 5.1. To probe the time-dependent response of the particle-laden interfaces, frequency sweep measurements were conducted between 0.1 Hz (0.63 rad/s) and 5 Hz (31.40 rad/s), see Table 5.2 for experimental settings.

Table 5.2 Frequency sweep settings for the ISR measurements.

Surface pressure (mN/m)	0.01 M Na ₂ SO ₄		0.1 M Na ₂ SO ₄		0.55 M Na ₂ SO ₄	
	Initial	Initial	Initial	Initial	Initial	Initial
	voltage	displacement	voltage	displacement	voltage	displacement
	(V)	(μm)	(V)	(μm)	(V)	(μm)
0.5	0.05	300	0.1	300	0.1	150
1	0.05	300	0.1	200	0.2	20
2	0.05	300	0.2	20	1	15
3	0.2	100	1.5	15	4	12
4	0.5	50	3	12	5	10
5	2	40	4	10	7	8
6	2	20	7	8	8	6
7	2	15				
8	4	10				

5.3.2 Cryo-SEM

Particle-stabilized foams were generated using 10 mL of 1 wt% composite particles dispersed in either 0.1 M or 0.55 M Na₂SO₄ solution. Cryo-SEM (Quorum Technologies, UK) was used to study the structure of the particle-laden interfaces surrounding air bubbles (see Fig. 5.9a). Approximately 0.5 mL of the foam was pipetted onto a universal specimen shuttle (AL200077B) and plunged into liquid nitrogen at -196 °C.¹⁷¹ The frozen samples were then transferred to a Quilo cryo preparation chamber (T = -175 °C) using the system cryo transfer device (see Fig. 5.9b). The preparation chamber was used to remove excess ice by the twin fracturing

manipulators (see Fig. 5.9c). With the excess ice removed the cryo samples were transferred onto a highly stable SEM cold stage for observation.

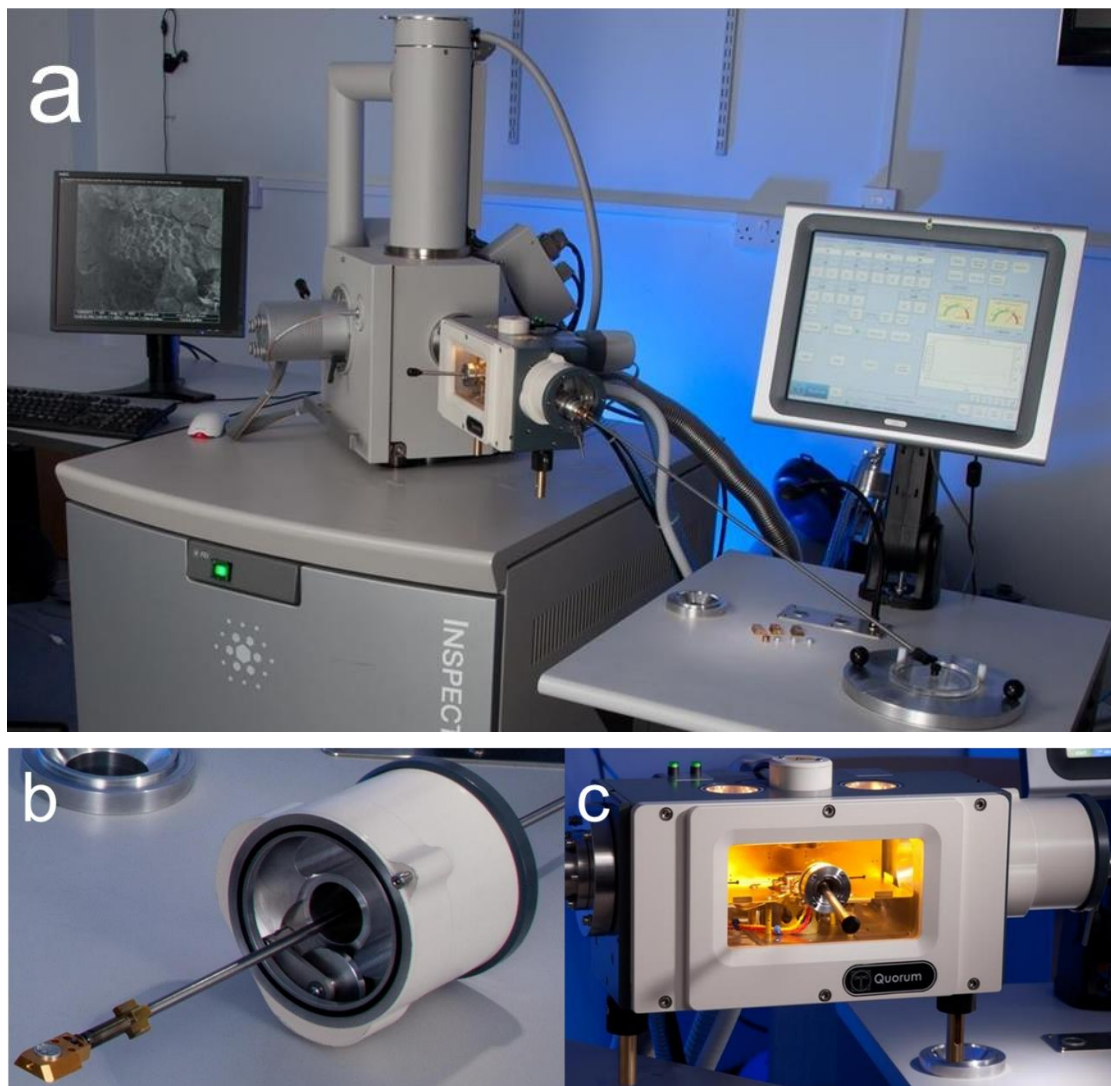


Figure 5.9 Photos of (a) the cryo-SEM system, (b) the cryo transfer device with a universal specimen shuttle (AL200077B) and (c) the Quilo cryo preparation chamber with the twin fracturing manipulators.

5.4 Results and Discussion

5.4.1 *II-A* isotherms and interfacial structure (BAM)

5.4.1.1 *II-A* isotherms. In the previous chapter, Fig. 4.14 compared the *II-A* isotherms for all particle types used in the current study. The Langmuir trough used

for collecting those Π - A isotherms had a maximum and minimum trough area of 80 cm^2 and 20 cm^2 respectively. The compression ratio of the Langmuir trough is defined as: $\frac{A_{max}-A_{min}}{A_{max}}$, where A_{max} is the maximum trough area, and A_{min} is the minimum trough area. The compression ratio of the aforementioned Langmuir trough was 0.75, which was not suitable to study the gas-liquid-solid phase transitions of the isotherms. Hence, the Π - A isotherms of the deposited composite particle films at the air-aqueous interfaces were re-measured using a Langmuir trough with a higher compression ratio (~ 0.93 , $A_{max} = 280 \text{ cm}^2$, $A_{min} = 20 \text{ cm}^2$).

Π - A isotherms of the deposited particle-laden interfaces are shown in Fig. 5.10. The effect of the sub-phase electrolyte concentration is evident, with the highest surface pressures measured for the highest electrolyte concentration. All particle-laden interfaces exhibit a clear gas (G), liquid (L), solid (S) phase transition, showing the increase in film collapse pressure from 8 mN/m to 11 mN/m and 22 mN/m with increasing Na_2SO_4 from 0.01 M to 0.1 M and 0.55 M, respectively.

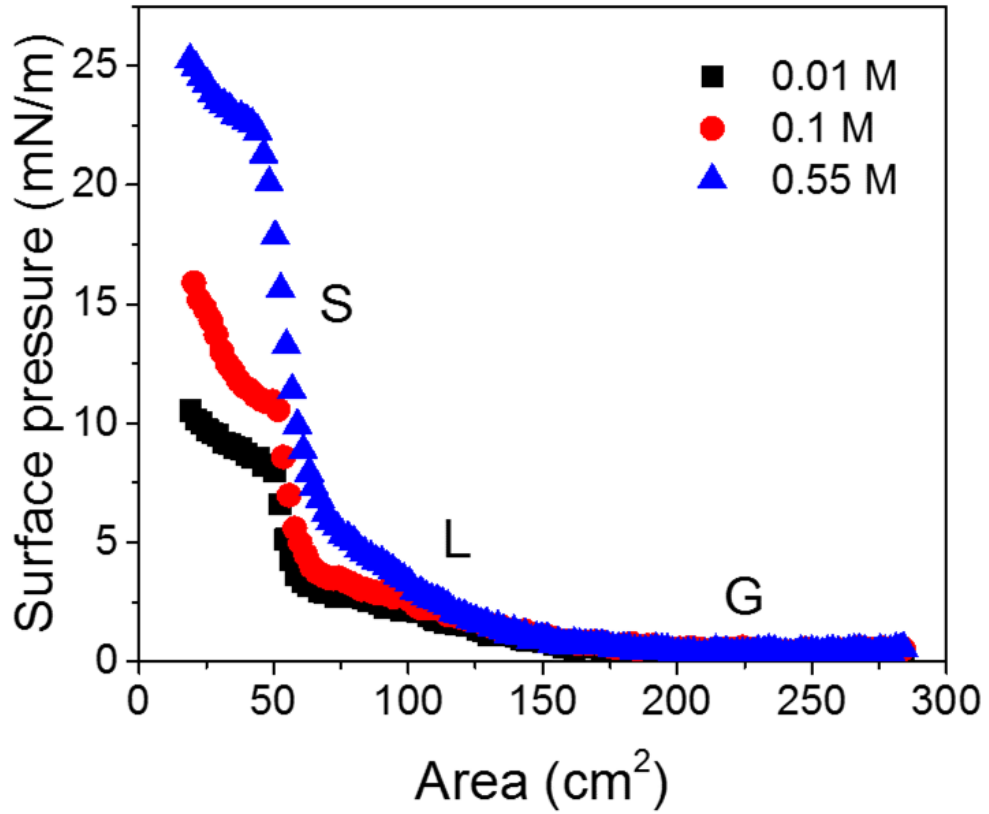


Figure 5.10 Π - A isotherms of composite particles deposited at the air-aqueous interface, with the particle concentration and spreading volume remained fixed at 0.5 wt% and 80 μL , respectively. The surface pressure was measured continuously at a compression rate of 50 cm^2/min . All particle-laden interfaces exhibit gas (G), liquid (L), and solid (S) phase transitions, with collapse of the particle-laden interfaces measured at approximately $\sim 50 \text{ cm}^2$.

The compressibility (C_s) of the particle-laden interfaces can be determined by

$$C_s = \left(\frac{-1}{A}\right) \left(\frac{dA}{d\Pi}\right) \quad (5.2)$$

where A is the trough area and Π is the surface pressure. An average compressibility (C_s^*) can then be calculated by integrating Eq. 5.2 to give

$$C_s^* = -\frac{\ln A_2 - \ln A_1}{\Pi_2 - \Pi_1} \quad (5.3)$$

where subscripts 1 and 2 refer to the start and finish positions of the compression.

Table 5.3 Average compressibility of particle-laden interfaces in the L- and S-phase.

Na₂SO₄ (M)	L-phase	S-phase
0.01	0.360	0.050
0.1	0.270	0.035
0.55	0.150	0.020

Table 5.3 compares the average compressibility of the three particle-laden interfaces (at 0.01 M, 0.1 M and 0.55 M) in the L- and S-phases. In the L-phase, an increase in the sub-phase electrolyte concentration leads to a reduction in the film compressibility, indicating a greater resistance to compression. It should be noted that the observed differences in compressibility are unlikely the result of particle removal from the air-aqueous interface. In Fig. 4.19, the differences between the first and second compression cycles at equivalent trough areas (0.01 M Na₂SO₄ particle-laden interface) were negligible when the surface pressure was greater than ~ 1.5 mN/m. Hence, the effect of particle removal under compression is considered to be negligible. At higher electrolyte concentrations, particle retention at the air-aqueous interface is enhanced, most likely as a result of increased particle aggregation and change in the particle wetting angle (increased hydrophobicity).⁵⁹ Therefore the possible effect of particle detachment from the interface should be even more unlikely. The decrease in film compressibility with increasing electrolyte concentration is thought to result from changes in the strength of particle-particle interactions. Fig. 4.9 confirmed aggregation of the composite particles at the critical electrolyte concentration of 0.1 M. This observation was supported by AFM data which showed attraction between composite particles in 0.1 M and 0.55 M Na₂SO₄ electrolyte solutions and apparent adhesion

measured during pull-off.⁵⁹ For 0.01 M Na₂SO₄, the interaction was purely repulsive with no measurable adhesion. Modulating the strength of particle-particle interactions will impact the ability for particles to re-organize under compression. Hence, strong particle-particle attraction (0.55 M Na₂SO₄) will inhibit particle mobility and lower the film compressibility. In the S-phase, film compressibility reduced by almost one order of magnitude for all systems, although there still remains an influence of the sub-phase electrolyte concentration.

5.4.1.2 Interfacial structure of the composite particle laden films. The structure of the composite particle-laden interfaces had been assessed by SEM using the LB deposition technique mainly for surface pressures ≥ 5 mN/m at 0.01 M and 0.1 M Na₂SO₄ (see Fig. 4.16). However, the LB imaging protocol was significantly impeded by salting on the mica substrate when the sub-phase electrolyte concentration increased to 0.55 M. In order to avoid the salting effect, the particle-laden interfaces were imaged using a Brewster angle microscope (BAM) at 0.01 M, 0.1 M and 0.55 M Na₂SO₄, respectively.

For 0.01 M Na₂SO₄ and at the lowest surface pressure ($\Pi = 0.5$ mN/m), the BAM image was featureless and of uniformly dark grey color, hence assessing the structure of the particle-laden interface was not possible (Fig. 5.11). However, as the particle-laden interface was compressed ($\Pi = 1, 2, 3$ mN/m) the BAM image becomes increasingly brighter as a result of increased densification of the particle-laden interface (increased surface coverage). The brightness of the image taken at the L-S phase boundary ($\Pi = 3$ mN/m) appears to be uniform throughout, suggesting that the deposited particle-laden interface is homogenous, although intricate detail of the particle network structure is difficult to visualize since the particles remain dispersed at the lowest electrolyte concentration.

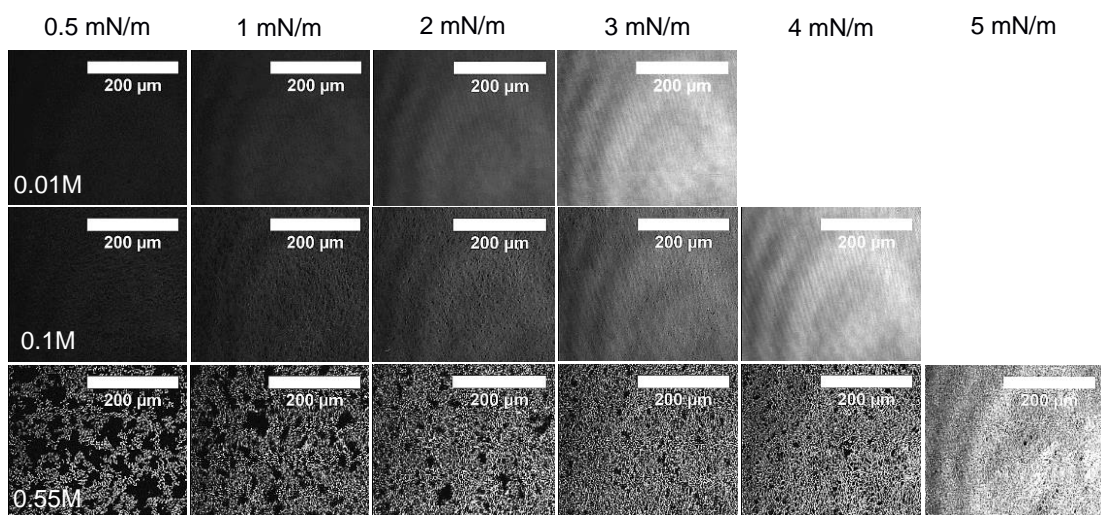


Figure 5.11 BAM images of deposited composite particles at the air-water interface as a function of the sub-phase electrolyte concentration (0.01 M, 0.1 M, and 0.55 M as labelled) and surface pressures. Increasing electrolyte concentration increases voidage in the particle-laden films, which can be attributed to aggregation of the composite particles. Surface pressure driven densification of the particle-laden films is qualitatively verified by reduced voidage and increased brightness of the BAM images.

The onset of particle aggregation allowed for more interesting structural features to be identified. With the consecutive increase in electrolyte concentration (0.1 M), it is readily shown that the particle-laden interface ($\Pi = 0.5$ and 1 mN/m) becomes less homogenous with dark spots (voids) and bright spots (particle aggregates/clusters) being clearly observed. At the highest electrolyte concentration (0.55 M Na_2SO_4) the voids in the particle-laden interface are significant, with the void size observed to decrease with increasing surface pressure.

The contrast between the particle network and the aqueous sub-phase can be used to provide an approximation of the particle surface coverage at the air-aqueous interface in different electrolyte concentrations (0.1 M and 0.55 M Na_2SO_4) and at different surface pressures, see Fig. 5.12. BAM images were processed using ImageJ software

with a band pass filter to correct for the varying illumination prior to thresholding.¹⁷² While different approaches were considered to determine the most appropriate threshold value for distinguishing the two phases (voids and particle aggregates), visual comparison of the BAM and grey-scaled images was found to be the most reliable. A sensitivity assessment on the chosen threshold value showed that a $\pm 5\%$ change in the threshold value would result in a 4.5 – 6 % variability in the quoted apparent particle surface coverage. Assessment of the apparent particle surface coverage was made by analysing three images (dimensions – $390 \times 490 \mu\text{m}$) along the centreline of the trough from the barrier edge to the mid-point between the two Langmuir trough barriers.

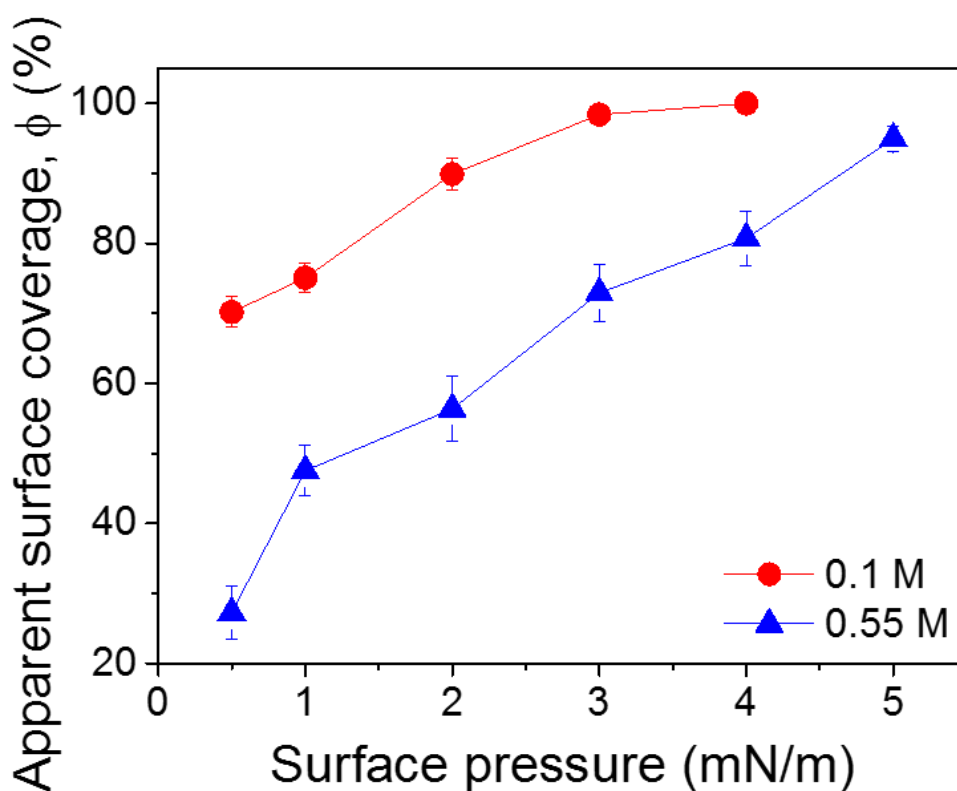


Figure 5.12 Apparent particle surface coverage (ϕ) of 0.1 M and 0.55 M Na_2SO_4 particle-laden interfaces. BAM images were processed using ImageJ, first correcting for varying illumination using a band pass filter and thresholded to differentiate between the sub-phase and particle layer.

Fig. 5.12 compares the apparent particle surface coverages for the 0.1 M and 0.55 M Na₂SO₄ particle-laden interfaces as a function of the surface pressure. Intuitively, as the surface pressure is increased the particle network compresses, hence the particle surface coverage increases. Also, the apparent particle surface coverage of the 0.55 M particle-laden interface is consistently below that of the 0.1 M particle-laden interface at equivalent surface pressures. As is clearly shown, the lower particle surface coverage results from a higher degree of particle aggregation which has been shown in the last chapter.⁵⁹ For 0.1 M Na₂SO₄, the apparent particle surface coverage increases from ~ 70 % to almost complete coverage (~ 99%), while the average void size reduced from approximately 4 μm² (~4.1 μm²) to less than 1 μm² (~ 0.7 μm²) as the surface pressure is increased from 0.5 mN/m to 4 mN/m. At the highest electrolyte concentration (0.55 M Na₂SO₄), the apparent particle surface coverage increased from ~ 27% to ~ 80%, with the average void size reducing from greater than 1000 μm² (~1135 μm²) to less than 10 μm² (~7 μm²) across the same range of surface pressures.

5.4.2 Linear rheology

The shear rheology of the particle-laden interface was investigated using the ISR needle rheometer, with the elastic (G') and viscous (G'') contributions being measured as a function of the sub-phase electrolyte concentration and surface pressure. Having attained the target surface pressure, the Langmuir trough barriers were operated in feedback mode to ensure that the surface pressure remained constant during the rheology measurement.

5.4.2.1 Strain sweep. To assess the mechanical properties of the particle-laden interfaces, the magnetic needle was oscillated at an amplitude within the linear viscoelastic region and at constant frequency of $F = 0.5$ Hz (3.14 rad/s).

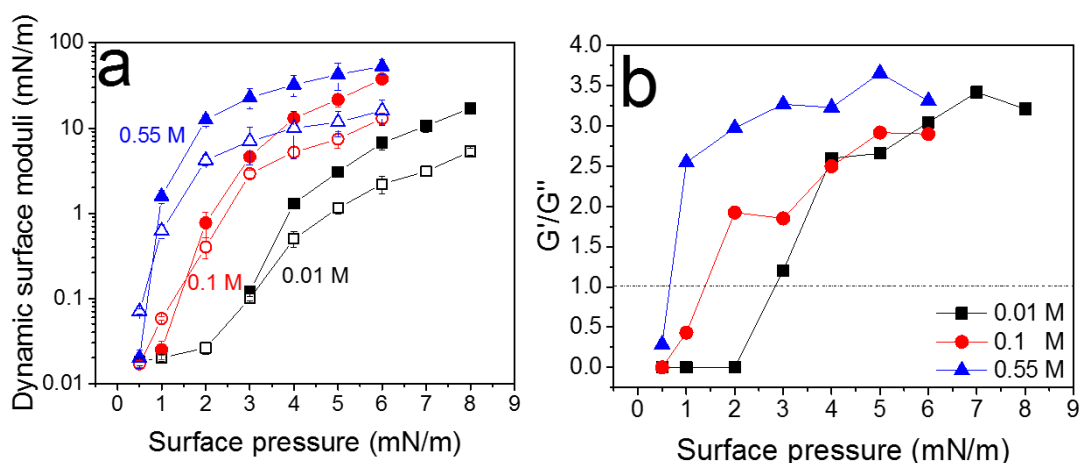


Figure 5.13 (a) Dynamic surface shear moduli (G' – closed symbols and G'' – open symbols) and (b) G'/G'' ratio of the particle-laden interfaces as a function of the sub-phase electrolyte concentration and surface pressure. The magnetic needle was oscillated at constant frequency ($\omega = 3.14$ rad/s) and amplitude in the linear viscoelastic region. The dynamic surface shear moduli were determined using Eq. 5.1.

Fig. 5.13a compares the dynamic surface shear moduli of the three particle-laden interfaces under increased compression. The viscoelastic response to the compressional force was consistent for all three particle-laden interfaces, and resembled the typical rheology profiles of an aging interface, for example oil-water interfaces stabilized by asphaltenes which exhibit a time-dependent viscous-to-elastic transition as the asphaltenes accumulate at the oil-water interface (increased surface coverage) and reorganize.¹⁷³ At the lowest surface pressure ($\Pi = 0.5$ mN/m) all three particle-laden interfaces were viscous dominant and can be considered liquid-like. However, as the imposed surface pressure increased, the contribution of the two viscoelastic moduli increased at different rates, eventually reaching an elastic dominate (i.e. solid-like) interface. It is interesting to note the critical surface pressure to promote this transition ($G' = G''$) was a function of the sub-phase electrolyte concentration (Fig. 5.13b).

At the lowest electrolyte concentration (0.01 M) and low surface pressures ($\Pi < 3$ mN/m), the particle-laden interface is purely viscous with an immeasurably small shear elasticity. At these surface pressures the particle-laden interface was in the L-phase, and due to the repulsive interaction between the composite particles,⁵⁹ the particles were freely mobile under the applied shear. The viscous and elastic contributions measured at $\Pi = 3$ mN/m were almost equivalent, while at higher surface pressures in the S-phase ($\Pi = 3 - 8$ mN/m) the viscoelastic ratio (G'/G'') increased sharply up to $\Pi = 4$ mN/m, indicating an elastic nature of the interface. Eventually a maximum viscoelastic ratio of ~ 3.2 was reached as the particle-laden interface approached the collapse pressure.

As the electrolyte concentration of the sub-phase increased, similar trends in the viscoelastic response to increasing surface pressure were observed. However, the critical surface pressure for liquid-like to solid-like transition of the interface decreased (Fig. 5.13b), with the 0.55 M Na₂SO₄ particle-laden interface being strongly elastic at $\Pi = 1$ mN/m, a condition which can be considered well below the L- to S-phase transition pressure (Fig. 5.10) as measured under compression. The increased elasticity at low surface pressures can be attributed to the higher degree of particle aggregation, which promotes the formation of a contiguous, space spanning network, when the apparent particle surface coverage is low.

As shown in Fig. 5.13a, the magnitude of the viscoelastic response when compared at equivalent surface pressures increased with increasing the sub-phase electrolyte concentration. This type of response is indicative of the structural differences, most likely governed by the particle coverage and the strength of particle-particle interactions at the interface. The relative influence of the two governing mechanisms is not readily discernible, although the strength of particle-particle interactions

controlled by the sub-phase electrolyte concentration is shown to have a dramatic influence on the magnitude of the viscoelastic moduli, in good agreement with previous observations (see Fig. 4.20).¹⁷⁴ However, while the magnitude of the viscoelastic responses is different, it is interesting to note that the viscoelastic ratio for all three systems appears to plateau towards $G'/G'' \sim 3.0$ (Fig. 5.13b), underlining that the shear viscoelastic response becomes independent of the surface pressure when the particles at the interface reach a certain jammed state. Fig. 5.10 confirms that the viscoelastic ratio plateaus within the S-phase for 0.01 M and 0.1 M Na₂SO₄ particle-laden interfaces, while it was observed in the L-phase for the highest electrolyte concentration. Although the viscoelastic moduli are often described by the previously mentioned governing mechanisms (particle-particle interaction strength and particle coverage),^{155, 174, 175} the exact mechanism for this independence is not fully understood. Nevertheless, this characteristic response may indicate that the particle networks become self-similar at high surface pressure when the axial compression dictates the structure forming parameters (i.e. a jamming state).

5.4.2.2 Frequency sweep. To better understand the time-dependent dynamics of the particle-laden interfaces, frequency-sweep measurements were performed in the linear viscoelastic regime. The viscoelastic moduli measured as a function of the oscillation frequency, ω (0.63 to 31.4 rad/s) are shown in Fig. 5.14. At low surface pressure ($\Pi = 0.5$ mN/m), the response of all three particle-laden interfaces was characteristically viscous, varying with $\sim \omega^1$ and independent of the sub-phase electrolyte concentrations. At higher frequencies, G' was immeasurable as the phase difference between the stress and strain approaches 90°. ¹⁶⁸

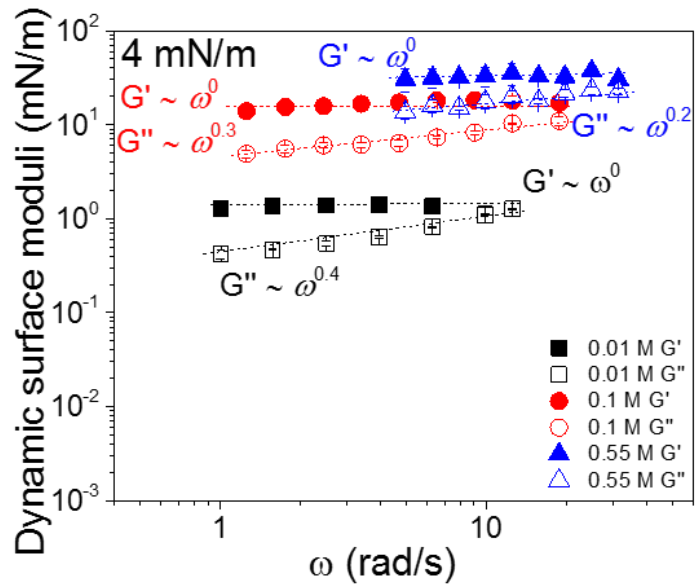
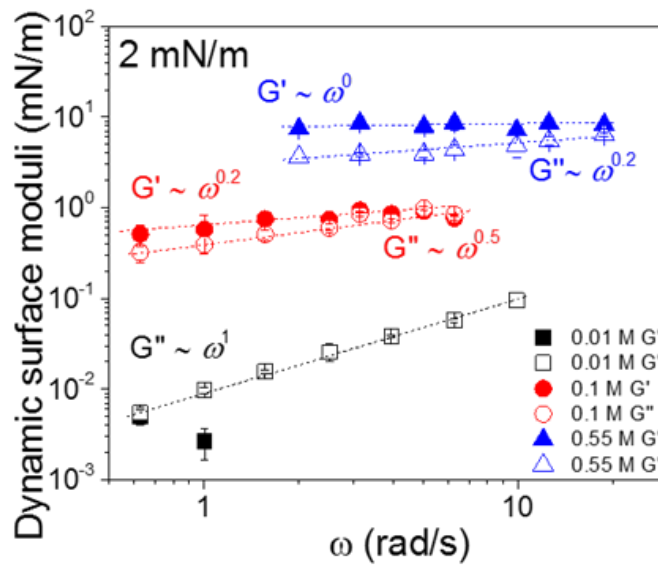
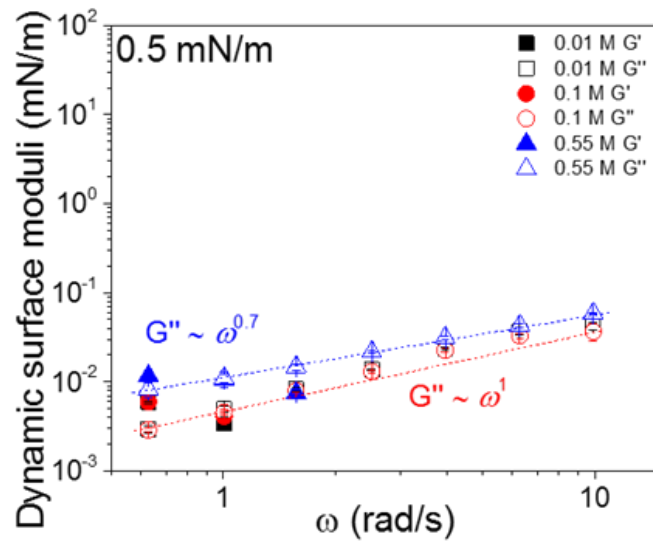


Figure 5.14 Frequency dependent viscoelastic moduli (G' – closed symbols and G'' – open symbols) of the particle-laden interfaces as a function of the sub-phase electrolyte concentration and surface pressure. The power-law scaling confirms the transition from liquid-like at $\Pi = 0.5$ mN/m (all systems) to solid-like behaviour with increasing surface pressure and sub-phase electrolyte concentration.

At the intermediate surface pressure ($\Pi = 2$ mN/m), the 0.01 M particle-laden interface remained viscous in nature, while a viscoelastic transition was observed for the 0.1 M and 0.55 M particle-laden interfaces. The dependence of both G' and G'' on the oscillation frequency decreases with increasing electrolyte concentration. For example, the G' response of the 0.55 M particle-laden interface shows a frequency independent plateau, signifying the onset of the glassy state where the dynamics of the system becomes frozen.¹² At $\Pi = 4$ mN/m, all particle-laden interfaces exhibited a frequency independent plateau of G' , which was expected as the apparent particle surface coverage approached 100%, although such conditions can be attained at a much lower apparent particle surface coverage when the attractive potential between the composite particles is strong, such as for electrolyte solutions of 0.55 M Na₂SO₄. While no definitive crossover in the viscoelastic moduli was measured in the frequency range, the dependence of G'' on ω (at a surface pressure of 4 mN/m) suggests that the high frequency response is influenced by the viscous forces,¹⁷⁵ i.e. the sub-phase fluid viscosity and confined polymer layers.

5.4.3 Nonlinear rheology

In the solid-like state ($G' > G''$) particle-laden interfaces exhibit a critical yield value which must be exceeded for the particles (particle domains) to flow. Dynamic strain-amplitude sweeps at a constant frequency ($\omega = 0.5$ Hz) were performed to measure the yield modulus as a function of the sub-phase electrolyte concentration

and surface pressure. Fig. 5.15 shows the characteristic responses of the particle-laden interfaces to the increased strain. At low amplitude (strain) the viscoelastic moduli were independent of the applied deformation, signifying the characteristic linear viscoelastic response. With increasing strain, both moduli decreased as the mechanical strength of the particle-laden interface was weakened. A critical strain was attained when $G' = G''$ at which the particle-laden interface had yielded. Beyond this point the film response to the deformation (strain) was dominated by viscous forces. In the nonlinear regime the slopes of G' and G'' versus strain exhibited a ratio of ~ 2 ($G' \sim \gamma_0^{-\nu'}$ and $G'' \sim \gamma_0^{-\nu''}$ where $\nu' \sim 2\nu''$) which is consistent with previously reported values for yielding interfaces.¹⁷⁶

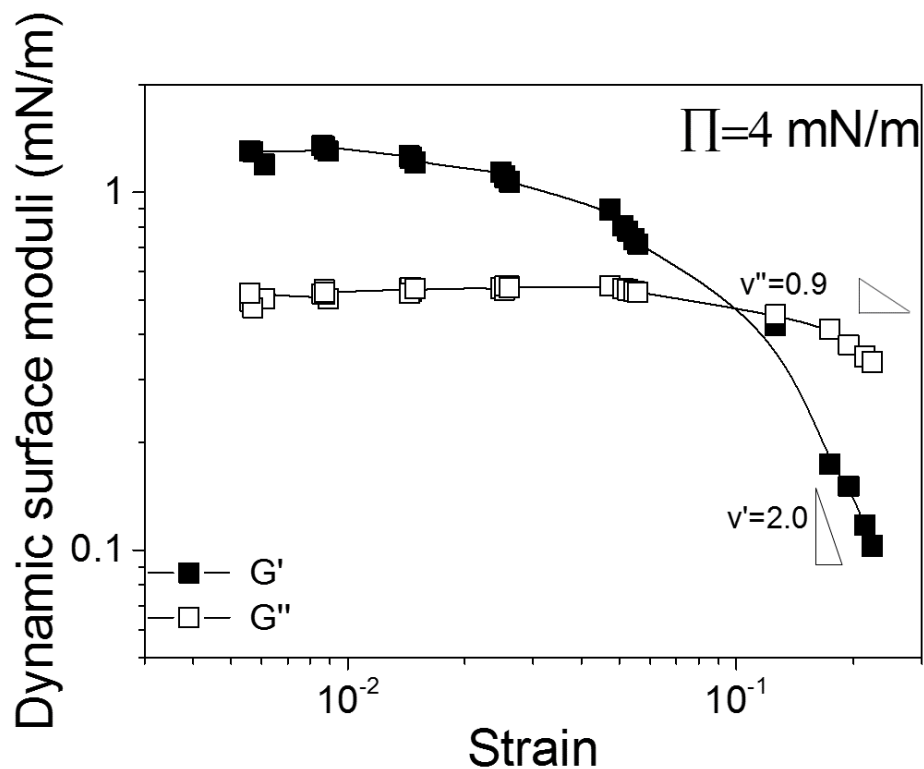


Figure 5.15 Dynamic strain sweep of an elastically dominant particle-laden interface (0.01 M Na₂SO₄). At small strains the dynamic shear moduli are independent of strain before the particle-laden interface yields ($G' = G''$) at higher strains, lines to guide the eye.

Fig. 5.16a shows the dependence of the particle-laden interface yield modulus (where $G' = G''$) on the sub-phase electrolyte concentration and surface pressure. For all systems investigated, the yield modulus increases with surface pressure and increasing electrolyte concentration (yield modulus at equivalent surface pressures), which directly correlates to the increased particle aggregation due to stronger attraction between the composite particles in 0.1 M and 0.55 M Na_2SO_4 electrolyte solution. At the lowest electrolyte concentration (0.01 M) the particle-laden interface yield modulus was only measurable in the S-phase region, i.e., measurable under severe compression. The increase in yield modulus is moderate and almost linear with increasing surface pressure. For the intermediate electrolyte concentration (0.1 M) the yield modulus is measured in both the L-phase and S-phase (slightly beyond the transition pressure). The linear dependence of the yield modulus on surface pressure is once again observed up to $\Pi = 4$ mN/m, beyond which the yield modulus becomes almost independent of the surface pressure in the S-phase region. The reduced dependency of yield modulus on surface pressure in the S-phase is in good agreement with the data measured using 0.01 M Na_2SO_4 electrolyte solution. At the highest electrolyte concentration (0.55 M), the yield modulus was measured in the L-phase region (L-to-S phase transition ~ 6 mN/m). While there is slight fluctuation in the data, the trend is approximately linear (yield modulus vs. surface pressure) and in good agreement with the L-phase characteristic response.

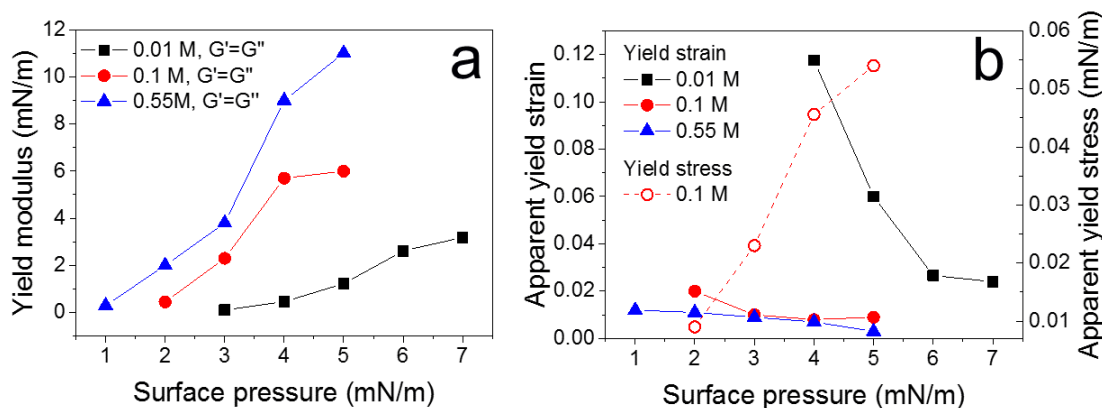


Figure 5.16 (a) Yield modulus ($G' = G''$) and (b) apparent yield strain and apparent yield stress (0.1 M Na₂SO₄) of particle-laden interfaces as a function of the surface pressure and the sub-phase electrolyte concentration. The apparent yield strain and apparent yield stress were determined based on the cross-over ($G' = G''$) condition as shown in Fig. 5.15.

Fig. 5.16b shows the apparent yield strain for all systems and directly compares apparent yield strain to apparent yield stress for the 0.1 M Na₂SO₄ particle-laden interfaces. Yield strain reflects the amount of interfacial deformation required to yield the particle-laden interface, with a lower yield strain and a higher yield stress interface often described as brittle.¹⁷⁰ While the apparent yield strain remains relatively low for the two cases where attraction between the composite particles is prevalent, the apparent yield strain of the 0.01 M Na₂SO₄ particle-laden interface appears more sensitive to the surface pressure, with the yielding properties characterized by ductile and brittle responses at low and high surface pressures, respectively.

5.4.4 Rheology of particle-laden interfaces surrounding bubbles

A unique feature of the ISR is the ability to accurately adjust the surface pressure of the particle-laden interface and measure the interfacial rheology. Correlating the rheology and film structure can then provide new insights to the likely rheology of particle-stabilized bubbles and droplets. Extrapolating the rheology measured at a

planar interface to that of a curved interface is only sensible if the two radii of curvature (particle and bubble) are sufficiently contrasting such that the particle ‘sees’ the interface as being effectively planar.

5.4.4.1 Particle positioned at a planar interface and a curved interface. Fig. 5.17 illustrates the geometry associated with a particle residing at a planar and curved interface. At a planar interface (Fig. 5.17a), dimensions AD and BC are equivalent (within consideration of any contact line undulation), and any significant curvature will lead to greater disparity between the two lengths (Fig. 5.17b). Hence, the uniformity of a planar interface no longer holds and the ability to correlate rheological properties of a curved interface to those measured at a planar interface is lessened.

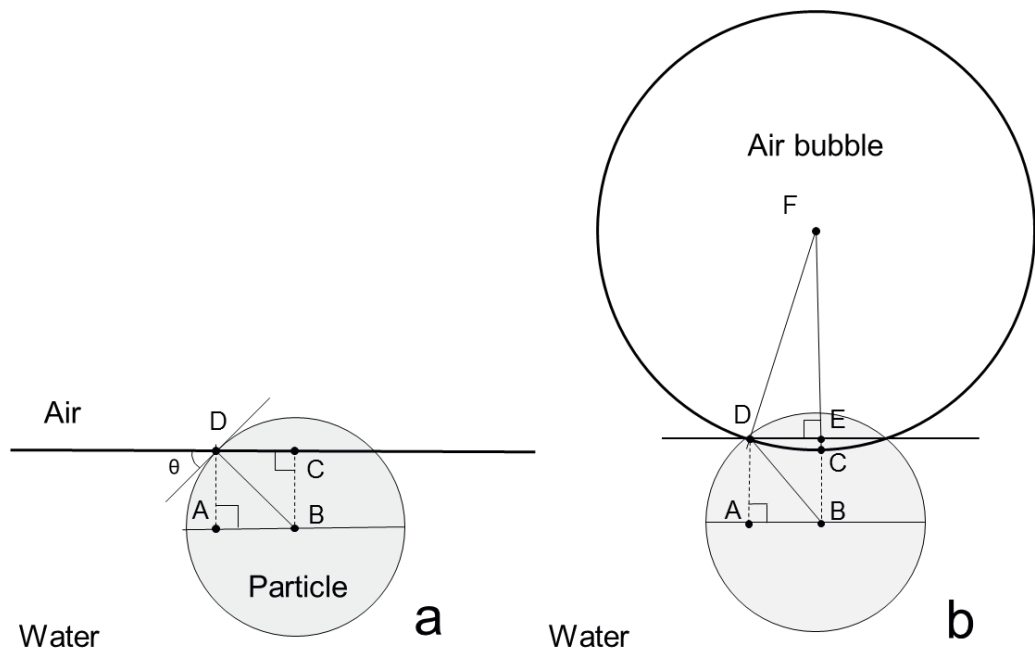


Figure 5.17 Schematics of a particle positioned at (a) a planar interface and (b) a curved interface. The particle centre is point B and the bubble centre is point F. Centre-to-contact line (BC), and edge-to-contact line (AD) are identified by the dashed lines.

Particle-stabilized foams were imaged using cryo-SEM such that the structure of the particle-laden interface surrounding the air bubble could be elucidated. Fig. 5.18 shows low and high magnification images of single bubbles isolated in foams prepared with composite particles dispersed in 0.1 M (Fig. 5.18a) and 0.55 M (Fig. 5.18b) Na_2SO_4 electrolyte solutions. The typical bubble size (D_b) following foaming (via handshaking) was greater than $100\ \mu\text{m}$, while the hydrodynamic diameter (D_h) of the composite particle was $\sim 52\ \text{nm}$, leading to a D_b/D_h ratio of $\sim 10^3$.

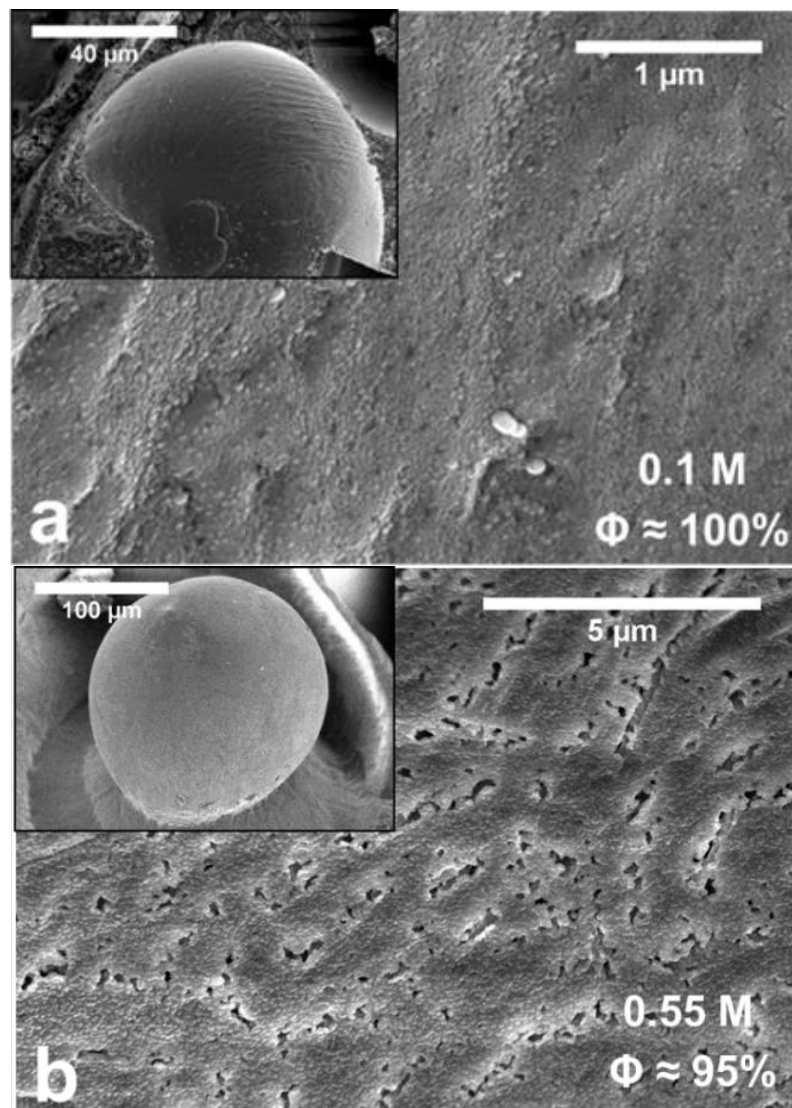


Figure 5.18 Particle-laden interfaces surrounding air bubbles: a) 0.1 M Na_2SO_4 foam, and b) 0.55 M Na_2SO_4 foam. The individual bubbles are shown in the inset of the higher magnification interfacial images.

At this ratio a simple geometry calculation was solved to determine whether or not the particle ‘sees’ the interface (surrounding bubbles) as being effectively planar. As shown in Fig. 5.17, the hydrodynamic diameter (D_h) of the composite particle is ~ 52 nm, with the electrolyte concentration dependent contact angle (θ) measured to be $30^\circ - 40^\circ$ (Fig. 4.10), hence it is reasonable to assume $\theta = 30^\circ$.

For the right triangle $\triangle BCD$ in Fig. 5.17a,

$$BD = 26 \text{ nm} = 0.026 \text{ } \mu\text{m}$$

$$\angle CBD = \theta = 30^\circ$$

$$\text{So } BC = \frac{\sqrt{3}}{2}BD = 0.022 \text{ } \mu\text{m}$$

Hence, in Fig. 5.17b, $BC = 0.022 \text{ } \mu\text{m}$.

According to Fig. 5.18, the diameter of the foam bubble (D_b) is $\sim 100 \text{ } \mu\text{m}$. Thus, in Fig. 5.17b:

$$FC = DF = 50 \text{ } \mu\text{m}$$

$$BF = BC + FC = 50.022 \text{ } \mu\text{m}$$

$$DE \perp BF$$

In the right triangle $\triangle BED$, based on the Pythagorean theorem, $ED^2 = BD^2 - BE^2$

In the right triangle $\triangle EDF$, $ED^2 = DF^2 - EF^2$

$$BE + EF = BF = 50.022 \text{ } \mu\text{m} \rightarrow EF = BF - BE = 50.022 - BE$$

$$BD^2 - BE^2 = DF^2 - EF^2 = DF^2 - (BF - BE)^2$$

$$BE = AD = 0.022 \text{ } \mu\text{m} = BC$$

The simple calculation confirms that the length scale of centre-to-contact line (BC), and edge-to-contact line (AD) is equivalent. It is therefore reasonable to evaluate the likely rheology of particle-stabilized bubbles from the rheology measured at a planar interface.

5.4.4.2 Rheology of particle-stabilized bubbles. Firstly, on assessment of the cryo-SEMs, the structure of the two particle-stabilized bubbles show good similarity to those measured by BAM. At the highest electrolyte concentration (0.55 M) the structure of the particle-laden interface is heterogeneous with fractures sparingly distributed throughout the film (Fig. 5.18b), which contrasts the homogenous and densely packed particle-laden interface observed for the intermediate electrolyte (0.1 M) foam (Fig. 5.18a). These structures visually correspond to the BAM images obtained at the higher surface pressures. Applying the same thresholding method used to determine the apparent particle surface coverage from the BAM images, we determined the apparent particle surface coverage stabilizing air bubbles in foams to be approximately 100% and 95% for 0.1 M and 0.55 M Na₂SO₄ foams, respectively. Referring to Fig. 5.12, these apparent particle surface coverages suggest that the surface pressure of the particle-laden interface surrounding the air bubbles is in the region of ~ 4 mN/m (0.1 M Na₂SO₄) and ~ 5 mN/m (0.55 M Na₂SO₄). Quite interestingly both of these surface pressures correspond to a particle-laden interface at the L-S phase transition, and an interfacial shear rheology which is elastic dominant. The heterogeneous structure of the particle-laden interface (0.55 M Na₂SO₄) results from the macroscopic clustering of the composite particles (particle aggregation). As such, we may conclude that stability of foams formed via simple handshaking corresponds to the structure of the particles at the L-S phase transition as the jammed state of the particle network is attained.

5.5 Conclusion

The current chapter considered the influence of sub-phase electrolyte concentration and surface pressure on the rheology of particle-laden interfaces. Silica nanoparticles

stabilized by PVP formed highly dispersed and homogenous particle-laden interfaces, which evolved into aggregated, space spanning networks with increasing electrolyte concentration. Under axial compression all particle-laden interfaces underwent gas-liquid-solid phase transitions before collapse of the network structure at high surface pressures.

The surface shear moduli of all particle-laden interfaces exhibited a liquid-like to solid-like transition with increasing surface pressure, and the critical surface pressure where the transition occurred was shown to be a function of the sub-phase electrolyte concentration. The strength of particle-particle interactions determined predominantly the shear rheology of the particle-laden interfaces, with the magnitude of the viscoelastic moduli increasing with increasing electrolyte concentration. At higher surface pressures the viscoelastic ratio (G'/G'') became almost independent of the sub-phase electrolyte concentration, potentially indicating self-similarity of the particle networks once the axial compression dictates the structure forming parameters.

The use of nanoparticles as the stabilizing species enabled insight to the likely interfacial rheology of particle-stabilized bubbles. The 2D structure of particle-laden interfaces surrounding an air bubble and deposited at a planar interface were correlated using cryo-SEM and BAM images. At intermediate and high electrolyte concentrations it would appear that the structure of the particle-laden interface is at the L-S phase transition boundary. At this condition the shear rheology of the particle-laden films is elastic dominant, although the particle-laden interface exhibits a low yielding strain due to its brittleness.

Chapter 6: Conclusions and Future Work

Interfacial behaviour and foaming potential of the PVP coated silica composite particles are studied in this project. Comprehensive investigations have been carried out to understand foaming potential of the composite particles, structure-rheology relationship of the particle-laden interfaces, and destabilization mechanism of the composite particle-armed bubbles, etc. The following conclusions are drawn from this research work:

6.1 Conclusions

6.1.1 PVP adsorption and lubricating properties of PVP films

The adsorption behaviour of PVPs with different molecular weights (between 8 kDa and 1300 kDa) on silica a surface was investigated at ultra-low concentrations (≤ 1 ppm). OR measurements showed that the adsorption of PVP on silica was irreversible, with a saturated surface excess around 1 mg/m^2 . Along with the QCM-D data, the amount of water trapped in the 8 kDa PVP film was found out to be ~ 10 wt%, much less than the retained water ($\sim 40\text{-}55$ wt%) in films formed using higher molecular weight PVPs. The equilibrium dissipation values obtained by QCM-D for the 8 kDa PVP film was more than 4 times smaller than those measured of the higher molecular weight PVPs, suggesting that the 8 kDa PVP conformed to a flat film (predominantly in a train orientation), while the high molecular weight PVPs slowly reorganized into more lossy films (more loops and tails).

Lateral forces measured by the AFM colloid probe technique between 8 kDa PVP-PVP surfaces matched very closely to that between uncoated silica surfaces at all

normal loads that being used. By contrast, a ~ 50% reduction in the lateral forces between 40 kDa PVP-PVP, 360 kDa PVP-PVP, and 1300 kDa PVP-PVP surfaces was found, suggesting that above a critical molecular weight (40 kDa), the friction between silica surfaces can be reduced by approximately a factor of 2 by introducing PVP coatings. The molecular weight dependent lubricating effect of PVP films was further verified by measuring the yield stress of concentrated particle suspensions, where a 50% reduction in yield stress was found for the 40 kDa PVP-coated particle suspension comparing with the yield stress of the uncoated and 8 kDa PVP-coated particles at high particle suspension concentration (≥ 60 vol%).

6.1.2 Foaming behaviour of the composite particles

PVP-coated silica nanoparticles (composite particles) were simply prepared by polymer physisorptions, and the foaming potential of the composite particles was found to increase with increasing electrolyte concentration. The enhanced foam stability was attributed to the formation of solid-like (elastic dominant) interfacial particle layers surrounding bubbles. The increased particle film rigidity (elasticity) at high electrolyte concentration (≥ 0.1 M) resulted from adhesion of interpenetrating polymer chains and a higher degree of particle aggregation. The absence of bubble coalescence in foams prepared using 0.55 M Na₂SO₄ was attributed to the formation of large particle aggregates (thick liquid films), separating neighbouring bubbles apart. Hence, bubble coarsening was identified to be the dominant foam destabilization mechanism for the 0.55 M bubbles. The foams prepared at lower electrolyte concentrations (≤ 0.1 M Na₂SO₄) showed the contribution from bubble-bubble coalescence to be more significant.

6.1.3 Interfacial rheology of composite particle-laden planar and curved interfaces

The influences of sub-phase electrolyte concentration and surface pressure on the rheology of a particle-laden planar interface were considered first. The composite particles spread homogeneously at the air-aqueous interface when the sub-phase electrolyte concentration was low (≤ 0.01 M). As the electrolyte concentration increased, aggregated structures and space filling networks were observed. Under axial compression, all particle-laden interfaces underwent gas-liquid-solid phase transitions before film collapse.

The surface shear moduli of all particle-laden interfaces exhibited a liquid-like ($G' < G''$) to solid-like ($G' > G''$) transition with increasing surface pressure, and the critical surface pressure where the transition ($G' = G''$) occurred was shown to be a function of the sub-phase electrolyte concentration. The 2D structure of particle-laden interfaces surrounding an air bubble and deposited at a planar interface were finally correlated using cryo-SEM and BAM images to elucidate the interfacial shear rheology of particle-stabilized bubbles. At 0.1 M and 0.55M Na_2SO_4 , it would appear that the structure of the particle-laden bubble surfaces is close-packed, with a compressional surface pressure at the L-S phase transition boundary, where the shear rheology of the particle-laden interface was found to be elastically dominant ($G' > G''$).

In summary, PVP (40 kDa) coated silica composite particles were prepared via polymer physisorption, with the irreversibly adsorbed and highly hydrated 40 kDa PVP films behaving as steric particle stabilizers. The composite particles (core-shell structure) were shown to be efficient foaming stabilizers, and the observed foam

lifetimes increased with increasing electrolyte concentration. The enhanced foam stability (0.1 M and 0.55 M) was attributed to the formation of solid-like (elastic dominant) interfacial particle layers surrounding bubbles. Although bubble coalescence in foams prepared using 0.55 M Na₂SO₄ was significantly retarded, bubble coarsening cannot be stopped even when the particle-laden films were highly elastic.

6.2 Initial Investigations and Future Work

Although stable foams can be generated using the composite particles as foaming agents in the presence of 0.55 M Na₂SO₄, bubble coarsening cannot be avoided, resulting in bubble vanishing in about two weeks' time. Hence, future work is worth carrying out to stop bubble coarsening. Once bubble coarsening is avoided, particle stabilized foams can then be used as templates to prepare porous and light-weight materials.

Light-weight material fabrication using foam based method has already been reported, however, the particle concentration being used was high (> 10 wt%).^{37, 77, 78} Future work will focus on developing foam based light-weight materials but using lower concentrations of particles. To stop bubble coarsening, several initial attempts have been carried out using the existing composite particle system, and these are presented below.

6.2.1 Increase particle surface coverage and solidify particle-laden

interface

Background: according to the cryo-SEM images (Fig. 5.18), foams prepared in 0.1 M Na₂SO₄ had a higher apparent particle surface coverage. However, the particle film

was found to be pseudo-solid-like, which can stop neither bubble coarsening nor coalescence.

Idea: prepare foams at 0.1 M Na_2SO_4 to guarantee a high particle surface coverage, and then rigidify the close-packed particle film on bubble surface to stop bubble coarsening.

Two samples, labelled as sample 1 and sample 2 were prepared with sample 1 (foams prepared in 0.55 M Na_2SO_4) served as a reference. For the preparation of sample 1, 10 mL of 1 wt % composite particles was prepared in a 40 mL glass vial with the electrolyte concentration fixed at 0.55 M Na_2SO_4 and foams were generated by 1 min of vigorous handshaking. For sample 2, foams was first generated at 0.1 M Na_2SO_4 (7.5 mL of 1.33 wt % composite particles, 0.1 M Na_2SO_4), after which 2.5 ml of 2 M Na_2SO_4 solution was injected into the bulk liquid to make sure the final particle concentration, electrolyte concentration and liquid volume in sample 2 were equal to those in sample 1 (1 wt%, 0.55 M and 10 ml respectively). The foamability and foam stability were visually measured by tracking foam heights.

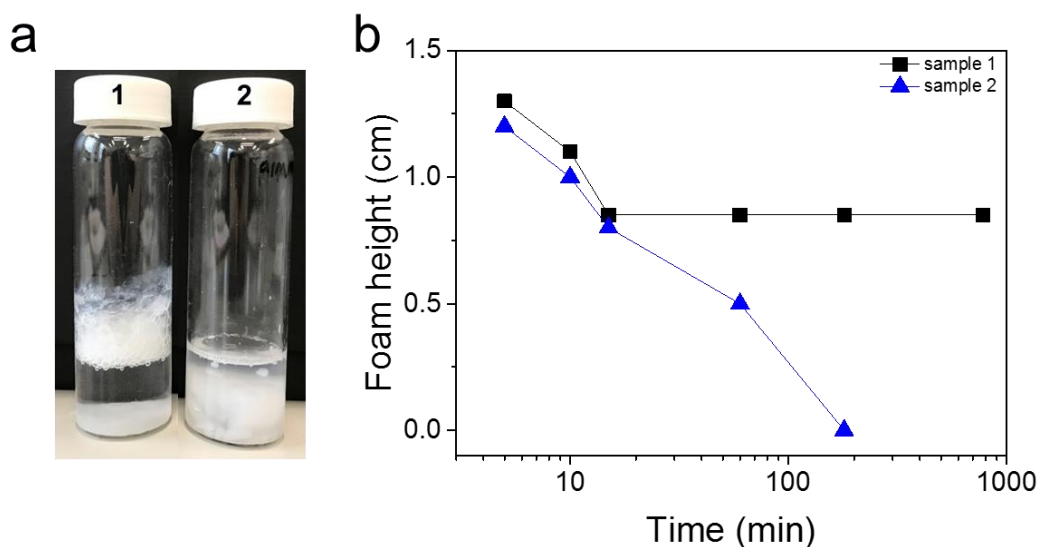


Figure 6.1 (a) Images of sample 1 and sample 2 when $t = 150$ min; (b) Measured foam height for sample 1 and sample 2 as a function of time.

We expected that the addition of 2 M Na₂SO₄ solution would rigidify the particle-laden film on bubble surface and enhance its mechanical strength. In practice, it was found that this method even accelerated foam extinction (see Fig. 6.1). A possible reason may be as follows: after the addition of the 2 M Na₂SO₄ solution, liquid with higher electrolyte concentration diffused into thin films between bubbles, resulting in particle aggregation on the bubble surface. This aggregation process immediately created a porous particle film, facilitating bubble coalescence. Further work needs to investigate alternative routes to solidify the particle-laden interface whilst keeping the particle film close-packed (high particle surface coverage).

6.2.2 Seal the pores on the bubble surface and rigidify the particle-laden interface using beta-escin

Background: it has been shown that the particle-laden interface at 0.55 M is highly elastic, but forms a porous structure (see Fig. 5.18).

Idea: seal the pores on the 0.55 M particle film may help to stop bubble coarsening.

Fig. 6.2 shows that beta-escin (saponin) is a strong surface active surfactant which can adsorb at the air-water interface very rapidly (within seconds), forming interfacial films with significant shear elasticity ($G'/G'' \sim 10$, at concentrations ≥ 0.01 wt%). Beta-escin was added into the composite particle dispersion as a co-foaming-agent to fill up the pores on bubble surface, whilst rigidifying the particle-laden film. The electrolyte concentration in the aqueous phase was 0.55 M.

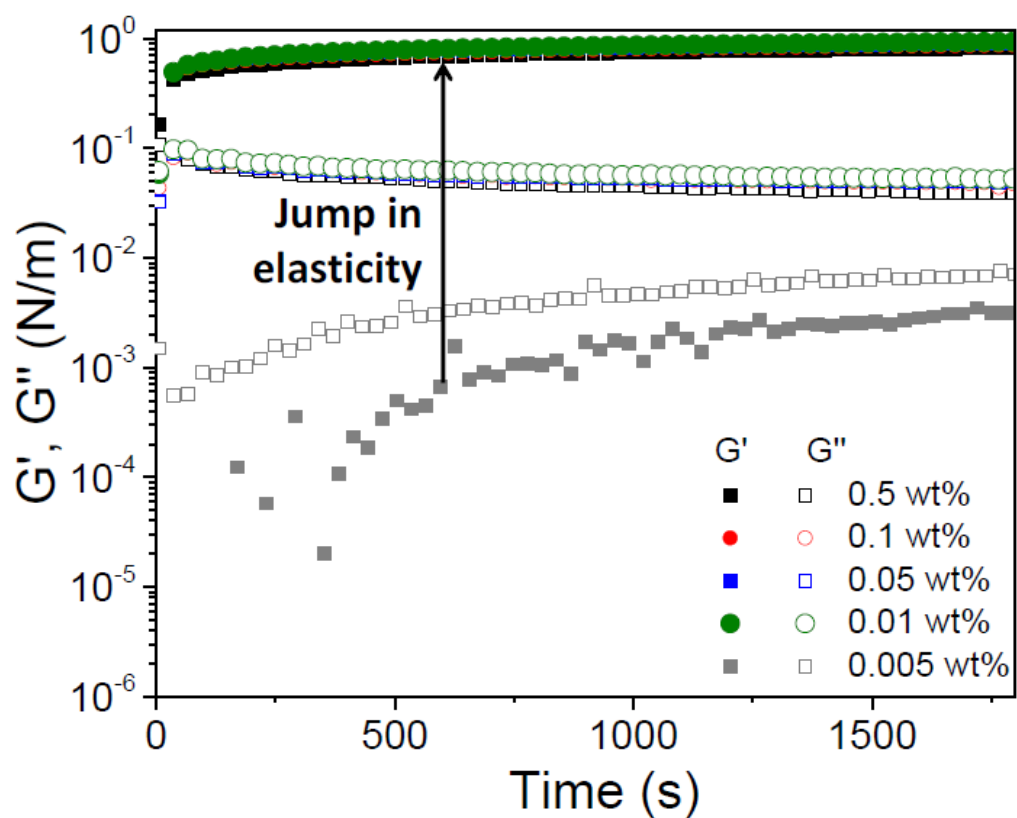


Figure 6.2 Viscoelasticity of beta-escin films as a function of time and solution concentration, measured by PhD student Emily James in our group.

Fig. 6.3 shows the combination of beta-escin and composite particles in 0.55 M Na_2SO_4 enhanced both foamability and foam stability compared with the individual components (composite particle in 0.55 M Na_2SO_4 , or beta-escin alone). These results indicate beta-escin addition may be a promising route to stop bubble coarsening, which needs further investigation (e.g. use higher concentrations of beta-escin).

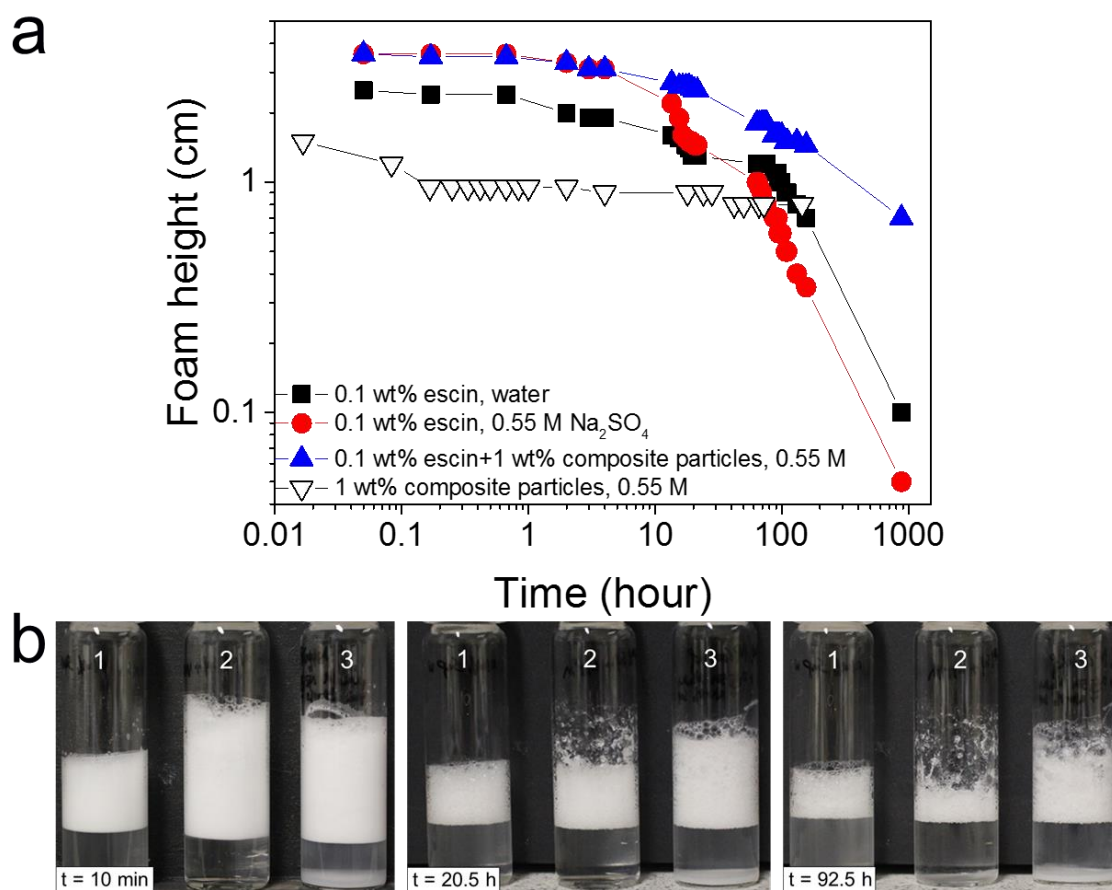


Figure 6.3 (a) Time-dependent stability of foams prepared using 0.1 wt% beta-escin in water, 0.1 wt% beta-escin in 0.55 M Na₂SO₄, 0.1 wt% beta-escin + 1 wt% composite particles in 0.55 M Na₂SO₄, and 1 wt% composite particles in 0.55 M Na₂SO₄ (lines to guide the eye); (b) Images showing changes in foam height with aging time. Sample 1: 0.1 wt% beta-escin in water; sample 2: 0.1 wt% beta-escin in 0.55 M Na₂SO₄; sample 3: 0.1 wt% beta-escin + 1 wt% composite particles in 0.55 M Na₂SO₄. Height of glass vial = 9 cm.

6.2.3 Enhance particle affinity at the interface and increase the yield stress of the particle-laden interface

Enhancing the particle affinity at the interface can potentially stop particle desorption from the surface, which is useful in arresting bubble coarsening. To achieve this, several methods could be employed: (a) use larger particles instead of the

30 nm Ludox silica particles to increase the particle desorption energy at the interface; (b) use particles that are more hydrophobic than silica particles (e.g. polystyrene particles)¹⁷⁷.

It was reported recently that coarsening of particle-stabilized foams can be arrested even at sub-monolayer particle surface coverage when the yield stress of the particle-laden interface was significant.¹⁷⁷ Therefore methods should be developed to increase the yield stress of the particle-laden interfaces. It should be noted that strong lateral interactions between neighbouring particles is usually necessary in order to enhance the yield stress of particle films. Several strategies can be used to increase lateral interactions between particles at interfaces, such as changing particle size, particle surface roughness, particle surface chemistry, and/or solution conditions (pH or electrolyte concentration).^{59, 177}

List of References

1. Banhart, J. Metal foams: Production and stability. *Adv Eng Mater* **2006**, 8 (9), 781-794.
2. Li, R. F.; Yan, W.; Liu, S. H.; Hirasaki, G. J.; Miller, C. A. Foam Mobility Control for Surfactant Enhanced Oil Recovery. *Spe J* **2010**, 15 (4), 934-948.
3. Subramaniam, A. B.; Abkarian, M.; Mahadevan, L.; Stone, H. A. Non-spherical bubbles. *Nature* **2005**, 438 (7070), 930-930.
4. Subramaniam, A. B.; Abkarian, M.; Stone, H. A. Controlled assembly of jammed colloidal shells on fluid droplets. *Nat Mater* **2005**, 4 (7), 553-556.
5. Subramaniam, A. B.; Abkarian, M.; Mahadevan, L.; Stone, H. A. Mechanics of interfacial composite materials. *Langmuir* **2006**, 22 (24), 10204-10208.
6. Binks, B. P.; Duncumb, B.; Murakami, R. Effect of pH and salt concentration on the phase inversion of particle-stabilized foams. *Langmuir* **2007**, 23 (18), 9143-9146.
7. Binks, B. P.; Murakami, R. Phase inversion of particle-stabilized materials from foams to dry water. *Nat Mater* **2006**, 5 (11), 865-869.
8. Fujii, S.; Iddon, P. D.; Ryan, A. J.; Armes, S. P. Aqueous particulate foams stabilized solely with polymer latex particles. *Langmuir* **2006**, 22 (18), 7512-7520.
9. Rio, E.; Drenckhan, W.; Salonen, A.; Langevin, D. Unusually stable liquid foams. *Adv Colloid Interfac* **2014**, 205, 74-86.
10. Binks, B. P. Particles as surfactants - similarities and differences. *Curr Opin Colloid In* **2002**, 7 (1-2), 21-41.

11. Folmer, B. M.; Kronberg, B. Effect of surfactant-polymer association on the stabilities of foams and thin films: Sodium dodecyl sulfate and poly(vinyl pyrrolidone). *Langmuir* **2000**, *16* (14), 5987-5992.
12. Maestro, A.; Deshmukh, O. S.; Mugele, F.; Langevin, D. Interfacial Assembly of Surfactant-Decorated Nanoparticles: On the Rheological Description of a Colloidal 2D Glass. *Langmuir* **2015**, *31* (23), 6289-6297.
13. Pinaud, F.; Geisel, K.; Masse, P.; Catargi, B.; Isa, L.; Richtering, W.; Ravaine, V.; Schmitt, V. Adsorption of microgels at an oil-water interface: correlation between packing and 2D elasticity. *Soft Matter* **2014**, *10* (36), 6963-6974.
14. Saigal, T.; Dong, H. C.; Matyjaszewski, K.; Tilton, R. D. Pickering Emulsions Stabilized by Nanoparticles with Thermally Responsive Grafted Polymer Brushes. *Langmuir* **2010**, *26* (19), 15200-15209.
15. Schulze-Schlarmann, J.; Buchavzov, N.; Stubenrauch, C. A disjoining pressure study of foam films stabilized by tetradecyl trimethyl ammonium bromide C(14)TAB. *Soft Matter* **2006**, *2* (7), 584-594.
16. Bolten, D.; Turk, M. Experimental Study on the Surface Tension, Density, and Viscosity of Aqueous Poly(vinylpyrrolidone) Solutions. *J Chem Eng Data* **2011**, *56* (3), 582-588.
17. von Klitzing, R.; Muller, H. J. Film stability control. *Curr Opin Colloid In* **2002**, *7* (1-2), 42-49.
18. Richtering, W. Responsive Emulsions Stabilized by Stimuli-Sensitive Microgels: Emulsions with Special Non-Pickering Properties. *Langmuir* **2012**, *28* (50), 17218-17229.
19. Robinson, S.; Williams, P. A. Inhibition of protein adsorption onto silica by polyvinylpyrrolidone. *Langmuir* **2002**, *18* (23), 8743-8748.

20. McFarlane, N. L.; Wagner, N. J.; Kaler, E. W.; Lynch, M. L. Poly(ethylene oxide) (PEO) and Poly(vinyl pyrrolidone) (PVP) Induce Different Changes in the Colloid Stability of Nanoparticles. *Langmuir* **2010**, *26* (17), 13823-13830.
21. Pattanaik, M.; Bhaumik, S. K. Adsorption behaviour of polyvinyl pyrrolidone on oxide surfaces. *Mater Lett* **2000**, *44* (6), 352-360.
22. Biggs, S.; Labarre, M.; Hodges, C.; Walker, L. M.; Webber, G. B. Polymerized rodlike micelle adsorption at the solid-liquid interface. *Langmuir* **2007**, *23* (15), 8094-8102.
23. Kang, T.; Banquy, X.; Heo, J. H.; Lim, C. N.; Lynd, N. A.; Lundberg, P.; Oh, D. X.; Lee, H. K.; Hong, Y. K.; Hwang, D. S.; Waite, J. H.; Israelachvili, J. N.; Hawker, C. J. Mussel-Inspired Anchoring of Polymer Loops That Provide Superior Surface Lubrication and Antifouling Properties. *Acs Nano* **2016**, *10* (1), 930-937.
24. Hodges, C.; Biggs, S.; Walker, L. Adsorption Studies of a Polymerizable Surfactant by Optical Reflectivity and Quartz Crystal Microbalance. *Langmuir* **2009**, *25* (19), 11503-11508.
25. Szilagyi, I.; Trefalt, G.; Tiraferri, A.; Maroni, P.; Borkovec, M. Polyelectrolyte adsorption, interparticle forces, and colloidal aggregation. *Soft Matter* **2014**, *10* (15), 2479-2502.
26. Koczur, K. M.; Mourdikoudis, S.; Polavarapu, L.; Skrabalak, S. E. Polyvinylpyrrolidone (PVP) in nanoparticle synthesis. *Dalton T* **2015**, *44* (41), 17883-17905.
27. Duncan, T. V. Applications of nanotechnology in food packaging and food safety: Barrier materials, antimicrobials and sensors. *J Colloid Interf Sci* **2011**, *363* (1), 1-24.

28. Theng, B. K. G. Clay-Polymer Interactions - Summary and Perspectives. *Clay Clay Miner* **1982**, *30* (1), 1-10.
29. Mate, C. M.; Novotny, V. J. Molecular-Conformation and Disjoining Pressure of Polymeric Liquid-Films. *J Chem Phys* **1991**, *94* (12), 8420-8427.
30. Gregory, J.; Barany, S. Adsorption and flocculation by polymers and polymer mixtures. *Adv Colloid Interfac* **2011**, *169* (1), 1-12.
31. Alagha, L.; Wang, S. Q.; Yan, L. J.; Xu, Z. H.; Masliyah, J. Probing Adsorption of Polyacrylamide-Based Polymers on Anisotropic Basal Planes of Kaolinite Using Quartz Crystal Microbalance. *Langmuir* **2013**, *29* (12), 3989-3998.
32. Hitchcock, J. P.; Tasker, A. L.; Baxter, E. A.; Biggs, S.; Cayre, O. J. Long-Term Retention of Small, Volatile Molecular Species within Metallic Microcapsules. *Acs Appl Mater Inter* **2015**, *7* (27), 14808-14815.
33. Pan, M.; Rosenfeld, L.; Kim, M.; Xu, M. Q.; Lin, E.; Derda, R.; Tang, S. K. Y. Fluorinated Pickering Emulsions Impede Interfacial Transport and Form Rigid Interface for the Growth of Anchorage-Dependent Cells. *Acs Appl Mater Inter* **2014**, *6* (23), 21446-21453.
34. Tan, H.; Sun, G. Q.; Lin, W.; Mu, C. D.; Ngai, T. Gelatin Particle-Stabilized High Internal Phase Emulsions as Nutraceutical Containers. *Acs Appl Mater Inter* **2014**, *6* (16), 13977-13984.
35. Pihan, S. A.; Emmerling, S. G. J.; Butt, H. J.; Berger, R.; Gutmann, J. S. Soft Nanocomposites-From Interface Control to Interphase Formation. *Acs Appl Mater Inter* **2015**, *7* (23), 12380-12386.
36. Aranberri, I.; Binks, B. P.; Clint, J. H.; Fletcher, P. D. I. Synthesis of macroporous silica from solid-stabilised emulsion templates. *J Porous Mat* **2009**, *16* (4), 429-437.

37. Lesov, I.; Tcholakova, S.; Kovadjieva, M.; Saison, T.; Lamblet, M.; Denkov, N. Role of Pickering stabilization and bulk gelation for the preparation and properties of solid silica foams. *J Colloid Interf Sci* **2017**, *504*, 48-57.
38. Lin, Y.; Skaff, H.; Emrick, T.; Dinsmore, A. D.; Russell, T. P. Nanoparticle assembly and transport at liquid-liquid interfaces. *Science* **2003**, *299* (5604), 226-229.
39. Yuan, Q. C.; Cayre, O. J.; Fujii, S.; Armes, S. P.; Williams, R. A.; Biggs, S. Responsive Core-Shell Latex Particles as Colloidosome Microcapsule Membranes. *Langmuir* **2010**, *26* (23), 18408-18414.
40. Sanz, E.; White, K. A.; Clegg, P. S.; Cates, M. E. Colloidal Gels Assembled via a Temporary Interfacial Scaffold. *Phys Rev Lett* **2009**, *103* (25).
41. Rey, M.; Elnathan, R.; Ditcovski, R.; Geisel, K.; Zanini, M.; Fernandez-Rodriguez, M. A.; Naik, V. V.; Frutiger, A.; Richtering, W.; Ellenbogen, T.; Voelcker, N. H.; Isa, L. Fully Tunable Silicon Nanowire Arrays Fabricated by Soft Nanoparticle Templating. *Nano Lett* **2016**, *16* (1), 157-163.
42. Sirotkin, E.; Apweiler, J. D.; Ogrin, F. Y. Macroscopic Ordering of Polystyrene Carboxylate-Modified Nanospheres Self-Assembled at the Water-Air Interface. *Langmuir* **2010**, *26* (13), 10677-10683.
43. Zhang, H. G.; Kim, Y. K.; Hunter, T. N.; Brown, A. P.; Lee, J. W.; Harbottle, D. Organically modified clay with potassium copper hexacyanoferrate for enhanced Cs⁺ adsorption capacity and selective recovery by flotation. *J Mater Chem A* **2017**, *5* (29), 15130-15143.
44. Wu, J. D.; Shi, M. X.; Li, W.; Zhao, L. H.; Wang, Z.; Yan, X. Z.; Norde, W.; Li, Y. Pickering emulsions stabilized by whey protein nanoparticles prepared by thermal cross-linking. *Colloid Surface B* **2015**, *127*, 96-104.

45. Zhang, N. N.; Zhang, L.; Sun, D. J. Influence of Emulsification Process on the Properties of Pickering Emulsions Stabilized by Layered Double Hydroxide Particles. *Langmuir* **2015**, *31* (16), 4619-4626.
46. Zhu, Y.; Jiang, J. Z.; Liu, K. H.; Cui, Z. G.; Binks, B. P. Switchable Pickering Emulsions Stabilized by Silica Nanoparticles Hydrophobized in Situ with a Conventional Cationic Surfactant. *Langmuir* **2015**, *31* (11), 3301-3307.
47. Hunter, T. N.; Pugh, R. J.; Franks, G. V.; Jameson, G. J. The role of particles in stabilising foams and emulsions. *Adv Colloid Interfac* **2008**, *137* (2), 57-81.
48. Zhang, H.; Yu, K.; Cayre, O. J.; Harbottle, D. Interfacial Particle Dynamics: One and Two Step Yielding in Colloidal Glass. *Langmuir* **2016**, *32* (50), 13472-13481.
49. Nakayama, S.; Yusa, S.; Nakamura, Y.; Fujii, S. Aqueous foams stabilized by temperature-sensitive hairy polymer particles. *Soft Matter* **2015**, *11* (47), 9099-9106.
50. Nazli, K. O.; Pester, C. W.; Konradi, A.; Boker, A.; van Rijn, P. Cross-Linking Density and Temperature Effects on the Self-Assembly of SiO₂-PNIPAAm Core-Shell Particles at Interfaces. *Chem-Eur J* **2013**, *19* (18), 5586-5594.
51. Nakahama, K.; Fujimoto, K. Thermosensitive two-dimensional arrays of hydrogel particles. *Langmuir* **2002**, *18* (26), 10095-10099.
52. Ngai, T.; Behrens, S. H.; Auweter, H. Novel emulsions stabilized by pH and temperature sensitive microgels. *Chem Commun* **2005**, (3), 331-333.
53. Heyes, D. M.; Branka, A. C. Interactions between microgel particles. *Soft Matter* **2009**, *5* (14), 2681-2685.
54. Schwenke, K.; Isa, L.; Cheung, D. L.; Del Gado, E. Conformations and Effective Interactions of Polymer-Coated Nanoparticles at Liquid Interfaces. *Langmuir* **2014**, *30* (42), 12578-12586.

55. Style, R. W.; Isa, L.; Dufresne, E. R. Adsorption of soft particles at fluid interfaces. *Soft Matter* **2015**, *11* (37), 7412-7419.
56. Destribats, M.; Lapeyre, V.; Wolfs, M.; Sellier, E.; Leal-Calderon, F.; Ravaine, V.; Schmitt, V. Soft microgels as Pickering emulsion stabilisers: role of particle deformability. *Soft Matter* **2011**, *7* (17), 7689-7698.
57. Alvarez, N. J.; Anna, S. L.; Saigal, T.; Tilton, R. D.; Walker, L. M. Interfacial Dynamics and Rheology of Polymer-Grafted Nanoparticles at Air-Water and Xylene-Water Interfaces. *Langmuir* **2012**, *28* (21), 8052-8063.
58. Mathew, M. D.; Manga, M. S.; Hunter, T. N.; Cayre, O. J.; Biggs, S. Behavior of pH-Sensitive Core Shell Particles at the Air-water Interface. *Langmuir* **2012**, *28* (11), 5085-5092.
59. Yu, K.; Zhang, H.; Hodges, C.; Biggs, S.; Xu, Z.; Cayre, O. J.; Harbottle, D. Foaming Behavior of Polymer-Coated Colloids: The Need for Thick Liquid Films. *Langmuir* **2017**, *33* (26), 6528-6539.
60. Reynaert, S.; Moldenaers, P.; Vermant, J. Interfacial rheology of stable and weakly aggregated two-dimensional suspensions. *Phys Chem Chem Phys* **2007**, *9* (48), 6463-6475.
61. Vignati, E.; Piazza, R.; Lockhart, T. P. Pickering emulsions: Interfacial tension, colloidal layer morphology, and trapped-particle motion. *Langmuir* **2003**, *19* (17), 6650-6656.
62. Midmore, B. R. Preparation of a novel silica-stabilized oil/water emulsion. *Colloid Surface A* **1998**, *132* (2-3), 257-265.
63. Harbottle, D.; Chen, Q.; Moorthy, K.; Wang, L. X.; Xu, S. M.; Liu, Q. X.; Sjoblom, J.; Xu, Z. H. Problematic Stabilizing Films in Petroleum Emulsions: Shear

Rheological Response of Viscoelastic Asphaltene Films and the Effect on Drop Coalescence. *Langmuir* **2014**, *30* (23), 6730-6738.

64. Park, B. J.; Pantina, J. P.; Furst, E. M.; Oettel, M.; Reynaert, S.; Vermant, J. Direct measurements of the effects of salt and surfactant on interaction forces between colloidal particles at water-oil interfaces. *Langmuir* **2008**, *24* (5), 1686-1694.

65. Abkarian, M.; Subramaniam, A. B.; Kim, S. H.; Larsen, R. J.; Yang, S. M.; Stone, H. A. Dissolution arrest and stability of particle-covered bubbles. *Phys Rev Lett* **2007**, *99* (18).

66. Reynaert, S.; Moldenaers, P.; Vermant, J. Control over colloidal aggregation in monolayers of latex particles at the oil-water interface. *Langmuir* **2006**, *22* (11), 4936-4945.

67. Hansen, P. H. F.; Bergstrom, L. Perikinetic aggregation of alkoxyated silica particles in two dimensions. *J Colloid Interf Sci* **1999**, *218* (1), 77-87.

68. Li, X. L.; Karakashev, S. I.; Evans, G. M.; Stevenson, P. Effect of Environmental Humidity on Static Foam Stability. *Langmuir* **2012**, *28* (9), 4060-4068.

69. Barnes, G. T. The Effects of Monolayers on the Evaporation of Liquids. *Adv Colloid Interfac* **1986**, *25* (2), 89-200.

70. Saint-Jalmes, A. Physical chemistry in foam drainage and coarsening. *Soft Matter* **2006**, *2* (10), 836-849.

71. Langevin, D. Aqueous foams and foam films stabilised by surfactants. Gravity-free studies. *Cr Mecanique* **2017**, *345* (1), 47-55.

72. Martinez, A. C.; Rio, E.; Delon, G.; Saint-Jalmes, A.; Langevin, D.; Binks, B. P. On the origin of the remarkable stability of aqueous foams stabilised by nanoparticles: link with microscopic surface properties. *Soft Matter* **2008**, *4* (7), 1531-1535.

73. Horozov, T. S. Foams and foam films stabilised by solid particles. *Curr Opin Colloid In* **2008**, *13* (3), 134-140.
74. Binks, B. P.; Horozov, T. S. Aqueous foams stabilized solely by silica nanoparticles. *Angew Chem Int Edit* **2005**, *44* (24), 3722-3725.
75. Fujii, S.; Akiyama, K.; Nakayama, S.; Hamasaki, S.; Yusa, S.; Nakamura, Y. pH- and temperature-responsive aqueous foams stabilized by hairy latex particles. *Soft Matter* **2015**, *11* (3), 572-579.
76. Arriaga, L. R.; Drenckhan, W.; Salonen, A.; Rodrigues, J. A.; Iniguez-Palomares, R.; Rio, E.; Langevin, D. On the long-term stability of foams stabilised by mixtures of nano-particles and oppositely charged short chain surfactants. *Soft Matter* **2012**, *8* (43), 11085-11097.
77. Zhang, Y.; Wang, S. C.; Zhou, J. R.; Benz, G.; Tcheimou, S.; Zhao, R. Y.; Behrens, S. H.; Meredith, J. C. Capillary Foams: Formation Stages and Effects of System Parameters. *Ind Eng Chem Res* **2017**, *56* (34), 9533-9540.
78. Zhang, Y.; Allen, M. C.; Zhao, R. Y.; Deheyn, D. D.; Behrens, S. H.; Meredith, J. C. Capillary Foams: Stabilization and Functionalization of Porous Liquids and Solids. *Langmuir* **2015**, *31* (9), 2669-2676.
79. Kyrychenko, A.; Korsun, O. M.; Gubin, I. I.; Kovalenko, S. M.; Kalugin, O. N. Atomistic Simulations of Coating of Silver Nanoparticles with Poly(vinylpyrrolidone) Oligomers: Effect of Oligomer Chain Length. *J Phys Chem C* **2015**, *119* (14), 7888-7899.
80. Pattanaik, M.; Biswal, S. K.; Bhaumik, S. K. A comparative physicochemical study of hematite with hydroxamic acid and sodium oleate. *Separ Sci Technol* **2000**, *35* (6), 919-930.

81. Knappe, P.; Bienert, R.; Weidner, S.; Thunemann, A. F. Characterization of poly(N-vinyl-2-pyrrolidone)s with broad size distributions. *Polymer* **2010**, *51* (8), 1723-1727.
82. Sulek, M. W.; Sas, W.; Wasilewski, T.; Bak-Sowinska, A.; Piotrowska, U. Polymers (Polyvinylpyrrolidones) As Active Additives Modifying the Lubricating Properties of Water. *Ind Eng Chem Res* **2012**, *51* (45), 14700-14707.
83. Zhang, Q.; Zhang, T. R.; Ge, J. P.; Yin, Y. D. Permeable silica shell through surface-protected etching. *Nano Lett* **2008**, *8* (9), 2867-2871.
84. Graf, C.; Vossen, D. L. J.; Imhof, A.; van Blaaderen, A. A general method to coat colloidal particles with silica. *Langmuir* **2003**, *19* (17), 6693-6700.
85. Thibaut, A.; Misselyn-Bauduin, A. M.; Broze, G.; Jerome, R. Adsorption of poly(vinylpyrrolidone)/surfactant(s) mixtures at the silica/water interface: A calorimetric investigation. *Langmuir* **2000**, *16* (25), 9841-9849.
86. Stuart, M. A. C.; Fler, G. J.; Scheutjens, J. M. H. M. Displacement of Polymers .2. Experiment - Determination of Segmental Adsorption Energy of Poly(Vinylpyrrolidone) on Silica. *J Colloid Interf Sci* **1984**, *97* (2), 526-535.
87. Zeng, H.; Walker, V. K.; Ripmeester, J. A. Approaches to the design of better low-dosage gas hydrate inhibitors. *Angew Chem Int Edit* **2007**, *46* (28), 5402-5404.
88. de Vos, W. M.; Cattoz, B.; Avery, M. P.; Cosgrove, T.; Prescott, S. W. Adsorption and Surfactant-Mediated Desorption of Poly(vinylpyrrolidone) on Plasma- and Piranha-Cleaned Silica Surfaces. *Langmuir* **2014**, *30* (28), 8425-8431.
89. Spruijt, E.; Biesheuvel, P. M.; de Vos, W. M. Adsorption of charged and neutral polymer chains on silica surfaces: The role of electrostatics, volume exclusion, and hydrogen bonding. *Phys Rev E* **2015**, *91* (1).

90. Guo, Y.; Hao, Z. X.; Wan, C. Tribological characteristics of polyvinylpyrrolidone (PVP) as a lubrication additive for artificial knee joint. *Tribol Int* **2016**, *93*, 214-219.
91. Li, Y.; Rojas, O. J.; Hinestroza, J. P. Boundary Lubrication of PEO-PPO-PEO Triblock Copolymer Physisorbed on Polypropylene, Polyethylene, and Cellulose Surfaces. *Ind Eng Chem Res* **2012**, *51* (7), 2931-2940.
92. Ram, A.; Finkelst.E; Elata, C. Reduction of Friction in Oil Pipelines by Polymer Additives. *Ind Eng Chem Proc Dd* **1967**, *6* (3), 309-&.
93. Jahn, S.; Klein, J. Hydration Lubrication: The Macromolecular Domain. *Macromolecules* **2015**, *48* (15), 5059-5075.
94. Klein, J. Shear, friction, and lubrication forces between polymer-bearing surfaces. *Annu Rev Mater Sci* **1996**, *26*, 581-612.
95. Liu, X. M.; Song, J. L.; Wu, D.; Genzer, J.; Theyson, T.; Rojas, O. J. Surface and Friction Behavior of a Silicone Surfactant Adsorbed on Model Textiles Substrates. *Ind Eng Chem Res* **2010**, *49* (18), 8550-8557.
96. Dehghani, E. S.; Ramakrishna, S. N.; Spencer, N. D.; Benetti, E. M. Controlled Crosslinking Is a Tool To Precisely Modulate the Nanomechanical and Nanotribological Properties of Polymer Brushes. *Macromolecules* **2017**, *50* (7), 2932-2941.
97. Nomura, A.; Okayasu, K.; Ohno, K.; Fukuda, T.; Tsujii, Y. Lubrication Mechanism of Concentrated Polymer Brushes in Solvents: Effect of Solvent Quality and Thereby Swelling State. *Macromolecules* **2011**, *44* (12), 5013-5019.
98. Dehghani, E. S.; Du, Y. H.; Zhang, T.; Ramakrishna, S. N.; Spencer, N. D.; Jordan, R.; Benetti, E. M. Fabrication and Interfacial Properties of Polymer Brush

- Gradients by Surface-Initiated Cu(0)-Mediated Controlled Radical Polymerization. *Macromolecules* **2017**, *50* (6), 2436-2446.
99. Wijmans, C. M.; Zhulina, E. B.; Fler, G. J. Effect of Free Polymer on the Structure of a Polymer Brush and Interaction between 2 Polymer Brushes. *Macromolecules* **1994**, *27* (12), 3238-3248.
100. Witten, T. A.; Leibler, L.; Pincus, P. A. Stress-Relaxation in the Lamellar Copolymer Mesophase. *Macromolecules* **1990**, *23* (3), 824-829.
101. Nalam, P. C.; Ramakrishna, S. N.; Espinosa-Marzal, R. M.; Spencer, N. D. Exploring Lubrication Regimes at the Nanoscale: Nanotribological Characterization of Silica and Polymer Brushes in Viscous Solvents. *Langmuir* **2013**, *29* (32), 10149-10158.
102. Stokes, J. R.; Macakova, L.; Chojnicka-Paszun, A.; de Kruif, C. G.; de Jongh, H. H. J. Lubrication, Adsorption, and Rheology of Aqueous Polysaccharide Solutions. *Langmuir* **2011**, *27* (7), 3474-3484.
103. Starck, P.; Mosse, W. K. J.; Nicholas, N. J.; Spiniello, M.; Tyrrell, J.; Nelson, A.; Qiao, G. G.; Ducker, W. A. Surface chemistry and rheology of polysulfobetaine-coated silica. *Langmuir* **2007**, *23* (14), 7587-7593.
104. Wei, Q. B.; Cai, M. R.; Zhou, F.; Liu, W. M. Dramatically Tuning Friction Using Responsive Polyelectrolyte Brushes. *Macromolecules* **2013**, *46* (23), 9368-9379.
105. Xu, D.; Hodges, C.; Ding, Y. L.; Biggs, S.; Brooker, A.; York, D. Adsorption Kinetics of Laponite and Ludox Silica Nanoparticles onto a Deposited Poly(diallyldimethylammonium chloride) Layer Measured by a Quartz Crystal Microbalance and Optical Reflectometry. *Langmuir* **2010**, *26* (23), 18105-18112.
106. Crespo-Quesada, M.; Andanson, J. M.; Yarulin, A.; Lim, B.; Xia, Y. N.; Kiwi-Minsker, L. UV-Ozone Cleaning of Supported Poly(vinylpyrrolidone)-Stabilized

Palladium Nanocubes: Effect of Stabilizer Removal on Morphology and Catalytic Behavior. *Langmuir* **2011**, *27* (12), 7909-7916.

107. Bakhtiari, M. T.; Harbottle, D.; Curran, M.; Ng, S.; Spence, J.; Siy, R.; Liu, Q. X.; Masliyah, J.; Xu, Z. H. Role of Caustic Addition in Bitumen-Clay Interactions. *Energ Fuel* **2015**, *29* (1), 58-69.

108. Rodahl, M.; Hook, F.; Fredriksson, C.; Keller, C. A.; Krozer, A.; Brzezinski, P.; Voinova, M.; Kasemo, B. Simultaneous frequency and dissipation factor QCM measurements of biomolecular adsorption and cell adhesion. *Faraday Discuss* **1997**, *107*, 229-246.

109. Vandebriel, S.; Franck, A.; Fuller, G. G.; Moldenaers, P.; Vermant, J. A double wall-ring geometry for interfacial shear rheometry. *Rheol Acta* **2010**, *49* (2), 131-144.

110. Goodwin, D. J.; Sepassi, S.; King, S. M.; Holland, S. J.; Martini, L. G.; Lawrence, M. J. Characterization of Polymer Adsorption onto Drug Nanoparticles Using Depletion Measurements and Small-Angle Neutron Scattering. *Mol Pharmaceut* **2013**, *10* (11), 4146-4158.

111. Hodges, C. S.; Biggs, S.; Walker, L. Complex Adsorption Behavior of Rodlike Polyelectrolyte-Surfactant Aggregates. *Langmuir* **2009**, *25* (8), 4484-4489.

112. Sauerbrey, G. Verwendung Von Schwingquarzen Zur Wagung Dunner Schichten Und Zur Mikrowagung. *Z Phys* **1959**, *155* (2), 206-222.

113. Voinova, M. V.; Rodahl, M.; Jonson, M.; Kasemo, B. Viscoelastic acoustic response of layered polymer films at fluid-solid interfaces: Continuum mechanics approach. *Phys Scripta* **1999**, *59* (5), 391-396.

114. Kanazawa, K. K.; Gordon, J. G. The Oscillation Frequency of a Quartz Resonator in Contact with a Liquid. *Anal Chim Acta* **1985**, *175* (Sep), 99-105.

115. Qiu, H.; Bousmina, M. New technique allowing the quantification of diffusion at polymer polymer interfaces using rheological analysis: Theoretical and experimental results. *J Rheol* **1999**, *43* (3), 551-568.
116. Fleming, B. D.; Wanless, E. J.; Biggs, S. Nonequilibrium mesoscale surface structures: The adsorption of polymer-surfactant mixtures at the solid/liquid interface. *Langmuir* **1999**, *15* (25), 8719-8725.
117. Gao, J. P.; Luedtke, W. D.; Gourdon, D.; Ruths, M.; Israelachvili, J. N.; Landman, U. Frictional forces and Amontons' law: From the molecular to the macroscopic scale. *J Phys Chem B* **2004**, *108* (11), 3410-3425.
118. Dzuy, N. Q.; Boger, D. V. Yield Stress Measurement for Concentrated Suspensions. *J Rheol* **1983**, *27* (4), 321-349.
119. Wang, X. Y.; Feng, X. Y.; Ma, G. P.; Yao, L.; Ge, M. F. Amphiphilic Janus Particles Generated via a Combination of Diffusion-Induced Phase Separation and Magnetically Driven Dewetting and Their Synergistic Self-Assembly. *Adv Mater* **2016**, *28* (16), 3131-3137.
120. Tao, A.; Sinsersuksakul, P.; Yang, P. Tunable plasmonic lattices of silver nanocrystals. *Nat Nanotechnol* **2007**, *2* (7), 435-440.
121. Tao, A. R.; Huang, J. X.; Yang, P. D. Langmuir-Blodgett of Nanocrystals and Nanowires. *Accounts Chem Res* **2008**, *41* (12), 1662-1673.
122. Lee, Y. H.; Lee, C. K.; Tan, B. R.; Tan, J. M. R.; Phang, I. Y.; Ling, X. Y. Using the Langmuir-Schaefer technique to fabricate large-area dense SERS-active Au nanoprism monolayer films. *Nanoscale* **2013**, *5* (14), 6404-6412.
123. Kostakis, T.; Ettelaie, R.; Murray, B. S. Effect of high salt concentrations on the stabilization of bubbles by silica particles. *Langmuir* **2006**, *22* (3), 1273-1280.

124. San-Miguel, A.; Behrens, S. H. Influence of Nanoscale Particle Roughness on the Stability of Pickering Emulsions. *Langmuir* **2012**, *28* (33), 12038-12043.
125. Briceno-Ahumada, Z.; Langevin, D. On the influence of surfactant on the coarsening of aqueous foams. *Adv Colloid Interface Sci* **2015**.
126. Maestro, A.; Rio, E.; Drenckhan, W.; Langevin, D.; Salonen, A. Foams stabilised by mixtures of nanoparticles and oppositely charged surfactants: relationship between bubble shrinkage and foam coarsening. *Soft Matter* **2014**, *10* (36), 6975-6983.
127. Maestro, A.; Guzman, E.; Santini, E.; Ravera, F.; Liggieri, L.; Ortega, F.; Rubio, R. G. Wettability of silica nanoparticle-surfactant nanocomposite interfacial layers. *Soft Matter* **2012**, *8* (3), 837-843.
128. Erni, P.; Jerri, H. A.; Wong, K.; Parker, A. Interfacial viscoelasticity controls buckling, wrinkling and arrest in emulsion drops undergoing mass transfer. *Soft Matter* **2012**, *8* (26), 6958-6967.
129. Guerrini, R. M.; Lochhead, R. Y.; Daly, W. H. Interactions of aminoalkylcarbonyl cellulose derivatives and sodium dodecyl sulfate. 2. Foam stabilization. *Colloid Surface A* **1999**, *147* (1-2), 67-78.
130. Geisel, K.; Isa, L.; Richtering, W. Unraveling the 3D Localization and Deformation of Responsive Microgels at Oil/Water Interfaces: A Step Forward in Understanding Soft Emulsion Stabilizers. *Langmuir* **2012**, *28* (45), 15770-15776.
131. Li, Z. F.; Harbottle, D.; Pensini, E.; Ngai, T.; Richtering, W.; Xu, Z. H. Fundamental Study of Emulsions Stabilized by Soft and Rigid Particles. *Langmuir* **2015**, *31* (23), 6282-6288.

132. Niskanen, J.; Wu, C.; Ostrowski, M.; Fuller, G. G.; Hietala, S.; Tenhu, H. Thermoresponsiveness of PDMAEMA. Electrostatic and Stereochemical Effects. *Macromolecules* **2013**, *46* (6), 2331-2340.
133. Ullrich, S.; Scheeler, S. P.; Pacholski, C.; Spatz, J. P.; Kudera, S. Formation of Large 2D Arrays of Shape-Controlled Colloidal Nanoparticles at Variable Interparticle Distances. *Part Part Syst Char* **2013**, *30* (1), 102-108.
134. Isa, L.; Calzolari, D. C. E.; Pontoni, D.; Gillich, T.; Nelson, A.; Zirbs, R.; Sanchez-Ferrer, A.; Mezzenga, R.; Reimhult, E. Core-shell nanoparticle monolayers at planar liquid-liquid interfaces: effects of polymer architecture on the interface microstructure. *Soft Matter* **2013**, *9* (14), 3789-3797.
135. Geisel, K.; Rudov, A. A.; Potemkin, I. I.; Richtering, W. Hollow and Core-Shell Microgels at Oil-Water Interfaces: Spreading of Soft Particles Reduces the Compressibility of the Monolayer. *Langmuir* **2015**, *31* (48), 13145-13154.
136. Aston, M. S. The Study of Surfactant Monolayers by Surface Pressure Area Measurement. *Chem Soc Rev* **1993**, *22* (1), 67-71.
137. McNamee, C. E., Yamamoto, S., Butt, H., Higashitani, K. A Straightforward Way To Form Close-Packed TiO₂ Particle Monolayers at an Air/Water Interface. *Langmuir* **2010**, *27*, 887-894.
138. Razavi, S. C., K. D.; Lin, B.; Lee, K. Y. C.; Tu, R. S.; Kretzschmar, I. Collapse of Particle-Laden Interfaces under Compression: Buckling vs Particle Expulsion. *Langmuir* **2015**, *31*, 7764-7775.
139. Noskov, B. A.; Akentiev, A. V.; Loglio, G.; Miller, R. Dynamic surface properties of solutions of poly(ethylene oxide) and polyethylene glycols. *J Phys Chem B* **2000**, *104* (33), 7923-7931.

140. Noskov, B. A.; Akentiev, A. V.; Miller, R. Dynamic surface properties of poly(vinylpyrrolidone) solutions. *J Colloid Interf Sci* **2002**, *255* (2), 417-424.
141. Saint-Jalmes, A.; Langevin, D. Time evolution of aqueous foams: drainage and coarsening. *J Phys-Condens Mat* **2002**, *14* (40), 9397-9412.
142. Hackbarth, J. J. Multivariate analyses of beer foam stand. *J I Brewing* **2006**, *112* (1), 17-24.
143. Dale, C.; West, C.; Eade, J.; Rito-Palomares, M.; Lyddiatt, N. Studies on the physical and compositional changes in collapsing beer foam. *Chem Eng J* **1999**, *72* (1), 83-89.
144. Hunter, T. N.; Wanless, E. J.; Jameson, G. J. Effect of esterically bonded agents on the monolayer structure and foamability of nano-silica. *Colloid Surface A* **2009**, *334* (1-3), 181-190.
145. Carn, F.; Colin, A.; Pitois, O.; Vignes-Adler, M.; Backov, R. Foam Drainage in the Presence of Nanoparticle-Surfactant Mixtures. *Langmuir* **2009**, *25* (14), 7847-7856.
146. Haffner, B.; Khidas, Y.; Pitois, O. Flow and jamming of granular suspensions in foams. *Soft Matter* **2014**, *10* (18), 3277-3283.
147. Vella, D.; Aussillous, P.; Mahadevan, L. Elasticity of an interfacial particle raft. *Europhys Lett* **2004**, *68* (2), 212-218.
148. Bhamla, M. S.; Giacomini, C. E.; Balemans, C.; Fuller, G. G. Influence of interfacial rheology on drainage from curved surfaces. *Soft Matter* **2014**, *10* (36), 6917-6925.
149. Israelachvili, J. N. *Intermolecular and Surface Forces*; Third ed.; Elsevier: USA, 2011.

150. Natarajan, A.; Kuznicki, N.; Harbottle, D.; Masliyah, J.; Zeng, H.; Xu, Z. Molecular Interactions between a Biodegradable Demulsifier and Asphaltenes in an Organic Solvent. *Energy & Fuels* **2016**.
151. Dickinson, E.; Ettelaie, R.; Kostakis, T.; Murray, B. S. Factors controlling the formation and stability of air bubbles stabilized by partially hydrophobic silica nanoparticles. *Langmuir* **2004**, *20* (20), 8517-8525.
152. Dickinson, E. Biopolymer-based particles as stabilizing agents for emulsions and foams. *Food Hydrocolloid* **2017**, *68*, 219-231.
153. Grauzinyte, M.; Forth, J.; Rumble, K. A.; Clegg, P. S. Particle-Stabilized Water Droplets that Sprout Millimeter-Scale Tubes. *Angew Chem Int Edit* **2015**, *54* (5), 1456-1460.
154. Dickinson, E. Food emulsions and foams: Stabilization by particles. *Curr Opin Colloid In* **2010**, *15* (1-2), 40-49.
155. Cicuta, P.; Stancik, E. J.; Fuller, G. G. Shearing or compressing a soft glass in 2D: Time-concentration superposition. *Phys Rev Lett* **2003**, *90* (23).
156. Horozov, T. S.; Aveyard, R.; Clint, J. H.; Neumann, B. Particle zips: Vertical emulsion films with particle monolayers at their surfaces. *Langmuir* **2005**, *21* (6), 2330-2341.
157. Horozov, T. S.; Binks, B. P. Particle-stabilized emulsions: A bilayer or a bridging monolayer? *Angew Chem Int Edit* **2006**, *45* (5), 773-776.
158. Jarrett, E.; Ireland, P. M.; Webber, G. B.; Wanless, E. J. Particle-liquid structures formed by electric fields. *Powder Technol* **2016**, *297*, 1-7.
159. Danov, K. D.; Kralchevsky, P. A.; Naydenov, B. N.; Brenn, G. Interactions between particles with an undulated contact line at a fluid interface: Capillary multipoles of arbitrary order. *J Colloid Interf Sci* **2005**, *287* (1), 121-134.

160. Horozov, T. S.; Aveyard, R.; Binks, B. P.; Clint, J. H. Structure and stability of silica particle monolayers at horizontal and vertical octane-water interfaces. *Langmuir* **2005**, *21* (16), 7405-7412.
161. Binks, B. P.; Horozov, T. S.; Eds. *Colloidal Particles at Liquid Interfaces*; Cambridge University Press: Cambridge, U.K., 2006.
162. Morse, A. J.; Tan, S. Y.; Giakoumatos, E. C.; Webber, G. B.; Armes, S. P.; Ata, S.; Wanless, E. J. Arrested coalescence behaviour of giant Pickering droplets and colloidosomes stabilised by poly(tert-butylaminoethyl methacrylate) latexes. *Soft Matter* **2014**, *10* (31), 5669-5681.
163. Stancik, E. J.; Hawkinson, A. L.; Vermant, J.; Fuller, G. G. Dynamic transitions and oscillatory melting of a two-dimensional crystal subjected to shear flow. *J Rheol* **2004**, *48* (1), 159-173.
164. Tambe, D. E.; Sharma, M. M. The Effect of Colloidal Particles on Fluid-Fluid Interfacial Properties and Emulsion Stability. *Adv Colloid Interfac* **1994**, *52*, 1-63.
165. Pensini, E.; Harbottle, D.; Yang, F.; Tchoukov, P.; Li, Z. F.; Kailey, I.; Behles, J.; Masliyah, J.; Xu, Z. H. Demulsification Mechanism of Asphaltene-Stabilized Water-in-Oil Emulsions by a Polymeric Ethylene Oxide Propylene Oxide Demulsifier. *Energ Fuel* **2014**, *28* (11), 6760-6771.
166. Xu, R.; Dickinson, E.; Murray, B. S. Morphological changes in adsorbed protein films at the air-water interface subjected to large area variations, as observed by Brewster angle microscopy. *Langmuir* **2007**, *23* (9), 5005-5013.
167. Verwijlen, T.; Moldenaers, P.; Stone, H. A.; Vermant, J. Study of the Flow Field in the Magnetic Rod Interfacial Stress Rheometer. *Langmuir* **2011**, *27* (15), 9345-9358.

168. Brooks, C. F.; Fuller, G. G.; Frank, C. W.; Robertson, C. R. An interfacial stress rheometer to study rheological transitions in monolayers at the air-water interface. *Langmuir* **1999**, *15* (7), 2450-2459.
169. Naumann, C. A.; Brooks, C. F.; Fuller, G. G.; Knoll, W.; Frank, C. W. Viscoelastic properties of lipopolymers at the air-water interface: A combined interfacial stress rheometer and film balance study. *Langmuir* **1999**, *15* (22), 7752-7761.
170. Truzzolillo, D.; Sharaf, H.; Jonas, U.; Loppinet, B.; Vlassopoulos, D. Tuning the Structure and Rheology of Polystyrene Particles at the Air-Water Interface by Varying the pH. *Langmuir* **2016**, *32* (27), 6956-6966.
171. Binks, B. P.; Kirkland, M.; Rodrigues, J. A. Origin of stabilisation of aqueous foams in nanoparticle-surfactant mixtures. *Soft Matter* **2008**, *4* (12), 2373-2382.
172. LoPresti, C.; Massignani, M.; Fernyhough, C.; Blanz, A.; Ryan, A. J.; Madsen, J.; Warren, N. J.; Armes, S. P.; Lewis, A. L.; Chirasatitsin, S.; Engler, A. J.; Battaglia, G. Controlling Polymersome Surface Topology at the Nanoscale by Membrane Confined Polymer/Polymer Phase Separation. *Acs Nano* **2011**, *5* (3), 1775-1784.
173. Verruto, V. J.; Le, R. K.; Kilpatrick, P. K. Adsorption and Molecular Rearrangement of Amphoteric Species at Oil-Water Interfaces. *J Phys Chem B* **2009**, *113* (42), 13788-13799.
174. Barman, S.; Christopher, G. F. Role of capillarity and microstructure on interfacial viscoelasticity of particle laden interfaces. *J Rheol* **2016**, *60* (1), 35-45.
175. Trappe, V.; Weitz, D. A. Scaling of the viscoelasticity of weakly attractive particles. *Phys Rev Lett* **2000**, *85* (2), 449-452.

176. Zang, D. Y.; Langevin, D.; Binks, B. P.; Wei, B. B. Shearing particle monolayers: Strain-rate frequency superposition. *Phys Rev E* **2010**, *81* (1).
177. Beltramo, P. J.; Gupta, M.; Alicke, A.; Liascukiene, I.; Gunes, D. Z.; Baroud, C. N.; Vermant, J. Arresting dissolution by interfacial rheology design. *P Natl Acad Sci USA* **2017**, *114* (39), 10373-10378.